

Journal Pre-proofs

Advances in structural engineering and electrochemical insights of MXene-based derivates for next generation micro-supercapacitor with tuneable ink, microelectrode design, and scalable manufacturing strategies

Jyoti Prakash Das, V. Navakoteswara Rao, Sang-Jae Kim

PII: S0079-6425(25)00179-3

DOI: <https://doi.org/10.1016/j.pmatsci.2025.101599>

Reference: JPMS 101599



To appear in: *Progress in Materials Science*

Received Date: 25 February 2025

Revised Date: 5 September 2025

Accepted Date: 1 November 2025

Please cite this article as: Das, J.P., Navakoteswara Rao, V., Kim, S-J., Advances in structural engineering and electrochemical insights of MXene-based derivates for next generation micro-supercapacitor with tuneable ink, microelectrode design, and scalable manufacturing strategies, *Progress in Materials Science* (2025), doi: <https://doi.org/10.1016/j.pmatsci.2025.101599>

This is a PDF of an article that has undergone enhancements after acceptance, such as the addition of a cover page and metadata, and formatting for readability. This version will undergo additional copyediting, typesetting and review before it is published in its final form. As such, this version is no longer the Accepted Manuscript, but it is not yet the definitive Version of Record; we are providing this early version to give early visibility of the article. Please note that Elsevier's sharing policy for the Published Journal Article applies to this version, see: <https://www.elsevier.com/about/policies-and-standards/sharing#4-published-journal-article>. Please also note that, during the production process, errors may be discovered which could affect the content, and all legal disclaimers that apply to the journal pertain.

© 2025 Elsevier Ltd. All rights are reserved, including those for text and data mining, AI training, and similar technologies.

**Advances in structural engineering and electrochemical insights of MXene-based
derivates for Next Generation Micro-Supercapacitor with Tuneable Ink, Microelectrode
Design, and Scalable Manufacturing strategies**

Jyoti Prakash Das¹, V. Navakoteswara Rao¹, Sang-Jae Kim^{1,2,3,4*}

¹Nanomaterials & System Lab, Major of Mechatronics Engineering, Faculty of Applied Energy System, Jeju National University, Jeju- 63243, Republic of Korea.

²Nanomaterials & System Lab, Major of Mechanical System Engineering, College of Engineering, Jeju National University, Jeju- 63243, Republic of Korea.

³Green Hydrogen Glocal Leading Research Center (gH₂-RC), Jeju National University, Jeju 63243, Republic of Korea

⁴Research Institute of New Energy Industry (RINEI), Jeju National University, Jeju- 63243, Republic of Korea.

*Corresponding Email id: kimsangj@jejunu.ac.kr

Abstract

MXenes, an exceptional class of materials that are present in all dimension forms, have garnered significant interest owing to their enormous potential in electrochemical energy storage. The article encompasses different synthesis techniques and their effect on the structure, electrical properties, and surface properties of MXenes. We highlighted the recent development in composition optimization, surface engineering, and structure design has achieved remarkable device performance with reported specific capacitance values ranging from 100 to 1000 mF/cm². The application of machine learning to surface feature optimization and MXene structure prediction is also mentioned. Furthermore, the efficacy of operando and in situ characterization techniques such as in situ Raman spectroscopy, synchrotron XRD, and XANS is discussed. These methods explored the structure evolution, oxidation state, and charge transport upon operation. In short, we envision the integration of MXene with advanced techniques of electrode preparation like inkjet printing, screen printing, and additive manufacturing. These methods provide high-resolution, tuneable, and scalable patterning of electrodes and hence establish possibilities for applications in microsupercapacitors. The purpose of this review is to give a holistic picture of the design approaches of MXene properties by synthesis and processing techniques, and to describe the scaling from laboratory-scale concepts to energy storage applications.

Keywords: MXene; SWOT analysis; Morphology; In-situ analysis; and rheology

1. Introduction

The advent of the Internet of Things (IoTs) and Artificial Intelligence (AI) has attracted tremendous research interest in extremely sustainable, efficient miniature energy storage systems like micro-supercapacitors (MSCs) and micro-batteries [1], [2]. The ease of fabrication technique, fast charging, and wide range of material availability made micro-supercapacitors a potential candidate for energy storage applications in recent times [3], [4], [5], [6]. The drastic reduction in the size of portable and wearable electronics urged to reduce the size of power sources to the micro level without compromising the electrochemical properties [7], [8], [9]. The traditional supercapacitors limit their application in real-time microelectronics due to the conventional sandwich-type structure and thicker size[1].To address this barrier, MSCs with flexible substrates and in-plane electrode designs are explored for enhanced compatibility with the existing low-power electronics [1], [2]. The MSC's performance greatly depends on the electrode material [3], [4], [5], [6], [7], [8], [9], [10], [11]. Therefore, materials with excellent electrochemical properties, unique structures, Conductivity, and higher porosity are desired for energy storage applications[1], [12], [13], [14], [15] Classification of materials based on their dimensions is summarized in **Table 1**. Among those materials, 2D materials with remarkable surface area, quantum confinement effect, and unique crystal structure are explored for high-performance electrochemical supercapacitors. Among 2D materials wonder material graphene, Transition metal dichalcogenides (TMDs)[16], layered double hydroxide (LDH)[17], [18][19], metal-organic framework (MOF)[20], covalent organic framework (COF) [21], [22]

hexagonal boron nitrides[23], [24], germanene, silicene, phosphorene, antimonene, bismuthine, and tellurene, etc are widely employed in various energy storage devices[25], [26], [27], [28]. The atomic layer of thin materials with distinct electronic structures and, higher surface-to-volume ratios stand ahead of the bulk materials for energy storage and revolutionize the arena of material science by leading to the discovery of the wonder material MXene[15], [29], [30], [31], [32].

MXene belongs to the class of 2D layered transition metal carbides, nitrides, or carbonitrides[33], [34], [35]. High electrical conductivity, tuneable layered structure, higher ionic diffusion, thermal stability, and superior hydrophilicity make MXenes a promising electrode material[36], [37], [38], [39]. MXene stands with the formula $M_{n+1}X_nT_x$ ($n=1-4$), where M symbolizes transition metal (e.g., Ti, V, or Mo), X represents C, N, or CN, and T_x for the surface functional groups (F, O or OH) attached during the synthesis process as illustrated in **Fig. 1(a)**. The MAX phase undergoes selective etching of Al, Ga, or Si from its parent MAX phase through various techniques. As of now, around 30 MXene derivatives have been synthesized [40], [41], [42], [43], [44], [45]. Being a pseudocapacitive material, various factors attribute to the excellent electrochemical properties of MXene[33].

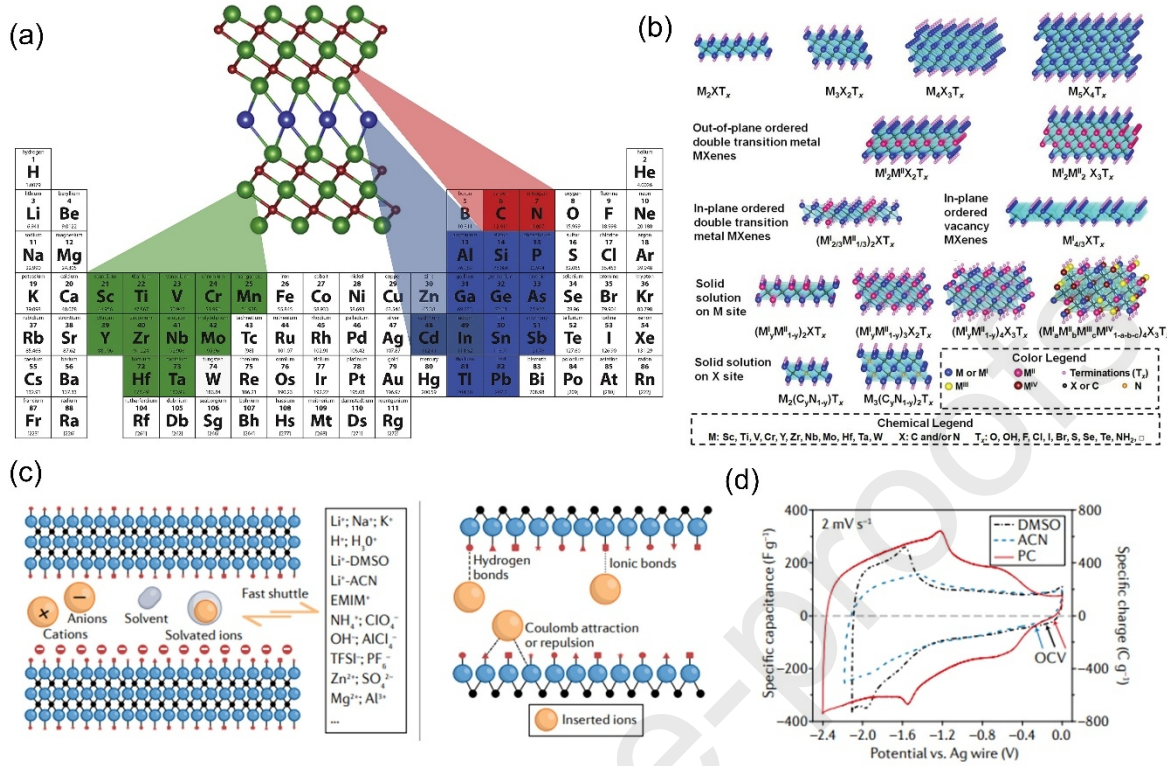


Fig. 1 (a) MAX phase forming elements $M_{n+1}AX_n$. Reproduced with permission from [69] © 2019 Elsevier Ltd (b) Broad classification of MXene structure and composition with formula $M_{n+1}AX_n$, where M sites are occupied by early transition metals, A belongs to carbide or nitride, n value varies from 1 to 4. Reproduced with permission from [193] © 2021 Wiley-VCH GmbH (c) illustration of pseudocapacitive energy storage mechanism in MXene electrodes and Intercalated ion and MXene electrode interaction (d) CV curve of Titanium carbide MXene electrode under 1M organic electrolytes. Reproduced with permission from [194] © 2022, Springer Nature Limited.

Firstly, (i) free electrons present in MXene sheets provide higher metallic conductivity, (ii) 2D sheet structure enables faster ion migration and enhanced electrochemical activity, and tuneable interlayer spacing provides abundant space for ion storage (iii) Superior hydrophilicity along with surface functional groups enables faster redox reaction. The aforementioned properties make MXene a wonder material in electrochemical energy storage applications and suitable for high-performance MSC fabrication. With the advancement in material science, researchers have triggered the formulation of new MAX phases. The atomistic model of MXene is diversified based on the MAX phases and etching process. Fig.

1(b) illustrates the wide variation in the atomistic model of MXene synthesized to date. The diversity in the atomic model of MXene differs according to the order of planes comprising transition metals. Broadly, the structure is classified as out-of-plane ordered double TM MXene, In-plane ordered TM MXene, in-plane vacancy structure, or out-of-plane ordered structure. Owing to the excellent inherent physicochemical properties like hydrophilicity, excellent conductivity, and lamellar structure of 2D MXene sheets makes it an excellent material for electrochemical energy storage. The electrochemical signature of MXene varies for charge storage and stable electrochemical performance under different electrolyte conditions. The charge-storage performance varies from EDLC to pseudocapacitive based on the salt solution. **Fig. 1(c)** illustrates the ion migration along the interlayer spacing of the MXene sheets. The interlayer spacing facilitates the migration of both cations and anions in solvated and non-solvated states. Further, the interaction of ions and their inherent properties governs the electrochemical behavior of MXene. The intercalated ion and MXene electrodes interact, which leads to the charge increment, neutralization, or decrement. CV curves under various electrolytes, as depicted, represent pseudocapacitive behavior resulting from the net cation storage in the organic electrolyte (**Fig. 1(d)**). With the remarkable development of microfabrication techniques and advanced equipment, the MSC fabrication techniques provide precise control and reproducibility performance on a large scale[46], [47], [48], [49], [50]. To attain the properties of conductive MXene, ink synthesis has attracted the attention of the broader research community[51], [52], [53], [54]. MXene ink properties govern the microelectrode design and properties that reflect the energy storage performance[55]. Among the microelectrode fabrication techniques, screen printing, casting, electrospinning, direct ink writing, laser engraving, inkjet printing, etc, are noteworthy. The hydrophilicity and negative zeta potential of MXene make it compatible with various printing and coating techniques[56], [57]. A wide range of solvents is compatible with MXene and form stable colloidal solutions, enabling microelectrode printing[58]. Besides these advantages, several challenges in ink formulation limit the widespread applicability of MXene inks in electrode printing[59], [60]. The MXene ink rheology varies according to the particle size, binder, and solvents, which result in the changes in viscosity and surface tension affecting the printability and reproducibility of the electrochemical properties[52], [61], [62]. Another crucial challenge to achieve better wettability and high-precision printability, the surface charge of both ink and

substrate needs to be matched. The mismatch between surface energies lead to the deformation in electrodes and poor adhesion of the active material over curing. Considering these challenges, an in-depth analysis of MXene ink rheology is crucial for fabricating high-quality electrodes with enhanced electrochemical properties[63]. In addition to this, MXene-based composite films have undergone laser engraving techniques to form free-standing IDT electrodes for micro energy storage units[49], [64], [65]. The laser engraving technique is independent of ink rheology, which needs MXene slurry coated over any substrate or free-standing MXene /MXene composite films. Laser power, exposure time, and computer-aided design are the factors that affect the fabrication of laser-scribed MXene-based energy storage devices.

The Planar IDT structure of MSC offered access to integrate energy storage and microelectronics over a single substrate[66], [67], [68], [69], [70], [71]. Peng et al.,[72] fabricated an MXene based on chip MSC through the conventional spray coating technique. The electrochemical performance was influenced by the flake sizes as evidenced by the specific capacitance of 27 mF cm^{-2} with an excellent capacitance retention of 100 % over 10k cycles. Haibo and co-workers examined the combination of vacuum-assisted filtration and laser engraving techniques for fabricating planar IDT electrodes comprised of MXene-based symmetric electrodes[73]. The porosity and conductivity of MXene contributed to the remarkable specific capacitance of 27.29 mF cm^{-2} which is around 460 % higher as compared to carbon-based MSCs. Benefiting from the synergetic effect of graphene and MXene Yang et al.,[74] fabricated hybrid composite yarns via wet spinning for flexible energy storage application, 372.2 mF cm^{-2} . Salles et al.,[75] developed a simple dip-coating and mechanical etching technique to fabricate high-performance MSC, benefiting from the metallic conductivity and solution processability. The Ti_3C_2 -based MSC exhibited a capacitance of $283 \mu\text{F cm}^{-2}$ on increasing the electrode thickness. Increasing the deposition time, the electrode conductivity was enhanced remarkably which favoured the rise in electrochemical performance. Zhang et al.,[62] introduced an additive-free direct printing technique of MXene-based MSC to reduce the influence of additives and surfactants on the electrochemical properties. Benefiting from the binder-free printing technique, the MSCs exhibited a specific capacitance of 563 F cm^{-3} . Researchers have utilized the metallic conductivity of MXene flakes

that favors faster ion migration and abundant active sites for uninterrupted electrochemical reactions. Asymmetric planar MSCs offer higher energy density in a confined area as compared to symmetric MSCs. Xu et al.,[76] fabricated an AMSC by screen printing technique, which attains an energy density of $8.84 \mu\text{Wh cm}^{-2}$ and remarkable stability of 92 % over 10,000 cycles. The large interlayer spacing of MXene was utilized for fabricating the high-performance coplanar AMSC. Yang et al.,[77] introduced a novel fabrication technique of free-standing MXene electrodes. The freeze-dried current collector-free MSC acquires a high specific area and unique architecture containing 1-3 nm MXene sheets. Benefiting from the novel architecture and unique fabrication technique, the MSC attains a specific capacitance of 2.1 F cm^{-2} with a 90 % capacitance over 10,000 cycles. Qin et al.,[78] reported a unique electro-polymerization technique to synthesize a hybrid composite that exhibits a unique porous structure grown over MXene sheets. The EP contributes excellent pseudocapacitive behaviour that attains a specific capacitance of 69.5 mF cm^{-2} , benefiting the structure engineering of MXene sheets. Large-scale fabrication of MSCs is limited owing to the lack of an advanced fabrication strategy. Zheng et al.,[79] addressed the issue by developing screen-printed MXene MSCs that deliver a specific capacitance of 1.1 F cm^{-2} . The tuned rheology of MXene ink enables the fabrication of a high-performance microenergy system. Kim et al.,[80] reported a dimension-tuning strategy to fabricate high-performance MSC electrodes. FIB technique utilized coplanar electrodes that exhibit a specific capacitance of 317 mF cm^{-2} benefiting the unique structure of the composite where CNT prevents the restacking of the MXene sheets and enhances the interlayer spacing, which allows faster ion migration through the stable interlayer channels. Cao et al.,[81] addressed the issue of restacking MXene sheets by incorporating bacterial nanocellulose, which widens the ion migration path and enhances the electrochemical performance that exhibits an energy density of $34.0 \mu\text{Wh cm}^{-2}$.

The aforementioned research highlights the versatility of MXene in micro-supercapacitors. Despite the overwhelming research interest in MXene MSC fabrication technology, there is still a lack of systematic research into MXene physicochemical properties, including ink rheology, electrode fabrication techniques, and design optimization. Considering these factors, we've organized this review as follows: Initially, we have discussed various MXene synthesis techniques to date, and the effect of the etchant on the

physicochemical properties is highlighted. Followed by the synthesis technique MXene ink formulation and necessary rheological properties are discussed. Based on the ink rheology and MXene composites, various advancements in printing techniques and microelectrode design are summarized as shown in **Fig. 2**. The fabricated microelectrodes with optimized design and superior electrochemical behavior are discussed. In the final verdict, we have provided our views on the challenges and prospects of high-performance MXene MSCs.

Table 1 Dimensional Classification of Materials with Their Advantages and Challenges for Electrochemical Energy Storage Applications

Material	Advantages	Challenges
0D	<ul style="list-style-type: none"> a) High area-to-volume ratio b) Abundant active sites for charge storage c) Higher electron access d) Tuneable electrochemical properties 	<ul style="list-style-type: none"> a) Challenging synthesis techniques b) Difficult mass production c) Agglomeration decays inherent properties
1D	<ul style="list-style-type: none"> a) Rapid electron transport b) A high aspect ratio provides a large electrochemical active area c) Better mechanical stability 	<ul style="list-style-type: none"> a) Complex synthesis techniques b) Limited scalability c) Defects and interfaces with electrolytes compromise the electrochemical properties.
2D	<ul style="list-style-type: none"> a) Higher surface area b) Higher ionic conductivity c) Fast charge transfer d) Thin and lightweight 	<ul style="list-style-type: none"> a) Prone to restacking b) Interlayer resistance hinders ion diffusion c) Limited active sites at edges and defects
3D	<ul style="list-style-type: none"> a) Large electrochemical active area 	<ul style="list-style-type: none"> a) Complex synthesis technique b) Critical material selection

- b) Efficient ion transport path
- c) Stable robust 3D structure

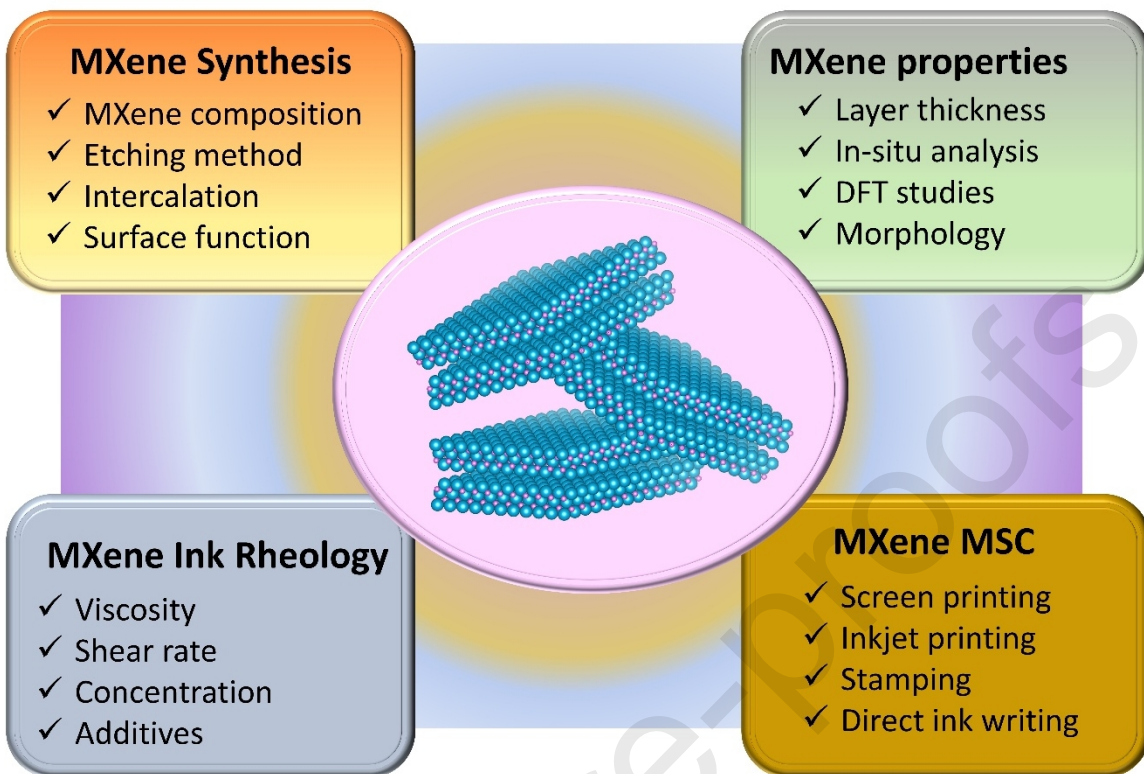


Fig. 2 Recent Progress in MXene-Based Electrode Engineering a Holistic Review of Synthesis Methods, Ink Formulation, Rheological Tuning, and Advanced Fabrication Techniques for Printable Energy Storage Applications

2. MXene SWOT analysis for energy storage application

The unique structural and structural features of MXene make it a promising candidate for energy applications. However, the emergence of this young material has broadened the widespread application and faced numerous challenges in real-time applications. An in-depth literature survey has provided insight into the reliability of this emerging material in energy applications. **Fig. 3** summarizes the SWOT analysis of MXene in energy storage applications to unveil the core contribution of physicochemical properties.

2.1 Strength

MXene has several strengths that make it an emerging candidate for energy storage applications. The electronic structure, interlayer spacing, and physical properties contribute to the strength of MXene in energy storage applications.

- a) *High electrical conductivity:* The electrochemical property is greatly influenced by the conductivity of the electrode material. The higher the conductivity smoother the electron migration, which facilitates improved electrochemical behavior. MXene attains an excellent metallic conductivity of ~10,000 S/cm, which favors fast electron transport [82], [83], [84], [85]. The excellent conductivity of MXene makes it a superior electrode material for energy storage applications.
- b) *Ion intercalation:* The MXene synthesis technique leads to intercalation of surface functional groups induced from the etchants, which act as active sites for improved redox reaction, make favour enhanced electrochemical performance. The presence of (OH, F, and O) ions across the MXene sheets accelerates the reaction kinetics with improved capacity.
- c) *Negative surface potential:* The presence of surface functional groups results in the negative surface potential of MXene naturally. The negative surface potential improves ion adsorption, which enhances the charge storage capacity. Negative potential and electrostatic attraction between MXene layers reduce the charge transfer resistance, ensuring fast charge-discharge during electrochemical reaction. Owing to the negatively charged surface, a wide range of electrolytes are compatible with MXene. Benefiting the surface potential, MXene gets functionalized with a wide range of materials.
- d) *Superior electrochemical properties:* High metallic conductivity, Layered structure, negative surface potential, and redox-active sites contribute to the excellent electrochemical properties of MXene and make it a promising electrode material. The superior electrochemical performance enables MXene to be used in different types of energy storage units like batteries, supercapacitors, micro-capacitors, etc. The higher specific capacity of MXene-based energy storage devices exhibits excellent reliability to power a wide range of miniature electronics.
- e) *Tunable architecture:* MXene holds a structural advantage over other materials, where electronic properties can be enhanced by tuning the material architecture. Reaction time and etchant play a vital role in designing the MXene electronic structure. Post operations like functionalization, ultrasonication, etc, widen the interlayer spacing, which can hold a huge number of ions and exhibit excellent electrochemical properties.

Induced porosity provides smooth and short pathways for ions to migrate to the core of the electrode material, which overall results in superior electrochemical properties. So, the tuneable architecture is a huge strength of MXene for its application in energy storage.

2.2 Weakness

MXene, though, acquires excellent properties favorable for enhanced electrochemical performance, has several weaknesses that lag its legacy in energy storage and stand challenging up to some extent.

- a) *Prone to oxidation:* MXene suffers from oxidation in aqueous media, which weakens the structural integrity and leads to degradation in electrochemical performance. Additives and surface modifications are required to overcome the oxidation issue and perform in the long run.



Fig. 3 Strategic SWOT Analysis of MXenes for Electrochemical Energy Storage Evaluating the Strengths, Weaknesses, Opportunities, and Threats of Transition Metal Carbides in Advancing Next-Generation Energy Storage Technologies.

- Limited working window:* Devices composed of MXene-based electrodes exhibit a limited working window, which is a major concern for the fabrication of high-capacity devices. The window is greatly influenced by the type of electrolyte. The narrow potential window offers limited energy density. However, Researchers have implemented different strategies to mitigate this weakness by grafting and functionalization of pristine MXene.
- Eco-friendly synthesis:* MXene synthesis is comprised of harsh chemical reactions, including strong acids like HF, which is a limitation and major safety concern. The property of MXene, including dimensions, greatly varies from batch to batch, making the synthesis technique a major weakness.
- Structural instability:* Strong van der Waals forces lead to the restacking of MXene, which destroys the layered architecture. The restacking issue is a major concern for

energy storage applications, as restacking leads to blockage of ion migration pathways and drastically reduces the specific capacitance.

- e) *Lack of scalability:* MXene synthesis is still limited to laboratory scale, where yield is at the gram level. MAX phase synthesis and the lack of highly efficient synthesis techniques make MXene synthesis challenging. A high yield with uniform physicochemical properties is desired to overcome the weakness of MXene up-scaling.

2.3 Opportunity

- a) *Green synthesis technique:* As MXene and MXene derivative holds great potential for high-performance energy storage devices, a green synthesis technique of MXene is a great opportunity. The green HF-free synthesis technique will be safer to operate, and the environmentally friendly process will open paths for mass production and commercialization of MXene as an active electrode material.
- b) *Hybridization:* Pristine MXene, though, exhibits excellent favorable properties for electrochemical properties, oxidation, and layer restacking leads to failure of MXene and freezes the inherent properties. Here, an opportunity comes to synthesize MXene-based composites by grafting foreign atoms and functionalization MXene with other materials that not only protect the structure but also enhance the electrochemical performance. Hybridization takes advantage of the unique MXene architecture and inherent electrochemically favorable properties to boost the overall specific capacity and energy density.
- c) *Multi-functional application:* Advancements in microelectronics and IoTs have broadened the need for smart devices for the ease of accessing multiple functions from a single device. The inherent physical properties of MXene make it an ideal candidate for energy storage and also sensing, and energy harvesting. So, the implementation of MXene in smart applications can open up opportunities for developing multi-functional devices for energy storage and sensing.
- d) *Broad range of electrolytes:* The negative surface potential and superior hydrophilicity enable MXene to be compatible with a wide range of electrolytes. The tuneable structure of MXene allows smooth ion migration and shorter reaction pathways for improved electrochemical performance. The ions present in various electrolytes contribute to the enhanced electrochemical properties.

- e) *Structural modification:* Structural optimization is a great opportunity to improve the electrochemical performance of MXene. Nanoengineering of MXene helps in tuning the porosity and widening the interlayer spacing. The addition of supporting materials prevents the retaking of MXene layers, which enhances the electrochemical stability and life cycle of MXene. This enables MXene to be utilized as a sustainable supercapacitor electrode material. This opportunity prevents the weakness of the structural instability of MXene.

2.4 Threat

Growing demand for sustainable high-performance electrode materials has led to the invention of high-performance electrode materials. MXene as an electrode material for supercapacitors faces various threats as discussed below.

- a) *Limited resources:* The MAX phase of MXene comprised early transition metals like titanium (Ti), niobium (Nb), molybdenum (Mo), and Vanadium (V). Those materials are relatively rare and hard to purify after extraction. The global supply chain of these materials is vulnerable to global geopolitics and economic variation due to limited reserves in specific corners of the world. Furthermore, the huge demand for transition metals in other well-established markets like aerospace, electronics, and catalysts creates competition, resulting cost of the precursor and limitations for large-scale MXene production. So expensive and limited precursor is a threat to commercially viable MXene, with the advantage of high-performance electrochemical activity.
- b) *Lack of standard protocol:* MXene lacks any universal standard protocol for synthesis, characterization, and energy storage applications. Researchers have obtained MXene with different surface terminations, layer spacing, and defect sites from similar synthesis protocols, which makes it hard to set any benchmark to obtain comparative electrochemical performance metrics. The absence of a standard protocol is the primary threat to reproducing consistent results. The batch-to-batch variation in property makes it challenging to commercialize and delay the availability of MXene-based energy storage devices in the market.
- c) *Environmental issue:* The corrosive etching agents used to yield MXene from the MAX phase led to environmental threats. Corrosive etching agents pollute the land and

water bodies. The aquatic and terrestrial ecosystem also gets affected by the leached transition metals from the MXene. Airborne MXene nanoparticles and antibacterial properties often become a major environmental concern. Suitable preventive techniques, eco-friendly synthesis, and proper MXene recycling can mitigate the threat of MXene to the environment.

- d) *Competitive alternatives:* Advancements in material science have developed a wide range of high-performance energy materials like graphene and transition metals and their derivatives. The evolution of high-performance electrode materials creates a threat to MXene in the field of energy storage applications. Multi-functional applications, high specific capacity, and long cycle life can overcome the threat of MXene from competitive alternatives.
- e) *Cost constraint:* The lack of a scalable synthesis technique and restriction in upscaling of MXene make the cost higher as compared to other 2D energy materials. The high electrochemical performance material needs to be cost-effective for commercialization as an economic alternative and compete with existing electrode materials effectively.

The SWOT analysis of MXene provides an insight into the strength of MXene for electrochemical applications, existing weaknesses, probable opportunities, and threats in the advancement and widespread application in energy storage applications. Inspired by the SWOT analysis, the electronic structure, the influence of synthesis technique, surface engineering, morphological features, and overall electrochemical performance are summarised in the following sections.

3. MXene synthesis

The MXene synthesis is classified into various types based on the etchant or etching technique [15], [31], [86]. Primarily based on the exfoliation of MXene sheets by selective removal of metal from the MAX phase is defined as the top-down approach, and during the bottom-up approach, different elements are combined to form the MXene sheet/film. Weak Vander Waals bonds are easier to break to form the 2D layers from the 3D structure by weakening the interlayer spacing, like the extraction of graphene from graphite using scotch tape [87]. To extract MXene sheets from the MAX phase is crucial implementing this technique is difficult owing to the strong bond between the M and A layers. So meticulously remove A

layer from the M layer by selectively using particular chemicals or specific temperatures [88]. Ion intercalation into the MAX phase removes the A layer and attaches the functional group into the MAX phase, forming a stacking of 2D lamellar sheets with a tuneable interlayer spacing HF etching, molten salt etching, fluoride salt etching, and electrochemical exfoliation are widely employed top-down approaches to synthesize MXene. Various MXene synthesis process is summarized in **Table 2**, and the evolution of MXene synthesis is portrayed in **Fig. 4**.

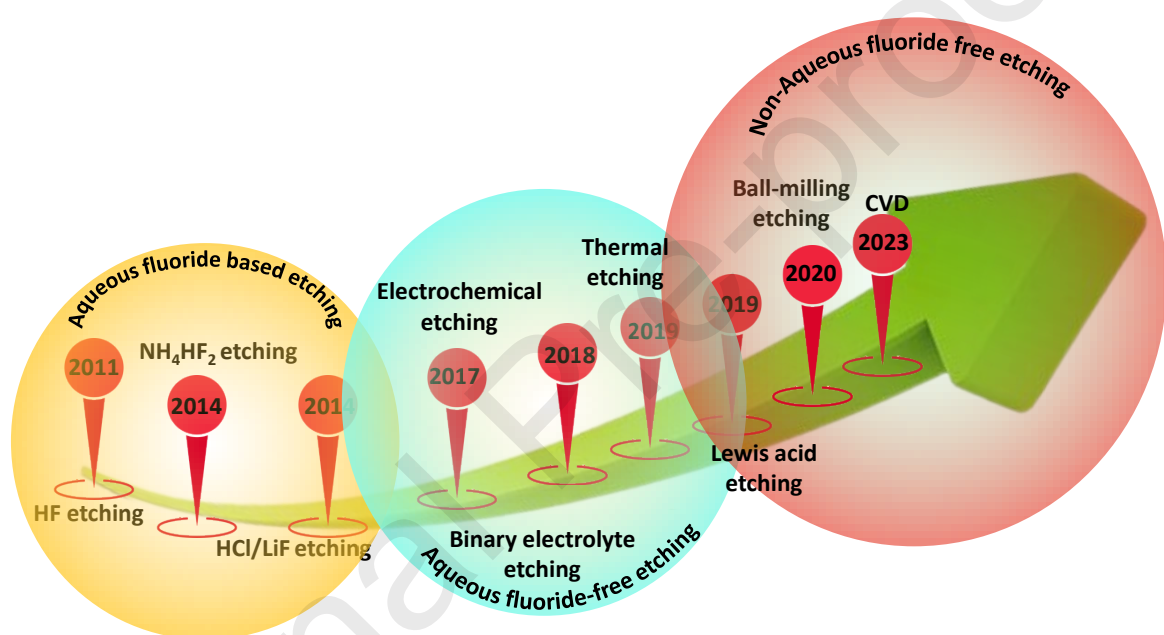


Fig. 4 Evolution of MXene Synthesis Techniques A Comprehensive Overview of Methodological Advancements from Initial Selective Etching to Emerging Bottom-Up Approaches for Tailored Structural and Electrochemical Performance

3.1 HF etching

HF etching is one of the widely used MXene synthesis techniques from the very beginning. MAX phase is immersed in the aqueous HF solution to remove the Al layer and replace it with the surface terminal groups (-F, -O, -OH) according to the etchant and vigorous chemical reaction [89]. Separate MXene layers are formed after the removal of selective layers. The thickness of the interlayer spacing can be tuned further by the sonication technique. After a specific etching time, the MXene dispersion undergoes a washing process until the pH

reaches 6. The washing process cleans the residues and by-products formed during the chemical reaction that took place during the removal of the Al layer from the MAX phase. Thoroughly washed MXene is collected by centrifugation or vacuum filtration technique and dried in a vacuum oven[90]. Ti_3AlC_2 was reduced to $Ti_3C_2T_x$ by the HF etching technique at room temperature for 2 h[91]. Researchers believe that HF intercalation in the MAX phase terminates edge Ti atoms, increasing interlayer spacing and allowing for HF insertion[92]. This process produces AlF_3 and H_2 , leaving behind fluorinated MXene. H_2O molecules cause the formation of MXene with -OH terminations. Computational studies show that -OH-terminated MXene converts to -O-terminated MXene through the emission of H_2 gas[93]. The etching process involves highly exothermic reactions and corrosive chemicals that must be closed and accommodated with chemically inert vessels. The HF-etched MXene acquires layers bonded with both hydrogen and weak van der Waals bonds[94]. **Fig. 5(a)** reveals the selective etching of Al from the V_2CT_x MAX phase using the HF etchant at room temperature. The etching time was 92 h in a concentrated HF environment. Morphology of the MXene after etching illustrates an accordion-like structure with stacked layers. Further XRD analysis confirms the corresponding peak of V_2CT_x MXene, confirming the successful synthesis from the MAX phase by selectively etching the Al layer. Further researchers have synthesized $Hf_3C_2T_z$ by the HF etching technique from the MAX phase $Hf_3[Al(Si)]_4C_6$. The solid-state synthesized powders were etched in 35% HF to selectively remove the Al layer. **Fig. 5(b)** represents the atomic structure of the MAX phase and the corresponding etching process for MXene synthesis. The etching interface exists between the Hf and C atom, which breaks during the synthesis process. DFT calculation was employed to study the weak point and adhesive energy by incorporating the Si atom to remove the Al smoothly from the MAX phase. The numerical studies align with the experimental studies, which confirm the addition of Si atom reduces the adhesion energy. This HF etching technique represents the structure engineering of the MAX phase by Si alloying and ease of synthesis by selective removal of Al by tuning the atomic structure. **Fig. 5(c)** illustrates the HF etching process of Ti_3AlC_2 to synthesize $Ti_3C_2T_x$. The MAX phase undergoes HF treatment for 24h. The HF etching breaks the metallic bond between Ti and Al and leads to the formation of $Ti_3C_2T_x$ sheets.

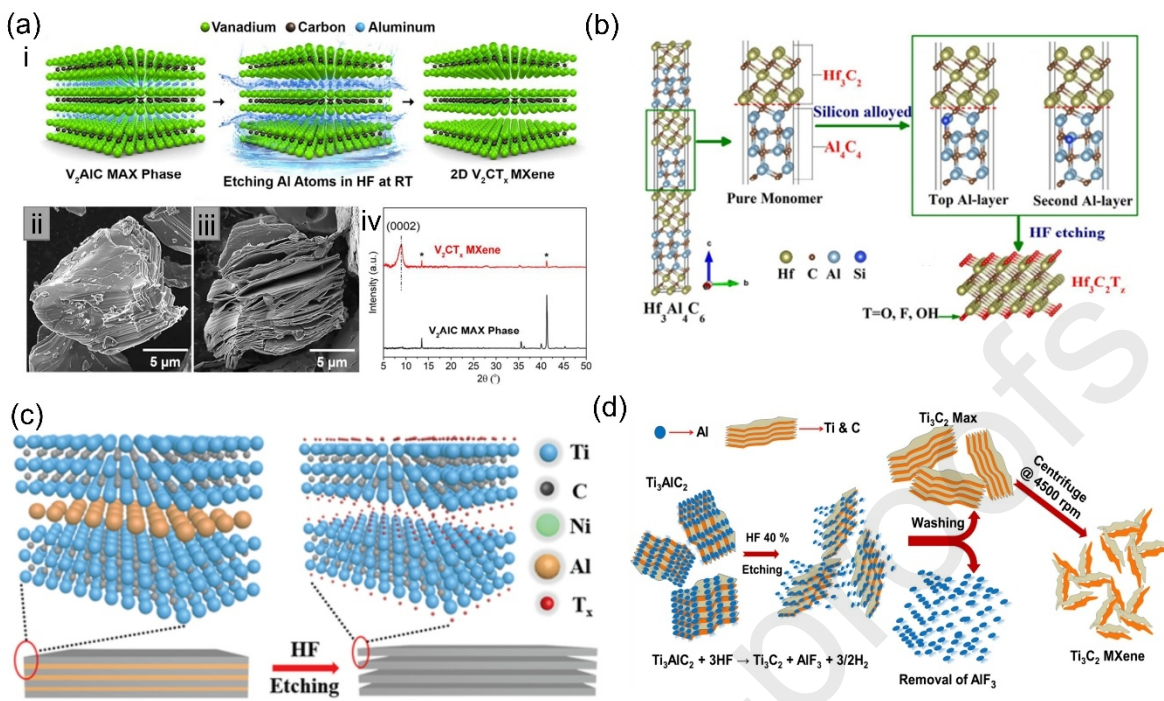


Fig.5 (a) i. Schematic presentation of selection etching of V_2AlC MAX phase to yield V_2CT_x ii. SEM image of V_2AlC MAX phase iii. SEM image of 50 % HF-treated MAX phase at room temperature iv. XRD analysis of MAX phase and MXene. Reproduced with permission from [195] ©American Chemical Society. (b) Synthesis process and DFT analysis of Hf_3C_2Tz MXene. Reproduced with permission from [90] © American Chemical Society. (c) HF etching process of MAX phase to synthesize Ti_3AlC_2 . Reproduced with permission from [196] © 2020 WILEY-VCH (d) Illustration of Ti_3C_2 MXene under 40 % HF. Reproduced with permission from [95]© 2024 Elsevier.

In addition to this etching technique was modified by utilizing a mixture of HF with another acid to reduce the influence of the terminal group (F^-) and increase the hydrophilicity, favouring superior electrochemical performance [96]. The formation of layers and the removal of A from M-A rely on the M-A bond as well as the HF concentration and reaction time. The lower the concentration, more the reaction time is required to remove the Al layer. To acquire lamellar stacking of MXene layers, the threshold concentration is 10 % HF[97]. **Fig.5(d)** illustrates the HF etching carried out to selectively remove the Al from the MAX phase[95]. The reaction was carried out in 10 mL of 40 % concentrated HF for 24 h by stirring at an RPM of 400. Post-etching residue was collected by centrifuging at an RPM of 4500 and washed

multiple times until the pH reached 6. The dried precipitate was collected as MXene after drying for 8 h at 60 °C. The weak metallic bonds between Ti-Al break, leading to the combination of fluorine and Aluminium ions to form AlF_3 . The elimination of Al leaves a hexagonal lattice of MXene.

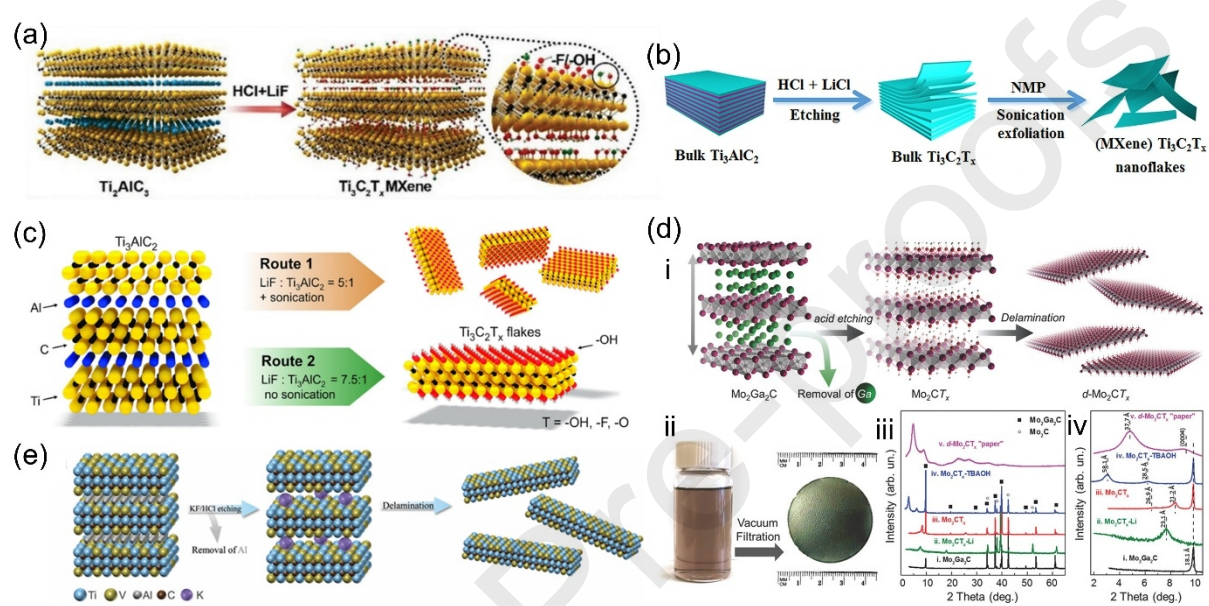


Fig. 6 (a) In-situ etching process of Ti_3AlC_2 MAX phase to synthesize $\text{Ti}_3\text{C}_2\text{T}_x$. Reproduced with permission from [98] ©2018 WILEY-VCH (b) Liquid phase exfoliation of MXene. Reproduced with permission from [99] 2022 Elsevier. (c) MXene flakes synthesis through various techniques. Reproduced with permission from [100]©2016 WILEY-VCH (d) i. Pictorial representation of Mo_2CT_x synthesis ii. Diluted MXene solution and free-standing paper produced by filtering the delaminated solution iii-iv. XRD pattern of MAX phase and MXene phases. Reproduced with permission from [101] ©2016 WILEY-VCH (e) Pictorial representation of Ti_2VALC_2 etching. Reproduced with permission from [102] ©2023 WILEY-VCH

Higher HF concentration distorts the MAX structure and hinders the Al layer removal owing to higher fluorine injection. An increase in temperature during the reaction process reduces the etching time and provides higher interlayer spacing. Over-etching leads to the degradation of properties, whereas under-etching fails to provide the required 2D sheets and interlayer spacing. Etching provides excess F- termination groups which are not desirable. The

F⁻ termination groups are harmful as well and restrict the performance of the MXene electrodes. Thus, to mitigate this issue, researchers have developed a controlled in-situ HF etching technique by mixing acid and fluoride salt.

3.2 In-situ HF etching

Fluoride salts mixed with HCl/H₂SO₄ yield in-situ HF for the controlled etching of MXene from the MAX phase. This etching method is reliable, safe, economical, and less aggressive nature and the LiF mixture has been widely implemented for etching that resulted from efficient faster reaction and better intercalation[103] **Fig. 6(a)** illustrates a selective delamination process of Ti₃AlC₂ to remove the Al layer to form the Ti₃C₂T_x[98]. 2 g of the LiF was added to 20 mL of 9 M HCl for 30 min thoroughly. 1 g of MAX phase was added slowly to the above-mentioned etchant and stirred for 24 h at 35 °C. Further, the solution was centrifuged repeatedly to yield the Ti₃C₂T_x colloidal suspension. The controlled in-situ HF slowly etches the Al layer from the MAX phase and forms the multilayer MXene. Besides LiF, other fluoride salts have also shown potential to act as effective etchants. Iron fluoride employed for etching the MAX phase provides higher interlayer spacing due to cation intercalation. The etching process performs better over mild temperatures and intercalates Li⁺, Na⁺, and K⁺ ions, limiting the F⁻ termination. Despite such advantages, sometimes it leaves some in-situ formed HF or fails to etch the MAX phase due to a less aggressive reaction. To overcome these bottlenecks, fluoride-free etching techniques have been explored in the recent past [92][93][94].

Fig. 6(b) illustrates the in-situ HF-assisted MXene synthesis technique by stirring 1g MAX phase in 20 mL etchant containing 1.6g LiF and 9mol/L HCl [99]. The MAX phase was stirred for 24 h at 40 °C. The etched MXene was washed thoroughly and dried for 12 h at 60 °C. The bulk MXene undergoes sonication-assisted exfoliation into MXene nanosheets. The sonication loses the bonding between layers and converts the bulk MXene into nanoflakes. MXene synthesis techniques influence the geometry and electronic structure based on the molar ratio and MAX phase. **Fig. 6(c)** represents different routes to the synthesis of MXene flakes[100]. Route 1 represents the MXene synthesis by immersing the MAX phase in an etchant with a molar ratio of LiF to the MAX phase as 5:1. This synthesis technique leads to the formation of monolayer MXene flakes. Further, Route 2 illustrates the modified procedure

with a LiF to MAX phase ratio of 7.5:1 that leads to excess Li^+ ion intercalation inside the etchant. No additional sonication is required for the delamination of MXene. Further analysis reveals the range of MXene flakes produced by route 1, between 200-500 nm in diameter. In contrast, route 2 yields larger uniform flakes with a dimension ranging from 4-15 μm . This work unleashed the influence of the etching agent and MAX phase ratio for tuning the electronic structure of MXene.

This process reduces the synthesis steps involved in HF etching by eliminating intercalation, delamination, and filtration with simple washing and sonication. This process yields MXene with less impurity as compared to HF etching and larger flakes with fewer defects. Further F^- termination groups are reduced and replaced with O^- groups, providing better performance and hydrophilicity. This etchant enhances the interlayer spacing due to the Cl functional group and enhances the electrochemical properties owing to a larger ion diffusion path and more active sites over the MXene sheets. The larger interlayer spacing is proven by the shift of the (002) plane to a lower diffraction angle[104]. $\text{Mo}_2\text{Ga}_2\text{C}$ powders underwent an in-situ HF etchant prepared by mixing 3M LiF and 12M HCl. The etched MAX phase yields MoCT_x multi-layered MXene as shown in Fig. 6(d) [101]. The Li^+ ions are further removed by adding 2 g of the MXene in 40 mL DI water and further hand-shaking. The thoroughly mixed solution was centrifuged for 1h to yield the delaminated MXene sheets. A mild reaction etching reaction was employed for the removal of Al from the Ti_2VAlC_2 MAX phase as depicted in Fig. 6(e) [102]. The in-situ HF formation was employed by mixing KF and HCl to remove the Al layer. The etched particles were cleaned thoroughly and air-dried to obtain the $\text{Ti}_2\text{VC}_2\text{T}_x$ MXene. Post-synthesis XRD analysis exhibits the presence of a significant (001) peak. This mild method is less vigorous and can be controlled by regulating the reaction time and concentration.

Though in-situ HF etching has been proven a reliable, less harmful synthesis technique for MXene, research towards fluoride-free etching is evolving owing to several advantages and controllable synthesis techniques.

3.3 Fluoride-free etching

3.3.1 Electrochemical etching

The electrochemical etching technique involves the process of removing the A layer from the MAX phase by applying a voltage in a certain electrolyte [105]. The electrolyte involved in this process is free of F⁻, which makes it an eco-friendly process. Researchers synthesized Ti₂C by removing Al from the Ti₂AlC MAX phase in an HCl atmosphere. The etching time and applied voltage, along with electrolyte concentration, are the important factors in this process. A longer etching time results in the degradation of the MAX phase, leading to the formation of carbide-derived carbon instead of MXene[106]. Further studies carried out under TMAOH and ammonium chloride electrolytes led to the formation of Ti₃C₂. The obtained yield is around 90 % and the flake size is around 18.6 μm as shown in **Fig. 7(a)** [107]. A simple electrochemical etching technique was employed for the delamination of the MAX phase under a one-pot molten salt solution. A pellet made up of Ti, Al, and C is employed as the working electrode, and glassy carbon as a reference electrode. MAX phase with 1D and 2D structure was synthesized at an annealing temperature of 950 °C followed by an etching step carried out under 500 °C to yield the Ti₃CT_x MXene. Before establishing the electrochemical etching, LiCl and KCl solution was heated up to 950 °C where the salt phase converts into the liquid phase as shown in **Fig. 7(b)**[108]. Further electrochemical etching is established when the cell temperature reduces to 500 °C. The weaker bond between Ti-Al helps to selectively etch out Al from the MAX phase with an applied voltage of 1.3 V. At the applied potential, Al atoms are oxidized into Al³⁺ and selectively etch out. Further researchers have synthesized Ti, C, and V-based MXene by electrochemical exfoliation. However, the formation of carbide-derived carbon leads to lower yield and affects performance. **Fig. 7(c)** illustrates the schematic of molten salt-based electrochemical etching of MXene.[109] The delamination process was carried out with an applied voltage of 2V at 450 °C. Benefiting from the weak bond between Ti-Al, Al was converted to AlCl₃, which is further evaporated at the applied temperature, leaving behind Ti₃C₂T_x.

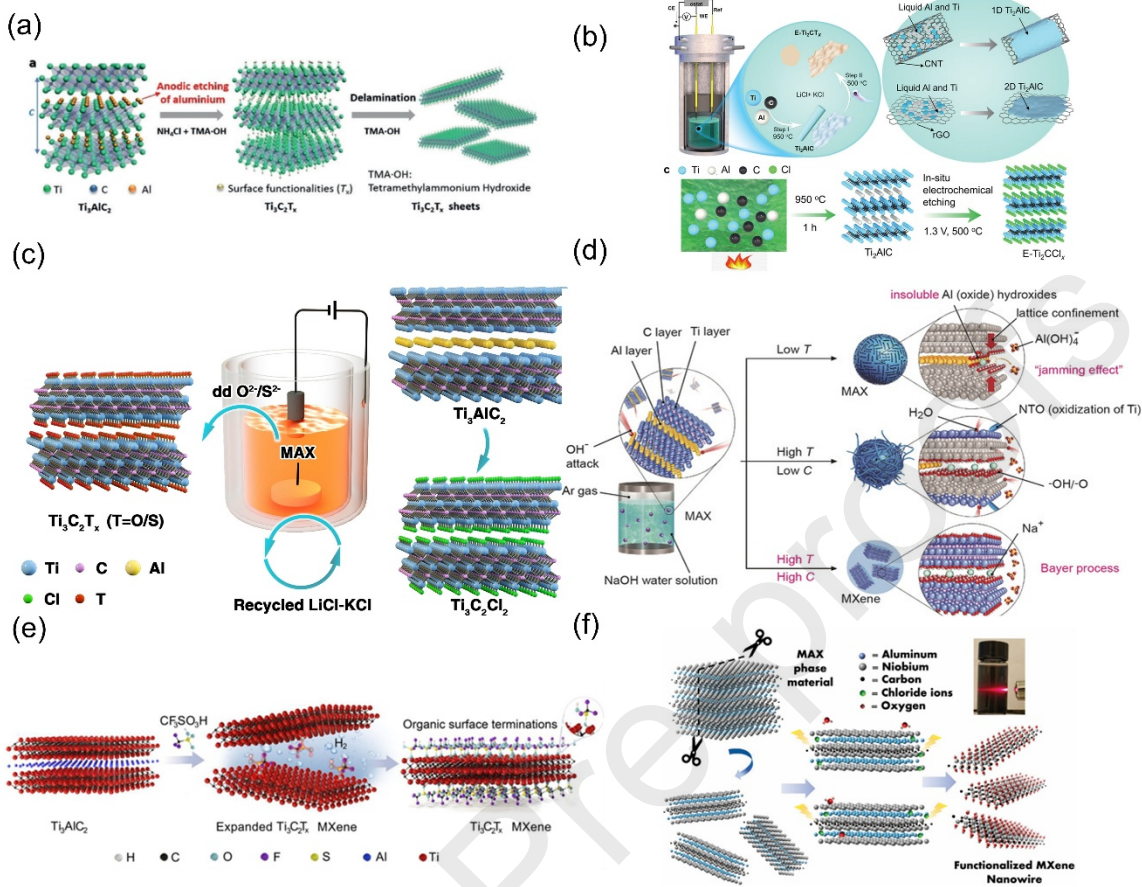


Fig. 7 (a) Electrochemical etching process of Ti_3AlC_2 . Reproduced with permission from [107] ©2018 WILEY-VCH (b) Molten salt assisted MXene synthesis technique. Reproduced with permission from [108] ©2023 WILEY-VCH (c) Schematic illustration of Molten salt assisted electrochemical MXene synthesis. Reproduced with permission from [85] ©2021 WILEY-VCH (d) NaOH-assisted MXene synthesis process. Reproduced with permission from [51] ©2019 WILEY-VCH (e) Surface functionalized CFSO₃H assisted MXene synthesis. Reproduced with permission from [110] ©2024 WILEY-VCH (f) HF-free E-etching of Nb_2CT_x . Reproduced with permission from [111] ©2023 WILEY-VCH

Table 2 Summary of Diverse MXene Synthesis Protocols Including Etching Methods, Precursors, and Reaction Conditions

Sr No	Methods	Derivatives	MAX phase	Etchants	Temperature (°C)	Time (h)	Refs.
1	HF etching	Ti ₃ C ₂ T _x	Ti ₃ AlC ₂	50 Wt% HF	25	2	[112]
2	HF etching	Mo ₄ VC ₄	Mo ₄ VAIC ₄	50 Wt % HF	50	192	[113]
3	HF etching	Zr ₃ C ₂ T _x	Zr ₃ Al ₃ C ₅	50 Wt % HF	25	72	[114]
4	HF etching	V ₂ CT _x	V ₂ AlC	50 Wt % HF	25	90	[115]
5	HF etching	Nb ₂ CT _x	Nb ₂ AlC	50 Wt % HF	25	90	[115]
6	HF etching	Nb ₄ C ₃ T _x	Nb ₄ AlC ₃	50 Wt % HF	25	96	[116]
7	HF etching	Ti ₃ CNT _x	Ti ₃ AlCN	30 Wt % HF	25	18	[117]
8	HF etching	Ta ₄ C ₃ T _x	Ta ₄ AlC ₃	50 Wt % HF	25	72	[117]
9	HF etching	Mo ₂ TiC ₂ T _x	Mo ₂ TiAlC ₂	50 Wt % HF	55	90	[118]
10	HF etching	Mo ₂ C	Mo ₂ Ga ₂ C ₂ T _x	50 Wt % HF	55	160	[119]
11	HF etching	(Ti, Nb) ₂ C _x	(Ti,Nb) ₂ AlC	50 Wt % HF	25	28	[117]
12	HF etching	Mo ₂ Ti ₂ C ₃ T _x	Mo ₂ Ti ₂ AlC ₃	50 Wt % HF	25	48	[118]
13	In-situ HF	Ti ₃ C ₂ T _x	Ti ₃ AlC ₂	1 M NaHF ₂	60	24	[120]
14	In-situ HF	Ti ₃ C ₂ T _x	Ti ₃ AlC ₂	1 M KHF ₂	60	24	[120]
15	In-situ HF	Ti ₃ C ₂ T _x	Ti ₃ AlC ₂	2 M NH ₄ HF ₂	25	24	[90]
16	In-situ HF	Ti ₃ C ₂ T _x	Ti ₃ AlC ₂	12 M LiF + 9 M HCl	25	24	[90]
17	In-situ HF	Ti ₃ C ₂ T _x	Ti ₃ AlC ₂	2 g FeF ₃ + 6 M HCl	60	50	[121]
18	In-situ HF	Ti ₃ C ₂ T _x	Ti ₃ AlC ₂	4 M KF+12 M HCl	40	48	[122]
19	In-situ HF	Ti ₂ CT _x	Ti ₂ AlC	6 M LiF + 0.9 M HCl	40	15	[104]
20	In-situ HF	Ti ₂ CT _x	Ti ₂ AlC	4 M NaF + 12 M HCl	60	24	[122]
21	In-situ HF	Ti ₂ CT _x	Ti ₂ AlC	4 M KF + 12 M HCl	40	48	[122]
22	In-situ HF	Mo ₂ CT _x	Mo ₂ Ga ₂ C	3 M LiF + 12 M HCl	35	144	[119]
23	In-situ HF	(Nb,Zr) ₄ C ₃ T _x	(Nb,Zr) ₄ AlC ₃	2.3 M LiF + 12 M HCl	50	168	[123]
25	In-situ HF	Ti ₃ CNT _x	Ti ₃ AlCN	7.5 M LiF + 6 M HCl	30	12	[124]
25	In-situ HF	V ₂ CT _x	V ₂ AlC	2 g NaF +12 M HCl	90	72	[125]

26	In-situ HF	Ti ₂ NT _x	Ti ₂ AlN	6 g KF + 6 M HCl	40	1	[126]
27	Electrochemical etching	Ti ₂ CT _x	Ti ₂ AlC	2 M HCl	25	120	[127]
28	Electrochemical etching	V ₂ CT _x	V ₂ AlC	1 M HCl	RT	9	[128]
29	Electrochemical etching	Cr ₂ CT _x	Cr ₂ AlC	1 M HCl	50	9	[128]
30	Electrochemical etching	Ti ₃ C ₂ T _x	Ti ₃ AlC ₂	1 M NH ₄ Cl + 0.2 M TMAOH	25	5	[129]
31	Molten salt etching	Ti ₂ CT _x	Ti ₂ AlC	1.5 M ZnCl ₂	550	5	[130]
32	Molten salt etching	Ti ₂ NT _x	Ti ₂ AlN	1.5 M ZnCl ₂	550	5	[130]
33	Molten salt etching	V ₂ CT _x	V ₂ AlC	1.5 M ZnCl ₂	550	5	[130]
34	Molten salt etching	Ta ₂ CT _x	Ta ₂ AlC	AgCl	700	24	[131]
35	Molten salt etching	Nb ₂ CT _x	Nb ₂ AlC	AgCl	700	24	[131]
36	Molten salt etching	Ti ₃ CNT _x	Ti ₃ AlCN	CuCl ₂	700	24	[131]
37	Alkali etching	Ti ₃ C ₂ T _x	Ti ₃ AlC ₂	27.5 M NaOH	270	12	[132]
38	Alkali etching	Ti ₃ C ₂ T _x	Ti ₃ AlC ₂	125 M KOH	180	24	[133]
39	Alkali etching	Ti ₃ C ₂ T _x	Ti ₃ AlC ₂	1 M NaOH + 1 M H ₂ SO ₄	80	100	[134]
40	Other etching process	Ti ₃ C ₂ T _x	Ti ₃ AlC ₂	Algae (HCOOH)	25	24	[135]
41	Other etching process	Ti ₃ C ₂ T _x	Ti ₃ AlC ₂	0.05 M LiF	25	NA	[136]

3.3.2 Alkali etching

Alkali etching is another promising HF-free MXene synthesis technique [137]. Al tends to be etched out by both acid and base due to its amphoteric nature. $\text{Ti}_3\text{C}_2\text{T}_x$ was obtained by TMA^+ intercalation after treating the MAX phase with TMAOH[138]. $\text{Ti}_3\text{C}_2(\text{OH})_2$ MXene was derived in a KOH solution after reacting for 24 h at 180 °C [139]. NaOH-assisted MXene was synthesized in a hydrothermal process at 270 °C, and a purity of 92 % was achieved with -O and -OH functional groups as shown in Fig. 7(d) [140]. A^+ ions intercalate at a higher temperature and higher concentration of NaOH solution. Though the alkali etching provides higher interlayer spacing owing to the Na^+ intercalation, the overall yield is lesser, which needs an alternative scalable synthesis technique. Lewis acid-assisted MXene synthesis was employed by utilizing trifluoromethanesulfonic acid etchant. Fig. 7(e) exhibits the synthesis technique of MXene from the MAX phase [141], [142]. The MAX phase was immersed in an etching solution for 6h at room temperature. Benefiting from the more reactive Ti-Al bonds, H^+ ions remove the Al from the MAX phase selectively due to the moderate redox potential. Further ultrasonication was employed for 30 min., which delaminates the MXene nanosheets with an efficiency of 70 %. Further XRD analysis confirms the removal of the Al layer from the MAX phase, confirming the formation of MXene. A fluoride-free facile synthesis technique was employed fabrication of MXene nanowires. Fig. 7(f) represents the two-step etching process of Nb-MXene[111]. The first step involves hydrolysis, and further thermo-assisted etching is established to remove the Al from the MAX phase 6M KOH was used to hydrolyze Nb_2AlC . Followed by hydrolysis, intense stirring was carried out to generate crevices at the MXene surface comprised of Ti-C bonds.

3.3.3 Microwave-assisted synthesis

Conventional MXene synthesis techniques comprised corrosive, complex, and time-consuming reactions. Often, such reactions follow multi-step and post-synthesis treatments to obtain high-quality MXene, which limits the large-scale synthesis of MXene with consistent characteristics[143], [144]. Microwave-assisted synthesis technique overcomes the existing bottlenecks in harsh chemical reaction-assisted techniques and provides a single-step energy efficient MXene synthesis process[145]. Fig. 8(a) demonstrates the MXene synthesis process and reaction mechanism. The in-situ HF, along with the MAX phase, undergoes 90-

minute microwave irradiation with continuous stirring at 650 rpm to eliminate any heat accumulation. The fast-etching time reduces energy consumption by up to 75 % and yields high-quality MXene as compared to conventional synthesis techniques. Benefiting from the rapid microwave-assisted heating, researchers developed a fast, facile MXene synthesis in 15min. **Fig. 8(b)** demonstrates the microwave-assisted synthesis of MXene under an aqueous solution containing LiF and HCl[146]. The reaction vessel undergoes microwave irradiation for 15 min. with a power of 200W. The H⁺ from dissociated HCl reacts with the Al layer of the MAX phase and continuously reduces to H₂ gas, which weakens the bonding between metallic layers. The etching initiates from the edge of the MAX phase and extends further through exfoliation by the intercalation of Li⁺ and Cl⁻ ions. The microwave exposure yields MXene with surface terminal groups consisting of O, OH, Cl, and F.

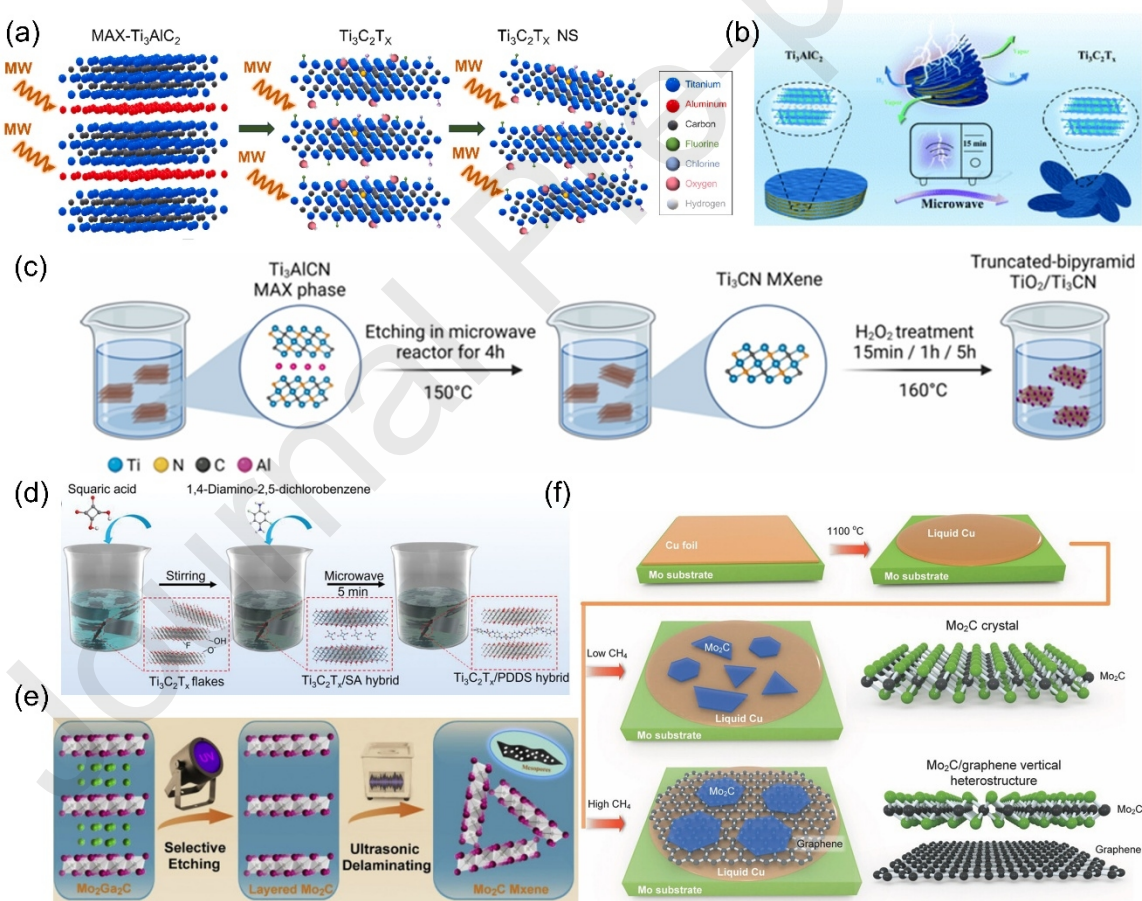


Fig. 8 (a) Microwave-assisted MXene synthesis. Reproduced with permission from[145] ©2025 Elsevier (b)Microwave-assisted Ti₃C₂T_x synthesis. Reproduced with permission from [146] © RSC (c) Illustration of microwave-assisted Ti₃CN MXene synthesis. Reproduced with

permission from[147] ©2024 American Chemical Society (d) Schematic presentation of microwave-assisted $Ti_3C_2T_x$ derivative synthesis. Reproduced with permission from [148] ©2022 WILEY-VCH (e) Ultrasonic assisted delamination of layered Mo_2C MXene. Reproduced with permission from [149]©2020 Elsevier (f)CVD assisted Mo_2C MXene synthesis. Reproduced with permission from [150] ©2017 WILEY-VCH

Fig. 8(c) demonstrates a facile synthesis of Ti_3CN by microwave-assisted hydrothermal treatment from the MAX phase Ti_3AlCN [147]. The MAX phase was exposed to microwave for 4h, which led to the formation of accordion-like multi-layered MXene. The as-synthesized MXene was treated with H_2O_2 to form a Ti_3CN / TiO_2 heterostructure. This technique unveils the utility of MW-assisted MXene and its derivative synthesis with tuned characteristics for specific applications. MXene polymer hybrids were synthesized by the researcher by a microwave-assisted synthesis technique (**Fig. 8(d)**)[148]. The precursor solution comprised $Ti_3C_2T_x$ and squaric acid with different ratios. Further, the composite was washed and underwent microwave treatment for 5 minutes under a power of 350 W. This approach provides a faster in-situ intercalation of MXene with a polymer that avoids drastic oxidation under prolonged chemical reactions. However, though MW-assisted MXene synthesis provides a faster approach to yield high-quality MXene, it is limited to microwave-reactive MAX phases and needs controlled parameter optimization to avoid any degradation of MXene[151], [152].

3.3.3 UV-assisted synthesis

UV-assisted synthesis is one of the reliable fluorine-free MXene synthesis techniques[153], [154]. The reaction mechanism involves photochemical oxidation, which enables faster reaction kinetics, reduced synthesis time, enhances surface functionalization, and serves eco-friendly. **Fig. 8(e)** depicts the UV-assisted Mo_2C MXene synthesis technique, which involves selective etching of the MAX phase followed by ultrasonication[149]. The Ga layer from the Mo_2Ga_2C MAX phase is removed under the exposure to UV irradiation in a phosphoric acid solution. The hexagonal single-crystal structure of Mo_2GaC converts to a graphene-like morphology with a thickness of 6nm.EDS analysis confirms the removal of the

Ga layer and the formation of Mo₂C MXene. The technique establishes a facile, fluorine-free, fast UV-assisted MXene synthesis technique.

3.3.4 CVD

Chemical vapor deposition offers a promising technique for the growth of MXene thin films[155], [156]. The film growth can be controlled directionally to tune the electronic property. **Fig. 8(f)** illustrates the preparation technique of Mo₂C MXene over graphene and Cu substrate[150]. The synthesis parameter was set at 1100 °C as growth temperature and H₂ as carrier gas. Liquid copper over Mo foil acts as a catalyst, and methane as a precursor material. The Co-Mo alloy forms inside the reactor at over 1086 °C and leads to surface segregation of Mo. Segregated Mo reacts with methane to form the Mo₂C crystals. The concentration of CH₄ flow governs the growth of the Mo₂C layer, as evidenced from the post-synthesis characterizations. A high concentration of methane leads to the formation of uniform hexagonal MXene sheets with a uniform thickness of 8 nm. The growth of MXene is inhibited over graphene, resulting in the formation of uniform thin layers without any rapid segregation of Mo atoms. CVD provides a reliable technique to yield MXene with reproducible characteristics; however, complex instrumentation lags the large-scale production.

Table 3 Comparative Summary of MXene Synthesis Techniques Key Advantages, Limitations, and Representative Methods

S1 no	Synthesis Technique	Advantages	Disadvantages	Ref.
1	HF-etching	Extensively used method due to ease of operation and higher yield. This method is reliable for a wide range of MAX phase etching and produces MXene with high	HF as a solvent poses an environmental threat and is hazardous for health unless used under high safety protocols. Post-synthesis treatment is	[157], [158], [159], [160]

		surface area, excellent mechanical strength, and remarkable conductivity.	required for delamination.
2	In-situ HF etching	Eco-friendly method due to in-situ generation of HF. The comparatively mild chemical reaction leads to the formation of MXene with less defect and a large d-spacing.	Comparatively longer reaction time and corrosive chemicals [161], [162], [163], [164], [165]
3	Electrochemical etching	The safe and easy method of MXene synthesis. Selective etching of Al from the MAX phase helps to retain the layered structure and provides scope to control the surface termination.	Relatively slower process and is limited to certain MAX phases with higher conductivity. [166], [167], [168], [169], [170], [171], [172], [173]
4	Alkali etching	Synthesize relatively pure and oxidation-resistant MXene. MXene acquires an excellent surface area, large interlayer spacing, and excellent electrochemical properties.	Time-consuming and requires very high temperatures. [174], [175], [176]

5	Microwave	Energy-efficient and faster synthesis technique. Results less defects, high conductivity, and uniform layers owing to reduced thermal gradients.	Expensive reactor setup. Challenging for uniform microwave irradiation in large-scale batches.	[177], [178], [179], [180]
6	Ultrasonication	This technique promotes faster and uniform removal of Al and leads to the formation of single or few-layer MXene with a small flake size and larger surface area.	Prolonged ultrasonication may damage the structure. It creates the risk of oxidation due to cavitation-induced local heating.	[169], [170], [171], [172], [173]
7	CVD	It leads to a uniform etching and forms high-quality MXene by limiting the usage of corrosive chemicals. The technique is scalable and reproducible. It offers better structural stability.	Complex instrumentation and longer reaction time.	[181], [182], [183], [184], [185]

3.4 Challenges in MXene synthesis and scalability

Since its inception, research on MXene synthesis has been explored extensively, which highlights the evolution of safer synthesis techniques and enhanced scalability for industrial-level bulk synthesis[186]. This section illustrates the challenges in MXene synthesis and the

bottlenecks in bulk synthesis. Commercialization and bulk synthesis of MXene face multiple challenges comprised of corrosive, toxic etching agents, and to high-energy-assisted energy assisted synthesis process[11], [187]. The small batch size limits the scalability, and impurity restricts the widespread applicability of MXene for various industrial applications[188]. The fundamental and practical challenges need to be overcome to utilize the tremendous potential of MXene.

- a) *Corrosive etchant:* The huge reliance on hazardous etchants, specifically HF, is one of the prime challenges for MXene synthesis. HF etching has been proven to be a promising method for lab-scale synthesis of MXene from the MAX phase[189], [190]. However, toxicity, corrosive, and disposal issues of HF hinder its widespread application in MXene synthesis[191]. Despite the low-cost etching agent HF, disposal creates environmental concern and increases the overall synthesis cost of MXene[192]. Additionally, though in-situ HF formation is less corrosive to the concentrated HF etching, fluoride waste causes environmental and safety concerns and restricts the widespread implementation beyond the laboratory[15], [34], [86], [193].
- b) *Longer exfoliation time:* To reduce the adverse effect of HF, alternative etchants have been implemented that contain difluoride salts like ammonium, potassium, or sodium. Though the etchant is safer as compared to HF, the exfoliation time ranges from 8-10h, limiting its potential for bulk synthesis of MXene[31].
- c) *Incomplete exfoliation:* Molten salt-assisted etching provides an alternative, greener synthesis method. The etching process is carried out at elevated temperature, which burdens the large energy consumption and induces structural defects in MXene owing to the high synthesis temperature[164], [178], [194].
- d) *Uneven surface termination:* MXene acquires specific surface terminal groups, which overall govern the functional property, like hydrophilicity, electronic structure, catalytic property, and life cycle[121], [195], [196]. The change in etching agents varies the surface terminal groups, which becomes a tough task to control with precision. The variation in batch size differs among the functional groups and affects the structure property correlation that restricts the reproducibility and lacks to set a standard protocol for upscaling the synthesis[128].

- e) *Rapid delamination:* The synthesis techniques, comprised of high temperature, pressure, or mechanical impulse, induce the mechanical delamination leading to surface defects of MXene, which faces a persistent challenge in synthesis[145], [164], [194], [197]. The ultrasonication-assisted delamination leads to structural failure, causing decay in conductivity and fragmentation of layers. The regulation of process parameters is inevitable for preventing the inherent properties of MXene during ultrasonic-assisted synthesis.
- f) *Complex reaction parameters:* Electrochemical exfoliation is one of the attractive, cost-effective green synthesis techniques. Despite numerous advantages, the complexity in electrolyte composition and delamination potential makes the MXene synthesis challenging[108], [143], [147], [166], [198], [199]. Further, the synthesis process is limited to a few MAX phases, which makes it complicated to become a universal etching method.

Overall, the current MXene synthesis methods suffer from toxic etchants, energy-intensive methods, and preliminary stages, which require both cutting-edge innovations along green etching agents can bridge the gap from laboratory scale to industrial scale. The lack of standard protocols of MXene synthesis results in inconsistent properties, which may be attributed to the purity of the MAX phase, etchant type, etching duration, etching condition, post-processing, which contribute to different structures and dimensions, surface functional groups, etc. The challenges can be overcome by improved process parameters, greener etching agents, continuous setup for scaling up the yield.

3.5 Cost-benefit analysis and industrial level bulk synthesis

The exceptional physicochemical property of MXene is yet limited to laboratory scale owing to various factors like lack of a standard synthesis method, raw material variation, variation in inherent property, and surface terminal groups[200], [201], [202]. The transition from lab scale to industrial level manufacturing of MXene counters numerous factors, including synthesis technique, MAX phases, environmental impact, scalability, reproducibility, and stable property. Each factor involves various constraints that govern the feasibility of MXene for commercialization and industrial-level bulk synthesis[203], [204], [205].

3.5.1 Industrial level synthesis:

Industrial level synthesis of MXene is not restricted to yield in bulk but requires to maintain high quality, eco-friendliness, and economic[206]. Though HF-assisted synthesis offers the desired MXene morphology and inherent properties, the toxicity severely restricts the industrial application[207], [208]. Hybrid synthesis protocols comprised of multiple techniques, i.e., microwave and ultrasonication, can be feasible for large-scale synthesis with cost benefits. Fluoride-free synthesis technique offers environmental compatibility and universal acceptance for industrial-level synthesis. Commercialization can be attained by fulfilling the criteria like safety, scalability, reproducibility, and economic viability. Among the current findings, electrochemical and alkali-assisted are promising for industrial-grade synthesis[209]. The tailored synthesis technique with minimal toxic waste can be a viable option for large-scale synthesis of MXene. Shuck et al.,[196] introduced a selected wet etching process inside a reactor for upscaling the MXene synthesis. As the bottom-up approaches suffer from upscaling issues due to substrate and precursor property variation on large-scale synthesis, the researchers developed a custom-designed chemical reactor which is safe to operate with controllable process parameters.

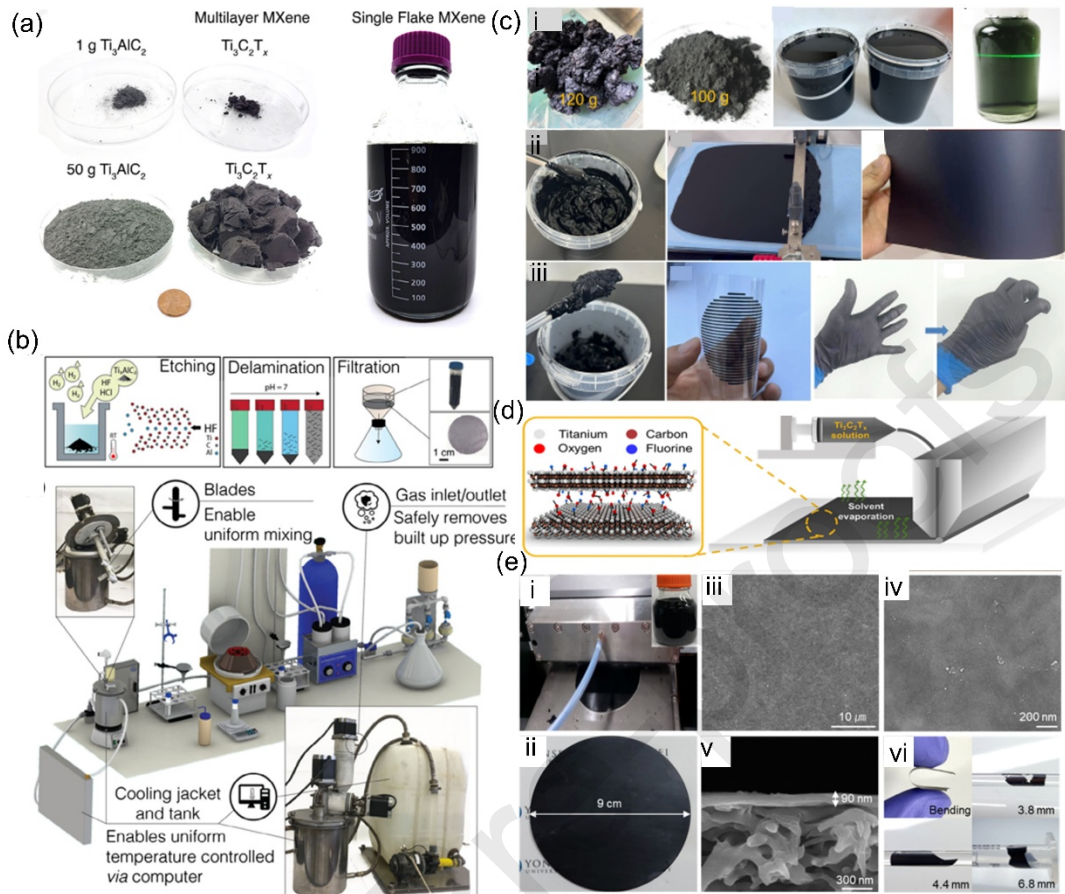


Fig. 9 (a) Real-time image of 1g and 50g batch of MAX phase, MXene and 1L solution of single flake MXene with a density of 10mg mL⁻¹ (b) Schematic representation of MXene synthesis and 3D model of 1L MXene reactor for large scale MXene synthesis. Reproduced with permission from [196]© 2020 Wiley-VCH (c) (i) Large scale synthesis of MXene in gram scale (ii) High concentration MXene ink for uniform film fabrication by blade coating technique (iii) Paste type MXene ink for screen printing over PET sheet and gloves for large scale customized coating. Reproduced with permission from [211]© 2024 Wiley (d) Schematic illustration of large scale MXene film casting using slot-die technique. Reproduced with permission from © 2022 Elsevier (e)(i-ii) Real-time photograph of slot-die coater and MXene membrane (iii-iv) Morphology of the MXene membrane (v) Cross-sectional morphology of the MXene membrane (vi) Bending test of MXene membranes. Reproduced with permission from[212]© 2021 Elsevier

Fig. 9a illustrates the different batch sizes of MAX phase precursor for upscaling the MXene synthesis. The wet etching yields a similar weight of multi-layer MXene as obtained after the vacuum drying process due to the balance between the removal of the Al layer with the substitution of surface terminal groups. The researchers obtained a yield of 52% and 60% from the large and small batch, respectively, from the customized batch reactor, as shown in

Fig. 9b. The batch reactor consisted of an automatic feeder, a cooling jacket, gas outlet for the controllable synthesis of MXene in different batch sizes without compromising the property. The physicochemical characterization of as-synthesized MXene from both small- and large-scale batch exhibits uniform characteristics that successfully demonstrate that the scalability of MXene up to an industrial level is possible without altering the properties. The reactor design with green etching agents can be a viable solution for the green synthesis of MXene in bulk quantities. The prototype developed by Murata Engineering for kg-scale production of MXene to meet the industry requirement[210]. As the low yield of MXene hinders the industrial level scalability Shi et al.,[211] introduced a high temperature-assisted ultrasound process for MXene synthesis. The hydrogen bonding was weakened between the terminal groups, resulting in single monolayer MXene sheets in a fraction of the time, which not only minimizes the time but also retains the inherent novel properties of MXene. The successful synthesis provides a promising yield of up to 95% making the process industrially feasible. **Fig. 9c** illustrates the large-scale synthesis of 120g MXene and its dispersion with a concentration of 10 mg mL^{-1} . The conversion of MXene powder into dispersion illustrates a greenish colour as depicted in the Fig.9c(i). The morphological analysis evidences the successful large-scale synthesis of high-quality MXene without significant oxidation or property degradation. To exhibit the industrial viability, various coating applications are demonstrated over different substrates, portraying the widespread potential of the MXene ink. The overall work suggests a simple but viable method for the production of high-quality gram-scale MXene, which serves as a stepping stone for bulk-level synthesis and industrial applications. bending at various radii, which evidences the robustness the reliability of the large-scale MXene membrane.

The industrial-scale synthesis can be productive if the synthesized MXene is successfully utilized for some industrial-level application. Kim et al.,[212] introduced a large-scale MXene membrane production. The fabrication process is continuous, fast, scalable, and controllable due to the customized setup. The as synthesised 100 nm thick membrane employed for water filtration for 30days, exhibiting excellent water permeance ability. **Fig. 9d** illustrates the slot-die-based film fabricator, which consists of a feed tank, syringe pump, and slot-die head. The solution of 5mg mL^{-1} was employed for the fabrication of a large-scale membrane by adjusting the slot die head to obtain a thin continuous layer. The real-time

image, as shown in **Fig. 9e (i-ii)**, depicts the smooth black layer over a PES substrate. The FE-SEM analysis demonstrates a flawless macro morphology and uniform thickness of the as-synthesised large membrane. In addition to this, the flexibility and robustness of the film were analysed by the overall process exhibits a fast, continuous coating process for industrial-grade high-performance membrane fabrication. Life cycle assessment is one of the tools for checking the viability of MXene for commercialization. Though MXene is not ruled out on an industrial scale, Firouzjaei et al.,[213] carried out a life cycle assessment study with 2 batches of MXene, comprised of 19.2g and 800g, respectively.

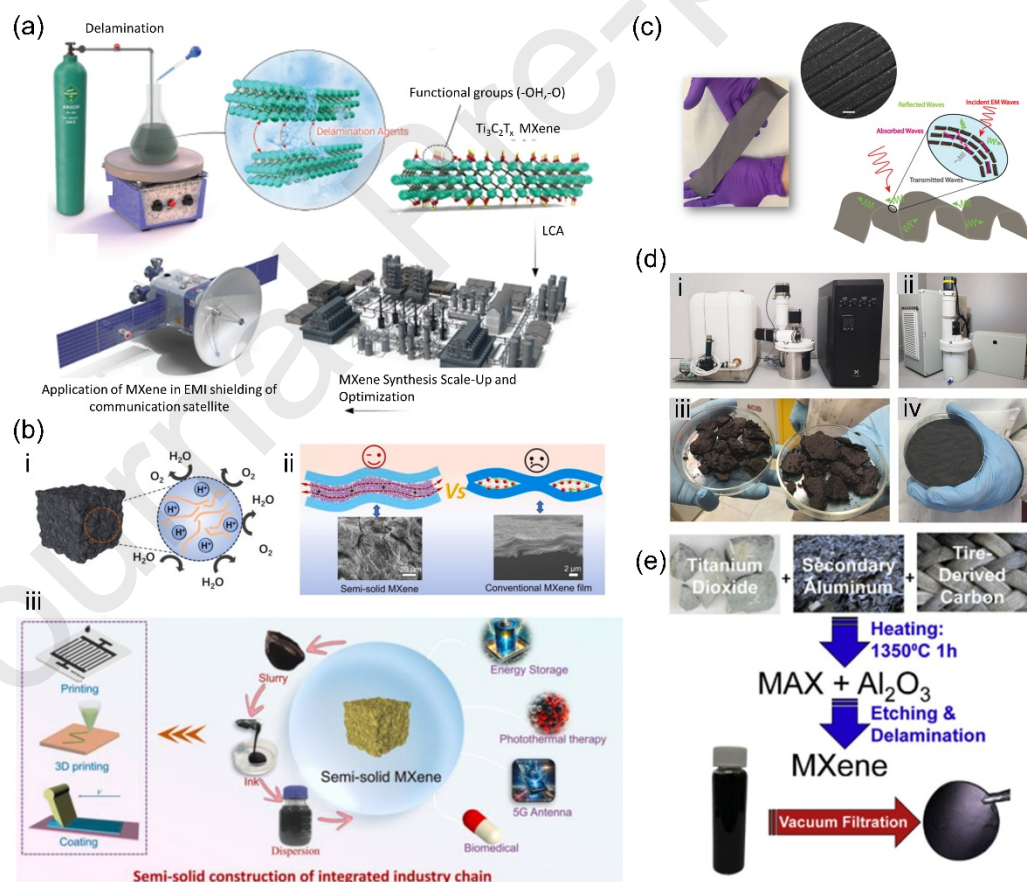


Fig. 10 (a) Schematic illustration of small scale MXene synthesis for industrial application and life cycle assessment for industrial level EMI shielding application. Reproduced with permission from[213]©2023 Wiley-VCH (b)(i) Oxidation prevention mechanism of MXene (ii) Illustration of long-term preservation and capture agent removal mechanism of MXene for

long term stability (iii) Illustration of diversified industrial application of semi-solid MXene. Reproduced with permission from[214]© 2024 Elsevier (c) Scalable fabrication of large scale MXene film for efficient EMI shielding. Reproduced with permission from[215]© 2020 Elsevier (d) (i-ii) Schematic representation of commercial level reactors for MXene synthesis with batch size of 0.5 L and 1L respectively (iii-iv) Bulk -synthesis of MXene with batch size of 70g and 40g respectively. Reproduced with permission from[216]© 2022 Elsevier (e) Schematic illustration of MXene synthesis from low-cost precursors. Reproduced with permission from[201]© 2021 Elsevier

Fig. 10a illustrates the schematic representation of MXene synthesis and life cycle assessment for industrial-scale application. The study was carried out to evaluate the energy and environmental impact of MXene for EMI shielding by analysing three materials and four systems. The effectiveness of MXene for EMI shielding was analysed by considering various factors using the ecoinvent database and openLCA software. The bulk synthesis of MXene reduces the adverse impact, as evidenced by the preliminary analysis for life cycle assessment. The green synthesis of MXene on a large scale can reduce the adverse effects, and the high performance of MXene has the potential to reduce the environmental impacts. So, the preliminary life cycle assessment suggests that utilizing the green synthesis technique, recycling of etchants, and high-performance customized reactors can lead to industrial-scale synthesis of MXene. Large-scale synthesis of MXene can't open up an opportunity for commercialization of MXene until a safe transport and oxidation-free storage is developed. To overcome the issue Yin et al.,[214] introduced a rapid MXene synthesis and storage in a semi-solid with a high solid content of more than 85%. The method preserves the intrinsic properties of MXene and provides both stability and reproducibility. **Fig. 10b(i-ii)** illustrates the antioxidant mechanism of semi-solid MXene due to the limited availability of water content, minimizing the interaction with MXene. The presence of residual agents shields the MXene layer from both oxygen and water, which prolongs the life span and acts as an antioxidant. Schematic illustration suggests the presence of a water layer prevents the creation of blockages and enhances the life cycle in semi-solid form. Once the semi-solid MXene is utilized for film or layer casting, the water, along with the capture agent, evaporates, which demonstrates excellent applicability of the semi-solid MXene. Benefiting from the semi-solid MXene inks and the excellent preserved properties enables it for application for a wide range of industrial applications like energy, photothermal, electronics, and biomedical, as shown in

Fig. 10b(iii). To widen the industrial application Yu et al.,[215] have demonstrated scalable synthesis of MXene films for EMI shielding application.

The excellent hydrophilicity and tuneable surface functional properties make MXene films easier to fabricate with controlled thickness, with a customized setup. The controlled volume and rate of evaporation provide a key advantage to regulate the film property. **Fig. 10c** illustrates the real-time image of the large MXene film with an area of 126.5 cm² and a thickness from 2.3 to 23.2 μm. The drop casting method tends to be tuned into desired shapes by utilizing a patterned substrate, which enhances the EMI shielding property with tuned surface geometry. The tuned 3D surface geometry scatters the radiation more effectively to enable the versatility of the MXene film and enable it for industrial-level applications. **Fig. 10d** illustrates the commercial laboratory-scale reactors for MXene synthesis[216]. The **Fig. 10d(i)** represents a 0.5L reactor, which can be upgraded to 1L and 2L by customization. The Teflon-lined reactors are highly resistant to HF and HCl, which can convert the MAX phase into MXene by a top-down approach. The real-time images exhibit the bulk synthesis of MXene on a gram scale (**Fig. 10d(iii-iv)**). The batch reactors seem promising for the industrial-scale synthesis of MXene without compromising the intrinsic properties. In addition to this, standardising of synthesis protocols and reproducible properties are highly desired for the successful implementation of industrial-grade protocols.

3.5.2 Cost factors

The widely used HF-assisted MXene synthesis consists of low-cost raw materials due to easily available max phase and inexpensive etching agents[217], [218], [219]. The synthesis needs protective infrastructure to get rid of the adverse effects of HF, along with expensive waste disposal systems[203], [204]. These factors drastically hike the overall synthesis cost of MXene, which makes it a non-feasible process for industrial-scale synthesis[188]. Molten salt-assisted etching consumes a higher energy cost due to the need for elevated temperature operation, but it eliminates the disposal cost of HF waste[108], [220]. Alkali-assisted and hydrothermal etching methods are economic methods due to inexpensive reagents and moderate synthesis conditions[137], [209]. The electrochemical etching method is one of the most cost-effective MXene synthesis methods, which involves electrolyte and electricity as basic requirements for delamination of the MAX phase[167], [221]. The process can be employed for large-scale production by setting up a continuous flow type setup. Despite

initial large capital investment, the process is relatively cost-effective in the long run application. Further, CVD is one of the most expensive MXene synthesis methods due to the complex machinery and the need for costly precursors[181], [184]. This process is difficult to implement for the cost-effective production of MXene on a bulk scale.

- a. *Precursor:* The cost of the final product relies on the cost of the raw materials. The precursors for MXene are mostly transition metals, aluminium, and carbon[222]. Ti-based precursors are quite cheaper as compared to Zr-based precursors. Cuskelly et. al,[223] estimated that the Ti_3AlC_2 price for 1 ton reduces to \$4,300 on replacing the Ti with TiO_2 and adding an extra amount of Al. Despite a low-cost precursor, the as-synthesized MXene exhibits similar conductivity with a 2.6-fold price drop without compromising the property[224]. The change in raw material quantity and ratio of precursors regulates the price of MXene. Researchers have attempted to synthesise recycled tyre-derived carbon for MXene synthesis[201]. **Fig. 10e** demonstrates the MXene synthesis from low-cost precursors. The titanium dioxide, aluminium, and tire-derived carbon are processed under high temperature to synthesize the MAX phase, which is further etched and delaminated to synthesize the MXene. Though the purity of the precursor was 98-99%, the inherent properties were still comparable to the pristine pure MXene. The improvement in synthesis techniques of low-cost precursors and alternative recycled materials can reduce the cost of MXene synthesis.
- b. *Synthesis of MAX phase:* The MAX phase acts as the feedstock for MXene synthesis, which is prepared from the precursor materials by various techniques like ball milling, calcination, and grinding. Temperatures, milling time each act as an important cost factor. Mostly during the MAX phase, synthesis cost overall synthesis cost increases with more time and energy consumption in addition to the price of the precursor[225]. High-temperature-assisted MAX phase with longer ball milling time generally increases the cost of the MXene.
- c. *MXene synthesis:* MXene synthesis is the crucial step that overall governs the final structure and property. The synthesis cost is mostly comprised of the reaction setup and etchant price. The corrosion-resistant reactors, etching agent concentration, and energy utilized for the etching overall constitute the synthesis cost of MXene. The reaction time varies based on the batch size and synthesis protocols. The etching

solution undergoes vigorous washing via centrifugation to neutralize and collect the MXene. The overall washing capital price comprises energy consumption for the overall centrifugation time and speed.

- d. *Storage and transportation:* Safe storage and long-term preservation are the most vital factors for industrial applications of MXene. As MXene is prone to oxidation, safe keeping in an inert atmosphere is challenging, which must be dry and low temperature[226], [227]. Purging of inert gas inside the MXene storage unit prolongs the life of the material without altering the properties[228]. In addition to this vacuum desiccator protects MXene from oxidation. The transportation of MXene from the synthesis place to the industry needs a carrier with inert gas or air-tight containers for safe keeping of the material. The cost of the storage and safe transportation of MXene reflects the industrial application, which must be competitive as compared to the alternatives.
- e. *Quality control:* High-quality and pure MXene is desired for the successful commercialization and high-end applications[100], [198]. Here, advanced characterizations to access the quality of MXene and decide the prospective application area increase the overall cost of the MXene unless any industrial-grade synthesis technology is established. To standardize the synthesis protocols, extensive research and development are desired, which also consumes a huge cost. The above factors determine the overall cost of MXene[186]. Industrial application always prefers cheaper alternatives to gain profit, which can be possible with bulk synthesis, standard protocols, and unmatchable properties of MXene. Researchers have carried out various cost-benefit analyses of MXene, which suggest that 1g of MXene synthesis costs approximately \$20.33, including all the cost factors[200]. The development of each and every step of MXene synthesis with the help of AI and ML can facilitate commercialization and wide-scale industrial application.

To summarize, a detailed insight into challenges in MXene synthesis, industrial-level synthesis techniques, along with advantages, disadvantages, and cost competitiveness, is discussed to anticipate the advancements and scope of the 2D material.

Journal Pre-proofs

Table 4 A comparative analysis of scalability, environmental impact, cost effectiveness, and industrial suitability of MXene

Sl no	Synthesis technique	Scalability	Environmental Impact	Cost-Effectiveness	Industrial suitability	Ref.
1	HF-etching	Low (Lab scale)	Highly hazardous (Restricted etchant)	Low-cost material (High waste disposal cost)	Poor (Safety issue)	[95], [157], [158],[229]
2	In-situ etching	HF	Moderate	Less hazardous as compared to direct-HF	Moderate (Environmental restrictions prevail)	[159], [163]
3	Electrochemical etching	Highly scalable (With designated setup)	Environmentally friendly	Moderate	Potential process for industrial synthesis	[221], [230]
4	Alkali etching	Scalable batch-wise	Eco-friendly (Fluoride-free)	Cost-effective (Cheaper etchant and less energy requirement)	Best suited for large-scale	[137], [179]
5	Microwave	Highly scalable due to rapid, uniform heating	Greener synthesis process	Cost-effective and energy efficient due	Promising for industrial-level synthesis with a customized continuous synthesis setup	[146], [148], [178], [180]

				to fast reaction time		
6	Ultrasonication	Moderate	Eco-friendly	Cost-effective	Potential candidate for industrial-scale delamination	[172]
7	CVD	Lab scale (Thin film)	Eco-friendly	High cost	Limited to lab scale and designated electronics applications	[181], [183], [184]

4. Unveiling the potential of MXene for electrochemical energy storage

MXene a promising potential candidate for energy storage, is largely influenced by the morphology and sheet thickness. The electrochemical performance is enhanced by the intrinsically layered structure of MXene, which also makes them ideally suited for use as electrode materials in advanced energy storage systems. The morphology and sheet thickness of the electrochemical behavior are unveiled in this comprehensive review.

4.1 MXene Morphology

The Morphology of MXene is one of the most fascinating physical properties that has been explored extensively by the scientific society. The morphological properties like layered structure, flake size, layer spacing, porosity, etc, influence the electrical conductivity, specific capacitance, rate performance, stability electrocatalytic activity, etc. The electrochemical properties are regulated by tuning the interlayer spacing, surface defects, lateral flake size, etc. **Fig. 11** illustrates the classification of MXene based on the dimensionality of the MXene sheets. Based on the dimension, MXene belongs to 0D, 1D, 2D, and 3D architectures. The effect of morphology and tailored structure expedites the electrochemical property and influences the energy storage performance.

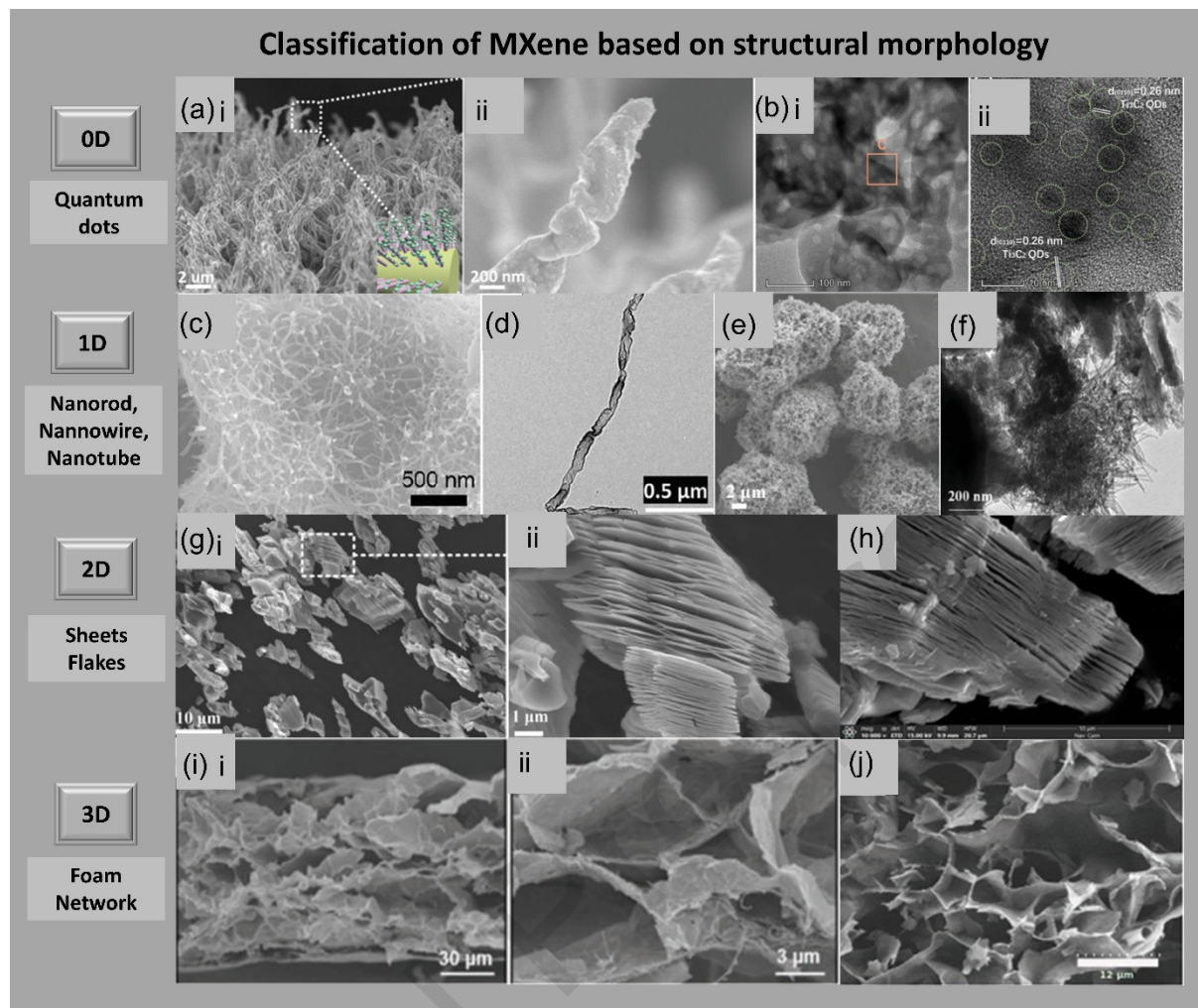


Fig. 11 (a-b) MXene quantum dots. Reproduced with permission from[231] ©2024 WILEY-VCH,[232]©2019 ACS. (c-f) 1D MXene in the form of wire, yarn, and fiber. Reproduced with permission from [233]©2019, [111]ACS ©2020 WILEY-VCH,[234] ©2019 Elsevier,[235]©2023Elsevier. (g-h) 2D-MXene sheets and flakes. Reproduced with permission from[236] ©2019 ACS,[237]©2022, Elsevier (i-j) 3-D MXene architecture in the bulk foam structure. Reproduced with permission from[238] ,[239]©2020 Elsevier.

4.2.1 0D MXene:

The development of synthesis techniques has widened the fabrication of tailored nanoparticles with tuneable physico-chemical properties. Zero-dimensional materials have gained huge interest in energy applications owing to their excellent electrochemical activity and unique structural entity. 0-D materials resemble spheres or clusters, which are defined as quantum dots (QDs). QD derived from MXene exhibits excellent electrochemical properties.

Conversion of 2D layered MXene into QD acquires excellent conductivity and abundant active sites, owing to the increased surface area that favors the enhanced electrochemical activity. The FE-SEM micrograph as depicted in **Fig. 11(a)** illustrates the Ti_3C_2 QD /CuO heterostructure that provides a better contact adhesion[231]. The MXene QD acts as a protective layer along provides improved electrochemical properties. The structural modification of MXene provides the opportunity to fabricate multifunctional MXene composites for energy applications. **Fig. 11(b)** illustrates the MXene QD synthesized by a simple one-step self-assembly technique[232]. The HF etched Ti_3C_2 sheets underwent tip sonication for 6 h at 120W under an inert atmosphere. Further bath sonication was carried out for 10 h at 300W. Further, this dispersion was added with PEI and heated overnight at 120 °C in an N_2 atmosphere, and the final MXene QD was extracted and freeze-dried. The TEM image reveals the lattice spacing of 0.26 nm, which is indexed to the MXene QD. Immobilization of MXene QDs on $\text{g-C}_3\text{N}_4$ provides a close adhesion, resulting in higher electronic conductivity and enhanced catalytic activity. The synthesis of O-D MXene opens up the opportunity for a new class of material in energy applications. The 0D structure has the advantage of coupling with rods, ribbons, or wires to construct a heterostructure with excellent electronic conductivity, and the advantage of a spherical structure provides abundant active sites for faster reaction kinetics.

4.2.2 1D MXene

1D MXene includes a wide range of structures in the form of nanowires, nanorods, ribbon tubes, etc. The conversion of 2D MXene into a 1D shape exhibits excellent anisotropic properties and is attributed to the enhanced electrochemical properties of the 1D structure, enhancing the aspect ratio that provides abundant active sites for electrochemical reaction. The structural conversion provides a customizable, scalable production of electrode material for energy applications 2D MXene acts as the feedstock for the synthesis of 1D structures. Solvothermal, scissoring, carbothermal, and etching are some of the widely employed techniques for 1D MXene synthesis. Nanofibers/wires are 1D nanostructures whose diameter ranges in the nanometre range and lengths in the range of a few nanometres to millimetres. If the MXene width belongs to a few nanometres and the length extends up to a few micrometres, the structure is defined as a nanoribbon. Nanorods' diameter falls within nanometres, whereas

the length extends up to several micrometres. Nanotubes are cylindrical hollow structures whose diameter ranges from a few nanometres and whose lengths extend up to a few micrometres. **Fig. 11(c)** unveils the MXene nanofiber synthesized by the hydrolysis process. OH⁻ ions present in 6M KOH acts as a scissoring agent that induces crack in the MXene framework[233]. The thickness of the nanofiber ranges from 40-60nm as revealed by the FE-SEM images. Further TEM analysis reveals the d-spacing of 0.97, confirming the elimination of Al from the MAX phase. The MXene nanofiber synthesis exhibits enhanced electrochemical properties as compared to the bulk counterpart, leaving behind a unique strategy for structurally modified MXene for enhanced electrochemical performance. **Fig. 11(d)** represents the Nb₂CT_x nanowire synthesized by the electrochemical etching technique at an applied voltage of 1V for 4h. The 1D interconnected nanowires exhibit excellent electrochemical performance and develop an HF-free tuneable MXene synthesis technique for energy applications. Alkalization-induced MXene nanoribbons are synthesized for Na/K-ion storage, followed by HF-etching. **Fig. 11(e)** reveals the 3D-porous network of MXene nanoribbons[234]. Abundant active sites and a large surface area for electrochemical reactions provide a structure modification strategy for smooth ion migration and enhanced specific capacity. The multi-layer nano ribbons acquire a thickness of 6-22 nm. HR-TEM analysis reveals the presence of flat, self-twisted, and jointed nano-ribbons throughout the MXene frame. The unique architecture of nanoribbons with expanded layers and porous frames provides pathways for faster electron transfer and efficient ion diffusion. Structure engineering of MXene 1D Nb₂C nanorods /2D Nb₂C and boron nitride nanoparticles helps to achieve optimum pseudocapacitive property and enhanced specific capacity[235]. The HR-TEM image depicted in **Fig. 11(f)** represents the heterostructure comprised of Nb₂C nanosheet-nanorod rod along with BCN nanoparticle. The unique architecture results in superior electrochemical properties and long cycle life. The unique 1D MXene architecture has humongous advantages for fabricating high-performance energy storage devices.

4.2.2 2D MXene

2D-MXene is comprised of a few layers, monolayer transition metal carbides/nitrides. The sheet thickness, interlayer spacing, and lateral flake length are the primary dimensional parameters that regulate the electrochemical properties. Etching, including etchant type and

duration, decides the sheet structure and layer structure of the 2D MXene. Mostly accordion-type stacking of layers constructs MXene flakes. HF-etched $\text{Ti}_3\text{C}_2\text{T}_x$ exhibits excellent 2D stacking of MXene layers with selectively removed Al from the MAX phase stack. The monolayer MXene was synthesized by *in situ* HF etching. **Fig. 11(g)** reveals the macroscopic MXene consists of thin flakes[236]. The weak interaction between sheets is unveiled by the irregular interlayer spacing between the sheets. Irregular staking is evidenced after the vacuum drying of the MXene sheets after the etching process. The 2D surface provides an abundant active area for electrochemical reaction, and interlayer spacing provides space for ion storage to facilitate energy storage reaction 2D monolayer MXene is favourable for energy applications owing to its higher active surface area. **Fig. 11(h)** represents the 2D accordion-type architecture that confirms the removal of the Al layer[237]. The release of heat and hydrogen stresses the structure during selective etching. Further, the interlayer spacing is regulated by the ultrasonication of the obtained MXene flakes. Ultrasound-assisted synthesised MXene attributes to better electrochemical performance, including higher capacity and long-term stability.

4.2.3 3D MXene

2D-MXene structures suffer structural instability due to restacking of layers. The structural failure blocks the ion migration paths, resulting in sluggish electron kinetics. To address this issue, 3D-MXene structures are being explored by researchers through hybridization with other materials. Researchers have proposed a simple ice-template strategy to synthesize a free-standing flexible 3D-PMCF comprised of $\text{Ti}_3\text{C}_2\text{T}_x$ and CNT. Freeze drying induces the *in-situ* formation of residual water molecules that lead to the formation of a 3D porous network. The 3D structure not only increases the active sites but also accelerates the rate of ion transport 3D architecture provides excellent flexibility and structural stability. **Fig. 11(i)** represents the porous structure of the 3D MXene[238]. The porous interconnected 3D network reduces the ion transport path and results in enhanced specific capacitance. The interconnected 3D chains eliminate the restacking issue of 2D MXene sheets and further provide unmatched rate capability and long-term stability. Foamy 3D MXene was synthesized by heating the MXene-Urea composite at 550 °C. The resulting porous MXene electrode exhibits excellent

electrochemical properties and 99 % capacitance retention after 5000 cycles. **Fig. 11(j)** illustrates the honeycomb-type morphology obtained by pyrolysis of MXene[239]. The synthetic synthesis technique induces numerous pores perpendicular to the surface. The structural engineering increased the electroactive area and promoted ionic mobility. Overall, this pyrolysis technique proposes a feasible synthesis technique to fabricate 3D MXene foam with enhanced electrochemical properties and excellent structural stability.

The structural engineering of MXene has widened the application of MXene in various energy storage sectors, including flexible supercapacitors, micro-supercapacitors, Metal-ion capacitors, micro-batteries, etc. The structure engineering enhances the capacity and stability of MXene in energy storage by overcoming shortcomings like being prone to oxidation, layer restacking, and sluggish reaction kinetics.

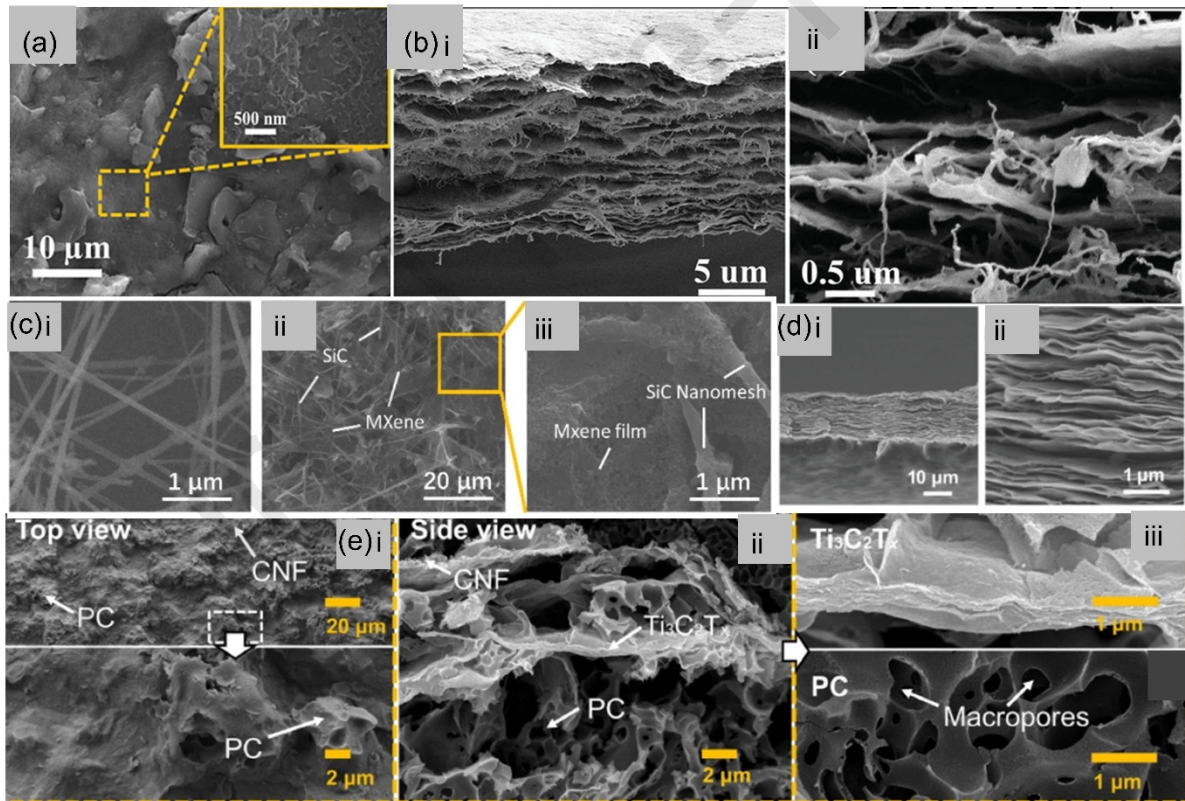


Fig. 12 (a)Morphology of MXene @NiCo MOF. Reproduced with permission from[240]© 2024 Elsevier (b) Cross-sectional image of MXene/BC composite over a paper substrate. Reproduced with permission from [241]©2019 WILEY-VCH. (c) SEM image of MXene-SiC composite. Reproduced with permission from [242]© 2022 Elsevier. (d) MXene/MPFs cross-

sectional image. Reproduced with permission from [243], [244]©2019 WILEY-VCH. (e)(i) Top view, (ii-iii) Side-view of MXene/CNF and PC composites. Reproduced with permission from[244]© 2021 Elsevier

4.2.4 MXene morphology influence over the electrochemical properties

The unique structure of MXene makes it a promising candidate for energy storage applications. The restacking of MXene leads to a drastic reduction of the electrochemical reaction. So, researchers have introduced various tactics to tackle this structural failure. Poor conductivity of MOF hinders the electrochemical performance, which is overcome by grafting MOF with highly conductive MXene[240]. **Fig. 12(a)** represents the NiCo MOF grown over expanded MXene. Expanded MXene attains a large surface area to grow NiCo-MOF. The thin MOF sheets make a stable structure with MXene and provide abundant active sites for electrochemical reactions. The MXene @MOF heterostructure exhibits a polycrystalline nature, and EDS analysis confirms the homogeneous distribution of C, Ti, O, Ni, and Co. The excellent conductivity of MXene helps to overcome the sluggish diffusion kinetics of relatively less conductive thin NiCo-MOF. However, the catalytic property of MOF nanosheets along with MXene enhances the redox activity and enhances the electrochemical performance. Zhang et al.,[245] introduced MXene nanoparticles as a supporting spacer between the MXene sheets to prevent the restacking issue.10 % nanoparticle was added as a spacer to support the MXene sheets. MXene suspension containing both sheets and particles was sonicated to form a uniform suspension and employed for filtration to fabricate the free-standing film. Researchers have analyzed the morphology of MXene-0 and MXene-10. The surface of the MXene sheet appears to be smooth with few wrinkles. The addition of 10 % MXene particles makes the MXene surface quite rough. The cross-sectional morphology of the MXene-0 film contains stacks of nanosheets, while the addition of nanoparticles induces a porous structure where nanoparticles are sandwiched between nanosheets. The structure seems to be stable with nanoparticle spacers. The nano-engineered structures allow electrolyte wetting and ion migration, leading to enhanced electrochemical performance. The nano-engineered MXene electrodes exhibit a specific capacitance of 372 Fg^{-1} and capacitance retention of 95 % over 5000 cycles. This work establishes a promising strategy to combat the restacking issue and develop high-performance supercapacitors. Stretchable micro-supercapacitor with excellent

electrochemical properties needs a high-performance electrode material with a stable structure and redox active sites. Jiao et al.,[246] reported an MXene /Bacterial cellulose composite with strain-engineered architecture with tailored interlayer spacing for energy storage application. A laser engraving technique was implemented for the Kirigami pattern micro-supercapacitor. The introduction of bacterial cellulose along with MXene modulates the interlayer spacing and provides mechanical stability. The corresponding SEM image of the MXene-BC composite represents the distribution of 1D BC fibers homogeneously between the MXene layers. **Fig. 12(b)** represents the closely packed MXene sheets provide excellent conductivity, and BC fibers, attributed to the mechanical strength. The composite electrodes exhibit excellent specific capacitance of 111.5 mFcm^{-2} along with remarkable cycle stability over mechanical bending and twisting of 5000 cycles. MXene sheets suffer agglomeration and irreversible capacity reduction, which raises a major concern about implementing it in energy storage. Xia et al.,[242] fabricated an MXene/SiC heterostructure by ionization bombardment. MXene nanosheets self-assemble over SiC nanocrystals to make a highly porous structure. **Fig. 12(c)** represents the SEM image of the MXene/SiC heterostructure, where the average diameter of the SiC nanowire ranges around 175 nm. MXene sheets interconnected with SiC nanowires frame a stable 3D structure. The overall surface area is enhanced, providing abundant surface area for electrochemical reaction. The specific capacitance exhibited was 97.8 mF cm^{-2} with an excellent capacitance retention of 90% over 10,000 cycles. Zhao et al. fabricated an MXene/Metal-porphyrin framework for a high-performance supercapacitor. The interlayer hydrogen bonds provide higher chemical stability, and synergetic effects provide a remarkable specific capacitance of 326.1 Fg^{-1} and excellent capacity retention of 30,000 cycles. **Fig. 12(d)** represents the cross-sectional image of MXene/MPF composites, which appears stacking of lamellar structures[243]. The compositing of MPF increases the thickness of the MXene film, and MPF acts as a spacer to avoid restacking of sheets. The porous composite acquires shorter ion transport paths and abundant active sites along with the synergetic effect of MXene and MPFs. Chen et al. developed an MXene /CNF/PC composite for a flexible supercapacitor. The MXene sheets provide excellent conductivity in the 3D porous structure provided by the porous carbon. CNF holds the structure, providing excellent mechanical stability. The presence of CNF and PC increases the porosity of the composite and provides abundant active sites for efficient ion migration. **Fig. 12(e)** represents

the bundle of MXene, PC, and CNF with a closely packed structure[244]. The cross-section represents PC acts as a spacer that prevents the restacking of MXene sheets. The macro-porous structure attributed to the porous carbon makes the composite an excellent candidate for energy storage. The SC attains a specific capacitance of 143 mF cm^{-2} and an excellent rate capability. Cheng et al. synthesized a structure engineered of MXene-BC composite for a hybrid-micro supercapacitor. The structure engineering widens the interlayer spacing and provides conductive connections between layers for effective ion migration and enhanced specific capacitance.

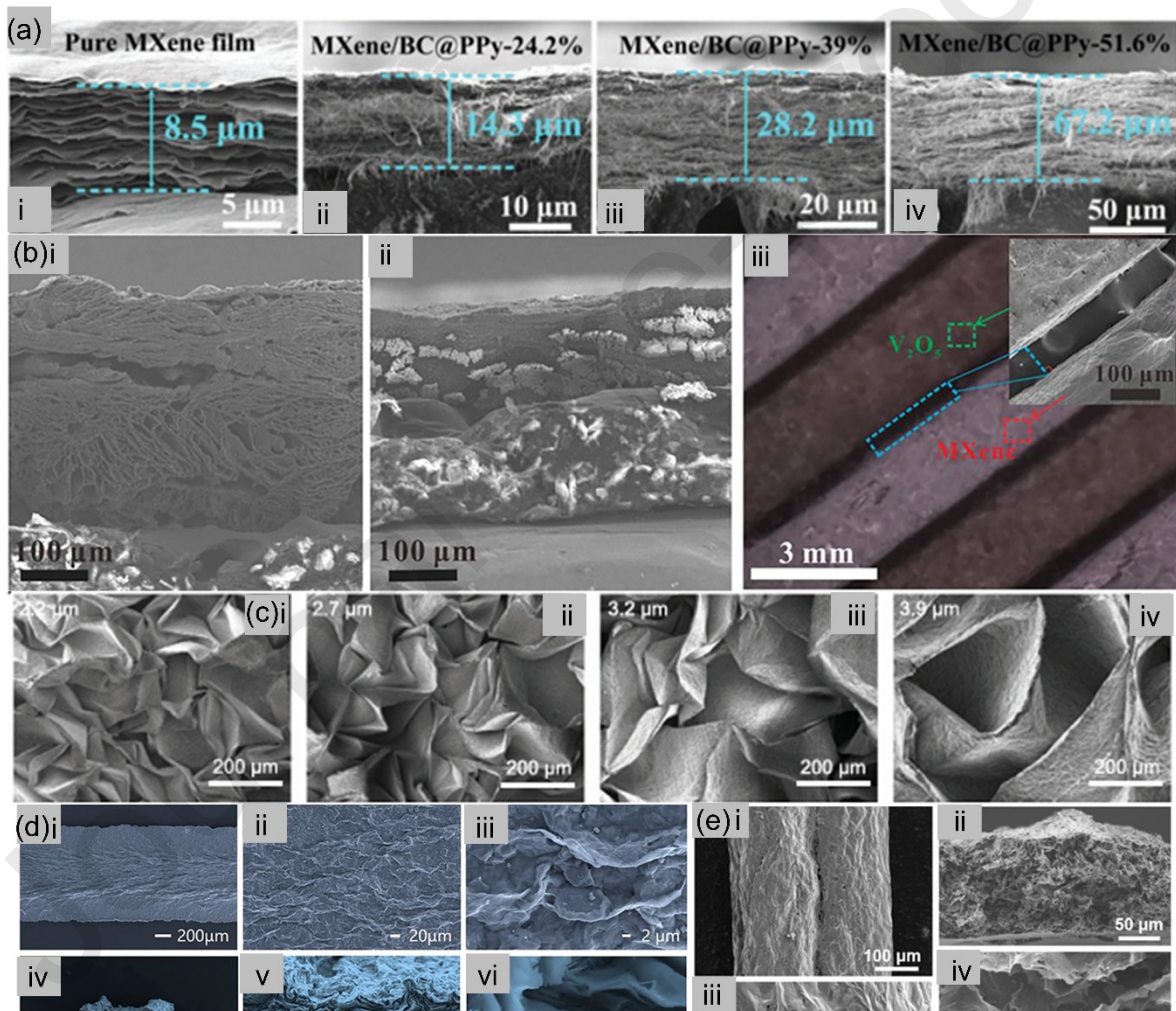


Fig. 13 (a)MXene/BC@ ppy cross-sectional SEM image. Reproduced with permission from [247]©2021WILEY-VCH. (b) (i)Side-view of MXene film, (ii)V₂O₅ cross-sectional image, (iii) MXene-V₂O₅ gaps. Reproduced with permission from [248]© 2021 Elsevier. (c) Morphology of crumpled MXene films. Reproduced with permission from[249] ©2023WILEY-VCH. (d) Surface and cross-sectional morphology of MXene-based electrodes. Reproduced with

permission from[250] © 2023 Elsevier. (e) Side and cross-sectional image of printed MXene electrodes. Reproduced with permission from [251]©2023 WILEY-VCH.

Fig. 13(a) represents well-aligned stacks of MXene layers. The addition of BC and PPy evenly expands the interlayer spacing with the introduction of conductive pathways that facilitate faster ion migration[247]. The composite electrode attains a specific capacitance of 388 mF cm^{-2} with an excellent capacitance retention of 95.8 % over 25,000 cycles. This unique structure engineering, as evidenced by the FE-SEM, unveils the effective contribution of BC and PPy over MXene in the composite flexible electrode for higher electrochemical performance. **Fig. 13(b)** depicts the cross-sectional view of MXene and V_2O_5 , which represents the stacking layers[248]. The asymmetric energy storage device attains a specific capacitance of 129 mF cm^{-2} and a cycle stability of 77%. Wang et al., [249] fabricated a stretchable micro-supercapacitor with MXene micro-supercapacitor. The crumpled surface texture of MXene attains a specific capacitance of 185 mFcm^{-2} with excellent mechanical stretchability up to 800 % strain without compromising the electrochemical properties. **Fig. 13(c)** illustrates the wrinkles over the MXene electrode, which gradually increase over increased thickness. The crumpled MXene texture is attributed to the excellent mechanical stability of the electrodes. The intact morphology of the MXene layers results in stable electrochemical properties. MXene films with thicknesses of 2.2 to $3.2 \mu\text{m}$ exhibit minimal changes in the resistance beyond $3.9 \mu\text{m}$ thickness of the MXene film and suffer reduced electrochemical performance due to induced cracks. Yuan et al. fabricated 3D-printed MSCs with additive-free MXene inks. **Fig. 13(d)** displays the morphology of the printed electrodes with 1mm thickness, which represents monolayer MXene[250]. The wrinkled sheets attain a uniform interlayer spacing that facilitates ion migration and abundant electrolyte exposure that favors excellent electrochemical performance. Benefiting from the unique architecture of the printed electrodes, the 3D printed MSC attains a specific capacitance of 2337 mF cm^{-2} and an excellent cycle life of 10,000 cycles. Zhu et al.,[251] fabricated a high-performance all-MXene-based micro-supercapacitor. **Fig. 13(e)** represents the closely stacked MXene layers in the printed electrode. The cross-section represents interconnected pathways with ion conduction pathways and an efficient electrolyte wetting area induced by freeze-drying. This dense and

porous morphology is attributed to the excellent electrochemical performance of the 3D-printed electrode.

The aforementioned studies provide a detailed insight into the correlation between the MXene morphology and electrochemical properties. The nano-engineered morphology plays a crucial role in levitating the electrochemical performance and stable performance of the MXene-based energy storage devices. Further advanced studies evaluate the electronic structure of MXene for enhanced electrochemical performance, and *in situ* analysis unveils the reaction mechanisms.

4.2 Sheet thickness

MXene sheet thickness varies based on the synthesis technique and post-treatments, which further governs the electrochemical performance owing to its dimensions. The MXene sheets, comprised of thin layers, provide a shorter path for ion diffusion that results in faster redox reaction and optimum charge storage kinetics. Gradual increase in sheet thickness hinders the ion migration and blocks the passages that restrict the ion movement, resulting a sluggish reaction kinetics.

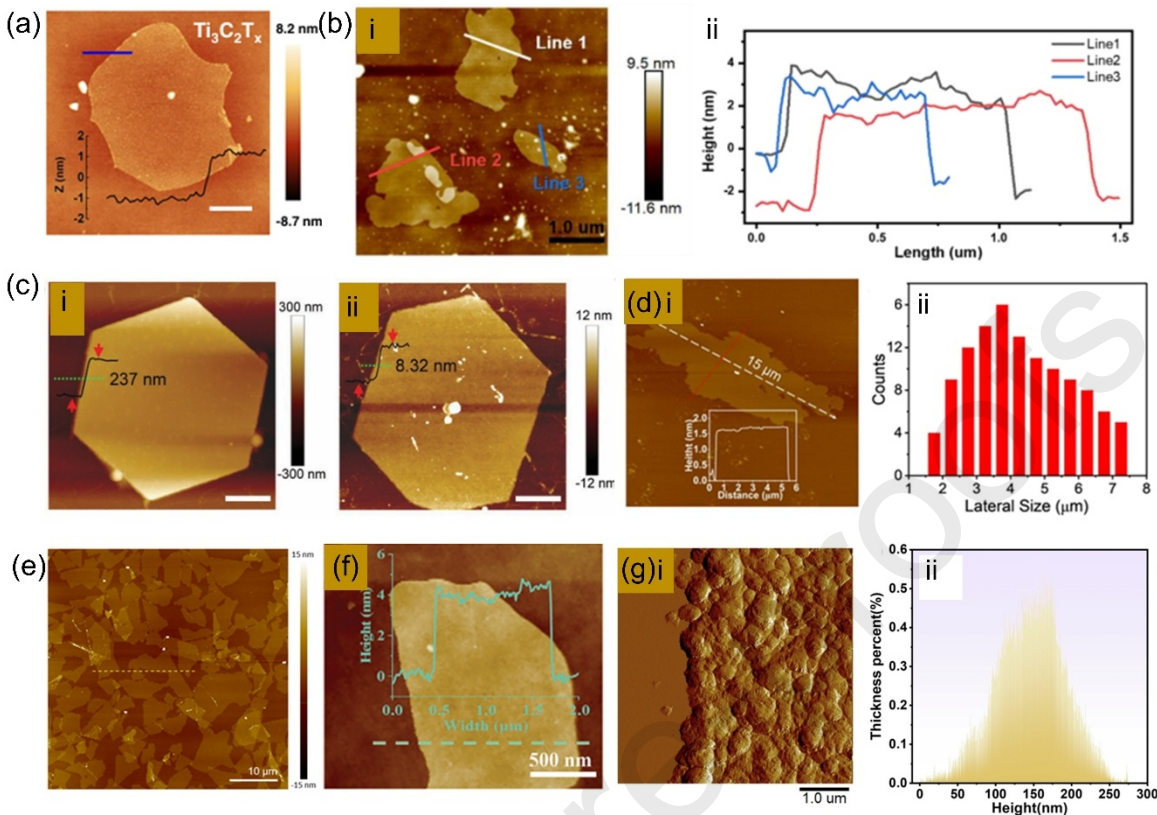


Fig. 14 (a) AFM image of $\text{Ti}_3\text{C}_2\text{T}_x$. Reproduced with permission from [252] ©2021 Springer nature (b) AFM image and corresponding height graph of MXene. Reproduced with permission from [110]©2022 Elsevier (c)(i) Mo₂C crystal growth over Cu and (ii) graphene substrate. Reproduced with permission from[253]©2017 WILEY-VCH (d) (i)AFM image of $\text{CF}_3\text{SO}_3\text{H}$ -MXene (ii) Lateral size distribution of functionalized MXene. Reproduced with permission from [141]©2024 WILEY-VCH (e) AFM sheets of MXene sheets. Reproduced with permission from[142] ©2023 AIP publishing (f) AFM micrograph of Py-MXene flakes. Reproduced with permission from[254] ©2024 WILEY-VCH (g) (i) AFM image of N, S-MXene MSC (ii) Size distribution of N, S-MXene. Reproduced with permission from[255] ©2022 Elsevier

However, thinner sheets often lead to structural failure. In addition to the ion transport, the MXene thickness alters the conductivity. Thin sheets exhibit excellent conductivity due to surface-exposed conductive pathways that provide faster charge transfer. In contrast, thicker MXene sheets lack excellent conductivity due to the presence of interlayer defects, unwanted pores, and limited active surface area. The thin layers of MXene acquire large exposure to the

electrolyte, that facilitates the higher capacitance due to the abundant active area for charge storage. Thicker sheets suffer from limited interlayer ion migration due to a lack of electrolyte exposure and fail to exhibit better capacitive properties as compared to their counterparts. Stable electrochemical performance for a longer cycle life is desirable, along with higher charge storage capacity. The thinner MXene sheets exhibit better cycle life during the charge-discharge cycle owing to their remarkable flexibility. The volume expansion and unstable structure restrict the cycle life of thicker MXene sheets. Further, the single-layer to a few layers of MXene sheets exhibit improved redox reactions due to the presence of abundant active sites. On increasing the sheet thickness, the exposure of active sites is restricted, which reduces the redox activity bargaining the electrochemical performance. Though thinner MXene is proven for excellent electrochemical performance, sometimes very thin sheets lead to structural failure and reduced electrochemical performance. This raises a major concern for the optimization and exploration of MXene thickness and roughness for accessing enhanced electrochemical performance. AFM analysis provides the precise thickness of single-layer and multilayer MXene sheets, where the single layer ranges from ~1-2 nm and the multi-layer MXene ranges from 2-10 nm based on the exfoliation and synthesis techniques. Etchant properties and vigorous reaction result in different roughness of the MXene sheets. A smooth surface is desired for enhanced electrochemical performance whereas rough sheets induce cracks and defects that hinder the ion diffusion and redox reaction. In addition to the layer thickness and surface roughness, lateral size length is a major physical parameter that impacts the electrochemical performance. The lateral size ranges from a few nanometers to several micrometers. The lateral size regulates the electronic structure and electrochemical properties. The larger flake size is attributed to enhanced electrochemical properties due to the better electrical conductivity, whereas smaller flakes provide active edges for redox activity. 3D printing parameters influence the surface morphology of the printed part, which governs the electrochemical properties and long-term performance of the printed part. Researchers have utilized a surface-functionalized MXene ink for 3D printing of electrodes that exhibit a homogeneous altitude throughout the active surface. **Fig. 14(a)** represents the thin MXene sheet with a thickness of 2 nm with a surface roughness of 514.3 pm [252]. The MXene sheets are converted into TiO_2 where the crystal structure converts to a tetragonal from a hexagonal lattice structure without deviating from the flake size or thickness. This

phenomenon indicates the surface tuning of MXene and synthesizes derivatives without compromising the sheet dimensions. The uniform distribution of MXene flakes results in a uniform surface owing to the closely interconnected nanosheets [256]. Sonication time and reaction mechanism influence the thickness of the MXene sheets[110]. The thickness of the MXene nanosheets, followed by ultrasonication, reveals the thickness of MXene, which ranges from 2-4 nm (**Fig. 14(b)(i-ii)**). The electrochemical property of the in-situ HF-assisted synthesis technique was carried out, followed by ultrasonication. The electrochemical performance of monolayer MXene with and without sonication was assessed. The monolayered sheets were obtained after 24h of etching of the MAX phase. The AFM study reveals the thickness of the MXene sheets around 1nm [237]. The ultra-thin sheets provide abundant active sites for faster reaction kinetics and surface redox reaction mechanisms. The reaction mechanism during the synthesis plays a crucial role in determining the size of the MXene flakes and surface terminal groups. MXene synthesized by the CVD technique is influenced by the concentration and flow of methane[253]. **Fig. 14(c)(i)** unveils the AFM image of MXene grown over cu substrate, which attains a thickness of 237nm with a hexagonal structure. The flake thickness ranges from 170-250 nm as obtained from the statistical analysis. As a higher methane concentration, the Mo₂C acquires a uniform crystal growth with a flake size of ~8nm. The presence of graphene regulates the controlled growth of Mo₂C flakes which resulting a uniform and thin layer growth. This study provides insight into the controlled and homogeneous growth of MXene flakes with tuneable thickness through the CVD technique. Researchers have established a one-step Lewis acid-assisted MXene synthesis technique to obtain abundant surface functional groups and enhanced interfacial chemistry (**Fig. 14(d))**[141]. AFM analysis reveals the ultra-thin thickness of the MXene sheet ranges around 1.6 nm. The statistical analysis of 100 flakes provides an average lateral size of around 4 μm up to 15 μm . This flake size is comparatively larger as compared to the MXenes synthesized by the HF/In-situ HF etching method. Larger flakes with ultra-thin sheets are favorable for enhanced electrochemical performance owing to the larger electrochemically active surface area. The etching solution and synthesis temperature influence the physical properties of the MXene flakes (**Fig. 14(e))** [142]. The AFM analysis reveals the anisotropic geometry of the MXene flakes. The average thickness of the monolayer flakes is around 1.96 nm. The lateral size of the MXene flakes is around $4.50 \pm 3.14 \mu\text{m}$. Nitrogen-doped MXene was implemented for a hybrid

aqueous supercapacitor. A few layers of MXene underwent a solvothermal reaction to dope nitrogen. The synthesized Py-Ti₃C₂ films appear to be rougher, comprised of grooves. Further AFM analysis reveals the lateral size of the flakes around 300nm to 1 μm as depicted in **Fig. 14(f)** [254]. The flake thickness ranges around 4 μm, which favors low contact resistance and comparatively higher electronic conductivity for faster ion migration and favourable electrochemical redox reaction. Additive-free MXene ink with hybrid doping of nitrogen and sulfur was carried out through electrostatic adsorption and self-assembly techniques (**Fig. 14(g)**) [255]. Three different protocols were used for the fabrication of the N, S-MXene. AFM analysis reveals the lateral size of N, S-MXene 750 flakes in the range of 0.2-1 μm. The MXene sheets are ultrathin with a thickness of 3.4 nm and an interlayer spacing of 1nm. The ultrathin MXene sheets provide abundant active sites for ion migration and electrolyte adhesion.

The thickness and size of the MXene flakes play a major role in determining the electrochemical performance of the electrodes. This crucial parameter can be regulated by controlled reaction kinetics and a suitable etchant. The desired ultra-thin sheets with stable accordion structure make MXene an excellent candidate for energy storage.

5. Unveiling electrochemical properties from in-situ analysis

In-situ studies unveil the crucial parameters and mechanisms of electrochemical reactions of MXene[257], [258], [259]. In-situ XRD analysis reveals the effect of ion migration on the interlayer spacing, change in phase, and stability of the electronic structure[260]. In-situ Raman studies provide details about surface chemistry and the interaction of electrolytes with the electrode material[261]. Morphological changes are accessed through in-situ TEM analysis[262], [263], [264]. Redox kinetics and state of oxidation can be revealed by in-situ SAX[265], [266]. Nanoscale diffusion and surface properties are explored by in-situ AFM[267], [268]. These studies help to engineer the MXene architecture to boost the electrochemical performance and prolong the stability. The charge storage mechanism of MXene depends on numerous factors, including layer thickness, electrode material, electrolyte, active sites, porosity, etc. **Fig. 15(a)** illustrates the in-situ Raman analysis of Ti₃C₂T_x MXene to unveil the charge storage mechanism. The non-destructive study provides a time-resolved and fast

detection of surface changes [269]. A selected CV profile was analysed for the detection of surface changes. The Raman appears at 703 cm^{-1} , which shifts to 720 cm^{-1} when the potential shifts from -0.5 to -0.3V. Further, a change in potential up to 0.3 V shifts the Raman peak to 737 cm^{-1} . The change in the Raman peak is attributed to the H^+ ion absorption and desorption from the oxygen present over MXene sheets. The color chart illustrates the oxygen atoms in purple and the hydrogen atoms in blue during the real-time electrochemical analysis. A high-intensity signal represents the presence of a large number of bonds over the MXene surface. The redox peak position, which is reflected around 512 cm^{-1} represents the absorbance of H^+ ions to form $\text{Ti}_3\text{C}_2(\text{OH})_2$. The study establishes the correlation between charge-discharge with the conversion between $\text{Ti}_3\text{C}_2(\text{OH})_2$ and $\text{Ti}_3\text{C}_2\text{O}_2$, respectively. **Fig. 15(b)** unveils the charge storage mechanism by in-situ XAS analysis of $\text{V}_4\text{C}_3\text{T}_z$ -based MXene [270]. The oxidation state of MXene was compared with various vanadium-based references (**Fig. 15(b)(i)**). The obtained oxidation state of the MAX phase was 2.08 and for MXene, 3.59, respectively. The electrode undergoes an applied polarizing potential of -0.35 and 0.4 V, respectively, for oxidation and reduction vs Ag/AgCl. The change in oxidation state over the working window reveals the oxidation states of MXene. The potential regions were further analyzed with a combined analysis of oxidation states, capacitance, and phase angle, which confirms the minimal change in oxidation state takes place at 0.05V to 0.25V vs Ag/AgCl. The rest of the potential regions experience a larger shift in oxidation state, confirming the pseudocapacitive contribution of the electrodes, which is attributed to the larger charge storage capacity of the MXene electrodes. In-situ XANES was employed to investigate the contribution of the Ti atom in energy storage the oxidation state of the Ti was unveiled during the redox reaction. The shift in the Ti K-edge energy was measured at various points during the charge-discharge cycles [271]. A weak pre-edge peak was observed at 4971 eV and a strong absorption peak at around 4985 eV. The pre-edge spectrum corresponds to the hybridization of metal and carbon orbitals. The strong absorption peak is induced due to the transition of the 1s electron to an unoccupied Ti 4p state. The K-edge shifts highlight the minute changes during charge and discharge cycles. The changes at each potential confirm the variation in the oxidation state. This obvious change in the oxidation state of the Ti-atom redefines the contribution of redox-active sites during the charge-discharge process. The charge storage behavior under acidic electrolytes was unveiled by in-situ XRD analysis. The pseudocapacitive behavior, including

proton migration and lattice parameter expansion, was analyzed to understand the reaction mechanism[272].

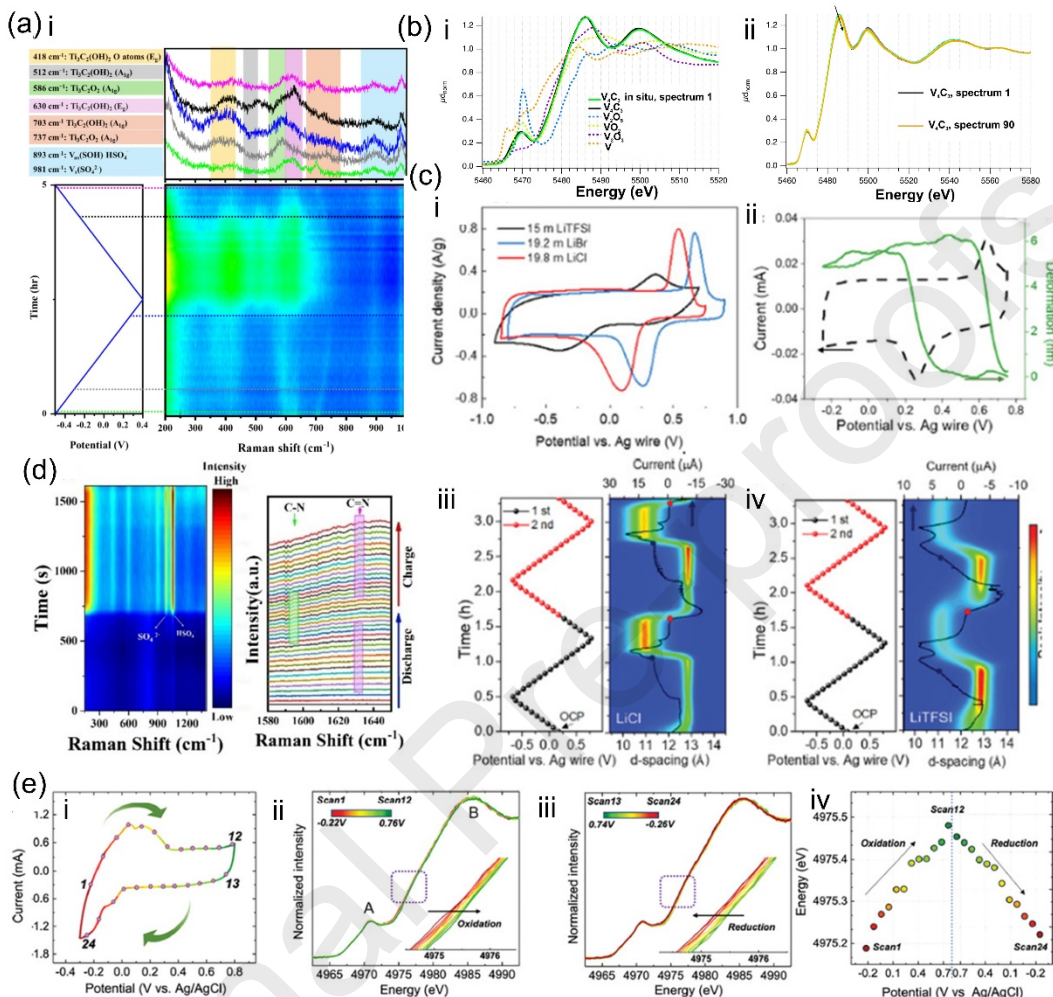


Fig. 15 (a) In-situ Raman analysis of MXene in 1M H_2SO_4 . Reproduced with permission from [269] © 2025 Elsevier (b) (i-ii) In-situ XAS spectra of $\text{V}_4\text{C}_3\text{T}_z$ electrodes with various references. Reproduced with permission from [270] © 2024 Elsevier (c) (i) CV analysis of MXene in WIS electrolyte (ii) CV profile during in-situ AFM analysis (iii-iv) Change in-d spacing during electrochemical analysis Reproduced with permission from[273] ©ACS (d) In-situ Raman analysis of S, N-MXene/rGO composite electrodes. Reproduced with permission from [274] © 2025 Elsevier (e) In-situ XAS analysis during electrochemical reaction and near-edge spectrum of MXene. Reproduced with permission from[275]© 2022 ACS

To evaluate the performance of MXene in water-in-salt electrolyte MXene electrode was analysed in highly concentrated salt solutions as depicted in **Fig. 15(c)(i)** [273]. The CV profiles illustrate the extension of CV peaks beyond 0.7-0.9V in water in salt electrolytes. The CV profiles exhibit excellent coulombic efficiency of MXene electrodes. The WIS electrolyte extends the potential window by nearly 60 % as compared to acidic and neutral electrolytes. The in-situ XRD analysis reveals the change in d-spacing during the redox reaction. The d-spacing change takes place during oxidation and reduction at the onset potentials. Further, the local electrode deformation is unveiled by the operand AFM analysis during the electrochemical reaction. The MXene electrodes experienced fast expansion, and reduction was observed while scanned across cathodic and anodic peaks under 19.8 m LiCl during the CV scan (**Fig. 15(c)(ii)**). The intercalation of ions into the interlayer spacing of MXene has a huge influence on the capacitance. MXene/r-GO composite exhibits excellent electrochemical performance attributed to the excellent conductivity and redox active sites [274]. **Fig. 15(d)** reveals the charge storage mechanism through in-situ Raman analysis during charge-discharge cycles. The peak induced due to the vibration of Ti_3C_2 was detected at 288, 430, and 598 cm^{-1} , respectively. Further, the electrolyte peaks are attributed to SO_4 and HSO_4 at 980 cm^{-1} and 1040 cm^{-1} . The highly intense electrolyte peaks dominate during the electrochemical reactions. The Raman shift recorded during discharge is attributed to the attenuation of C=N resulting from the change in a local chemical environment. The peaks gradually disappear along with the discharge cycle and create new chemical species, as evidenced by the appearance of a new peak at 1594 cm^{-1} . The C=N peak reappears during the charging process, with the disappearance of the C-N peak. The reversible peak appearance confirms the redox reversibility of MXene/rGO electrodes in H_2SO_4 electrolyte. The reversible redox reaction plays a significant role in high-performance energy storage applications with a prolonged cycle life.

Reversible redox reaction attains the advantage of the enhanced capacitive property that was revealed by the in-situ XAS analysis[275]. **Fig. 15(e)(i)** illustrates the in-situ XAS analysis carried out at a scan rate of 2mV/s under LiBr aqueous electrolyte. Different points on the CV curve represent the charging state when the XAS scan is carried out, which is attributed to the Ti-k edge spectrum (**Fig.15(e)(ii)**). The relatively weak pre-edge peak

appeared at around 4971, and the absorption peak was observed at around 2985 eV. The pre-edge weak peak is induced due to the transition of Ti 1s peak to 3d and 2p peaks of metal and carbon, respectively. The strong peak is attributed to the transition of 1s electron to an unoccupied Ti 4d state. The scanned spectra exhibit edge shifts in both anodic and cathodic scans. **Fig. 15(e) (iv)** exhibits consistent changes in energy position and reversibility during redox reactions that portray the contribution of surface redox reactions during ion intercalation and deintercalation. MXene synthesis involves a vigorous reaction in an acidic environment, which influences the crystal phases and electronic structure. The synthesis was explored by in situ XRD analysis.

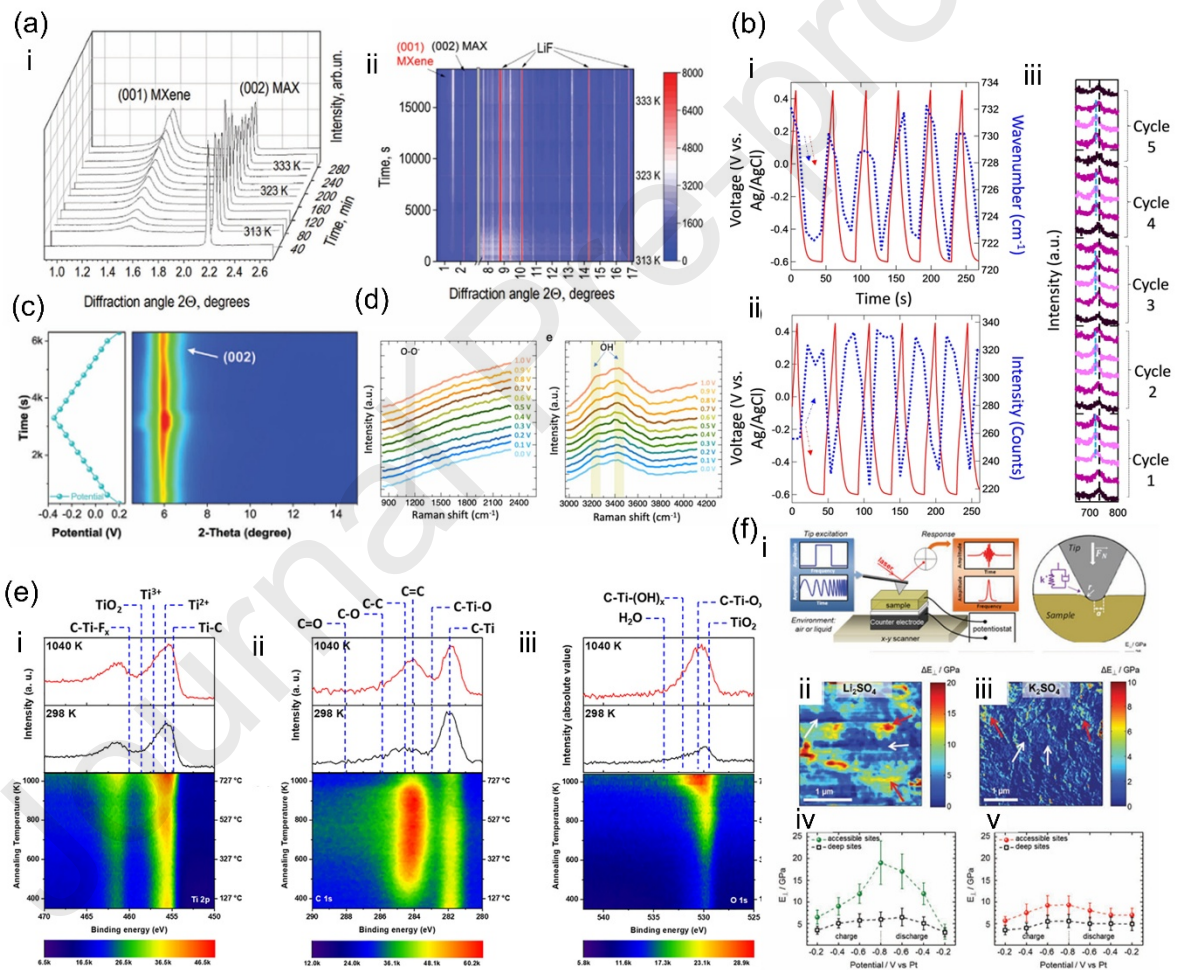


Fig. 16 (a)(i) In-situ XRD pattern during synthesis of MXene (ii) Corresponding heat map. Reproduced with permission from [276]©2024 WILEY-VCH (b) In-situ Raman profile during electrochemical reaction. Reproduced with permission from [277]©2022WILEY-VCH. (c) In-situ XRD map during the electrochemical cycle. Reproduced with permission from [102]©2023

WILEY-VCH. (d) In-situ Raman spectra of Ti_2N in 1M KOH electrolyte. Reproduced with permission from[278] ©RSC (e) Temperature-dependent XPS spectra of MXene and corresponding spectral intensity. Reproduced with permission from[142] ©2023AIP publisher (f) (i) In-situ AFM set up (ii-iii) Ion exchange sites during charge-discharge under 1M Li_2SO_4 and 0.5M K_2SO_4 . (iii-iv) Elastic modulus during charge-discharge. Reproduced with permission from[279] ©2016 WILEY-VCH.

Fig. 16(a) represents the in-situ XRD profiles, which exhibit a shift in the (001) plane to (002) after weakening the precursor material[276]. The heat map for the recorded spectrum was displayed with the full range of diffraction. The expansion of c-lattice observed from the in-situ XRD confirms the induction of interlayer spacing, which is attributed to enhanced electrochemical performance by providing adequate space for ions to migrate and intercalation sites. The charge storage mechanism of MXene is elucidated by the researchers by employing in-situ Raman analysis. The effect of ions in electrolyte and functional groups of the electrode material was unveiled by this operand study. **Fig. 16(b)** represents the peak shift from 730 to 722 cm^{-1} during the charging process, which is attributed to the proton formation and formation of the -O(OH) functional group[277]. Further, the change in peak intensity was observed during the redox reaction. The migration of electrons into MXene overcharges the termination group and draws protons towards the surface. Once the CV attains the oxidative region, the original electronic structure reverses back to the initial state. Further, the shift in functional groups was observed to be reversed back to the predominant -O- functional group. These studies exhibit the charge storage mechanism of MXene, which involves the migration of proton and electron corresponding to the -O- group. The in-situ Raman analysis in acidic and neutral electrolytes reveals the influence of surface terminal groups over the electrochemical behavior, and the shift in terminal groups under acidic media contributes to enhanced specific capacitance. The operand study not only reveals the energy storage mechanism but also helps to select suitable electrolytes for energy storage applications. **Fig. 16(c)** illustrates the in-situ XRD analysis to study the interlayer spacing of Ti_2VC_2 MXene under a CV scan at 0.5 mV/s[102]. The analysis exhibits an expansion and contraction of d-spacing during charging and discharging. The first charging cycle d-spacing increased around 0.08 Å and led to the formation of two new diffraction peaks. On the reverse cycle, the peaks

shift in a similar direction, exhibiting an expansion of d-spacing slightly. The combination of in-situ and ex-situ analysis reveals the contribution of the pseudocapacitive property of Ti_2VC_2 in acidic electrolytes. **Fig. 16(d)** illustrates the catalyst and electrolyte interface during an electrochemical reaction[278]. During the electrochemical reaction in an alkaline atmosphere, no remarkable change in the peak was observed, which confirms the structural stability of the electrode material. An increase in peak intensity results from the high electron density, which is attributed to the OH peak from this analysis. Overall, this in-situ analysis reveals the subsurface of Ti_2N that contributes to stable electrochemical performance. Designing electrode material needs concerns of both physical and chemical stability for uncompromised performance in harsh atmospheres. MXene is prone to oxidation, which restricts its widespread application. Researchers have studied the atomic transition of MXene under high temperatures from the XPS analysis as depicted in **Fig. 16(e)**[142]. The XPS spectrum of MXene was analyzed from a temperature range of 25-777 °C. The corresponding peaks of Ti2p, C1s, and O1s exhibit the formation of additional bonds at elevated temperatures, which confirms the inevitable oxidation of MXene at higher temperatures. In addition to the chemical and mechanical stability of the MXene, designing of electrodes is crucial to attain the optimum electrochemical performance. In situ AFM was employed to analyze the mechanical stability of the electrode as depicted in **Fig.14(f)** [279]. The intercalation sites were accessed after completely discharging the electrodes. The drastic variation of Li^+ and K^+ was evidenced by the contrast. The cation intercalation and regions with various potentials were accessed, which exhibited changes over 15 GPa at some places, confirming the macroscopic deformation of the active area. The ion intercalation influences the elastic modulus of the electrode as revealed by the in-situ AFM analysis. Localization of ions and continuous charge discharge affect the elasticity of the active sites over the electrode material. The formation of by-products, water layer, and intercalating ions plays a crucial role in the stiffness of the electrode, to study and improve the electrode performance.

The overall in-situ studies are major tools to study the reaction mechanism and unveil the optimization technique for improving the electrochemical properties along with long-term stability.

6. Comparative properties of MXene with other 2D materials

In the last decade, advancements in developing 2D materials have unlocked huge potential in a wide range of sectors, including energy storage, conversion, and harvesting[280]. The exceptional properties of these materials captivate the interest of researchers in the energy and electronics sector[281], [282], [283]. Among 2D materials, MXene has attained huge attention for diverse applications attributed to its unique structure and excellent physicochemical properties, such as layered architecture, high surface-to-area ratio, and ultra-thin architecture, has been summarized in **Table 3**. Though graphene, borophene, phosphorene, antimonene, and MXene have been widely explored for energy storage applications, a few of the unique characteristics make MXene a stand-alone candidate for energy applications. MXene attains a unique, tuneable layered structure which allows it to penetrate electrolytes and provides abundant active sites to hold ions. High porosity provides ion migration channels and facilitates faster ion migration through shorter pathways[284], [285]. The presence of transition metal carbides and nitrides offers excellent conductivity and catalytic properties owing to the unique electronic structure. The transition metals offer remarkable electronic conductivity with a narrow bandgap, allowing better electron transport. The negative surface potential of MXene makes it dispersible in a wide range of electrolytes and solvents, which allows close contact between the electrode and electrolyte interface, limiting the charge transfer resistance. Further, the super-hydrophilic nature of MXene makes it a unique electrode material and provides excellent adherence over a wide range of substrate materials. MXene synthesis provides the advantage of functional group intercalation that enhances the electrochemical activity and broadens the potential area of application[286], [287], [288], [289]. In contrast, graphene possesses excellent mechanical strength and conductivity, and some of the features provide performance as compared to MXene. Graphene exhibits excellent conductivity but suffers from surface inertness, owing to which it behaves as an EDLC-type electrode material and exhibits lesser specific capacitance[290]. Graphene lacks any functional group, unlike MXene, which restricts to acquisition of any pseudocapacitive property. Graphene is hydrophobic by nature, which sometimes creates ion repulsion from the electrode surface during electrochemical reaction. Though graphene provides unmatched electrochemical stability, the charge storage ability is compromised concerning MXene. The following table summarizes the physicochemical properties attributed to MXene and graphene (**Table 5**).

Table 5 : Comparative Overview of Structural, Electrical, and Electrochemical Properties of Graphene and MXene

Properties	MXene	Graphene	Ref.
Structure	MXene is derived from thin layers of ternary carbides or nitrides denoted as $M_{n+1}X_nT_x$, where M stands for early transition metal, represents nitrogen or carbon, n is the number of layers, and Tx denotes the surface functional groups.	Graphene is comprised of a monolayer of carbon atoms. It acquires a hexagonal lattice structure.	[291], [292], [293]
Conductivity	MXene attains electrical conductivity up to $2.4 \times 10^4 \text{ S cm}^{-1}$	Graphene exhibits a conductivity of $\sim 2 \times 10^3 \text{ Scm}^{-1}$	[292], [293]
Surface chemistry	MXene acquires various surface functional groups, which enhance the catalytic activities and energy storage properties.	The surface chemistry of graphene is chemically inert.	
Mechanical strength	The presence of transition metal carbides/nitrides is attributed to the excellent mechanical strength of MXene. The Young's modulus of monolayer MXene is around 0.33 TPa, and UTS is around 167 MPa	Graphene attains Young's modulus of 1TPa and UTS of 130 GPa.	[294], [295], [296], [297]
Thermal conductivity	The thermal conductivity of MXene ranges between 10-100 W/mK	Graphene exhibits remarkable thermal conductivity of around 3000-5000 W/mK	[298], [299]
Transparency	MXene film with around 80 % transparency can be prepared	Graphene exhibits excellent optical transparency of 97 %	[300], [301]

Types	Almost 60 types of MXene are available	Graphene belongs to a single composition
--------------	--	--

7. MXene-based composites for electrochemical energy storage

7.1 Limitations of MXene in energy storage applications

MXene, despite possessing numerous advantages over other 2D materials, lags in a few aspects for reliable and stable electrode materials for energy storage applications. The drawbacks of MXene in energy storage are summarized as follows.

The unique layered structure is both a boon and a ban for MXene, which suffers from restacking and leads to electrochemical performance degradation[302]. The sheets tend to restack during electrode fabrication or electrochemical analysis and block the ion migration paths, which drastically reduce the electrochemical performance. The presence of surface functional groups sometimes interferes with redox activity and degrades during electrochemical cycles. MXene exhibits comparatively higher areal capacitance and fails to attain higher gravimetric capacitance without proper densification[303], [304]. MXene is prone to oxidation when exposed to air and aqueous electrolytes, which fail to provide a stable performance in the long run. Oxidation degrades the electrical conductivity and electronic structure, resulting in poor energy storage performance. Batteries and supercapacitors need to exhibit consistent electrochemical performance for real-time applications. However, rapid oxidation and property alternation limit the long cycle life of MXene-based energy storage devices.

7.2 Tactics to enhance the electrochemical performance of MXene

The electrochemical performance is widely dependent on the structure and inherent electronic properties[305]. To retain or enhance the electrochemical performance, the MXene architecture must be protected or modified. Restacking of layers needs to be prevented by interlayer spacers, or modified 3D architecture must be created by the freeze-drying method[302], [306], [307]. Removal of unwanted surface terminal groups enhances the pseudocapacitance of the MXene electrodes. Less oxidative or ionic liquids can be utilized in place of corrosive electrolytes. Surface treatment or composites prolong the cycle life and enhance the electrochemical performance. Researchers have developed a wide range of

MXene-based composites, i.e., MXene-carbon allotropes, MXene-MOF, MXene-LDH, MXene COF, and MXene-polymer, etc[308]. These composites exhibited excellent electrochemical performance by overcoming the existing bottlenecks in pristine MXene. A detailed insight into MXene-based composites is provided in **Table 6**.

Table 6: Overview of MXene-Based Composites and Their Enhanced Electrochemical properties and limitations

Electrodes	Advantages	Limitations	Ref
MXene-Carbon	<ul style="list-style-type: none"> Mechanical stability Enhanced conductivity High specific capacity 	<ul style="list-style-type: none"> Complex synthesis Agglomeration Limited stability 	[309], [310], [311], [312]
MXene-MOF	<ul style="list-style-type: none"> Enhanced electrical conductivity High surface area Improved functionality 	<ul style="list-style-type: none"> Poor interfacial adhesion Prone to degradation Limited scalability 	[313], [314], [315], [316]
MXene-LDH	<ul style="list-style-type: none"> Abundant active sites Enhanced electrochemical performance Tuned electronic structure 	<ul style="list-style-type: none"> Weak interfacial bonding Structural restacking Critical interface engineering 	[317], [318], [319], [320]
MXene-COF	<ul style="list-style-type: none"> Prevents oxidation Enhanced capacitive performance Tuned functional property 	<ul style="list-style-type: none"> Low conductivity Hard to scale up Complex synthesis 	[321], [322], [323]
MXene-polymer	<ul style="list-style-type: none"> Improved mechanical strength Enhanced redox activity Improved thermal stability 	<ul style="list-style-type: none"> Hard to disperse Weak interfacial bonding Challenging uniform dispersion 	[324], [325], [326], [327]

7.3 MXene-Carbon

MXene carbon composites have attained research attention due to the synergetic effect of carbon and MXene to boost energy storage performance. MXene-based thin film supercapacitors deliver excellent specific capacity, however, the performance of supercapacitors reduces drastically at low temperatures due to the sluggish reaction kinetics at the electrode and electrolyte interface. To overcome this Zhao et al., [328] engineered ion transport channels to initiate fast ion migration even at low temperatures res [328]. The fabrication of the process of vertically aligned channels is depicted in **Fig. 17(a)**. The vertically aligned channels are obtained by directional freeze drying of blade-coated MXene /CNT thin film. The concentration of MXene/CNT was optimized to analyze the influence on electrochemical performance.

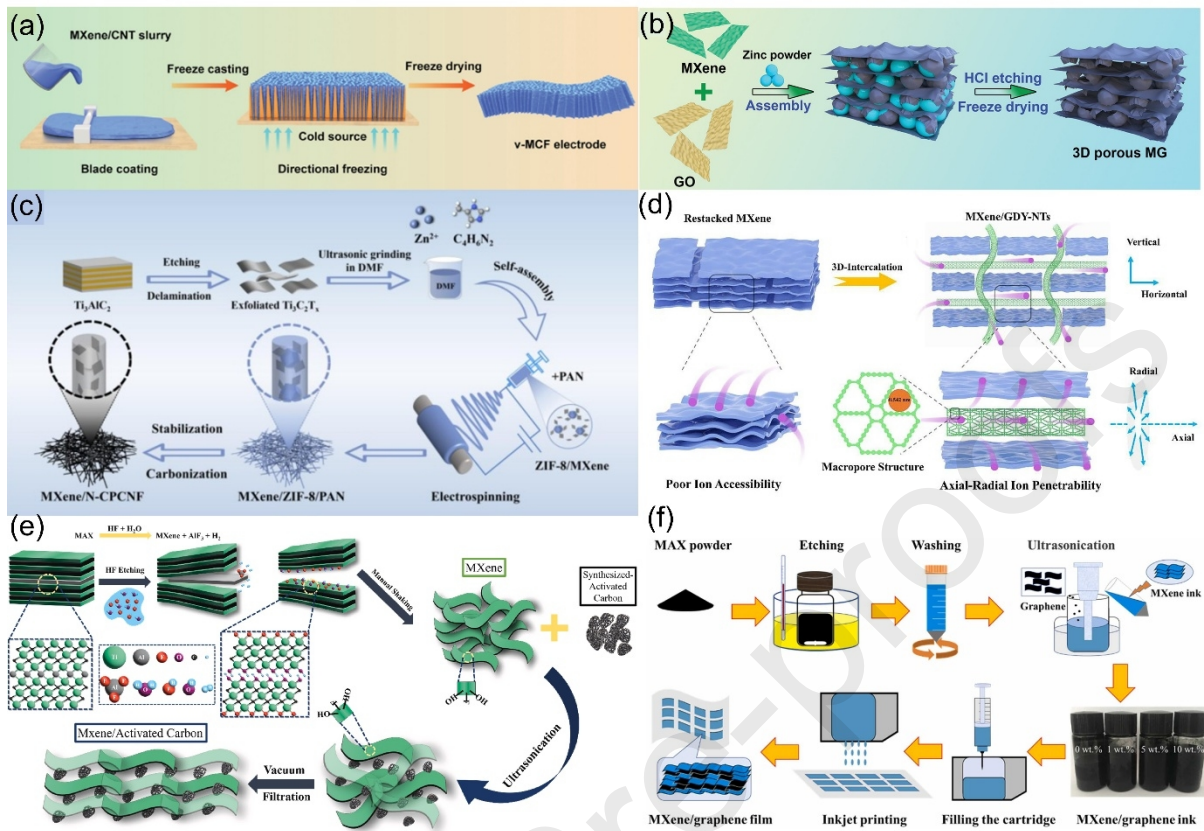


Fig. 17 (a) Schematic illustration of MXene-CNT composite with vertically aligned channels. Reproduced with permission from [328] ©2024 WILEY-VCH (b) Pictorial representation of 3D MXene-GO nanocomposite. Reproduced with permission from[329] ©2021 WILEY-VCH (c) Schematic representation of MXene-N-CPCNF composite. Reproduced with permission from [330] ©2024 Elsevier (d) Synthesis of MXene-GDY-NTs and illustration of ion diffusion mechanism. Reproduced with permission from [331] ©2022 Elsevier (e) MXene-activated carbon composite synthesis. Reproduced with permission from [332] © 2025 Elsevier (f) Pictorial representation of MXene/graphene composite film by 3D printing technique. Reproduced with permission from [333] ©2022 Elsevier

The freeze-dried porous structure attains a large surface area and facilitates faster ion transport with negligible interfacial resistance. The 40 % concentrated film acquires a large number of vertically aligned channels that provide the shortest ion migration pathways. Benefiting the structural advantage of the CNT/MXene electrode exhibits a specific capacitance of 421 Fg^{-1} with a cyclic retention of 86 %. The inclusion of anti-freezing ionogel

enables the supercapacitor to perform under extremely low temperatures of -50 °C with a 92 % capacitance retention. Self-restacking of MXene-based electrodes has raised a concern that needs immediate prevention for the uninterrupted performance of the supercapacitor. Wang et al.,[329] proposed a self-assembly technique for the synthesis of oxidation-resistant MXene-graphene electrodes. **Fig. 17(b)** illustrates the synthesis of MXene/graphene nanosheet under the presence of Zn powder, which acts as the sacrificial template for the freeze-dried MXene graphene composite. SEM analysis reveals the 3D porous structure, which eliminates the stacking issue to both MXene and graphene. The rationally designed porous architecture provides enormous active sites and electrolyte wetting area, which results in a remarkable specific capacitance of 393F g⁻¹ with an excellent long-term cyclic stability of 30,000 cycles. This work eliminates the threat of oxidation as well as layer restacking of pristine MXene and provides insight into developing high-performance electrodes for energy application. **Fig. 17(c)** represents a non-pre-oxidation synthesis of MXene-carbon composite [330]. The fabrication steps involve electrospinning and MOF derivatives. MXene/PAN film with ZIF-8 was carbonized to form the 3D porous architecture. Benefiting from the synergetic effect of N-species, ZIF 8, and PAN molecules, the synthesized electrode attains a larger specific area, abundant active sites, and excellent conductivity, which results in an excellent energy density of 26.2 Wh kg⁻¹ at a power density of 500 W kh⁻¹. The study established a unique advantage of the synergetic effect between the structure-property correlation for enhanced electrochemical performance. Wang et al.,[331] introduced an MXene /Graphdiyne nanotube-based composite electrode for flexible supercapacitor application. **Fig. 17(d)** illustrates the 3D intercalation of GDY-NTs to combat the restacking issue of the pristine MXene. The tuned porpoise architecture selectively allows ion penetration and provides a shorter ion diffusion path for faster electrokinetics. The morphology analysis portrays the incorporation of GDY-NTs as a spacer between the MXene sheets. Benefiting from the excellent structural integrity, the flexible supercapacitor exhibits an energy density of 19.7 Wh kg⁻¹ and cyclic retention of 88.2 % over 10,000 cycles. The restacking of MXene can be prevented by introducing biomass-derived carbon as depicted in **Fig. 17(e)** [332]. Sinha et al., [333] introduced a cost-effective spacer into the MXene layer, which holds the structure unaltered over 5000 electrochemical cycles. Colloidal precursor mixed thoroughly via ultrasonication grafts the activated carbon along the MXene layers, forming an MXene-activated carbon composite. The composite reveals the

3D porous structure comprised of layered MXene and porous activated carbon spacer between the MXene sheets. The stable architecture allows unhindered ion migration through the porous pathways and attains a capacity retention of 92.98 % over 5000 cycles. Further, Wen et al. [333] introduced an MXene graphene composite for ink-jet printing. **Fig. 17(f)** [333]. Represents the fabrication steps involved in MXene/graphene film synthesis. The TEM analysis reveals the stacking of graphene nanosheets with MXene. Further cross-sectional morphology analysis shows the well-maintained increased interlayer spacing as compared to the pristine MXene. The composite electrode exhibits an excellent volumetric capacitance of 183 g F cm^{-3} . This work provides a facile technique to prepare MXene/graphene composite for high-performance supercapacitors by 3D printing.

7.4 MXene-MOF

MXene-MOF composites have been proven as a promising candidate for energy applications, benefiting from the porous architecture of MOF and the excellent conductivity of MXene. The incorporation of MOF enhances the active sites over the highly conducting MXene backbone, which facilitates faster ion transport. The mechanical strength and structural stability of MXene are enhanced by the incorporation of MOF. A hybrid MOF network enhances the ion transport pathways for fast electrochemical reactions.

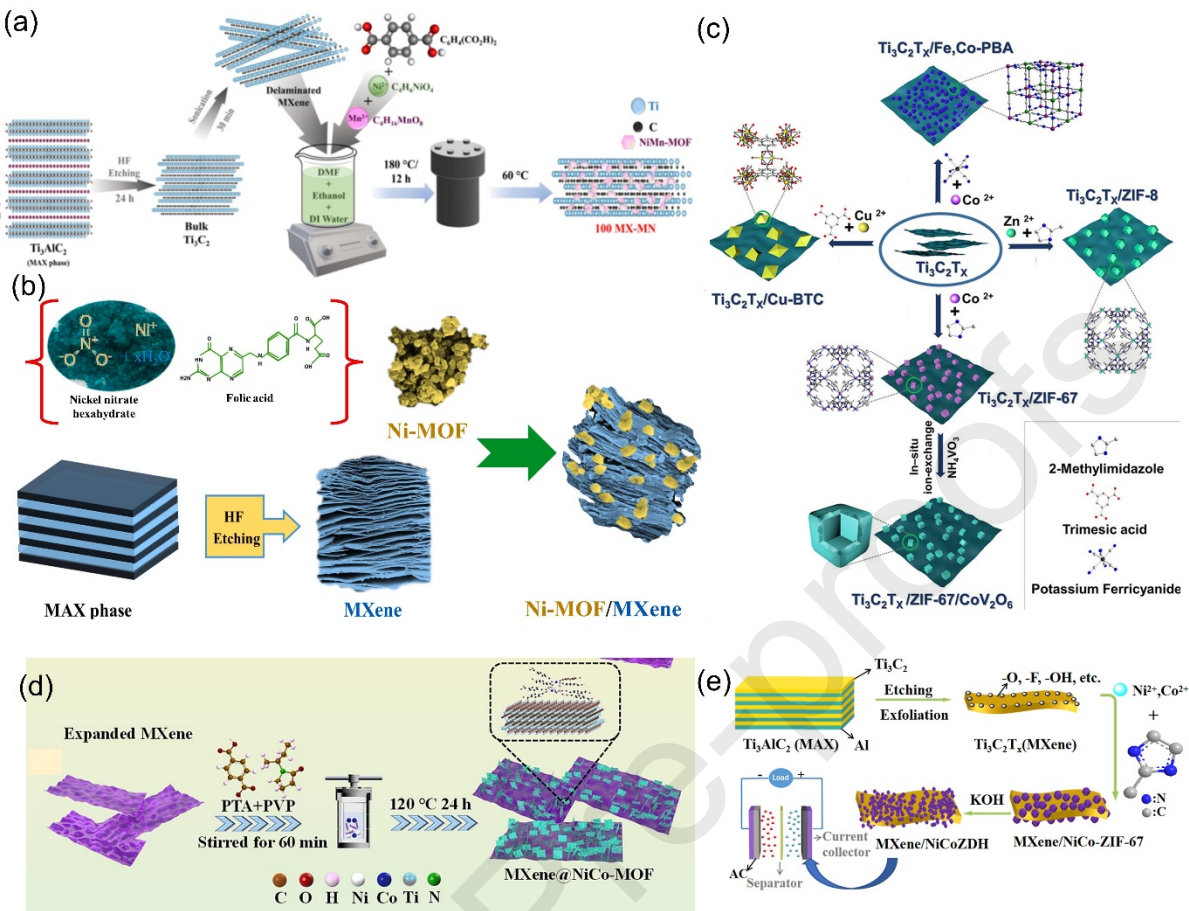


Fig. 18 (a) Schematic representation of MXene/NiMn MOF composite. Reproduced with permission from [334] ©2024 Elsevier (b) Schematic representation of Ni-MOF /MXene composite synthesis. Reproduced with permission from[335] ©2024 Elsevier (c) Schematic representation of in-situ grown 3D MXene /MOF composite. Reproduced with permission from [336] ©2022 Wiley-VCH (d) Synthesis of MXene@ NiCo MOF composites. Reproduced with permission from [240] ©2024 Elsevier (e) Synthesis of MXene and ZIF-derived NiCo LDH composite. Reproduced with permission from [337] ©2021 Elsevier

Shalini et al.,[334] developed a MnNi MOF-MXene composite for energy storage applications. The redox property of MnNi MOF enhances the energy storage ability of MXene due to enhanced active sites and faster ion diffusion. Hydrothermal treatment was employed for synthesizing the composite at 180°C for 24 h. The

morphological analysis reveals the incorporation of MOF between the MXene layers that provides support to avoid any restacking of layers during electrochemical reactions. The structural integrity provides abundant pathways for shorter ion migration and storage space for enhanced capacity. Benefiting from the superior synergetic effect of MXene and MOF, the electrode exhibits a specific capacity of 1028 C g^{-1} and 88 % capacitance retention over 10,000 cycles. Shivade et al.,[335] introduced a facile synthesis method of MOF-MXene composite synthesis assisted with folic acid. The application of folic acid prevents oxidation and induces uniform distribution of Ni MOF over the MXene substrate. **Fig. 18(b)** represents the synthesis of Ni-MOF. The morphology of Ni-MOF /MXene reveals the decoration of nanograins formation over the MXene sheets. The nanograin growth prevents the agglomeration of MXene sheets, facilitating charge storage performance. MOF grains enhanced the surface area and provided an enlarged electrode/electrolyte interface, resulting in a superior specific capacity. The supercapacitor attains a specific capacitance of 76.19 Fg^{-1} . This method proposes the utilization of folic acid-assisted MXene /MOF composites for superior energy storage applications. Liu et al. developed an in-situ growth technique for MXene-MOF composites[336]. **Fig. 18(c)** illustrates the ion-exchange method where ZIF-67, CoV_2O_6 , was decorated over MXene as a supercapacitor electrode. The incorporation of MOF promoted the electrolyte transport and added pseudocapacitive performance. Further, CoV_2O_6 enhances the conductivity for efficient electronic movement, efficient electronic penetration, and additional pseudocapacitance. Benefiting from the unique composition of MXene attains a specific capacitance of 285.5 Fg^{-1} . This work compensates for the poor conductivity of MOF and facilitates the electrolyte transportation owing to the complex hollow structure. The incorporation of MOF with MXene introduces the electronic structure, which enhances the redox activity of the composite [240]. **Fig. 18(d)** represents the PTP, PVP-assisted solve thermal method for NiCo-MOF decoration over MXene. The morphology unveils the presence of ultra-thin NiCo-Sheets over expanded MXene

sheets. The hard template method effectively addressed the restacking issue of MXene and enhanced the active sites and oxygen vacancies over MXene, overcoming the poor electrical conductivity of individual MOF. The solid-state supercapacitor comprised of MXene-MOF exhibits a remarkable energy density of 40.23 Wh kg^{-1} at a power density of $1495.07 \text{ W. kg}^{-1}$. Further, Guo et al. [337] developed an MXene-MOF composite with ultra-stable cycle life over 30,000 cycles with a capacitance retention of 93.3 %. NiCo ZIF-67 was decorated over the MXene sheets to enhance the active sites of the composite. The presence of surface functional groups facilitates the faster ion diffusion and efficient charge transfer. **Fig.18(e)** represents the MXene-NiCo ZIF-67-based composite electrode and supercapacitor fabrication. The alkali treatment regulates the ZIF-67 size over the MXene substrate, which enhances the surface area and ion diffusion area as compared to the bulk counterpart. The composite electrode attained a specific capacitance of 877 Fg^{-1} and cyclic stability over 30,000 cycles. The facile composite synthesis technique established a promising path toward the fabrication of high-performance MXene-MOF composite electrodes.

The aforementioned studies highlight the versatility of MOF-MXene composites for high-performance energy storage applications. The individual bottlenecks of MXene and MOF are overcome by the combined synergetic effect in the composite form. New synthesis protocols and material configurations provide enhanced electrochemical performance, longer cycle life, and a wide range of applications.

7.5 MXene-LDH

Layered double hydroxides have significant theoretical capacity and tuneable architecture for energy storage applications. Despite its unique architecture, LDH suffers from poor intrinsic electronic conductivity and is prone to agglomeration over long electrochemical cycles. To mitigate the shortcomings MXene-LDH composite is a promising technique for enhanced electrochemical performance.

Zhang et al.,[338] introduced an ionic hetero assembly of FeNi LDH over 2D MXene utilizing the mutual coupling strategy. **Fig. 19(a)** illustrates the composite synthesis technique, which involves MXene etching, ultrasonic exfoliation, and hydrothermal growth of LDH over MXene. Post-synthesis TEM analysis reveals the stacking of LDH sheets over the MXene backbone, which improves the stability of the layered structure of both MXene and LDH and further prevents layer restacking. Growth of LDH provides additional active sites and smooth electrolyte wetting that boosts the electrochemical kinetics. Benefiting from the MXene LDH inherent properties, the supercapacitor attained a remarkable energy density of 94.1 Wkg^{-1} at a power density of 7431.8 Wkg^{-1} . The electrodes exhibit a stable performance of 88 % over 10,000 cycles. It provides a unique strategy to integrate LDH and MXene for enhanced electrochemical performance and long-term stability. The electron conductivity of MXene enhances the carrier mobility of Ni-Mn LDH, as shown in **Fig. 19(b)** [339].In addition to the excellent conductivity, LDH offers uniformly distributed active sites throughout that promote the energy storage performance. Benefiting from the synergetic integration, the composite attains long-term stability over 5,000 cycles. This work paves a path towards a highly efficient rationally engineered MXene-LDH structure. The sandwiched structure prevents restacking and enhances the electrolyte accessibility to the deepest core of the electrode. The electron conductivity is largely improved owing to the metallic conductivity of MXene. Rapid redox reaction takes place over a large specific electrode-electrolyte interface.

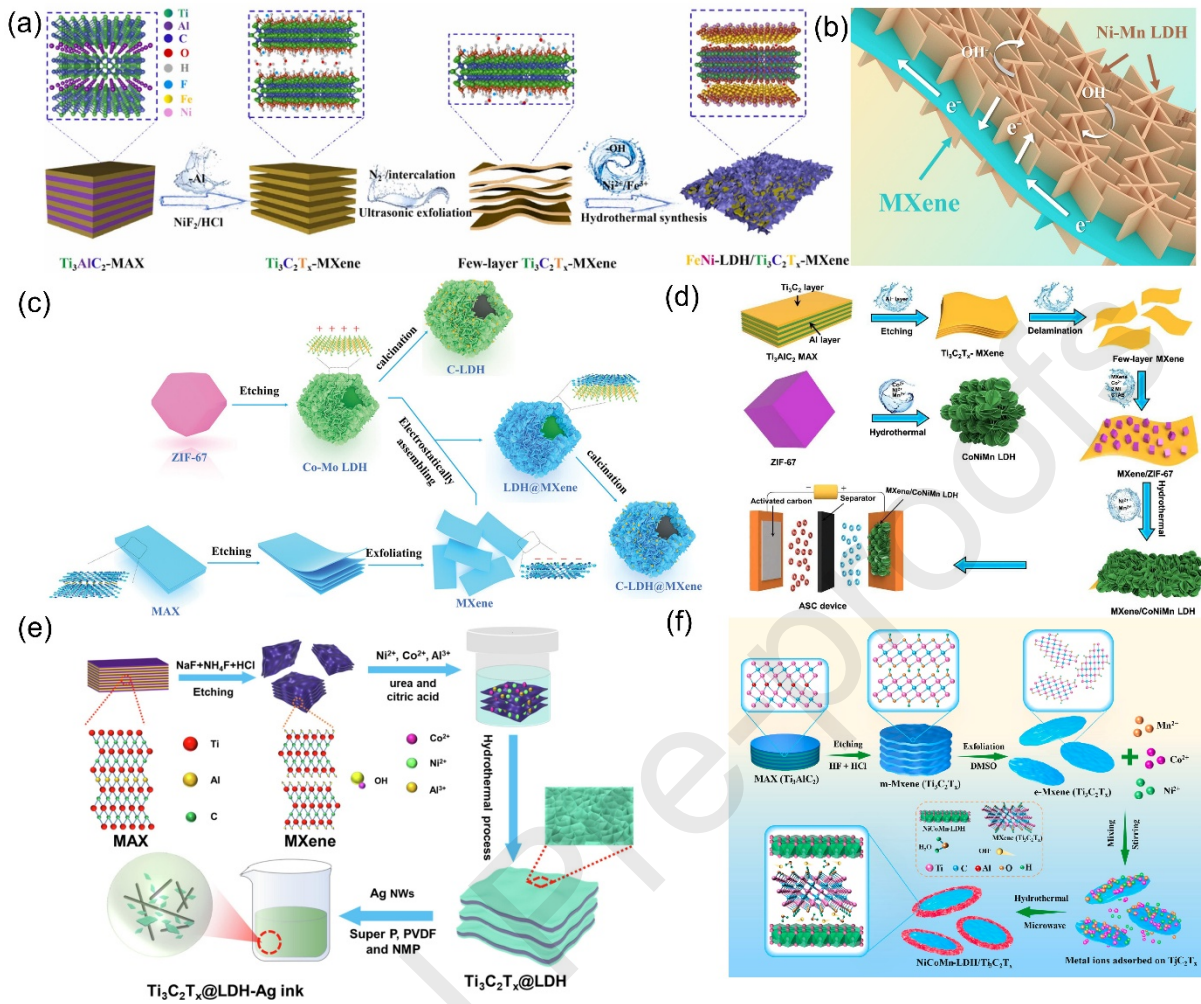


Fig. 19 (a) Hydrothermal synthesis of MXene/FeNi LDH composite. Reproduced with permission from [338] ©2022 Elsevier (b) Illustration of ion conduction path over Ni-Mn LDH and MXene composite. Reproduced with permission from [339] ©2020 Elsevier (c) Synthesis process of MXene-CoMo LDH composite. Reproduced with permission from [340] ©2023 Wiley-VCH (d) Schematic representation of MXene/CoNiMn LDH nanocomposite. Reproduced with permission from [341] ©2024 Elsevier (e) Illustration of MXene-NiCoAl LDH and MXene-NiCoAl-Ag composite ink synthesis. Reproduced with permission from [342] ©2022 Elsevier (f) NiCoMn-LDH -MXene composite synthesis. Reproduced with permission from [343] ©2024 Elsevier

Gao et al., [340] reported a unique synthesis technique of MXene LDH 3D hollow framework boosting the energy storage and microwave absorbance performance. The negatively charged MXene and positively charged C-LDH electrostatically self-assembled to

synthesize the supercapacitor electrode. As revealed from the morphology analysis, the composite acquires a 3D hollow structure and closely packed MXene sheets grafted with layered hydroxides. The composite acquired an excellent latent heat storage ability and efficient photothermal conversion of 96.5 %. The surface tuning and structure engineering of LDH/MXene composite unveils facile techniques for a wide range of applications. Kasiranjan et al.,[341] introduced an electrostatically self-assembling technique for the fabrication of MXene and trimetallic LDH composite as shown in **Fig. 19(d)**. The oppositely charged MXene and LDH particles assembled to form the active electrode material. The incorporation of LDH prevented the restacking of MXene, and MXene enhanced the electronic conductivity facilitating faster ion migration. Thus, the enhanced conductivity and abundant porous active sites enhanced the overall electrochemical energy storage performance of the MXene LDH heterostructure. The composite electrode attained a specific capacitance of 906 Fg⁻¹ and remarkable cyclic stability over 10,000 cycles. Textile-based supercapacitors suffer from high resistance and slower electrochemical kinetics, which is addressed by Zhang et al.,[342] by developing an electrode material comprised of NiCoAl-LDH and MXene composite. The synthesis steps are depicted in **Fig. 19(e)**, which involves the MXene etching, hydrothermal growth of LDH over MXene, and synthesis of MXene@ LDH-Ag ink for electrode fabrication. The super hydrophilic MXene surface provided an abundant active site for the growth of LDH, which enhanced the pseudocapacitive behavior of MXene along with the introduction of porous architecture for efficient ion migration. The composite acquires a stable architecture without any threat of structure restacking. The SEM analysis unveils the uniform growth of LDH over MXene sheets to create a nanoengineered heterostructure. The redox-active LDH and highly conductive MXene exhibit remarkable energy density, which attains a specific capacity of 592 Cg⁻¹ and an excellent cyclic retention of over 10,000 cycles. The synergetic integration of MXene and LDH has introduced a facile synthesis and nanoengineering of electrode material for the enhanced flexible textile-based energy storage application. Luo et al.,[343] introduced a ternary LDH-MXene composite to overcome the self-restacking of layers, poor conductivity, and structural instability of individual entities. The composite acquires multiple oxidation states that boost the overall electrochemical performance. The electrodes exhibit superior rate capability with remarkable specific capacity, benefiting from the synergetic effect of the LDH/MXene composite. The supercapacitor attained a specific

capacitance of 1102.9 Fg^{-1} and cyclic stability of over 5000 cycles. This work presents a simple but efficient technique for enhanced electrochemical performance by utilizing the excellent properties of LDH and MXene.

The research on LDH and MXene composite provides an enormous opportunity to develop high-performance electrode materials for energy applications. The material synthesis involves a simple, energy-efficient, and cost-effective technique that not only enhances the electrochemical property but also opens up opportunities to develop new electrode materials.

7.6 MXene-COF

MXene-COF composites have emerged as a potential candidate for energy storage applications. The integration of MXene and COF induces synergetic effects that address the limitations of MXene and COF individually in energy storage. The hybrid structure enhances the conductivity and surface area, and induces redox properties for energy storage applications. The MXene COF composite attains excellent conductivity owing to the MXene backbone, and a large surface area is attributed to the COF. COF regulates ion diffusion and provides additional active sites. The combined structure prevents the stacking of MXene layers and enhances structural stability.

Zhu et al.,[322] developed a fiber-shaped supercapacitor comprised of MXene-COF as electrode material. **Fig. 20(a)** represents the microfluid-assisted MXene-COF fiber electrode. The microfluidic device consists of four channels, which hold the MXene suspension, MgSO_4 solution, TFB, and PDA, respectively. The composite acquires a porous architecture, and 3D channels provide a shorter ion migration, resulting in improved reaction kinetics. The SEM analysis reveals the vertically aligned COF network over the cylindrical substrate. The supercapacitor attains a specific capacitance of 787 Fg^{-1} and an energy density of 27 Wh kg^{-1} . This tactic establishes a promising path to fabricate fiber-based electrode materials. An et al.,[321] introduced a cation-driven self-assembly technique to prepare COF/MXene composite. The negative surface potential of MXene induces electrostatic attraction to grow a uniform COF layer. The adherence of COF to the MXene structure prevents the restacking of MXene layers. The ordered structure of COF and the excellent conductivity of MXene enhance

the ion transfer and fast reaction kinetics. The flexible composite electrode exhibits a specific capacitance of 390 Fg^{-1} . COF MXene hetero structure acquires excellent pseudocapacitive properties for enhanced charge storage performance. Geng et al.,[323] introduced a COF-MXene heterostructure as illustrated in **Fig. 20(c)**. The amino-functionalized MXene acts as nucleation sites for the growth of COF, as evidenced by the TEM analysis. The COF/MXene electrodes exhibit excellent energy storage properties owing to the synergistic integration of inherent properties. The influence of C=O groups in COF/MXene heterostructure attains a specific capacitance of 290 Fg^{-1} . This work provides insight into the formation of MXene /COF-based electrode materials for high-performance energy storage devices.

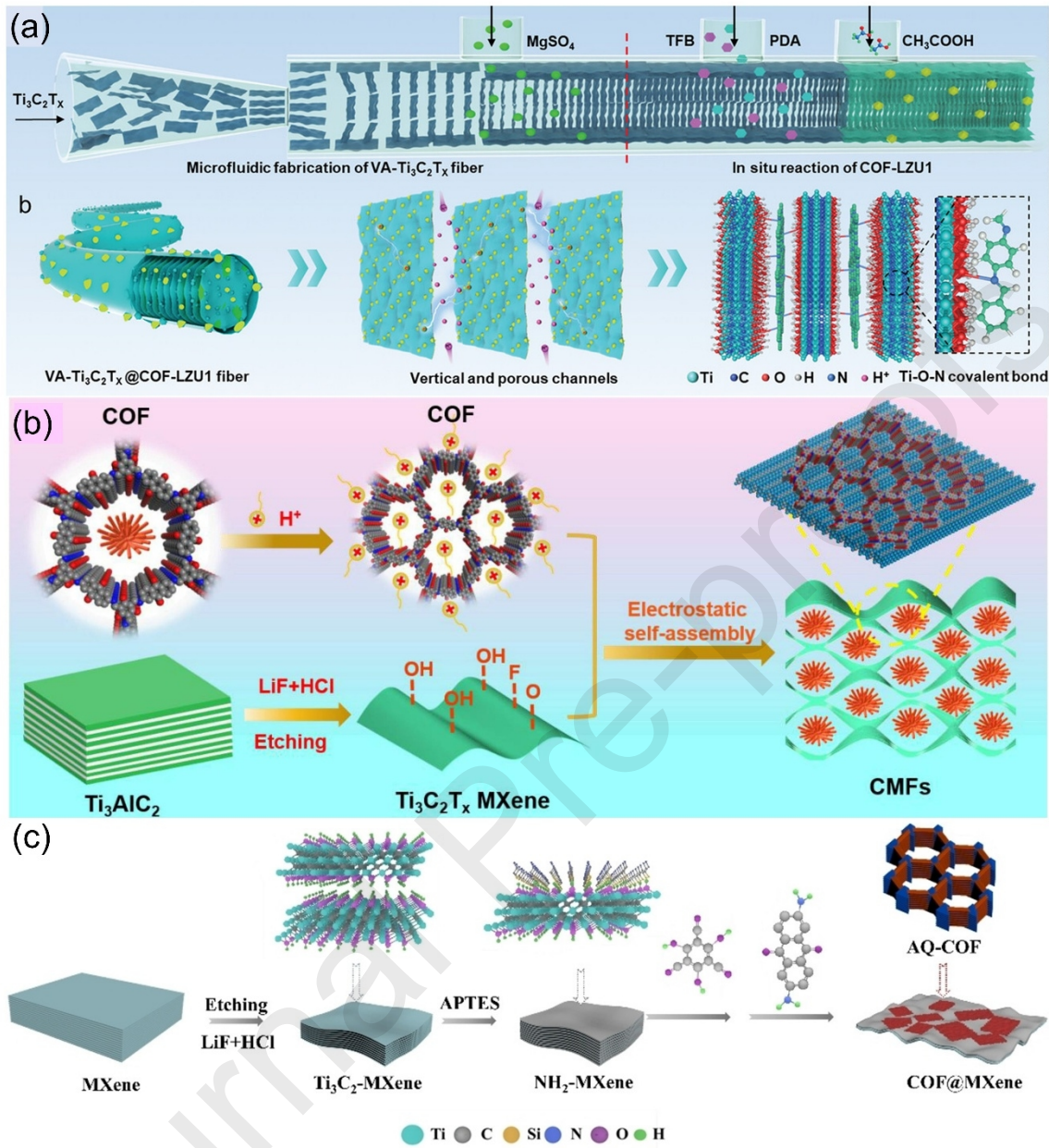


Fig. 20 (a) Schematic illustration of vertically aligned MXene-COF composite fibers. Reproduced with permission from [322] ©2023 Wiley-VCH (b) Synthesis of COF-MXene composite through electrostatic self-assembly. Reproduced with permission from [321] ©2023 Elsevier (c) Synthesis of amino-functionalized Ti₃C₂ MXene-COF composite. Reproduced with permission from [323] ©2022 Wiley-VCH

7.7 MXene-Polymer composites

MXene polymer composites enhance the processability, mechanical strength, and conductivity. The addition of conductive polymers introduces a 3D conductive network, which improves the charge storage capacity and enhances structural stability for prolonged electrochemical reactions. Conductive polymers suffer limited specific capacitance, whereas MXene acquires enhanced pseudocapacitance but lags in long-term stability. Ren et al.,[344] introduced an MXene PEDOT: PSS composite that overcomes the existing bottlenecks of flexibility, limited capacity, and long-term stability. The composite constructs a transparent flexible supercapacitor as shown in **Fig. 21(a)**. MXene and PEDOT: PSS solution were homogeneously mixed and spin-coated to form the transparent electrodes, which are further sandwiched between PVA-H₃PO₄ gel electrolyte to construct the supercapacitor. The composite films acquired an excellent planarly arrangement of MXenes in the PEDOT matrix that enhanced the charge storage capacity and resulted in a specific capacitance of 3.1 mF cm⁻². The incorporation of MXene into the polymer matrix provides a promising technique for high-performance supercapacitor fabrication. High conductivity broadens the application area of supercapacitors. Zhang et al. introduced a simple fabrication technique to fabricate highly conductive MXene: PEDOT: PSS composite modified with tartaric acid [345]. The additive restricts the oxidation of MXene in water and creates a strong adhesion between MXene and PEDOT: PSS. **Fig. 21(b)** illustrates the synthesis technique of MXene /PEDOT: PSS composite electrodes by a spray coating method. The composite attains a 4-fold rise in conductivity along with structural stability attributed to tartaric acid treatment. The excellent specific capacitance of 4,272 μF cm⁻² and superior conductivity make it a suitable candidate for energy storage and AC line filtering. The interlayer spacing can be retained by introducing conductive polymer spacers. Chen et al.,[346] introduced a unique strategy to introduce PANI-nano fibers as spacers between MXene layers. **Fig. 21(c)** illustrates the fabrication of PANI-MXene composite by the self-assembly technique. The opposite surface charge of MXene and PANI leads to the incorporation of PANI nanofibers inside the MXene layers, which acts as a spacer to prevent restacking and enhances the pseudocapacitive property, as well as resulting in better energy storage capacity. The morphology analysis reveals the ordered superposition of PANI fibers over MXene sheets. Benefiting from the synergetic composition of PANI and MXene, the composite electrode exhibits excellent specific capacitance of 645.7 Fg⁻¹ and cyclic stability of 98 % over 10,000 cycles. Zheng et al.,[345]

designed a lightweight MXene-polymer composite by the direction freeze drying process as shown in Fig. 21(d). Directional freezing provides a reliable method to obtain porous channels. The precursor solution gets exposed to directional temperature and freezes gradually. The polymer is concentrated with ice crystals, which upon removal form the aerogel. The PVA, BC, and MXene composite forms a hierarchical porous network that allows ion transport and enhances charge storage density. Benefiting from the composition and architecture, the electrodes exhibit a specific capacitance of 3948 mFcm^{-2} with a capacitance retention of 120 % over 10,000 cycles. The simple, facile composite synthesis technique offers a unique strategy to fabricate high-performance electrode material for energy storage and sensing applications.

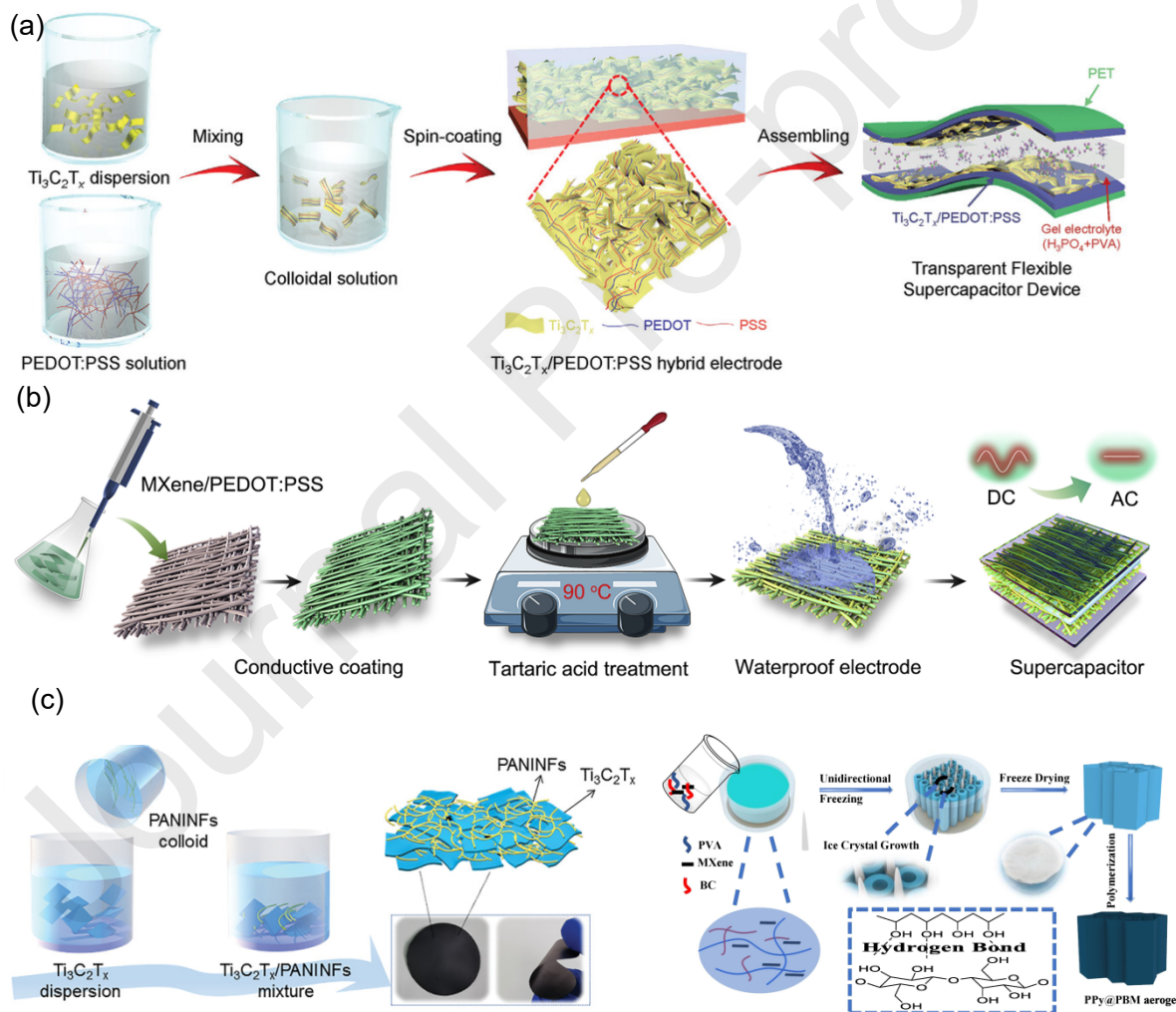


Fig. 21 (a) Schematic illustration of MXene PEDOT: PSS composite synthesis. Reproduced with permission from [344] ©2024 Wiley-VCH (b) Chemically stable MXene @PEDOT: PSS composite electrodes. Reproduced with permission from [347] ©2021 the authors (c)

Fabrication process of MXene-PANINFs composite films. Reproduced with permission from [346]©2021Wiley-VCH (d) Schematic illustration of PPy @MXene composite aerogel. Reproduced with permission from [345] ©2023 Elsevier

8. Computational studies and electronic structure optimization

Computational studies and electronic structure optimization play a significant role in determining the reason behind the enhanced electrochemical performance of MXene. Density functional theory (DFT) has been widely utilized to unveil the structure-property correlation of MXene-based electrode materials in energy storage applications. The band structure and density of states are prime factors that determine the electron affinity and govern the electrochemical properties. The influence of surface functional groups can be predicted by DFT analysis. The surface terminations induced during the synthesis of MXene impact the electrochemical performance and are unveiled by computational models. Further adsorption energy, electrochemical reaction kinetics, and charge storage mechanisms are widely explored by DFT studies. Metal ions adsorption/desorption over the active sites is thoroughly analyzed by DFT models to obtain a clear understanding of the energy storage mechanism and help in designing MXene-based electrode material with enhanced capacity. DFT provides insight into the stability of MXene-based materials under varying electrolyte conditions and unveils the phase change, oxidation state, and structural degradation during electrochemical reactions. A comprehensive analysis is carried out to highlight the DFT analysis of MXene-based electrode materials for energy storage applications.

The contribution of the electrostatic interaction of N, S MXene nanostructure over pristine MXene is accessed[255]. **Fig. 22(a)** depicts the simulated structures of N, S-MXene, and P-MXene, which influence the electrochemical reaction kinetics. The plane (002) is selected as the active surface for electrochemical reaction. The density of states of N, S MXene, and P-MXene unveils the enhanced carrier density that exists around the Fermi level. The N, S-MXene attains a higher metallic conductivity that is attributed to faster electron transport. **Fig. 22(a)(ii-iii)** exhibits the interfacial electron interaction and distribution of MXene and N, S-MXene.

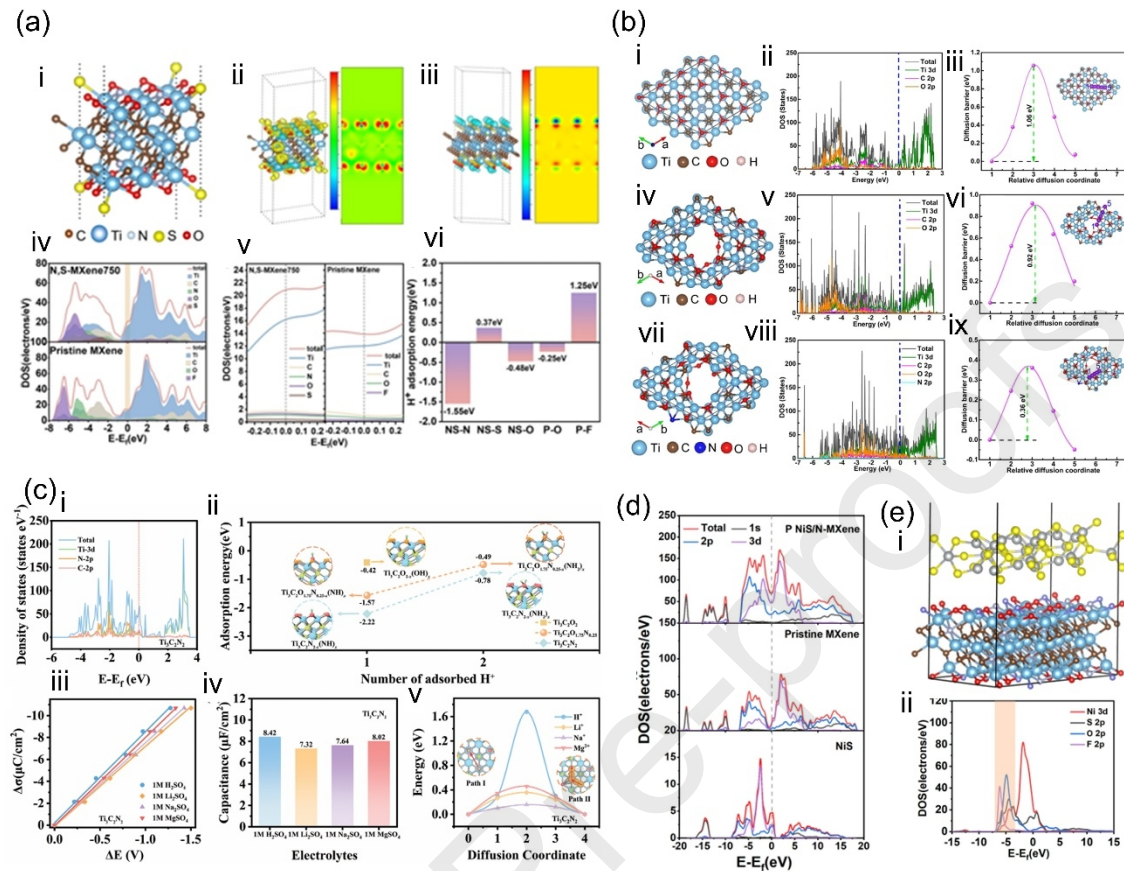


Fig. 22 (a) (i) Atomic model of MXene (ii-iii) Difference in charge density of N, S MXene (iv-v) Density of state of MXene (vi) H⁺ adsorption energy. Reproduced with permission from [255]©2022 Elsevier. (b) Optimised electronic structure of MXene nanosheets, QDs, and N-doped MXene QDs and their corresponding density of states and diffusion path. Reproduced with permission from[348] ©2024 Elsevier (c) (i) Density of state of MXene monolayer (ii)Corresponding adsorption energy (iii)Surface charge density to potential (iv) Capacitance value per unit surface (v) Diffusion barrier profiles. Reproduced with permission from[254] ©2023WILEY-VCH (d-e) Density of state of P-NiS/N-MXene, pristine MXene, and NiS. Reproduced with permission from [349]2022 Elsevier.

The depletion and accumulation of electrons around the Ti atom facilitate the migration towards the (002) plane. The preliminary electronic models agree with the Ti-N, Ti-S, and Ti-O as obtained from the XPS analysis. Further N, S-MXene offers more charges to the interface, unveiling the injection of the hole. The adsorption energy analysis illustrates that the lower adsorption energy of N, S-MXene favors the easy occurrence of adsorption

facilitating the smooth migration of ions and electrons. Additionally, lower charge transfer resistance attributed to the presence of lone pair electrons in N, S-MXene synergistically exhibits excellent capacitive behavior in acid electrolytes. **Fig. 22(b)** unveils the contribution of defect-rich N-doped MXene QDs for high-performance MSC[348]. The electronic models suggest the key role of Ti-Ti metallic bonds for improved electron conduction, which further increases on reducing the MXene dimension. The MXene QDs exhibit improved conductivity due to nitrogen doping. N-doped defect-rich MXene QDs exhibit a diffusion barrier of 0.36 eV that offers fast ion migration and improved redox reaction. The DFT study reveals the contribution of tuned electronic structure, improved chemical states, excellent conductivity, and lower diffusion barrier for the drastic performance enhancement of the N-doped MXene QDs. The ion interaction and migration play a crucial role in estimating the inherent property of the electrode material. **Fig. 22(c)** illustrates the optimized interaction sites of different ions present in the electrolyte[254]. The increased density of states around the Fermi level evidences the higher electron conductivity. The adsorption energy induced due to the protonation favors the higher pseudocapacitive behavior. Higher nitrogen content also contributes to the excellent pseudo capacity due to the higher electron affinity, which provides extra electrons and agrees with the Bader charge transfer. The effective contribution of different ions was explored by variation of charge storage. N-doping overall enhanced the electron conductivity and acts as an active site for the smooth charge transport between the electrode and electrolyte. The electrochemical performance of MXene is greatly influenced by the addition of functional groups and dopants. The synergetic effect of MXene and the dopant is analysed through the electronic models and simulated MXene structures. **Fig. 22(d)** demonstrates the DOS of NiS and P-NiS/N-MX containing continuous charge density close to the Fermi level. The (002) plane acts as the active plane for electron adsorption and desorption during electrochemical reactions. P NiS/N-MXene attained higher electron conductivity as compared to N-MXene. Owing to the less resistance, N-MXene acquires higher free electrons to react synergistically during redox cycles.

The aforementioned discussion suggests DFT study is one of the indispensable tools to tune the electrochemical properties. Atomic-level structural nano engineering predicted

stability, and selective electrolytes can develop a next-generation MXene-based energy storage device by utilizing the DFT analysis.

9. AI and Machine learning in MXene synthesis and electrochemical analysis

Artificial intelligence (AI) is revolutionizing the field of MXene synthesis and property prediction by allowing for data-driven discovery and optimization[350]. In MXene research, AI technologies, particularly machine learning models, are used to evaluate massive datasets of synthesis parameters and material properties to identify hidden patterns and connections[351], [352]. These findings help forecast ideal synthesis conditions and adapt MXene characteristics for specific applications like energy storage, catalysis, and sensing. Furthermore, AI speeds the discovery of novel MXene compositions by predicting their stability and functionality before experimental validation, saving time and money[353], [354], [355]. This incorporation of AI not only improves the efficiency of MXene research but also paves the path for rational materials design on a massive scale. Furthermore, AI-driven modeling is critical for process optimization, forecasting how synthesis parameters like as etching time, temperature, pH, and precursor composition affect MXene electrochemical performance. This helps to further the development of scalable, reproducible manufacturing routes[356], [357]. Combining AI tools with automation and robotics in the lab could lead to closed-loop experimentation systems in which ML models direct experiments in real time, dramatically speeding up the materials discovery pipeline[358], [359], [360], [361]. The combination of AI and machine learning with MXene-based electrochemical energy storage is redefining the research environment, allowing for more intelligent material design, lowering

development time, and opening the way for high-performance, cost-effective, and sustainable energy storage systems[362], [363].

Frey et al.,[364] employed a positive and unlabelled (PU) machine learning framework for the prediction of MXene properties and the effective synthesis route. **Fig. 23(a)** illustrates the possible MAX phases and possible MXene synthesis routes utilizing machine learning. 18 MXene compounds and 20 MAX phases are identified for establishing the synthesis technique. This strategy predicts around 800 potential synthesis techniques. Elemental information, structural, thermodynamic, and electronic data were utilized from the DFT calculations. The predicted models were validated with experimentally synthesized MAX phases. The phase stability analysis and comparison of properties were carried out based on 63 synthesized MAX phases and 10 MXene compounds. The PU learning model predicts 111 MAX phases and 18 MXenes as viable candidates for synthesis, guiding future synthesis efforts. Thermodynamic and elastic stability studies demonstrate that 87 % of the expected positive MAX phases are categorized as "viable crystals." PU machine learning was modified and applied to the synthesis of bulk and 2D materials, focusing on MXene and their parent MAX phases. The trained model demonstrated that thermodynamic stability, binding strength, and charge distribution were the most relevant features for making model predictions. The study found potential MAX and MXene systems for synthesis, offering a computational process for creating actionable predictions and bridging the gap between theory and experimental realization.

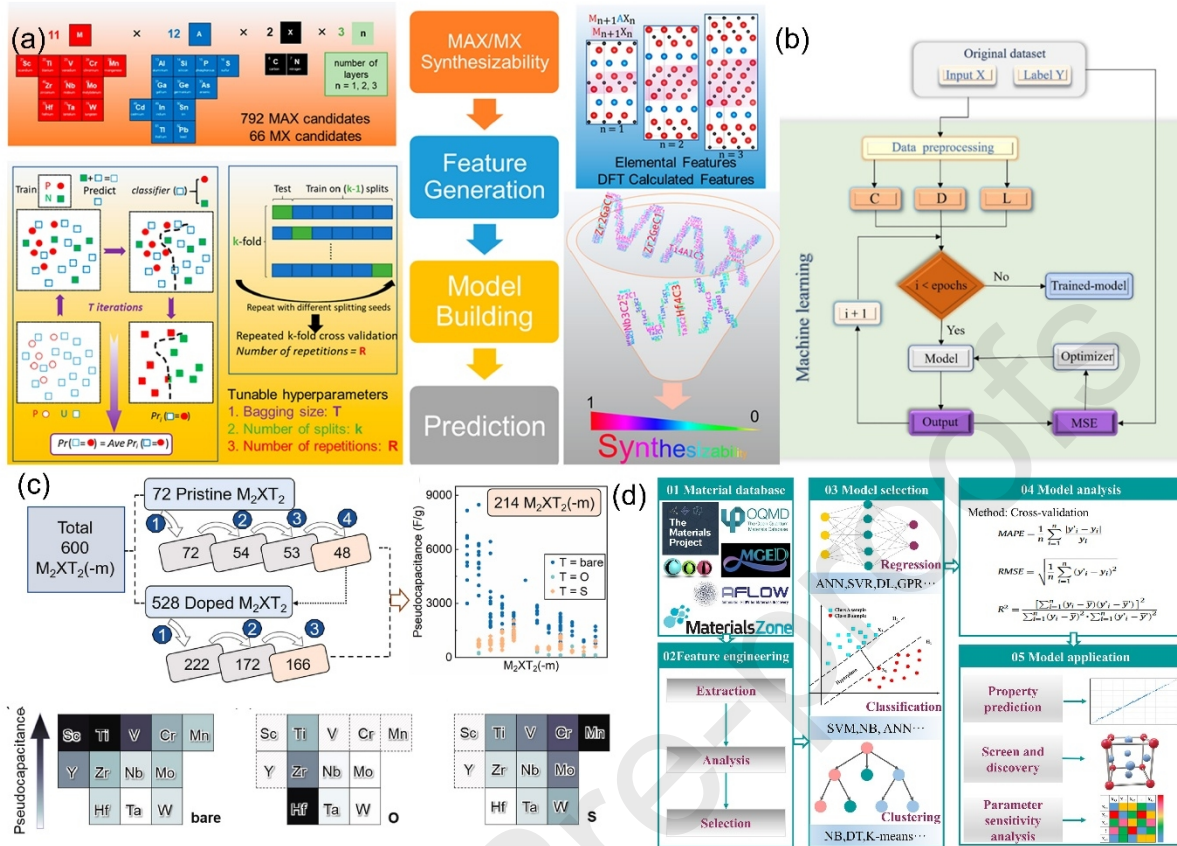


Fig. 23 (a) Schematic representation of chemical search space and computational model along with PU learning. Reproduced with permission from [364] ©2019 ACS (b) Illustration of machine learning prediction. Reproduced with permission from [365] ©2023 Elsevier (c) MXene elemental design and analysis of pseudocapacitance property. Reproduced with permission from [366] ©2023 Elsevier (d) A general idea about machine learning-based material development utilizing the database, modeling, and model selection, and real-time application. Reproduced with permission from [367] ©2021 Elsevier

Synthesis of MXene-based aerogels tends to be challenging due to the sensitive properties of MXene in open air and aqueous media. Though these aerogels have gained huge attention over the period, there is still no standard synthesis protocol or reproducible result to upscale for commercialization. To eliminate the variation in property Rong et al.,[365] developed a machine-learning tool based on the artificial neural network, support vector mechanism, and random forest models. In the analysis of 34 sets of MXene data, the ML is trained to predict the respective property. **Fig. 23b** represents the flow chart comprising the

machine learning prediction model. The obtained results predicted the compression modulus of MXene cellulose composites, which matches with the experimental results from the available literature. Additionally, the RF model provides the MXene percentage to prepare high-performance composite aerogels. Though MXene acts as a well-known pseudocapacitive material, the structure and synthesis technique largely influence the energy storage performance. So, to establish a standard correlation between the design and performance of MXene Wang et al.,[366] proposed a machine learning model comprised of 600 MXene and their derivates. DFT was employed to analyze each MXene property individually to avoid any misinterpretation of inherent properties. The SISSO method was employed to predict the pseudocapacitive property based on the electronic structure. The ion adsorption mechanism of the pristine and doped MXene systems was evaluated based on the generated hydrogen ions. The formation of pseudocapacitance relies on both ion migration and generation. **Fig. 23(c)** represents the 4-step screening of 600 MXene models based on the inherent properties and summarizes based on the pseudocapacitance owing to the surface groups. The materials are further classified into respective groups based on their distribution of respective metallic elements. This work suggests a standard method of estimating pseudocapacitive properties using machine learning to avoid complications and time consumption in material synthesis and the design of new materials. Liu et al., [367] have highlighted the prediction of energy materials by suitable machine learning methods. The AI and ML techniques are highly data-centric and need to be trained with experimental results to predict or validate any new proposed structure or composition for energy applications. The need for new materials for carbon neutrality, energy storage, and catalytic applications requires training and updated models for an accurate prediction. **Fig. 23(d)** summarizes the models for ML application and database construction, algorithm optimization, and model applications. The material database acts as a reservoir of data sets that provide the preliminary information as available from the database. Further, extraction and model selection lead to the process of the data based on the trained models and the required prediction of the property. The overall process estimates and evaluates the ML models and assists the user in optimizing the model and obtaining the required property parameters. The combination of 0D and 3D materials enhances the overall property of the composite for energy storage applications. Pradhan et al. developed an ANN model to optimize the material configuration, process parameters, and electrolyte

compatibility to enhance the overall energy storage performance of the composite [368]. **Fig. 24(a)(i)** illustrates a trained ANN model comprised of electrochemical analysis parameters and active materials to validate the theoretical calculation and experimental values. The CV curves based on the predicted and obtained current are depicted in **Fig. 24(a)(ii-iii)**. Based on the ML model, the active material concentration was optimized, and energy storage properties were well predicted from the simulation. Based on the optimized parameters, the supercapacitor was fabricated, and an electrochemical experiment was established. This study established an optimized multilayer ANN model for the prediction of the electrochemical performance of MXene-based composites. The increased trend on MXene-based composites has attracted the attention of researchers to optimize the process parameters with less waste of materials to save the cost and limit the experiment time. Shariq et al., an ML model to predict the performance of MXene /graphene composite based on the physicochemical properties. The composition of the active material was predicted from the real-time experiments [369]. **Fig. 24(b)** represents the ML model for performance prediction, which was trained with the electrochemical parameters. The experimental and predicted performance exhibits a linear relation as shown in **Fig. 24(b)(ii-iii)**. The artificial neural network model for electrochemical performance considers real-time correlations between input characteristics that impact supercapacitor electrode activity. It demonstrated a remarkable ability to learn and adapt to nonlinear datasets, resulting in the maximum prediction power for the investigated output features. Furthermore, it accurately predicted unperformed experimental results. The proposed model outperforms the existing model due to its self-adoptability and self-training method. The model opens up the opportunity to predict the properties of MXene derivatives for energy storage applications in a fast and accurate fashion.

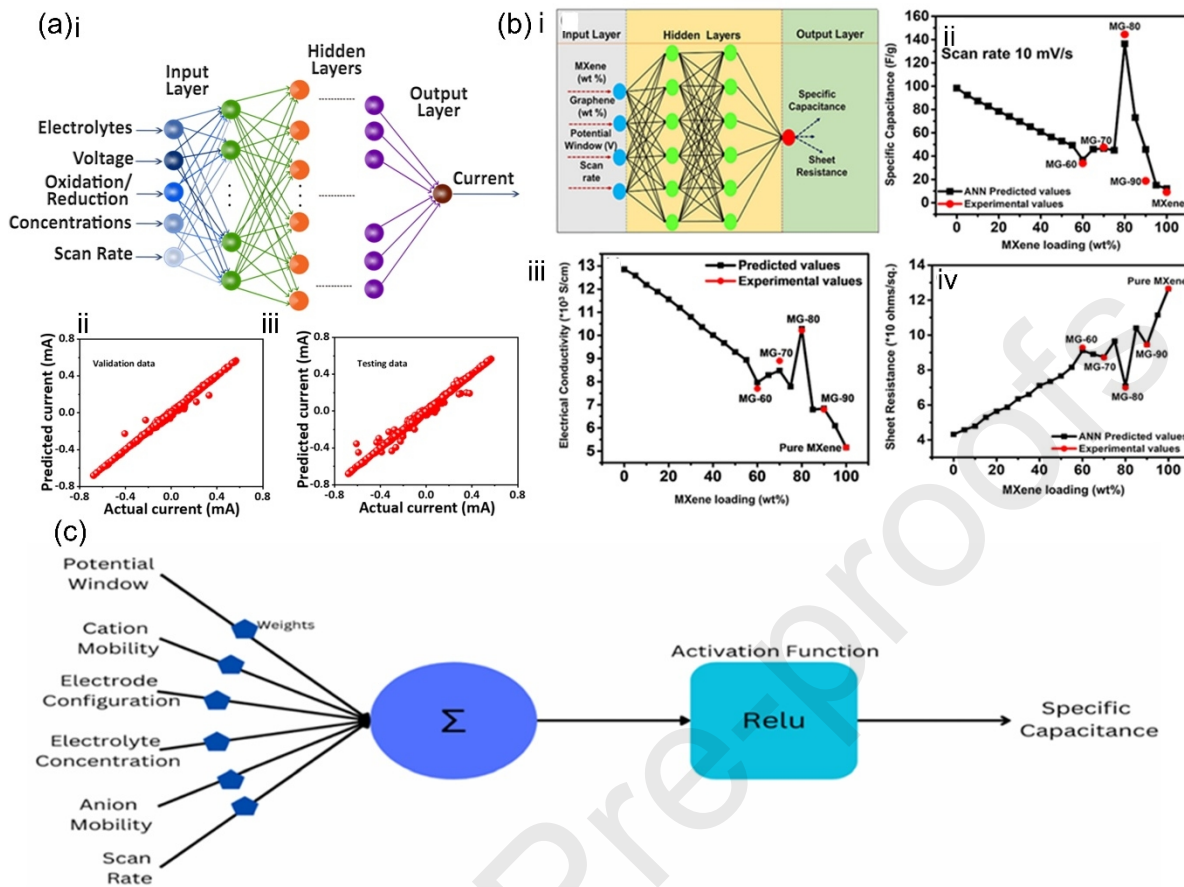


Fig. 24 (a) ANN-based multilayer machine learning model to analyze the CV performance. Correlation between actual and predicted current for the multilayer from the CV response. Reproduced with permission from [368] ©2024 Elsevier (b)(i) Representation of ANN model for MXene/GNP performance prediction. (ii-iii) Correlation between the experimental and predicted values of specific capacitance, electrical conductivity, and sheet resistance of MXene/GNP composites. Reproduced with permission from[369] ©2024 Elsevier (c) Illustration of the rectified linear unit for prediction of specific capacitance based on various input models and parameters. Reproduced with permission from [370] ©2024 RSC

The energy storage ability of Ti_3C_2 is predicted by researchers by implementing 3 different ML models, including BRR, KNN, and ANN. The models predicted the specific capacitance and correlated the complex parameters for accurate analysis. Cation mobility and scan rates were emphasized as contributing factors based on the SHAP values[370]. **Fig. 24(c)** illustrates the architecture of the ANN model. The model was trained by Python utilizing the tensor flow. The data sheet comprised of models where 75 % were used for training and 25 %

to validate the data. The rectified linear network analyses the input weights and predicts the specific capacitance by examining and validating. Overall, these ML and AI-assisted analysis predicts the required output based on the available database and calculate the specific capacitance to reduce the time and experimental complexity.

10. Classification of MXene-MSC fabrication techniques

MXene-based MSCs have acquired huge attention due to their excellent conductivity, mechanical strength and flexibility, higher capacitance, and tuneable electronic structure. Several fabrication techniques have been implemented for developing high-performance MXene-based MSCs. The following are some major fabrication techniques.

10.1 Inkjet printing

Inkjet printing is a versatile manufacturing technique of MXene-based MSC by utilizing MXene ink as the feedstock material[371]. The ink property governs the overall performance of the MSC[372], [373]. Solvents, additives, and MXene size are the major factors that influence the inkjet printing technique, along with the printed electrode[374]. This technique allows to customize the MSC electrodes. Mask-free fabrication makes complicated structures easy to imprint. It offers upscaling of MSC without compromising the electrochemical properties.

10.2 Direct writing

Direct writing is an extrusion-assisted printing technique in the computer-assigned design architecture[375]. The complex structure can be fabricated with ease of access with higher electrochemical performance[376], [377]. There is no material wastage and no substrate restriction for the fabrication of the MSC. So flexible, all-in-one integrated MSC can be fabricated by direct writing technique[378], [379], [380].

10.3 Laser engraving

Laser engraving is one of the versatile MSC fabrication techniques that can be implemented for the fabrication of MSC by additive and subtractive techniques[381]. Specific substrates can be carbonized into preassigned architecture and utilized as an MSC electrode in the additive technique[382]. A subtractive technique can be implemented to remove the

material in a pre-assigned pattern to yield the active electrode design of the MSC[383], [384]. Laser engraving provides a fast, scalable approach for manufacturing MXene-based MSCs. This is also a mask-free manufacturing technique that is fast, precise, and economical.

10.4 Screen printing

Screen printing utilizes a mask to imprint the designated MSC utilizing the MXene slurry over a substrate[385], [386]. This is a low-cost, scalable technique for upscaling the MSCs. Uniform thin film MSC can be fabricated by this technique however, the electrode resolution depends on the flow property of the slurry. MSC can be fabricated over both rigid and flexible substrates[387], [388], [389].

10.5 Electro-Spinning

Electrospinning is a versatile technique to fabricate flexible film-type electrodes comprised of nanofibers[390], [391]. The viscosity of the MXene ink plays a crucial role in governing the fiber thickness. Binders and gelling agents are often used to maintain the viscosity of the MXene ink, which influences the electrochemical property[392], [393]. Nanofibers enhance the ion surface area and provide an abundant ion migration path. Mechanically flexible, high-capacity MSC can be fabricated by the electrospinning technique; however, this technique lags for commercialization and large-scale application due to the lack of scalable performance[394], [395].

11. MXene-based Flexible and self-healing electrodes

The growing need for wearable electronics, soft robotics, and flexible energy systems has underlined the critical need for energy storage devices that are not only efficient but also mechanically durable and adaptive to changing situations[396], [397]. MXene-based supercapacitors have emerged as attractive possibilities due to their high pseudocapacitance, good electrical conductivity, and simplicity of manufacturing into flexible films or composites. MXene, like many other 2D materials, is susceptible to structural degradation, such as restacking or cracking under repeated mechanical stress, resulting in performance loss. To address this issue, researchers are developing self-healing and flexible MXene-based supercapacitors that can work even after physical damage[398], [399], [400], [401]. Flexibility

ensures that the device can bend, flex, or twist without losing electrochemical function, which is critical for incorporation into wearable and portable devices. Meanwhile, self-healing processes, which are frequently facilitated by dynamic polymer networks or ionic hydrogels, allow the device to restore conductivity and capacitance after damage, considerably increasing its operational lifetime[402], [403], [404], [405]. These advances not only improve longevity and user comfort but also help to ensure the sustainability of electronic systems by lowering electronic waste and maintenance expenses. As a result, the creation of self-healing, flexible MXene supercapacitors is an important step toward the implementation of next-generation, intelligent energy storage systems designed for smart and adaptable technology. The key advantages of MXene-based self-healing and flexible MXene-based composites are summarized in **Table 7**.

Table 7: Key Functional Features of MXene-Based Materials for Wearable and Flexible Energy Storage Applications

S1 no	Key features	Advantages	Ref.
1	Self-healing	Recovers being damaged	[406],
		Regains inherent properties	[407]
2	Flexibility	Retains performance under deformation	[408]
3	High conductivity	Enhances efficient ion migration	[409],
			[410],
			[411],
			[412]
4	Lightweight	Suitable for flexible wearable energy storage devices	[413], [414], [415]
5	Sustainable	Eliminates E-waste on device failure	[416], [417], [418], [419]

6	Transparency	Smart electronics	[420],
			[421],
			[422],
			[423],
			[424]

11.1 Transparent MXene electrodes

The future of wearable and consumer electronics shifting towards transparent electronics. **Fig. 25(a)(i)** represents the schematic illustration of MXene-based transparent electronics[425]. The spin casting was employed to fabricate the thin films and annealed at 200 °C in a vacuum condition. The flexible electrodes acquire a 3D conductive network. The CV and CD profiles obtained from different applied scan rates and currents show symmetric EDLC-type symmetric charge storage profiles (**Fig. 25(b)(i-ii)**). The assembled SC device delivers a remarkable specific capacitance of 676 F cm⁻³ attributed to the excellent metallic conductivity and redox activity of MXene. A prolonged cycle life of 20,000 without any capacitance decay ensures the MXene-based transparent supercapacitor for futuristic energy storage applications. Overall, this work provides a pathway toward the fabrication of MXene-based transparent energy storage devices that attains both excellent conductivity and transparency. **Fig. 25(c)** schematically represents the fabrication of an MXene-NiCo LDH-based transparent supercapacitor [426]. The negative surface charge of MXene and LDH is assembled layer by layer electrostatically. The combined composite enhances the strength of the electrode and enhances the electrochemical performance owing to the redox-active property of NiCo LDH over the high conductivity of MXene. The electrodeposition time over ITO was optimized to retain the excellent transparency of the electrodes. The composite transparent electrode exhibited a specific capacitance of 136.9 Fcm⁻² with a capacitance retention of 74.2%. The electrodes retain the transparency over electrochemical cycles as evidenced by real-time optical images and haze tests as depicted in **Fig. 25(d)(i-ii)**. This work opens up the opportunity to fabricate MXene-based composites for energy storage applications without compromising transparency over the long run. Conductive polymers attain excellent flexibility, but the specific capacity is limited. To attain excellent

electrochemical performance without compromising physical appearance, Ren et al., [344] prepared an MXene/PEDOT: PSS-based composite electrode through the spin coating method. The assembled supercapacitor over the PET substrate exhibits excellent transparency and flexibility as depicted in **Fig. 25(e)**. The optical transmittance spectra under different mass ratios of PEDOT: PSS exhibit a decline in transparency as a higher MXene percentage absorbs stronger light absorbance (**Fig. 25f(i)**). The CV profile shown in **Fig. 25(f)(ii)** represents a nearly rectangular CV profile attributed to the presence of PEDOT: PSS along with MXene within a potential window of 0.6V. The electrode with optimized transparency (61.6 %) and excellent electrochemical performance attained a specific capacitance of 3.1 mF cm^{-2} . Overall, this work addresses the bottleneck in the fabrication of high-performance transparent flexible MXene without compromising the electrochemical performance.

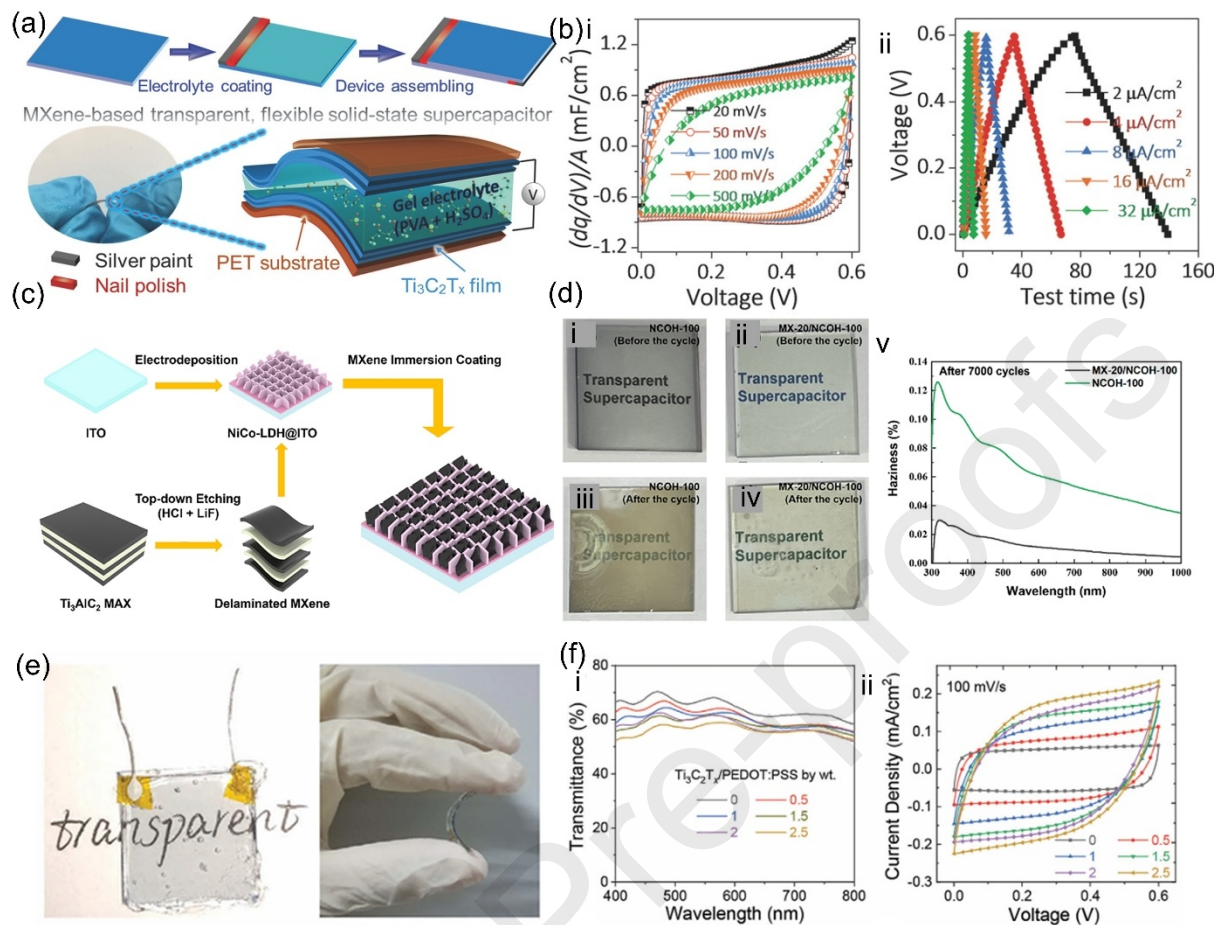


Fig. 25 (a) Schematic illustration of MXene-based transparent and flexible solid-state supercapacitor (b) (i-ii) CV and GCD profiles of MXene-based supercapacitor. Reproduced with permission from [425] ©2017 Wiley-VCH (c) Fabrication of MXene-coated NiCo LDH electrodes (d) Digital images representing the haziness of the electrodes over 7000 cycles. Reproduced with permission from [426] ©2024 Elsevier (e) MXene/PEDOT: PSS composite-based transparent electrodes (f) (i) Transmittance of MXene composite-based composite electrodes (ii) CV profiles obtained at a scan rate of 100 mV/s of transparent SC with various mass ratios of MXene and PEDOT: PSS. Reproduced with permission from [344] ©2024 Wiley-VCH

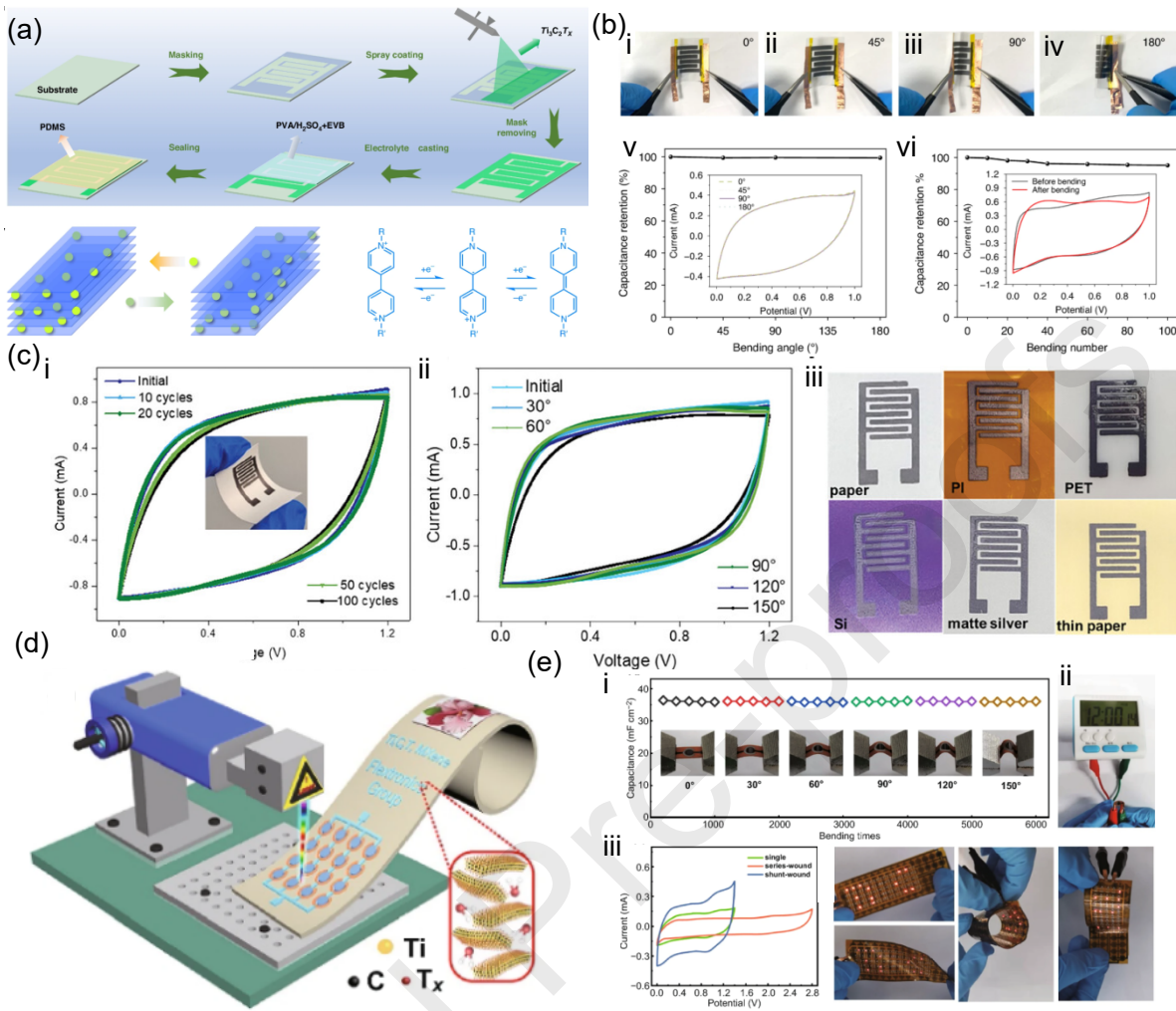


Fig. 26 (a) Schematic illustration of the fabrication process of the MXene-based in-plane energy storage device (b) (i) Schematic representation of flexibility test at various bending angles (ii-iii) Electrochemical performance analysis under various mechanical stimuli. Reproduced with permission from [427]© 2024 The authors (c) (i-ii) CV profile of MSC under various bending angles (iii) Representation of flexible MSC over various flexible substrates. Reproduced with permission from [428]©2024 Wiley-VCH (d) Schematic illustration of MXene-based MSC array through laser writing technology (e) (i) Areal capacitance of MSC under various mechanical stimuli (ii-iii) Digital image of powering flexible electronics with flexible MXene-based MSC. Reproduced with permission from [429] ©2021 Springer

11.2 Flexible MXene electrodes

Smart electrochromic supercapacitors have acquired huge research attention due to the unique colour-changing phenomena during charge-discharge, which broadens the application for smart sensing. **Fig. 26(a)** represents the fabrication technique of MXene-based smart flexible supercapacitor, which involves spray coating of MXene as active electrode material over the masking and encapsulation with PDMS after application of PVA-H₂SO₄ and EVB-based gel electrolyte[427]. The applied EVB exhibits the reversible change of color during charge-discharge cycles and attains a fast response time of 2.6s. Benefiting from the redox activity of EVB, the working window of the MSC extends up to 1V. The smart electrochromic MSC exhibits excellent electrochromic and energy storage performance without compromising flexibility, as shown in **Fig. 26(b)(i-ii)**. The flexible SC exhibits excellent electrochemical performance under different bending states from (0-180°) and stable performance over 100 bending cycles. Notably, this work portrays the possibility of integrating additives to add smart electrochromic features and tune the electrochemical performance of MXene-based energy storage devices. Flexible electronics need high-performance, smart, flexible supercapacitors. Wang et al., [428] developed a flexible MSC from MXene-based conductive ink and introduced a water-in slat electrolyte for enhanced electrochemical performance. The assembled planar-type printed electrode provides a facile route to produce high-performance supercapacitors on a large scale with reproducible electrochemical properties. **Fig. 26c(i)** represents the excellent reversible CV cycles at various bending angles, depicting the unmatched energy storage performance under mechanical stimulus. The MSC retains the CV cycle over 100 cycles without any deviation in the CV profiles; further, different bending angles portray the stable electrochemical performance of MXene-based MSC. **Fig. 26(c)(iii)** illustrates the versatility of MXene-based MSC fabrication over a wide range of flexible substrates, including paper, PI, and PET [429]. The work established a reliable approach towards the fabrication of MXene-based flexible energy storage devices. Li et al., developed a Zn-ion-based high-performance MSC for wearable and flexible electronics. **Fig. 26(d)**represents the fabrication of an MXene-based MSC array assisted

with a laser engraving technique over the PI substrate. The laser-engraved 4-MSC array can be accommodated over the fingernail, which enables it to form high-performance, flexible, and easily integrable MSC in future flexible electronics. **Fig. 26(e)(i-ii)** proves the unmatched flexibility of the MXene-based MSC, which retains the specific capacitance over 6000 cycles at various bending angles (0-150°). Upscaling of MSCs is depicted from the MSCs connected in series and parallel, providing the scope of integration of the MSC to a wide range of electronics by tuning the configuration and suitable integration. **Fig. 26e(iii)** exhibits the excellent flexibility of the MXene, which successfully powers the LEDs at various bending angles.

Overall, flexible MSCs largely depend on the mechanical properties of the substrate, electrode material, and fabrication technique, which govern the adhesion of active material over the substrate. However, MXene-based supercapacitors have proven reliability for futuristic flexible electronics owing to their mechanical strength, negative surface potential, and superior contact with the substrate. Additionally, MXene ink provides scope for printing energy storage units over a wide range of flexible substrates without compromising the electrochemical performance. So, design optimization and large-scale production of MXene can bridge the gap in flexible electronics in the future.

11.3 Self-healing MXene-based electrodes

Self-healing electrodes are a new type of material that restores structural and functional integrity after injury, considerably increasing the lifetime and dependability of electronic equipment[430], [431]. These electrodes use self-healing polymers, microcapsules, or dynamic covalent connections to initiate repair mechanisms when fractures or breaks occur. This self-repair capability is especially important in flexible electronics, energy storage devices such as batteries and supercapacitors, and wearable technology, where mechanical stress frequently causes performance loss. Self-healing electrodes represent a significant step

forward toward more sustainable and robust electronic systems since they extend operational lifespan and reduce maintenance requirements.

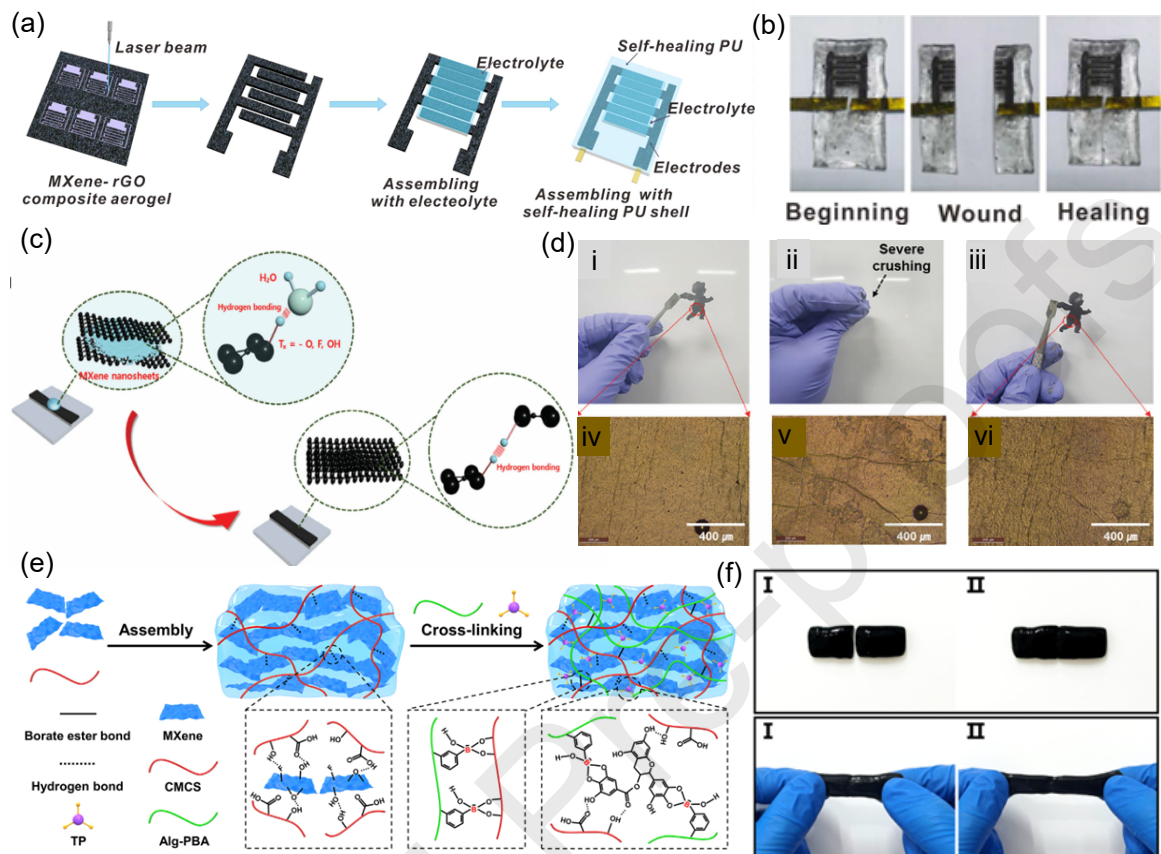


Fig. 27 (a) (i)Schematic representation of MXene-rGO composite aerogel-based self-healing PU shell (b) Digital image of 3D self-healing MSC. Reproduced with permission from [432] ©2018 American Chemical Society (c) Schematic representation of the self-healing mechanism of MXene-based MSC (d) MXene/PU electrode and self-healing mechanism induced by water droplet. Reproduced with permission from[433] © 2023 Wiley-VCH (e) MXene-based flexible, self-healing mussel-inspired hydrogel (f) Self-healing property illustration of MXene hydrogel. Reproduced with permission from [434] ©2023 Elsevier.

The layered structure of MXene makes it easier to integrate into polymer matrices, which are extensively employed in self-healing systems. The extensive surface terminations (such as -OH, -O, and -F) on MXene allow for strong interactions with self-healing polymers, which improve both electrical routes and mechanical cohesiveness. In self-healing electrodes, MXene can operate as conductive bridges, reconnecting fractured sections and restoring electrical conductivity after injury. Furthermore, their flexibility and processability make them

suitable for application in flexible and stretchable electronics. Researchers are developing next-generation electrodes with longer lifespans, greater dependability, and improved performance in demanding applications such as wearable electronics and energy storage devices by combining MXene conductivity with autonomous healing mechanisms. Yue et al., [432] introduced a high-performance self-healable MSC comprised of MXene-rGO composite aerogel and self-healable PU foam. The MXene-rGO composite exhibits excellent structural stability and attains a large surface area, which boosts the electrochemical performance of the MSC. The high-performance 3D electrode material relies on reversible structural and functional recovery after damage. **Fig. 27(a)** portrays the fabrication of MXene-graphene aerogel-based 3D electrode over PU substrate by laser engraving technique. The composite electrode was synthesized by freeze-drying followed by laser engraving. The self-healing electrodes can retain 70 % strain after the removal of the load. The MSC exhibits a specific capacitance of 34.6 mF cm^{-2} and cyclic stability over 15,000 cycles. The self-healing capacity was attained from the smart PU substrate, which enabled it to retain 81 % specific capacitance after the 5th healing. **Fig. 27(b)** exhibits the steps of retaining the shape of a self-healing structure that provides a strategy to prepare next-generation smart, flexible, and wearable electronics. MXene-based standalone self-healing electrodes extend the application beyond energy storage, which can be integrated with sensors and actuators to construct a self-powered, reliable system. Choi et al., [433] introduced a water-assisted self-healing mechanism for MXene-based free-standing films. This technique reveals the inherent property of MXene to retain its shape and functionality without compromising mechanical and structural failure. **Fig. 27(c)** illustrates the self-sealing mechanism of MXene electrodes assisted with water. The 2D layered structure and functional groups initiate the formation of hydrogen bonds and hold the layers utilizing the Vanderwaals force. The hydrophilic substrate allows water molecules to penetrate the damaged part and regain the previous structure by slipping MXene sheets into the space. Once the damage is healed, the water evaporates and the MXene structure retains its conductivity owing to the re-established hydrogen bonding. **Fig. 27(d)** illustrates the remarkable self-healing ability of an MXene structure being crushed severely by the application of a drop of water. Further analysis regarding conductivity retention and real-time application of the MXene electrodes exhibits uncompromised performance after being self-healed. Overall, this study repairs a wide range

of failures of MXene, which helps to retain structural stability and electrical functionality. Wearable sensors undergo extreme mechanical fluctuation during operation, which leads to structural failure or property decay. To address the constraint, a hydrogel-based epidermal sensor was prepared by Zhang et al., [434] as shown in **Fig. 27(e)**. The self-healing hydrogel was prepared by introducing MXene nanosheets into the polymer matrix comprised of CMCS and sodium alginate. The dynamic covalent bonding between the hydroxyl group of the CMCS, TP, and Na-alginate leads to the formation of MXene-based self-healing composite hydrogel. **Fig. 27(f) (i-ii)** reveals the self-healing property of MXene-based hydrogel, which retains excellent flexibility after being cut and healed in ambient conditions. The electrical property and mechanical properties of the hydrogel are retained after self-healing benefiting from the presence of strong covalent bonds. The electrical conductivity, biocompatibility, self-healing ability, and mechanical strength enable it to be utilized as reliable smart electronics.

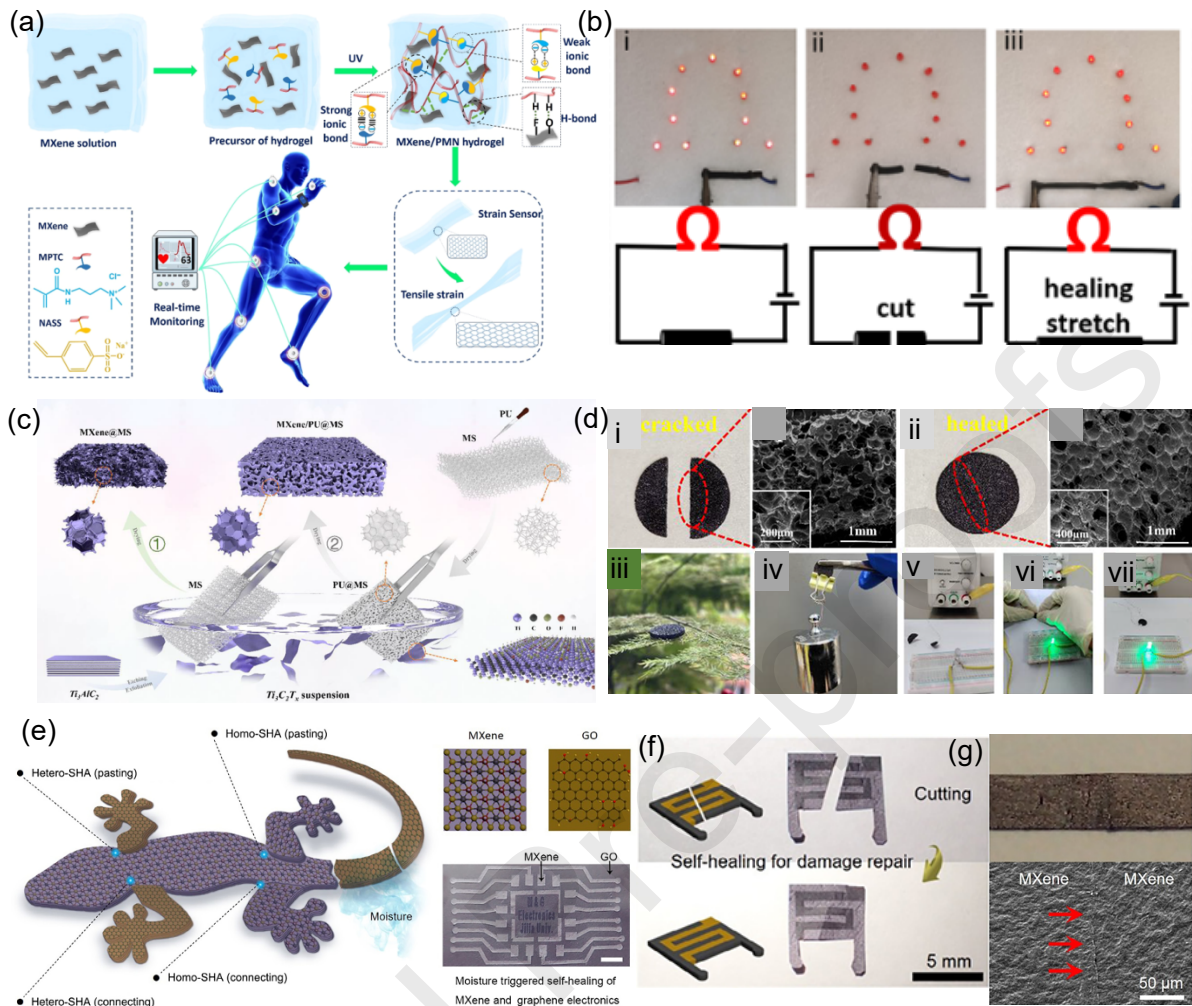


Fig. 28 (a) Illustration of MXene/PMN hydrogel synthesis (b) Self-healing property of conducting circuits. Reproduced with permission from [435] © 2022 Elsevier (c) Synthesis of MXene/PU composite (d) Illustration of SEM image and self-healing property of MXene/PU composite. Reproduced with permission from [436] ©2021 Elsevier (e) Schematic presentation of MXene and GO-based self-healing architecture (f) Self-healing illustration of MXene-based electrode damage repair. Reproduced with permission from [437] ©2022 Elsevier

Chen et al., [435] fabricated an MXene /polyampholyte composite hydrogel benefiting from the superior flexibility of the polyampholyte and excellent conductivity of MXene (**Fig. 28(a)**). Radical polymerization was employed to prepare the MXene-based composite hydrogel. The as-synthesized hydrogel exhibited an excellent tensile strain of 1200 % which retains its shape over unloading the stress. The flexibility, conductivity, and toughness made

it a suitable candidate for epidermal sensors. **Fig. 28(b)** illustrates the excellent self-healing property without losing conductivity, which acts as a conductive pathway in an LED circuit system. The optimized composition with 1 % MXene exhibited a conductivity of 2.02 S/m without compromising the mechanical strength. This study highlighted the fabrication of high-performance MXene-based reliable body motion sensors that can withstand extreme mechanical stimuli and retain the shape being damaged during application. Ma et al., [436] introduced an MXene-based sponge for a self-healing sponge for EMI shielding application. **Fig. 28(c)** represents the facile synthesis technique of EMI shielding electrode by dip coating in colloidal suspension, followed by drying. As high conductivity favors efficient EMI shielding, MXene layered over PU exhibits enhanced EMI shielding efficiency. The base matrix consists of PU foam and offers self-healing characteristics, making the composite a prime candidate for efficient EMI shielding without any structural failure. **Fig. 28(d)** illustrates the self-healing property of the MXene /PU composite. The presence of -NH-, -OH, and -NHCOO- groups introduces hydrogen bonding, which promotes the self-healing property. The MXene composite was cut and cross-sectioned analysed, which exhibits a porous architecture. Further, the separated parts are combined by application of force for a few seconds, which exhibits the complete removal of the cutting boundary. The composite attains extreme flexibility, which can carry a weight 1475 times higher than the sponge's weight. Further, the healed sponge connected in a circuit that demonstrates excellent conductivity and attained an EMI shielding efficiency of 65 % after 2nd healing cycle. The self-healing MXene PU composite provides a promising path toward high-performance MXene-based composites for smart flexible electronics. Smart self-repairable electronics attracted research attention for wearable and flexible electronics. Smart, flexible sensing and robotics need a high-performance composite to acquire functionality and mechanical stability. Ma et al., [437] introduced a nature-inspired moisture-induced self-healing technique for smart electronics (**Fig. 28(e)**). The self-healing tendency of homogeneous (MXene) and heterogeneous (MXene-graphene) was studied. The introduction of moisture hydration introduces interlayer swelling that recombines MXene and goes by hydrogen bonding. Benefiting from the unique structural advantage, MXene-GO composite-based electronics were fabricated for pressure and humidity sensing (**Fig.28(f)**). The high possibility of oxidation of MXene in energy storage limits its practical utility in sensitive electronics. To eliminate the adverse effect of oxidation,

Wu et al., [226] prepared a MXene bentonite composite through a competitive oxidation mechanism as depicted in **Fig. 29(a)**. The rise in temperature removes the intercalated water from the MXene layers, leading to the edge and surface oxidation of MXene forms TiO_x that decomposes the electronic structure. To reduce the adverse oxidation, bentonite nanosheets were introduced into the MXene matrix which is comprised of Si-O, -OH, and Si-O bonds which resulting from abundant hydroxyl groups on the surface and interlayer spaces of bentonite film, leading to the formation of polar Si-OH groups that establish a competitive oxidative environment to combat the MXene oxidation. Benefiting from the presence of huge exchangeable cations, bentonite attains a strong water absorption capacity, which uptakes water from the ambient atmosphere to keep the electrolyte hydrated. So, bentonite plays a crucial role in keeping both the electrode and electrolyte hydrated at a high temperature, that retains the charge storage ability. The unique advantage is that the MSC has high temperature tolerance and self-healing ability. **Fig. 29(b)** shows the schematic illustration of a self-powered temperature sensor integrated with MSC. The self-healing MXene-based MSC exhibited a specific capacitance of 22.8 mF cm^{-2} and restored the electrochemical performance once cooled to room temperature by absorbing the atmospheric moisture. The work provides a unique strategy to fabricate high-performance MXene-based self-powered and self-healing energy systems for futuristic smart electronics. Paper-based energy storage devices gained huge attention owing to characteristics like bio-compatibility and flexibility[438]. **Fig. 29(c)** represents the fabrication technique of MXene-based self-healing MSC through spray coating followed by laser engraving. The as-prepared MSC was encapsulated with PU to provide abundant hydrogen bonds for acquiring self-healing properties. The electrochemical property was analyzed by the particle size of the synthesized MXene. The MSC with optimized particle size attained a specific capacitance of 73.6 mF cm^{-2} with a capacitance retention of 87.5 % over 5000 cycles. Further, the self-healing property of the MSC was studied by repeated cutting and healing, respectively. The optical image shown in **Fig. 29(d)** illustrates the self-healing mechanism of PU-encapsulated MSC. The presence of numerous cross-linked chains and abundant hydrogen bonds initiates the self-healing mechanism of the PU. The cut leads to the hydrogen bond breaking at the interface, which, when attached, initiates intermolecular hydrogen bonds and re-joins the broken part. The cyclic cutting and healing retain the mechanical strength, electronic conductivity, and structural integrity of the MSC device. The

structure modification and self-healing property pave the path towards flexible and self-repairable energy storage devices, sensors, and miniature electronics.

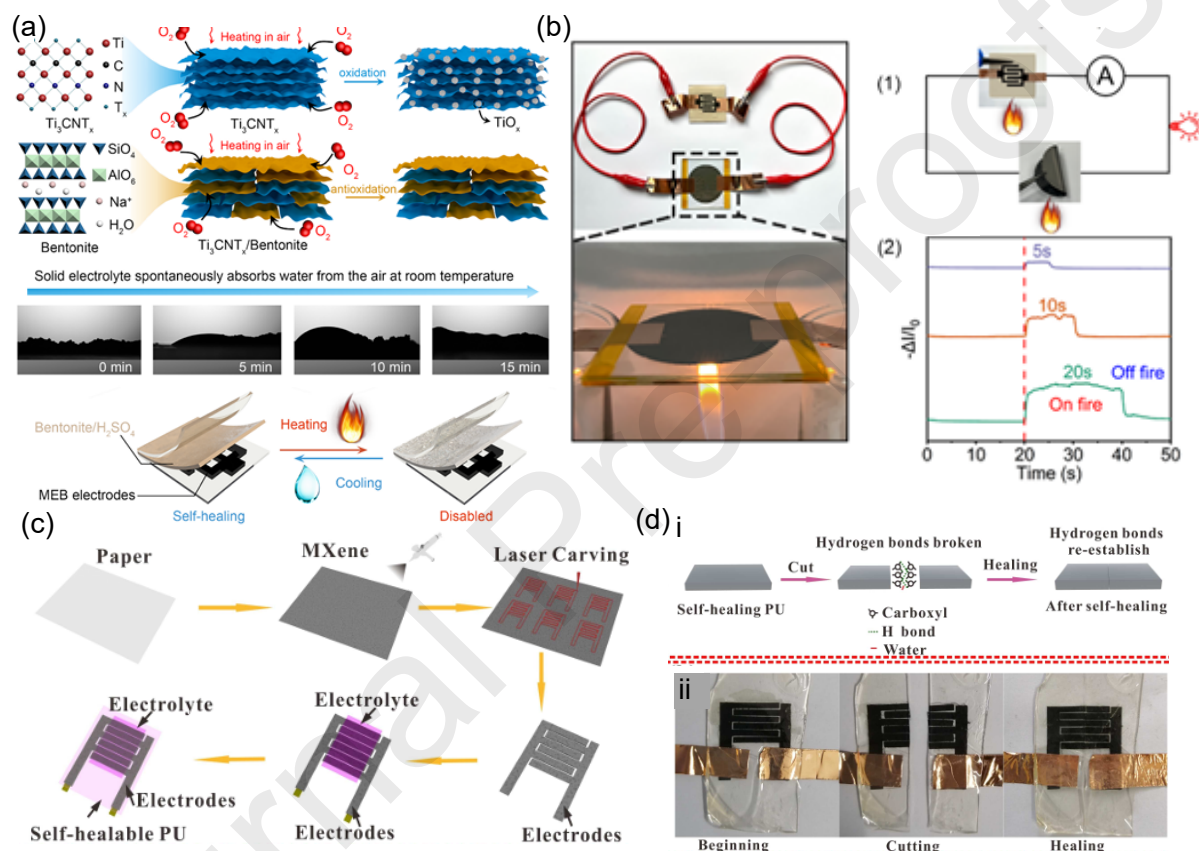


Fig. 29 (a) Solid-state MXene-based MSC and the self-healing mechanism illustration (b) Self-powered integrated temperature sensors and temperature-tolerant property. Reproduced with permission from [226] ©2025 Elsevier (c) Self-healing MXene based MSC (d) Self-healing mechanism illustration. Reproduced with permission from [438] ©2020 Wiley-VCH

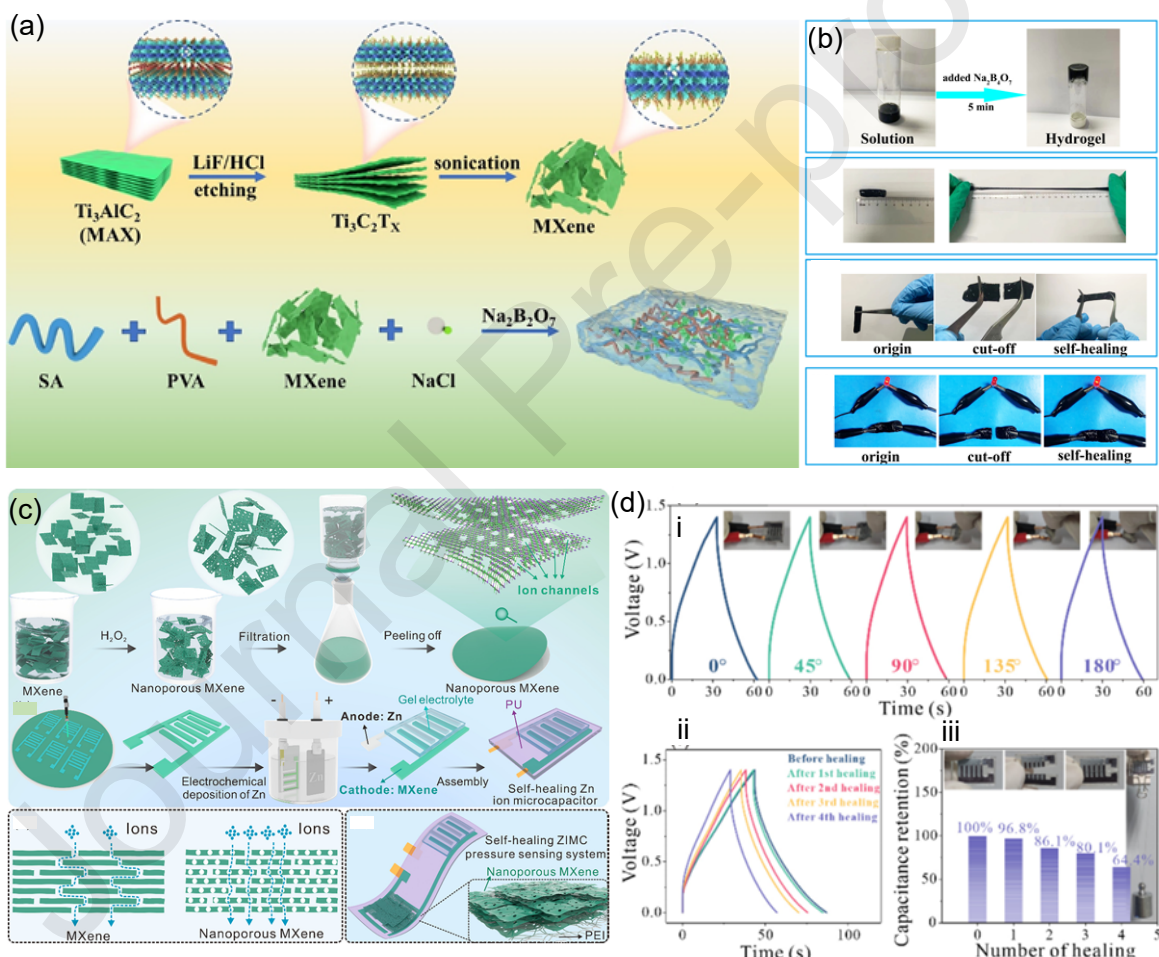


Fig. 30 (a) Illustration of MXene and double network hydrogel; (b) Illustration of self-healing MXene and conductivity retention. Reproduced with permission from [439] @2023 Elsevier (c) The design of MXene-based MSC and integrated self-healing pressure sensing system (d) (i) GCD curves at various bending angles (ii) GCD curves after various healing cycles (iii) Capacitance retention (%) vs Number of healing

Capacitance retention over various healing cycles. Reproduced with permission from [440] ©2022 Elsevier

Flexible energy storage devices lag in electrochemical performance due to the failure of the electrode, electrolyte, or substrate. The flexibility of electrolytes is crucial to retain the electrochemical performance during mechanical fluctuation. Tian et al., [439] synthesized a cross-linked dual network hydrogel by combining MXene /SA and PVA, as shown in **Fig. 30(a)**. NaCl is introduced as a source of ions for the energy storage application, which exhibits a specific capacitance of 130.8 mF cm^{-2} . MXene sheets incorporated with polymer solution were cross-linked by the introduction of $\text{Na}_2\text{B}_4\text{O}_7$, which introduces the borate bonds that strongly introduce a dual network inside the composite matrix. The free-dried entity exhibits a porous, stable 3D network for smooth and faster ion migration for efficient electrochemical reaction. **Fig. 30(b)** illustrates the fast cross-linking of the hydrogel and its ultra-flexible mechanical properties. The hydrogel attains an 8-fold increment from the original length and portrays an excellent self-healing property owing to the presence of abundant hydrophilic groups and the presence of borate bonds. The conductivity and functionality retention were analyzed by connecting to an electrical circuit after healing. The hydrogels exhibit a self-healing efficiency of 90 % over 20 h, demonstrating excellent reproducibility of the inherent properties. This work demonstrates the advantage of fast processing time and excellent self-healing properties of the composite hydrogel with a 3D dual-function network. Integration of micro-supercapacitors with in-plane miniature electronics provides an opportunity to design and fabricate flexible and wearable electronics. Cheng et al., [440] fabricated an MXene-based MSC integrated with a pressure sensor on board MXene as electrode material provides abundant active sites and ion migration pathways that enhance the electrochemical performance. **Fig. 30(c)** represents the fabrication technique of the MXene-based electrodes and Zn ion deposition by the electroplating technique. PAM hydrogel was applied over the IDT to construct Zn-ion solid-state MSC. The Zn-MSC encapsulated with PU foam makes it a self-healing entity that attains excellent energy storage capacity along with unmatchable mechanical stability. The Zn-ion MSC integrated with pressure sensing established an integrated flexible smart electronic unit. The MSC performances are stable under various bending conditions, as evidenced by the obtained CD profiles shown in **Fig. 30(d)(i)**. Further,

the MSC was cut into separate pieces and reassembled multiple times to analyze the healing efficiency. The MSC retains its shape, benefiting from the advantage of PU substrate and the excellent self-healing ability of MXene electrodes. After consecutive self-healing tests for repeated cycles, the Zn-MSC retains 64.4 % capacitance. The overall work proposed a unique strategy to construct high-performance flexible electronics comprised of flexible MSC and pressure sensors.

The aforementioned studies exhibited the huge potential of MXene-based self-healing electrodes for next-generation flexible and smart electronics. The self-healing property enables to broadening of the application aspect of MXene in advanced applications, including integrated electronics, E-Skins, sensors, and actuators.

12. MXene Ink Synthesis

Among 2D nanomaterials, MXene has huge potential for printing microenergy storage systems due to its unique electronic structure, nanometre-range particle size, superior conductivity, and excellent hydrophilicity. The major ink ingredients are MXene, binder, and solvent[441]. The ink components and their rheological properties are crucial for printing high-quality electrodes. The ink particle size varies from nanometres to micrometers based on the printing method[442], [443]. Micron-size particles can be printed through conventional printing techniques like screen printing, blade coating, or brush coating. However, sophisticated fabrication techniques like inkjet /DIW etc, need ink with particle size below 200 nm[444]. Larger particle size clogs the nozzle and leads to printing failure. Further binders are utilized to synthesize stable ink and well-dispersed particles in the solvent.

Though the binders maintain the stability of particles in ink, they lead to decay of the inherent properties of the ink. The conductivity and electrochemical properties are suppressed due to the hindrance of the binder. To overcome this, binder-free inks are synthesized that retain the MXene conductivity and electrochemical activity. Further to enhance the inherent properties of ink, graphene, carbon black, CNT, etc, are added to the MXene matrix to synthesize the composite ink[445] Fig. 31 highlights the advantages of MXene-based inks and various ink-based electrode fabrication techniques. The composite ink favors the widespread application of MXene ink with enhanced electrochemical performance.

In addition to this solvent plays a critical role in ink synthesis. The solvent holds the dispersed particles and plays a major role in printing electrodes with a constant viscosity. Water and organic solvents are widely implemented for MXene ink synthesis. Solvents with different polarities acquire different viscosities and varying rheological properties[446], [447]. Further ink synthesis is detailed, including MXene ink formulation and rheology optimization.

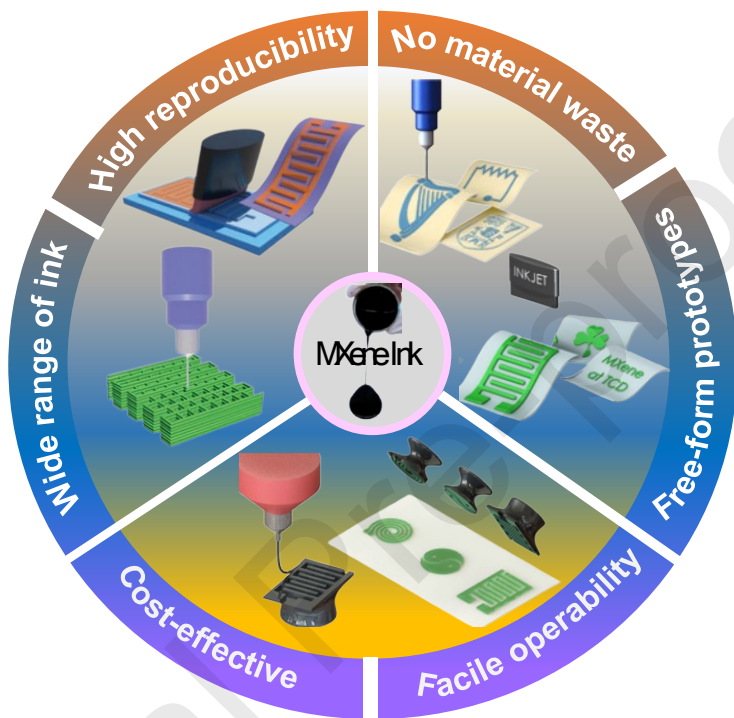


Fig. 31 Illustration of MXene ink advantages and various printing techniques

12.1 Ink formulation

The ink formulation determines the overall synergistic effect of ink components and determines the print resolution and final printed part. Conducting inks face numerous challenges for commercialization. Industrial-grade MXene inks require specific parameter metrics for printing high-precision electrodes over various substrates[420], [448], [449]. The industrial application needs ink with a high concentration of MXene, stability of the dispersed MXene particles, and freedom from oxidation over a prolonged period[450]. The tuneable rheology of ink with shear thinning behavior favors a wide range of printing techniques[451], [452]. A constant or homogeneous flake size is desirable for a uniform layer fabrication process to avoid any agglomeration or blockage[453], [454]. High electrical conductivity greater than 10,000 S/cm is required to overcome the internal resistance of the printed part and facilitate

faster ion migration for enhanced charge storage performance[198], [210], [455], [456]. The industrial-grade ink formulation must be reproducible with negligible variation in inherent properties. For environmental concerns, the ink must be free of hazardous chemicals and solvents for a safer application[199], [457], [458]. Generally, ink is classified into Newtonian fluid and non-Newtonian fluid as depicted in Fig. 32(a)[459] overall synergetic effect of ink components determines the print resolution and final printed part. Generally, ink is classified into Newtonian and non-Newtonian types [459]. Newtonian fluids are comprised of low molecular weight solvents like water or diluted polymers whose viscosity remains constant at varying shear rates. On the other hand, non-Newtonian fluid fails to show constant viscosity at varying shear rates and is further classified into time-independent and time-dependent fluids. The time-independent viscosity is further subdivided into dilatant, shear-thinning, and shear-thickening. Fluids, when undergoing stress, attain higher viscosity and are regarded as shear thickening behavior; in contrast, when viscosity reduces on the application of shear stress is defined as shear thinning behavior. Inks with shear-thinning behavior are favorable for printing applications, as the shear-thickening inks lead to distorted prints. Bingham fluid inks act as both Newtonian and non-Newtonian fluids. This kind of ink behaves like an elastic body up to a certain level of stress, beyond which the ink behaves like a viscous fluid. The time-dependent non-Newtonian fluids are classified into rheopectic and thixotropic. The apparent viscosity of rheopectic fluids increases during the application of stress, and thixotropy fluids experience a decrement in the viscosity during the time of applied stress. The time-dependent fluids require a finite time to recover to the original state, whereas the time-independent fluid reverts to the original state instantly on the removal of applied stress. Both behaviors are favorable for specific printing applications. Benefiting from the thixotropy or pseudoplastic behavior, the ink under stress attains lesser viscosity and is allowed to flow smoothly through the nozzle. Over extrusion on the removal of the applied stress, the ink regains its shape and forms the pattern over the substrate.

Table 8: Rheological Properties of MXene-Based Inks Formulated with Different Solvents and Their Implications for Printable Electrode Fabrication

Sr No	Solvent	Concentration (mg/mL)	Viscosity (cP)	Conductivity	Surface tension (mN/m)	Refs
-------	---------	-----------------------	----------------	--------------	------------------------	------

1	Water	5	1	119	73	[227]
2	Water	30	32	215	58.6	[460]
3	Water	18	5	9.8	76.5	[446]
4	Water	30	10	0.15	68.8	[461]
5	NMP/DMSO	12.5	14/13	2770	40.8/43.5	[54]
6	Ethanol	0.7	19.71	NA	22.1	[54]

The ink rheology differs for different printing processes as illustrated in **Fig. 32(b)**. Inkjet printing requires low-concentration inks, in contrast to extrusion-based printing, and screen printing requires thicker ink[462]. Further, the ink viscosity influences the resolution of the printing parts. Spray printing provides the highest resolution with less viscosity ink, whereas the higher viscosity ink is favorable for extrusion-based 3D printing. The increment in Ink viscosity and print resolution is depicted as per the following chronological order: Spray printing < Inkjet printing < Offset printing < Screen printing < Extrusion-based 3D printing. The print property is further dependent on the wetting behavior and drying method[463], [464]. The dispersion of ink over the print bed determines the print shape, and after curing, provides the final prototype. The overall process is critical to maintain the higher printing resolution based on the ink quality. Young's formula determines the wetting behavior of the ink. To obtain a better print, the contact angle of the ink drops over the substrate needs to be smaller, as the larger contact angle makes the extruded ink unstable and leads to print failure with a distorted surface[465].

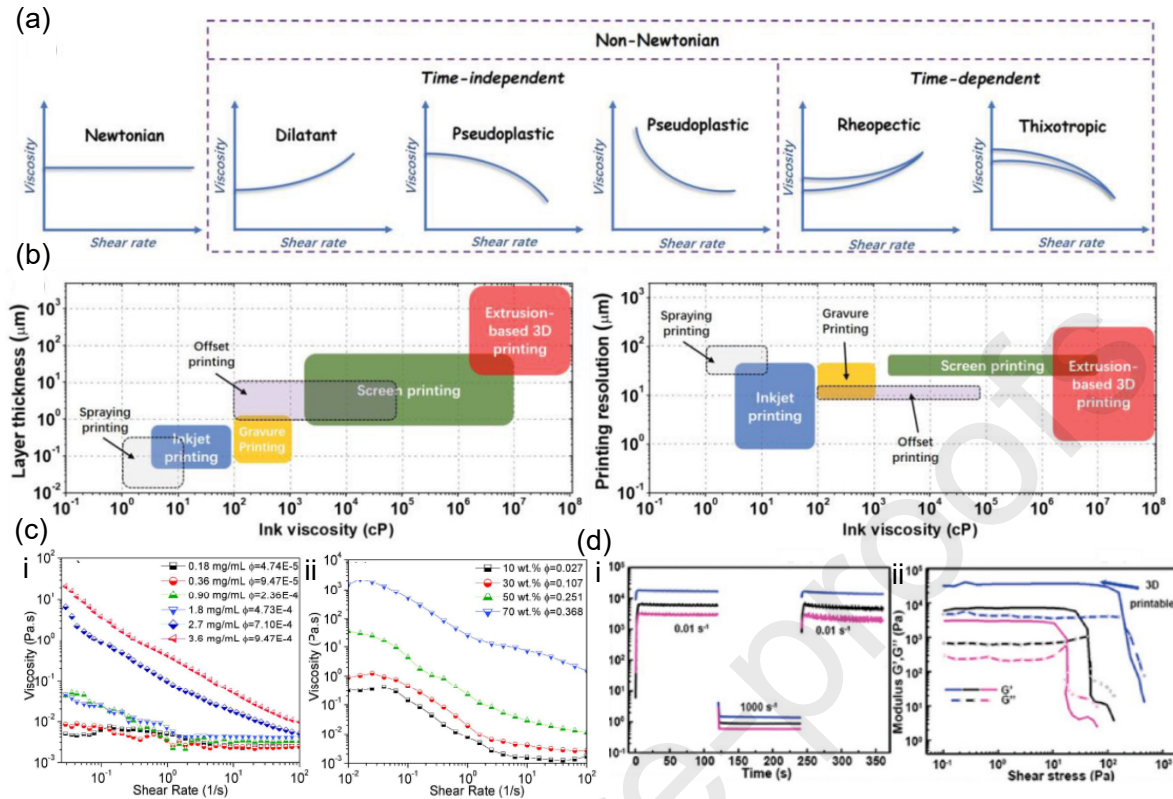


Fig. 32 (a) Classification of various fluids based on the shear properties. (b) A comparative presentation of printing layers, resolution, and ink viscosity. Reproduced with permission from [13] © 2020 WILEY-VCH (c) i. Viscosity with respect to shear rate of single layer- $\text{Ti}_3\text{C}_2\text{T}_x$ at various concentrations ii. Viscosity versus shear rate of multi-layer $\text{Ti}_3\text{C}_2\text{T}_x$ at various concentrations. Reproduced with permission from [158] © 2018 American Chemical Society (d) i. Ink viscosity measured at low and high shear rates, respectively ii. Viscoelastic behaviour of the ink depicting modulus vs shear stress. Reproduced with permission from [64] © 2019 WILEY-VCH

To achieve a smaller contact angle surface energy of the ink must be less than the print substrate. The surface energy of the substrate can be tailored with various surface modification techniques assisted with chemical, heat, or plasma[202], [466], [467]. The surface treatments enhance the hydrophilicity and lead to stable ink deposition with higher resolution. Further ink deposition with smaller droplets over a cold substrate leads to homogeneous nucleation of the ink and avoids the formation of the coffee ring effect. Hybrid solvents or additive-assisted inks also provide high-resolution prints[468], [469], [470], [471].

Considering the aforementioned tricks and effects, researchers have developed different MXenes inks with high-resolution prints and enhanced electrochemical properties. The tuneable surface chemistry of MXene makes it compatible with both organic and inorganic solvents[52], [472]. The surface terminal groups and negative zeta potential make it compatible with forming stable dispersion in a wide range of solvents like DMSO, DMF, and ACN[51], [472], [473], [474] Rheological properties and ink conductivity are summarized in **Table 8**. Additive-free aqueous and organic ink was synthesized by researchers with stable colloidal dispersion, which provides high-resolution printing with spatial stability[475]. The inks with larger flakes provide higher conductivity due to fewer defects and continuity in stacking flakes[476], [477], [478]. The ink contains smaller flakes, though it provides uniform dispersion, lacks conductivity, and reduces the electrochemical performance. The MXene ink property is further influenced by the intercalated ions during the synthesis technique. The size of the intercalation decides the interlayer spacing that further influences the electrochemical performance by allowing ion migration and providing the space for ion storage during the electrochemical reaction[479], [480], [481], [482]. Further, it is observed that aqueous MXene inks lead to oxidation, degrading the inherent properties of MXene.

Table 9: Comprehensive Summary of Emerging Printing Techniques for Microsupercapacitor (MSC) Fabrication: Process Mechanisms, Patterning Resolution, and Integration Strategies for MXene-Based Electrode Architecture

Sr No	Fabrication Technique	Speed (m/min)	Resolution(μm)	Viscosity (cP)
1	Screen printing	~70	30-1000	100-10 ⁷
2	3D printing	~4	10-50	10 ⁶ -10 ⁸
3	Gravure	~1000	10-50	100-1000
4	Inkjet printing	~1	10-50	1-100
5	Spray technique	~20	50-200	1-10

Elimination of dissolved oxygen helps in restricting the oxidation process and helps to retain the inherent properties. Various antioxidants are proven effective in reducing the degree of oxidation over a certain period. However, the addition of antioxidants hinders ion migration and reduces the electrochemical properties[228]. To avoid these bottlenecks, organic solvents are preferred to synthesize high-performance, stable ink[483]. It provides

endless opportunities to retain the electrochemical properties of MXene for the long run without any decay. Based on the ink ingredients, ink rheology is a further crucial factor for printed MSCs.

12.2 Rheology optimization

The MXene sheets, concentration, solvent, and additives determine the rheology of the MXene ink. The concentration of MXene particles and interaction with additives in the solvent matrix affect the printing parameters and the print quality. The rheology of MXene ink was analyzed by implementing shear stress over different concentrations[61], [62], [484]. A shear-thinning behavior was observed from the MXene ink containing various concentrations of both single-layer and multi-layer MXene, as depicted in **Fig. 32(c)(i)** [61]. Single-layer MXene ink dispersion was indifferent to the application of higher shear stress; however, in contrast, the MXene ink with multilayer MXene exhibited a variation of 3 orders from concentration variation from 70wt% to 10 wt%. The multilayer MXene viscosity was found to be twice that of the single-layer MXene with the highest concentration (**Fig. 32(c)(ii)**). The printing speed and required viscosity for various electrode printing techniques are summarized in **Table 9**.

The ratio of storage modulus to loss modulus is another critical rheological property of the MXene inks[484], [485]. The MXene ink with higher loss modulus is favorable for spray coating application, and extrusion-based printing techniques require a higher elastic modulus for producing high-quality printing[459], [486]. The low-concentration MXene inks exhibited a significant elastic modulus, which is suitable for coating and spraying techniques and provides uniform particle distribution without any hindrance[487]. MXene concentration beyond 0.9 mg/ mL acquires a quasi-solid state, which further becomes fluid on application of stress. This behavior is favourable for inkjet printing, where MXene flakes interact electrostatically from a distance. On increasing the concentration, G' increases significantly irrespective of the frequency, and the interaction point of G'' also shifts to a higher range, indicating a long-range order of the percolation network[471], [488]. This tendency of the material is suitable for the wet spinning technique with soft gel-type ink[489]. Gel transition and percolation of the ink take place on increasing the concentration, where G' becomes higher than G'' . This optimization in rheology, varying the ink concentration, favors a wide range of applications utilizing MXene inks[488]. G' value of single-layer MXene is inadequate

for extrusion-based 3D printing[490]. High-concentration MXene ink containing single-layer MXene higher than 10 mg is suitable for 3D printing[50], [491] Higher concentration enhances the viscoelasticity and optimized yield stress, favorable for 3D printing as shown in **Fig. 32(d)**[492]. MXene with a higher aspect ratio maintains the rheology rather than MXene with a lower aspect ratio. The balanced aspect ratio and concentration lead to the self-assembly of the MXene flakes, forming a liquid crystal. MXene with a larger flake size forms a liquid crystal with low concentration; in contrast, the smaller MXene needs a high concentration to form a Liquid crystal (LC). Further to match the G'/G'' and concentration small MXene concentration was increased without any change in the large MXene flakes. Tuning the shear frequency and G'/G'' , the rheology of MXene was tuned close to the LC phase[493]. The concentration of MXene ink was increased, shifting the liquid phase to the solid phase. N-doped MXene transit from the liquid state to the solid state over an applied shear stress of 170 Pa at a concentration of 300 mg mL⁻¹[494].

The ratio of G' and G'' plays a vital role in determining the flow property of the MXene ink. Spray coating requires high processability and viscous modulus, whereas extrusion printing needs high elastic modulus to retain the printed structure. **Fig. 33(a)** illustrates the viscoelastic properties of S-layer MXene at various concentrations[488]. At a low concentration, the single-layer MXene exhibits a low-frequency elastic behavior and gel-type viscosity. This is favorable for extrusion-based printing techniques, where it can retain its shape once extruded. A higher concentration of single-layer MXene exhibits a shift in elastic modulus to a higher frequency with ordered packing of particles. The higher concentration yields a soft-gel-type behavior. Further, the highest concentration of 3.60 mg mL⁻¹ Elastic modulus increases exponentially without the influence of frequency. The high concentration of MXene forms a percolation network where the viscous and elastic modulus shift to the non-linear region independent of frequency. **Fig. 33(b)** illustrates the viscosity of the AC ink and AC/M-N ink, which determines the 3D printing quality of the electrodes[53]. The rheological properties exhibit the shear-thinning property of the inks, which is favorable for 3D printing. The MXene composite ink and AC ink exhibit a yield stress of 300 and 70 Pa, which enables its printability of 3D electrodes(inset).

Particle dispersion in different solvents is depicted in **Fig. 33(c)**[447]. Among six solvents, ethanol exhibits the least surface tension as compared to the rest of the solvents. The boiling point of the ink is a major parameter that governs the final shape of the printed part. Faster and defect-free curing is desirable from the solvents while synthesizing ink with specific solvents. Boltzmann's fit is depicted in **Fig. 33(c)(ii)**, which correlates the concentration of MXene with the boiling point. The higher the boiling point more uniform the MXene dispersion. In the case of ethanol, despite its low boiling point, it exhibits excellent particle dispersion and is suitable for ink synthesis. Further studies confirm that the solvent molecular weight stands linearly with the increment in the enhancement in the MXene concentration as depicted in **Fig. 33(c)(iii)**. The kinetic dispersion is higher for solvents having high viscosity, which forms a stable extrusion of ink through the nozzle. The nanosheets need homogeneous flow when undergoing the spray coating technique, benefiting from the high viscosity of the dispersion as shown in **Fig. 33(c)(iv)**. Stable jetting is essential for the MXene ink to obtain a high-precision print. Further, to obtain stable MXene ink with higher stability and antioxidative properties, organic solvents are preferable. The MXene dispersibility and ink properties are studied by researchers to yield high-resolution prints. The organic solvents provide better substrate compatibility and better particle dispersion. Solvents having surface tension between 35 to 42 mNm^{-1} are found to be more suitable for ink preparation. A polar/dispersive ratio between 0.61 and 0.87 provides better dispersion of particles throughout the matrix-DMF, NMP, and N-DMF are some of the compatible organic solvents for MXene ink synthesis[495]. The ink rheology, like surface tension, dispersion, and viscosity, is easy to tune by switching the appropriate solvent. Surface terminal groups acquired by the MXene synthesis widely influence the MXene dispersion. TBAOH-assisted synthesis technique offers higher MXene dispersion in the organic solvent. Further researchers have synthesized MXene ink with DMSO, NMP, and ethanol, keeping the Ohnesorge number between 2.5 and 2.2. The ink was printed over AlO-coated PET with higher print resolution and stable structure after drying (**Fig. 33(d)**)[54].

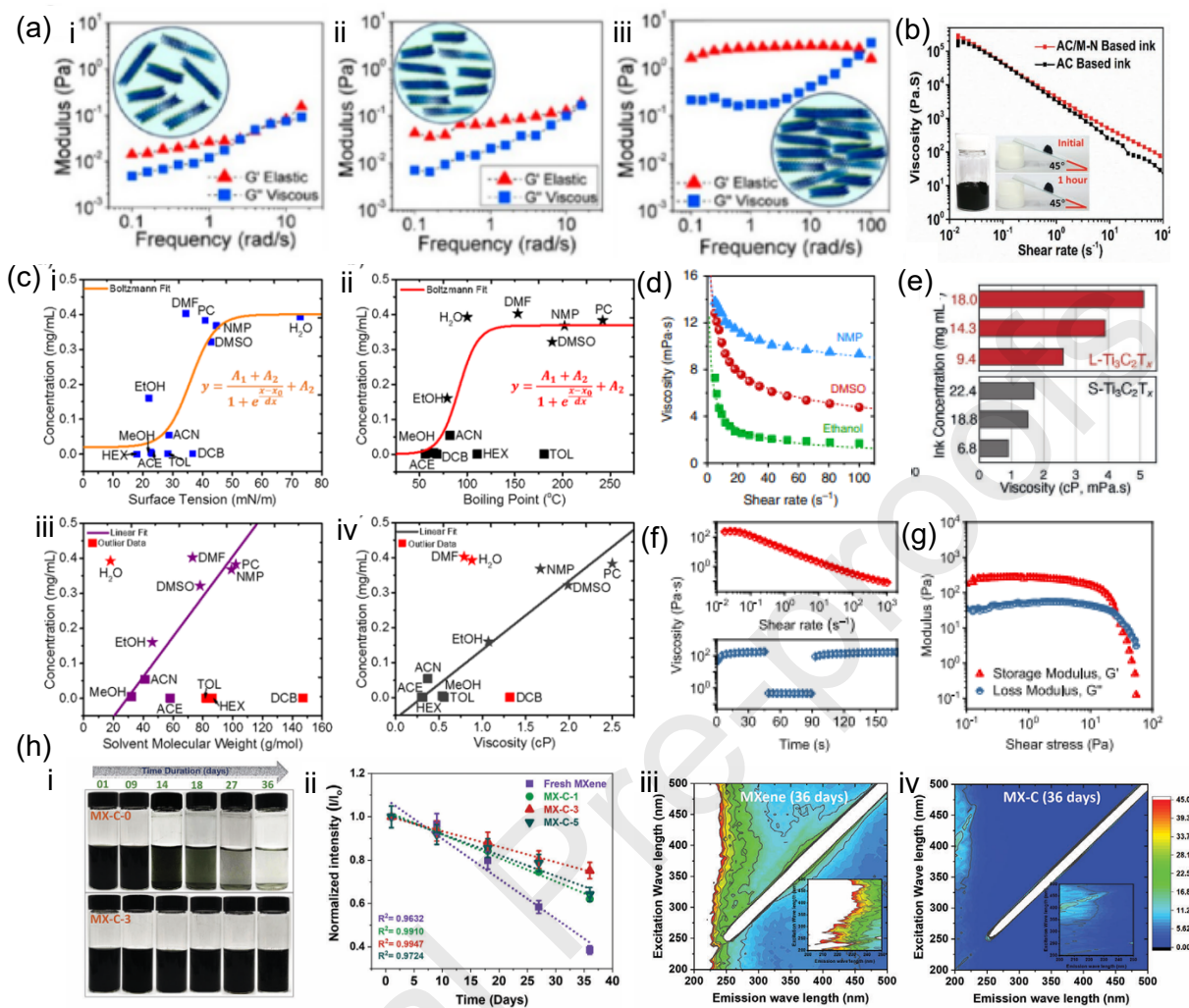


Fig.33 (a)(i-iii) Images illustrating the viscoelastic behaviour of single-layer MXene inks at different concentrations. Reproduced with permission from [158] ©2018 American Chemical Society (b) Rheological behaviour of AC/CNT/GO and MXene-composite ink. Reproduced with permission from [198] ©2019 WILEY-VCH (c) Effect of MXene concentration concerning various solvents. Reproduced with permission from [199] ©2017 American Chemical Society (d) Viscosity as a function of shear rate for different organic inks. Reproduced with permission from [200] © 2019 Springer Nature (e) Ink concentration with respect to the viscosity of different particle size MXene. Reproduced with permission from [201] ©2020 WILEY-VCH (f) Viscosity with respect to various shear rates at different time intervals (g) Modulus vs shear stress of MXene inks. Reproduced with permission from [167] © 2019 Springer Nature (h)(i) Colour degradation of MXene ink. (ii) Adsorption deviation plot with normalized intensity

with respect to the number of days. (iii-iv) Excitation emission matrix conduction after 36 days. Reproduced with permission from[256] ©2019 WILEY-VCH.

A similar stable structure was fabricated over a silicon substrate using MXene ink with acetone and water solvent[496].MXene inks with shear-thinning behavior over a wide range of concentrations have been proven suitable for printed electrode fabrication. Researchers have measured the dynamic viscosity of MXene ink with an average flake size of 350 nm. The ink with a concentration of 18 mg L^{-1} acquires a viscosity of 5.1 cP, whereas smaller flake size MXene exhibits a viscosity of 1.5 cP (**Fig. 33(e)**)[446]. Additive MXene has been widely explored for fabricating high-performance energy storage applications. The MXene ink with a higher concentration above 90 % of large monolayer MXene exhibits shear-thinning behavior. The desirable viscosity provides uniform extrusion of stable dispersion and quick curing of the extruded structure. The stable uniform ink with excellent viscoelastic acquires a viscosity of $2.5 \times 10^2 \text{ Pa.s}$ which yields high precision printed structures with a uniform extrusion rate (**Fig. 33 (f, g)**)[497] Ink stability over the long run offers an incredible opportunity to store the ink over a long period which opens up opportunity for commercialization of the ink for electrode printing application. **Fig. 33(h)** represents the ink rheology and stability over the long run[256] The Cysteine functionalized MXene ink exhibits constant colour over 36 days, exhibiting excellent stability. The EEM study confirms the non-fluorescent nature of the functionalized ink and the presence of in situ Titanium oxide in the non-functionalized ink. Further studies confirm the colloidal dispersity of MXene-cysteine ink as compared to pure MXene. The functionalization provides excellent stability to the MXene ink for a prolonged period without deteriorating the inherent properties.

Though there is major rheological property optimization carried out by tuning various parameters like concentration, elastic modulus, loss modulus, and various solvents, still, there are extensive research gaps for rheology optimization for composite MXene inks without compromising the electrochemical properties. Based on the optimized ink conditions, various microelectrochemical systems have been developed and utilized for energy storage applications as discussed in the next section.

13. Electrode Design and Electrochemical Performance of MXene-based MSC

The excellent physicochemical properties of MXene make it a promising candidate for micro-supercapacitor applications. High porosity, metallic conductivity, and abundant active sites enhance the electrochemical properties tuneable interlayer spacings provide an effective pathway for ion migration, whereas the conductive edges accelerate the electrochemical activities. Plenty of surface functional groups enhance the hydrophilicity and provide active sites for fast redox reactions. In addition to a remarkable physicochemical structure and electrochemical performance, MXene acquires superior mechanical strength and flexibility. Benefiting from the functional groups and negative surface charge, MXene forms finely dispersed stable inks with a wide range of aqueous solvents that favor printed micro-supercapacitors through various printing techniques like spray coating, spin-coating, screen printing, direct ink writing, and inkjet printing etc. Various MSC fabrication techniques, advantages, and their limitations are detailed in **Table 10**.

Table 10 Comparative Summary of Microsupercapacitor (MSC) Fabrication Techniques: Key Advantages, Limitations, and Suitability for MXene-Based Electrode Integration

Sr No	Printing technique	Printing resolution (μm)	Advantages	Limitations	Ref.
1	Inkjet printing	20-100	<ul style="list-style-type: none"> a) Fast printing b) Monolithic 3D structure electrodes 	<ul style="list-style-type: none"> a) Nozzle clogging b) Limited ink with optimized viscosity 	[459], [464], [486], [498]
2	Direct writing	1-2.1	<ul style="list-style-type: none"> a) Wide range of printing material b) Tuneable design of electrodes c) Substrate flexibility 	<ul style="list-style-type: none"> a) Nozzle clogging b) Viscosity optimization 	[499], [500], [501], [502]
3	Gravure printing	2-50	<ul style="list-style-type: none"> a) Fast printing b) Economic 	<ul style="list-style-type: none"> a) Limited ink with required viscosity (0.1-1 Pa.s) 	[503], [504], [505], [506]
4	Screen printing	40-150	<ul style="list-style-type: none"> a) Simple instrumentation b) Economic c) Readily available inks 	<ul style="list-style-type: none"> a) High-precision electrode pattern required 	[507], [508], [509], [510]

5	Laser engraving	1-100	a) Fast printing b) Independent of ink viscosity	a) Prone to heat-induced defects and limited to specific substrates	[511], [512], [513]
6	Spray coating	1-500	a) Mass production with low capital investment	a) High-resolution mask required	[514], [515], [516]

13.1 MXene MSC fabrication strategies

MXene micro-supercapacitors are fabricated by researchers by additive and subtractive methods[517], [518], [519]. Both fabrication techniques have their unique advantages and distinguished electrochemical properties[520], [521], [522]. Subtractive property involves the removal of additional material from the substrate to fabricate IDT planar type MSC using a laser/plasma source, whereas in the case of additive techniques, Mold-assisted free-standing electrodes are printed, or extrusion-based 3D printing techniques are followed[523], [524], [525].

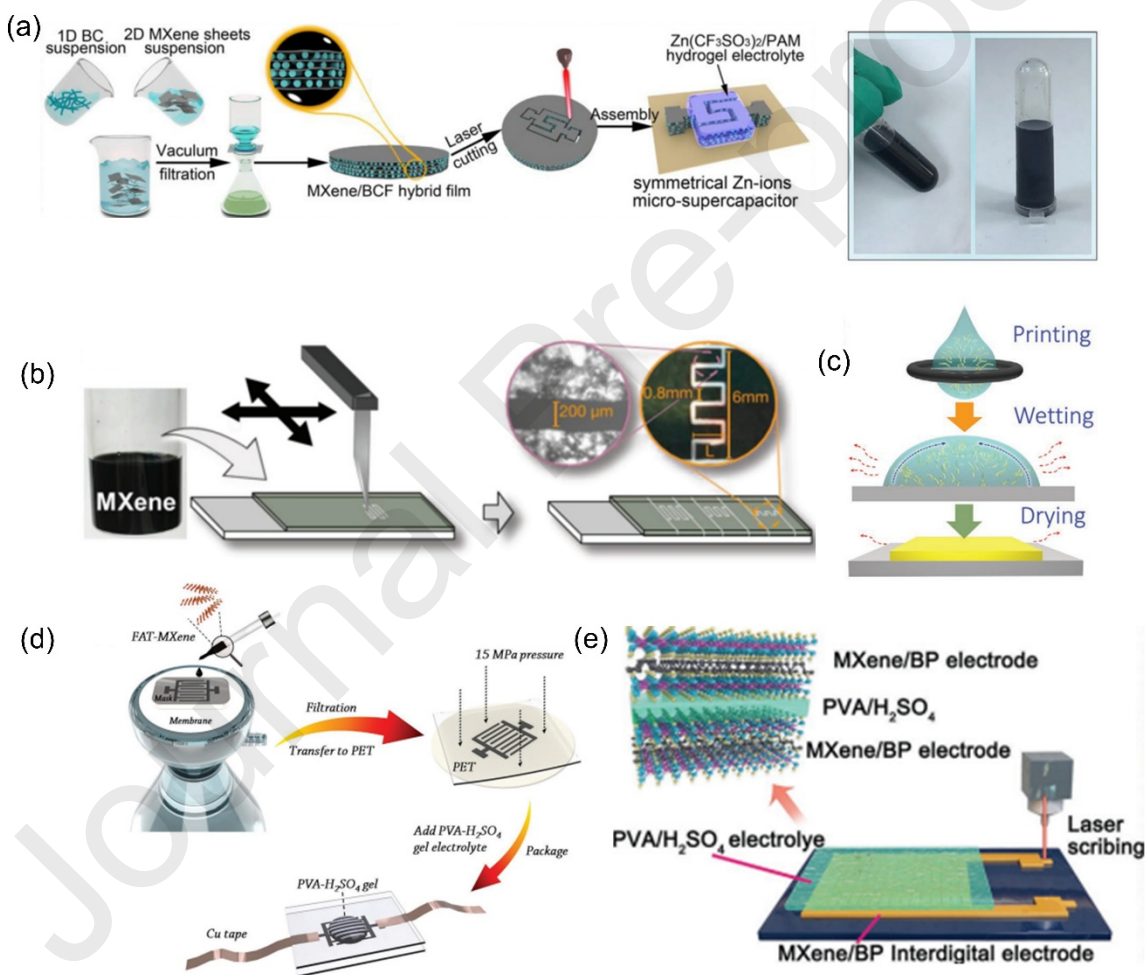


Fig. 34 (a) Schematic illustration of MXene-BCF composite-based Zn-ion MSCs. Reproduced with permission from [68] © 2021 Elsevier B.V (b) Scalpel engraving for MXene-based MSC. Reproduced with permission from [62] © 2018 WILEY-VCH (c) Digital photographs of MXene-PH1000 inks in normal and inverted states and inkjet printing process. Reproduced

with permission from [128] ©2021 WILEY-VCH (d) Schematic illustration of the mask-assisted MXene MSC fabrication technique. Reproduced with permission from [169] ©2020 WILEY-VCH (e)Laser scribed MSC/BP IDT MSC fabrication techniques. Reproduced with permission from [170] © 2021WILEY-VCH

$\text{Ti}_3\text{C}_2\text{T}_{\text{x}}$ -based IDT MSC was fabricated by the laser engraving technique, which exhibited a specific capacitance of 27 mF cm^{-2} [72]. Further paper-based MSC was fabricated utilizing a CO_2 laser. The electrode thickness obtained was around $120 \mu\text{m}$ [526]. The local heat generated during laser exposure creates rough and uneven edges. To overcome the edge defects, researchers have implemented a cold laser to fabricate the MSC. Laser exposure and power affect the electrode quality, which influences the electrochemical properties directly. Re-stacking of MXene layers leads to sluggish electron kinetics and restricts the diffusion of divalent electrons. Researchers have fabricated a bacterial cellulose fiber-MXene composite that restricts the restacking of MXene layers and increases the interlayer spacing, which widens the ion-transport channels, resulting in remarkable electrochemical performance[81].

Fig. 34(a) illustrates the fabrication steps of Zinc ion-MSC through a laser-assisted cutting technique. Firstly, the BCF solution was added slowly to the colloidal MXene solution and mixed thoroughly. The homogeneous solution was further filtered and dried for 24 h to obtain the composite film of different compositions of BCF (0-72.7%). The free-standing MXene-BCF film was exposed to a laser beam to obtain the printed MXene-BCF composite electrodes. The FE-SEM analysis of the film cross-section reveals the enhanced interlayer spacing, which increased to $60\mu\text{m}$ from $10\mu\text{m}$, along with the homogeneous distribution of the BCF. The enhanced interlayer spacing and stable structure with the presence of abundant oxygen promote ion migration, resulting in enhanced electrochemical performance. A solution-processable route was developed by researchers to fabricate thin films in a single-step dip coating method, as shown in **Fig. 34(b)**[75]. Benefiting from the negative zeta potential of MXene, water-based colloidal dispersion was used as a precursor for the dip coating technique. The negative charge of MXene particles keeps them distinct and restricts agglomeration in water. The cleaned glass substrate was dipped into the MXene colloidal solution for a certain time for the deposition of MXene sheets over the substrate. The deposition was governed by several dipping and concentrations of MXene solution. An

increased number of dips enhances the conductivity of the film owing to the deposition of more MXene flakes closely. The higher deposition reduces the transparency of the electrode from 98 to 35 %. The scalpel technique was engaged to fabricate IDT MXene electrodes in a single step. The electrode spacing varies from 0.1-0.2 mm.

The scalpel technique overcomes the roughness or heat-induced defects that are caused by the laser-engraving technique over thin films. Different thicknesses of films can be engraved into desired shapes. The high conductivity and binder-less electrode are attributed to the enhanced electrochemical performance of the MSC. Mass production of MSC for micro-electronics needs scalable fabrication techniques like inkjet printing[460]. The high precision, mask-free, customizable printing technique makes it versatile among various electrode fabrication techniques. The presence of functional groups forms a stable aqueous dispersion with high conductivity on various solvents like DMSO, NMP, DMF, etc. Researchers have developed MXene ink with PH 1000 (MP) for the printing of MSC with a defined shape and enhanced electrochemical properties. The stable ink prints high-precision electrodes over different substrates. The addition of PH 1000 restricts the restacking of the MXene layers and facilitates faster ion diffusion. The printed MSC was further coupled with a current collector and circuit for an integrated system for the sensory system. **Fig. 34(c)** depicts the ink-jet printing technique for smooth electrode fabrication by balancing substrate wetting and controlled ink drying. The water content from the printed part evaporates, leaving the glycol content that forms the coffee-ring effect, distorting the electrode shape. The MXene composite ink prints stable structures without any defects. The optimized viscosity results in exceptional structural stability. The FE-SEM images highlight the clear boundaries and distinguishable IDT spaces. The printed electrodes demonstrate excellent mechanical stability and adhesion to the surface. A non-hazardous solvent-based ink for printing customizable structures with high precision. Researchers have developed a Freeze and Thaw (FAT)-assisted MXene synthesis technique and fabricated an on-chip MSC[527]. The FAT-MXene exhibits a smooth surface with layers of large flakes, providing enhanced electrochemical performance owing to the higher conductivity. **Fig. 34(d)** represents the mask-assisted fabrication technique of all MXene-MSC. Firstly, MXene is vacuum filtered through a membrane masked with an IDT structure. The FAT-MXene forms a highly conductive, thick deposition of MXene along the

IDT shape. Further, the IDT electrode was transferred to a PET substrate under a pressure of 15 MPa. The transfer technique establishes a defect-free fabrication of IDT-on-plane MSC. The transferred electrode is further encapsulated with Kapton tape after adding gel electrolyte. MXene-based electrodes acted as both an active layer and a current collector. Researchers developed a self-powered sensory system by integrating MXene-based MSC with a sensing system[528].

A Self-assembly process was employed to fabricate the MXene-BP film, which further undergoes a laser engraving technique to fabricate the on-plane electrodes (Fig. 34(e)). Incorporation of BP with MXene results in higher interlayer spacing that promotes faster ion migration and is attributed to higher electrochemical performance. The as-fabricated composite film attains excellent flexibility, and BP intercalation yields a stable structure. FE-SEM analysis confirms the enhanced interlayer spacing and a homogeneous distribution of corresponding elements parallelly over the MXene. The large interlayer spacing and higher porosity promote faster ion diffusion and result in enhanced electrochemical performance. A fast, scalable technique was developed by researchers to print the MSC by the stamping method[529]. Hydrophilicity and higher conductivity make MXene a suitable candidate to formulate stable aqueous dispersion and further implement for printing the desired electrode shape. The stamping technique provides a fast and efficient technique for the production of MSCs.

Fig. 35(a) illustrates the fabrication technique of MSCs through the stamping technique. The desired shape of the electrode is printed by a 3D printing technique where the dimensions of the part are fixed. The MXene ink is adhered to the stamp by a manual brushing technique and imprinted over the paper substrate. Gel electrolyte is applied over the printed electrodes, and Ag wires are attached over it. After being dried, the solid-state MXene MSC is fabricated and employed for further analysis. The MXene ink consists of single-layer flakes with a hexagonal structure, as evidenced by the TEM micrographs. The viscous ink is printable over wide ranges of substrates, including paper, PET, and glass, portraying the versatility of the stamping technique to fabricate solid-state MSCs. Design flexibility can be obtained from the direct ink writing technique. Printable functional inks provide scope for fabricating high-performance MSCs. As surfactants and additives affect the conductivity of the ink, an

additive-free ink was developed by researchers for the direct writing of the MXene-based MSC[54]. Fig. 35(b) depicts the development of printable inks with different solvents. Negatively charged MXene particles form a stable viscous ink with MXene nanoflakes. In addition to this, organic ink with high polarity can be utilized as an organic solvent for organic MXene ink formulation. Low boiling point and medium to high boiling point inks affect the print quality based on the rate of evaporation and dispersion of MXene sheets. Both inks are employed for electrode printing via additive manufacturing techniques. Current developments in wearable electronics have tremendously generated a big void in flexible energy storage systems.

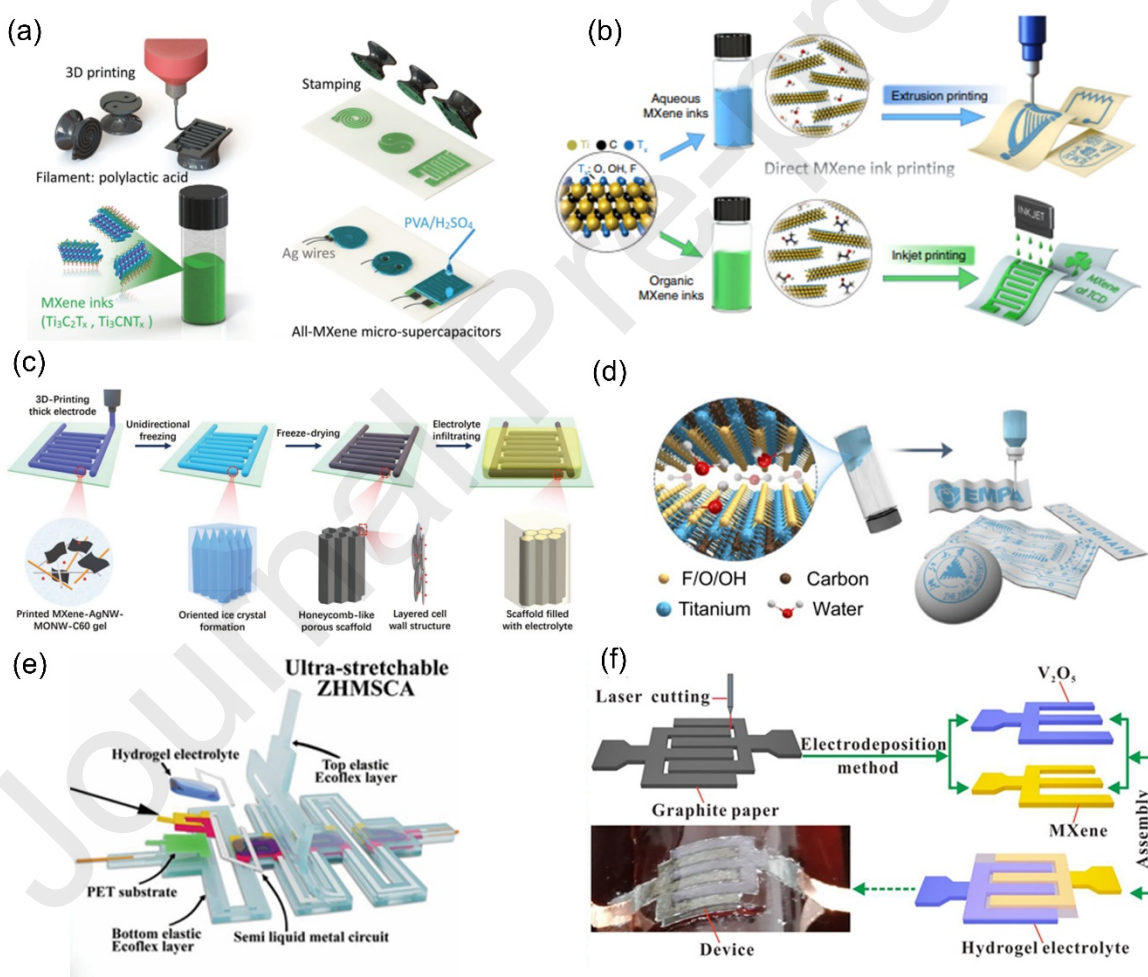


Fig. 35 (a) Schematic illustration of the stamp-assisted MXene MSC printing technique. Reproduced with permission from [202] ©2018 WILEY-VCH (b) MSC printing process utilizing organic and aqueous MXene inks. Reproduced with permission from [200] ©2019 Springer Nature (c) MXene MSC fabrication technique by unidirectional freezing of 3D

printed IDT electrodes. Reproduced with permission from [203] © 2020 WILEY-VCH (d) Room temperature direct printing of MXene-based flexible printed electronics. Reproduced with permission from [167] © 2022 Springer Nature (e) Representation of ultra-stretchable ZHMSCA. Reproduced with permission from [247] © 2023 WILEY-VCH (f) Illustration of MXene-based AMSC comprised of V_2O_5 and MXene electrodes. Reproduced with permission from [248] © 2022 Elsevier.

The existing stretchable energy systems are comprised of flexible substrates or prestrained substrates, which limits the design and integration scope of the electronics elements. Low adhesion of electro-material and inefficient electrochemical performance are the prime bottlenecks in coupling with low-power electronics. Stretchable MSC suffers from limited electrochemical performance due to a lack of high-performance electrode materials by compositing MnO_2 /Ag nanowires, and fullerenes display remarkable performance as shown in **Fig. 35(c)**[530]. The MXene ink was synthesized by the gelation technique. $Ti_3C_2T_x$ MXene sheets dispersed in water are mixed thoroughly with Ag NW, MnO_2 nanowires, and fullerene through ultrasonication and vacuum filtration to obtain the composite hydrogel. The as-obtained composite was redispersed in water to form a 3D cross-linked network structure of MXene. The 3D structure eliminates the need for any surfactant and additives for smooth, high-resolution printing. The Ag NW introduces a conductive network throughout facilitating faster ion conduction, and MnO_2 NW contributes pseudo capacitance. C-60 particles restrict the restacking of the MXene structure and promote faster ion transfer. Various ratios of the ingredients are prepared for the electrode printing. The formulated inks were printed over cleaned PDMS substrates in the form of thick deposits in the desired structure. The printed electrodes are further freeze-dried to obtain the solid-state IDT MSC. The unidirectional freezing technique results in a honeycomb-type scaffold structure with layered cell walls. PVA-KOH gel was added dropwise over the IDT electrodes, benefiting from the inherent porous structure, the gel infiltrated into the electrodes provides a higher surface area for electrode-electrolyte interaction. The nano-composite ink was further utilized to print various free-standing microelectrodes that prove the versatility of the ink for fabricating a wide range of electrodes with design flexibility.

In addition, the advances in microelectronics and IoTs stimulate scalable fabrication of high-performance energy storage devices and integrated self-powered systems. As the direct printing technique is a viable, fast fabricating technique, MXene ink was utilized to fabricate an all-in-one integrated printing system. Benefiting from the hydrophilicity and surface functional groups, an additive-free MXene ink was formulated[497]. **Fig. 35(d)** illustrates the room temperature printing technique for an in-plane integrated energy system. The highly concentrated inks are comprised of single-layer MXene flakes with an atomic arrangement in a hexagonal shape. The flake size ranges around $\sim 1.6 \mu\text{m}$ and a thickness of around 1.5 nm. The large flakes and high-concentration inks exhibit excellent shear-thinning behavior that provides excellent printability and a high-resolution stable structure. The room-temperature direct printing was employed by the additive-free MXene ink that efficiently prints various structures with high resolution. The formulated additive-free ink demonstrates excellent printability of highly packed structures and linear circuitry as well without compromising the electrochemical properties. **Fig. 35(e)** illustrates the fabrication technique of ultra-stretchable ZHMSCA-based MSC. The island bridge architecture comprised CNT@MnO₂ and MXene/BC @PPy electrodes[247]. PET films act as a supportive substrate for the active layers. Semi-liquid metal circuit acts as the current collector. The hydrogel electrolyte was encapsulated with the eco-flex layer to protect the device. The IDT electrode was later obtained by the laser scribing technique. The capacitor-type electrode attains a wide interlayer spacing and conductive paths among MXene layers. BC@ PPy acts as a nano spacer that prevents the restacking of the electrodes and enhances the overall electrochemical properties. A zinc-ion MSC comprised of MXene anode and V₂O₅ cathode was fabricated for energy storage application (**Fig. 35(f)**)[248]. The MSC electrode consists of flexible graphite paper engraved by laser power. Electrodeposition was carried out to deposit MXene nanosheets and V₂O₅ to form a thin layer. PAM hydrogel was applied over the thin film electrodes to construct the ZIHMSC. The asymmetric Zn-ion MSC opens up huge potential for high-performance MXene-based energy storage devices. MXene-based MSCs acquire a limited voltage window, which can further be extended by selecting the proper electrolyte

and tuning the electronic structure. Water-in-salt electrolyte was employed for the MXene-based Zn ion MSC, which exhibits an extended voltage window of 1.8 V.

Fig. 36(a) represents the 3D-printed MSC with IDT architecture[251]. The MXene ink was printed over a wide range of substrates, including PET, rubber, and cloth. The deformation and expansion of the substrate do not later the printed patterns, which confirms the excellent adhesion of the ink. Customized patterns can be precisely 3D printed that represent the esthetical appearance of integrated energy systems. The 3D-printed MXene MSC

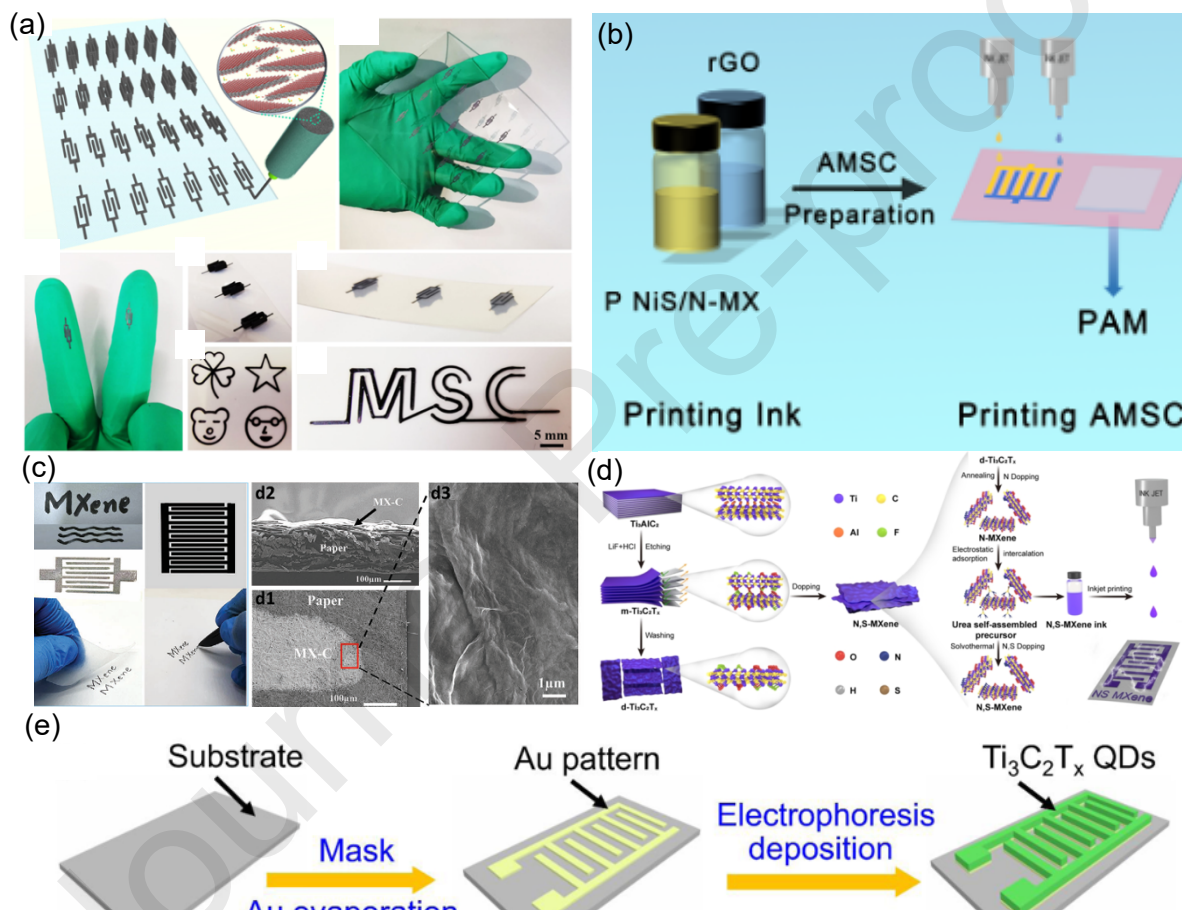


Fig. 36 (a) Pictorial representation of MXene based printed MSC over various substrates. Reproduced with permission from [251] ©2024 WILEY-VCH. (b) Schematic presentation of AMSC fabrication. Reproduced with permission from [349] ©2023 Elsevier (c) MXene ink for 3D printing of MSC and morphology of the printed specimens. Reproduced with permission from [256] ©2023 WILEY-VCH (d) N,S MXene ink for inkjet printing of MSC . Reproduced with permission from [255] ©2022 Elsevier (e) Fabrication technique of MXene QD based MSC. Reproduced with permission from [348] ©2024 Elsevier.

was freeze-dried for 24 h to remove the extra water. The water in the salt electrolyte was drop-cast over IDT electrodes to fabricate the MSC. NiS/N-MXene-based MSC was fabricated by the ink-jet printing technique. **Fig. 36(b)** illustrates the fabrication technique of the AMSC device and further makes a self-powered sensor system[349]. The appropriate surface energy, mechanical strength and flexibility, and water resistance make it a reliable substrate for the 3D printing of MXene MSC. **Fig. 36(c)** illustrates the handwritten patterns scribed by MXene ink over the paper substrate, which exhibits excellent contact adhesion[256]. The adhesion of ink over the paper substrate was confirmed from the SEM image. The MXene layer was positioned over the paper substrate, as evidenced from the cross-sectional image. Nitrogen and sulfur doping enhance the electrochemical property of MXene, which is further utilized to fabricate the planar MSC through inkjet printing. Electrostatic adsorption and self-assembly lead to the formation of homogeneous ink that is further printed into the desired shape over the substrate (**Fig. 36(d)**)[255]. The Planar IDT electrode was fabricated by a mask-assisted printing technique as depicted in **Fig. 36(e)**[348]. Defect-rich MXene QDs were employed as the electrode material for the MSC fabrication. The Au-integrated microelectrodes were coupled with an Alumina substrate, followed by a coating of MXene QDs. Further washing with DI water leads to the formation of MXene QD-based MSC for electrochemical analysis. The IDT electrodes attain a width of 300 μm and a spacing of 150 μm . The smooth surface attains a close interfacial contact over the Au-coated electrodes. The binder-free electrode promotes abundant electron transfer owing to the less charge transfer resistance. The stable nano-engineered MXene QD-based electrodes attain excellent specific capacity and long-term stability.

13.2 MXene-MSCs electrochemical performance.

MXene-based micro-supercapacitors' electrochemical performance is substantially driven by their intrinsic features, which include their layered structure, surface functional groups, and ion accessibility. These properties facilitate efficient charge storage via double-layer capacitance and redox pseudo-capacitance methods. Furthermore, the scalability of MXene production and the ability to construct specialized electrode configurations have pushed its use in sophisticated energy storage technologies. This review unveils the electrochemical properties of MXene micro-supercapacitors, including ion transport

dynamics, charge storage processes, and performance metrics such as specific capacitance, energy density, and cycling stability. It also emphasizes the challenges and potential for optimizing MXene-based systems to satisfy the needs of next-generation electronic gadgets. MXene-based MSCs and their electrochemical performance are summarized in **Table 11**.

The additive-free aqueous ink is depicted in **Fig. 37(a)**, which consists of water as a solvent and delaminated MXene flakes as the active components[446]. The additive-free ink contains large and single-layer MXenes with a height of 1.6 nm, and the dynamic rheology prints high-resolution electrodes for energy storage applications. The ink was employed for printing IDT MSC through the thermal inkjet printing technique. The electrochemical properties were evaluated by applying PVA-H₂SO₄ gel electrolyte. The effect of flake size on the electrochemical properties was evaluated as depicted in **Fig. 35(b)**.

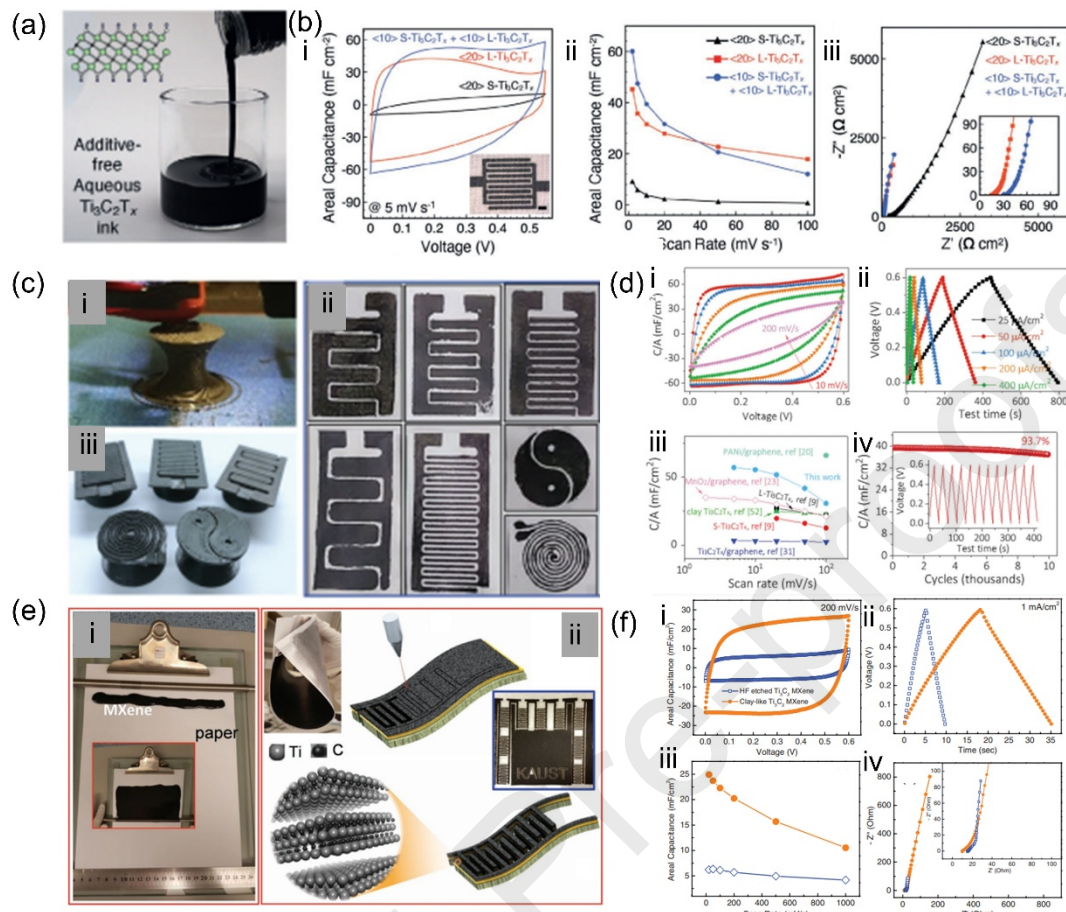


Fig. 37 (a) Pictorial presentation of additive-free aqueous $\text{Ti}_3\text{C}_2\text{T}_x$ ink (b) i. CV profile of printed MSCs with 3 different inks containing L-MXene, S-MXene, and a mixture of L-MXene and S-MXene ii. Areal capacitance at various scan rates iii. Nyquist plot of MXene MSCs. Reproduced with permission from [201] ©2020 WILEY-VCH (c) (i) 3D-printing of stamp (ii) Printed stamps at various shapes (iii) Stamped different architecture MSCs with MXene inks (d) i. CV-profiles of I-MXene ii. GCD profiles of printed MSCs at various current densities iii. Comparison of the areal capacitance of different printed MSCs iv. Capacitance retention of MSCs over 10,000 cycles (inset: GCD curves at a current density of 200 $\mu\text{A}/\text{cm}^2$). Reproduced with permission from [202] © 2018 WILEY-VCH (e) i. MXene slurry printing over A4 size paper substrate ii. Laser engraving over paper substrates with MXene coating (f) i. CV curves at a scan rate of 200 mV s^{-1} ii. Comparative GCD curves at a current density of 1 mA/cm^2 iii. Areal capacitance as a function of scan rates iv. Nyquist plot of MXenes with HF-etched and clay-like MXene devices. Reproduced with permission from [204] © 2016 WILEY-VCH

The CV curves from 5 to 50 mV/s exhibited the comparative charge storage capacity, where S-MXene stores less energy as compared to the other two sizes of MXene-flakes. The MXene ink containing both S-MXene and L-MXene exhibits higher energy storage ability and better capacitance retention as well. The areal capacitance calculated at various scan rates shows excellent rate capability. Small flakes exhibited better rate capability owing to the excellent electrolyte diffusion and higher electrical conductivities study of the printed electrodes exhibits smaller ESR values for larger flakes and a mixture of small and large flakes around whereas the small flakes portray a large resistivity of $203.7\ \Omega$. These values are well aligned with the obtained ink resistivity-MXene ink acquired the highest 45° slope as compared to other inks, which confirms the higher ion diffusion path which results in poor electrochemical performance as well. The imaginary axis of L-MXene inks and mixed MXene inks showed a close parallel to the -Z axis, which is attributed to the ideal capacitive behavior of the MSCs. This preliminary result makes the combination of S-MXene and L-MXene mixture the ideal composition for fabricating high-performance electrodes. The CV curves obtained from the MXene MSC with optimized dimensions exhibited a quasi-rectangular profile and GCD curves with minimal IR resistance.

Table 11: Summary of MXene-based MSCs and the comparative electrochemical properties

Sl No	Material	Fabrication technique	Electrolyte	Specific capacitance (mF cm ⁻²)	Energy density (µWh cm ⁻²)	Power density (mW cm ⁻²)	Stability (%) / No of Cycles	Ref
1	L-S-Ti ₃ C ₂ T _x	Laser cutting	PVA/H ₂ SO ₄	27.3	2.34–1.43	0.091.95	100/10,000	[531]
2	Ti ₃ C ₂ T _x	Laser cutting	1 M H ₂ SO ₄	25	0.77–0.22	7.644.6	92/10,000	[532]
3	Ti ₃ C ₂ T _x	Oxidative etching	PVA/H ₂ SO ₄	0.07	0.01	NA	87/1000	[533]
	Ti ₃ C ₂ T _x	Laser cutting	PVA/H ₂ SO ₄	340	13.646.16	0.244.79	82.5/5000	[534]
4	Ti ₃ C ₂ T _x	Automated scalpel	PVA/H ₃ PO ₄	~0.43	0.01–0.003	0.001–0.01	100/6000	[75]
5	Ti ₃ C ₂ T _x @RuO ₂	Screen printing	PVA/KOH	23.3	0.36–0.22	0.03–1.31	90/10,000	[57]
6	Ti ₃ C ₂ T _x	Scratch method	PVA/H ₃ PO ₄	25.5	1.84–1.04	1.281.61	90/8000	[535]
7	Ti ₃ C ₂ T _x	Direct writing	PVA/H ₂ SO ₄	5	NA	NA	NA	[536]
8	Ti ₃ C ₂ T _x	Inkjet printing	PVA/H ₂ SO ₄	12			100/10,000	[54]
9	Ti ₃ C ₂ T _x	Extrusion printing	PVA/H ₂ SO ₄	43	0.32–0.11	0.11–1.58	97/14,000	[54]
10	Ti ₃ C ₂ T _x	Ink injection	PVA/H ₃ PO ₄	276	28–12	1–8	95/1000	[537]
11	Ti ₃ C ₂ T _x @GO aerogel	Laser cutting	PVA/H ₂ SO ₄	34.6	2.18–1.33	0.06–0.18	91/15000	[431]
12	Ti ₃ C ₂ T _x @EG	Vacuum filtration	EMIMBF ₄	43.7	14	4.5	80/1000	[482]
13	Ti ₃ C ₂ T _x @BC	Laser cutting	PVA/H ₂ SO ₄	115.2	5.54	NA	100/5000	[241]
14	Ti ₃ C ₂ T _x @PEDOT	Spray coating	PVA/H ₂ SO ₄	2.4	2.4	0.0055–0.045	92/10,000	[59]

15	Ti ₃ C ₂ T _x	Laser cut mask	PVA/H ₂ SO ₄	2.4	0.26–0.015	0.06–0.33	90/10,000	[538]
16	Ti ₃ C ₂ T _x	Laser cutting	PVA/LiCl	52	2.62	1.26	100/10,000	[539]
17	Mo _{1.33} C MnO ₂	Photolithograph	PVA/LiCl	69.95	NA	NA	92/10,000	[78]
18	Ti ₃ C ₂ T _x CoAl LDH ^y	Screen printing	6 M KOH	40	10.8–8.43	0.34–1.09	92/10,000	[538]
19	Ti ₃ C ₂ T _x	Laser cutting	PVA/ H ₂ SO ₄	71.16	3.52–2.51	0.33–7.99	81.2/5000	[540]
20	Ti ₃ C ₂ T _x	Stamping	PVA/ H ₂ SO ₄	61	0.76–0.66	0.01–0.33	94.1/10,000	[529]
21	Ti ₃ C ₂ @CW	Electrodeposition	NaOH	72.3	206	1.94	89.3/10,000	[541]
22	Ti ₃ C ₂ T _x	Laser cutting	PVA/ H ₃ PO ₄	23	1.12–0.92	0.09–0.30	95/10,000	[542]
25	MXene @Ag	Inkjet Printing	PVA/H ₃ PO ₄	12.9	0.24	200.93	72/5000	[543]
26	N-S doped MXene	Inkjet Printing	PVA/H ₂ SO ₄	710000	8.9	411	94.6/10,000	[544]
27	Ti ₃ C ₂ T _x @C	Inkjet Printing	PVA/H ₂ SO ₄	40	1.39	50	83/10,000	[545]
28	Ti ₃ C ₂ T _x	3D Printing	PVA/H ₂ SO ₄	1035	51.7	5.7	NA	[50]
29	Ti ₃ C ₂ T _x graphene	Inkjet Printing	PVA/ Na ₂ SO ₄	3.84	0.533	10	63/2500	[546]
30	Ti ₃ C ₂ T _x	Inkjet Printing	PVA/H ₃ PO ₄	0.192	0.001 ~ 0.01	0.01 ~ 0.1	100.8/NA	[547]
31	Ti ₃ C ₂ T _x	Inkjet Printing	PVA/H ₂ SO ₄	294	12.36	0.16	98/10,000	[446]

Further, the specific capacitance of the MSC attained 294 mF cm^{-2} which outperforms other MXene-based printed MSCs. The thermal inkjet (TIJ)-printed MSC exhibits excellent cyclic stability of 10,000 cycles with a remarkable capacitance retention of 98 %. This work paved the path for fabricating high-performance MXene-based flexible energy storage devices without compromising the electrochemical properties. **Fig. 37(c)** illustrates the 3D printing technique of stamps containing desired electrode shapes and stamped MSCs in different shapes[529]. The FE-SEM images of the printed planar electrodes exhibit excellent resolution with a defined space between the consecutive electrodes. Various bending angles didn't alter the conductivity of the printed electrodes as measured over a PET substrate. The electrochemical performance of the stamp-assisted printed MSCs is carried out as shown in **Fig. 37(d)**. The CV profiles exhibit quasi-rectangular shapes from scan rates ranging from 10 mV s^{-1} to 200 mV s^{-1} within a potential window of 0.6V. The rectangular GCD profiles show symmetric behavior at different applied currents ranging from $25 \mu\text{A cm}^{-2}$. The MSCs attain a specific capacitance of 57 mF cm^{-2} that outperforms early reported works, as shown in **Fig. 37(d)(iii)**. The comparison graph for the specific capacitance at various scan rates of MXene MSC that outperforms other MSCs comprised of MnO_2 graphene, MXene/Graphene. Further stability analysis for stamped MXene MSC is depicted in **Fig. 37 (d)(iv)** exhibits excellent capacitance retention of 93.7 % over 10,000 cycles. The excellent capacity retention makes this MSC suitable for the long run for real-time applications. Repeated bending cycles at various bending angles over 1600 cycles portray excellent mechanical stability and uncompromised excellent electrochemical performance. Overall, this work proposes a standard synthesis strategy to tune the electrochemical performance and a fast-manufacturing process for upscaling high-performance supercapacitors.

A simple laser-assisted paper-based MXene MSC was fabricated by researchers with remarkable energy density. **Fig. 37(e)** represents the laser-assisted fabrication technique over a paper substrate coated with HF-etched MXene[526]. The Meyer rod process was employed for coating the MXene slurry over the paper. The slurry contains a homogeneous mixture of MXene, acetylene black, and PVDF at a ratio of 80:10:10. Benefiting the surface roughness and capillary properties MXene slurry is well dispersed throughout the paper, which is flexible and bendable, portraying excellent adhesion properties. The laser scribing technique removes

the active material and avoids any short-circuiting.1 MSC is fabricated within 17s by direct laser engraving, which paves a fast-manufacturing process. The electrochemical performance of the paper-based MSC was employed under 1M H₂SO₄. **Fig. 37(f)(i-ii)** illustrates the CV and GCD profiles of the printed MSCs, which demonstrate the excellent electrochemical performance of clay-like MXene (Ti₃C₂) as compared to HF-etched MXene. The rectangular CV curves demonstrate the EDL behavior of the printed MSC. The areal capacitance of the clay-type MSC exhibits four times higher capacitance as compared to the HF etched MXene. The higher interlayer spacing is attributed to the enhanced electrochemical performance of the clay-type MXene. **Fig. 37(f)(iv)** illustrates the EIS of the printed MXene MSCs. Clay-type MXene exhibits a parallel impedance curve, with the imaginary Z axis portraying excellent capacitive behavior as compared to HF-etched MXene. The semi-circles of the clay-type-MXene MSCs acquire a charge transfer resistance of 10Ω, which is comparatively lesser than HF-etched MXene, which exhibits a resistance of 15Ω. Over all EIS analysis agrees with the higher electrochemical performance of the printed MSCs. HF etched MXene acquires a specific capacitance of 6.2 mF cm⁻² whereas the clay-type MXene-based MSC exhibits a specific capacitance of 25 mF cm⁻². Further electrochemical performance of the multiple devices is carried out by connecting them in both series and parallel configurations, which demonstrate excellent scalability of the printed MSCs. Overall, this opens up opportunities for fabricating high-performance paper-based printed MXene-MSCs.

Fig. 38(a) depicts the laser-engraved MXene-BP composite MSC with PVA-H₂SO₄ gel electrolyte[528]. The CV curves of the MSC at various scan rates exhibit symmetric quasi-rectangular profiles within a voltage window of 0.8 (**Fig. 38b(i)**). Further GCD curves exhibit symmetric curves at different current densities ranging from 0.69 to 6.9 A cm⁻³. The GCD profiles exhibit excellent capacitive behavior, and the calculated specific capacitance is around 448.43 F g⁻¹. The obtained capacitance outperforms MSCs fabricated with only MXene and BP. The flexible MSC exhibits excellent electrochemical stability from the CV analysis at various bending angles. A capacitance retention of 91.74 % obtained after 10,000 cycles demonstrates the promising electrochemical performance for the long run in wearable and flexible electronics applications. These results elucidate the versatile free-standing composite film with active materials for the fabrication of high-performance flexible MXene-based MSC.

Further researchers have explored N-doped MXene inks for the fabrication of high-performance printed MSCs. **Fig. 38(c)** depicts the fabrication of a 3D architecture obtained from the extrusion printing technique[53]. The N-doped MXene was synthesized by an MF template-assisted printing technique in an inert atmosphere.

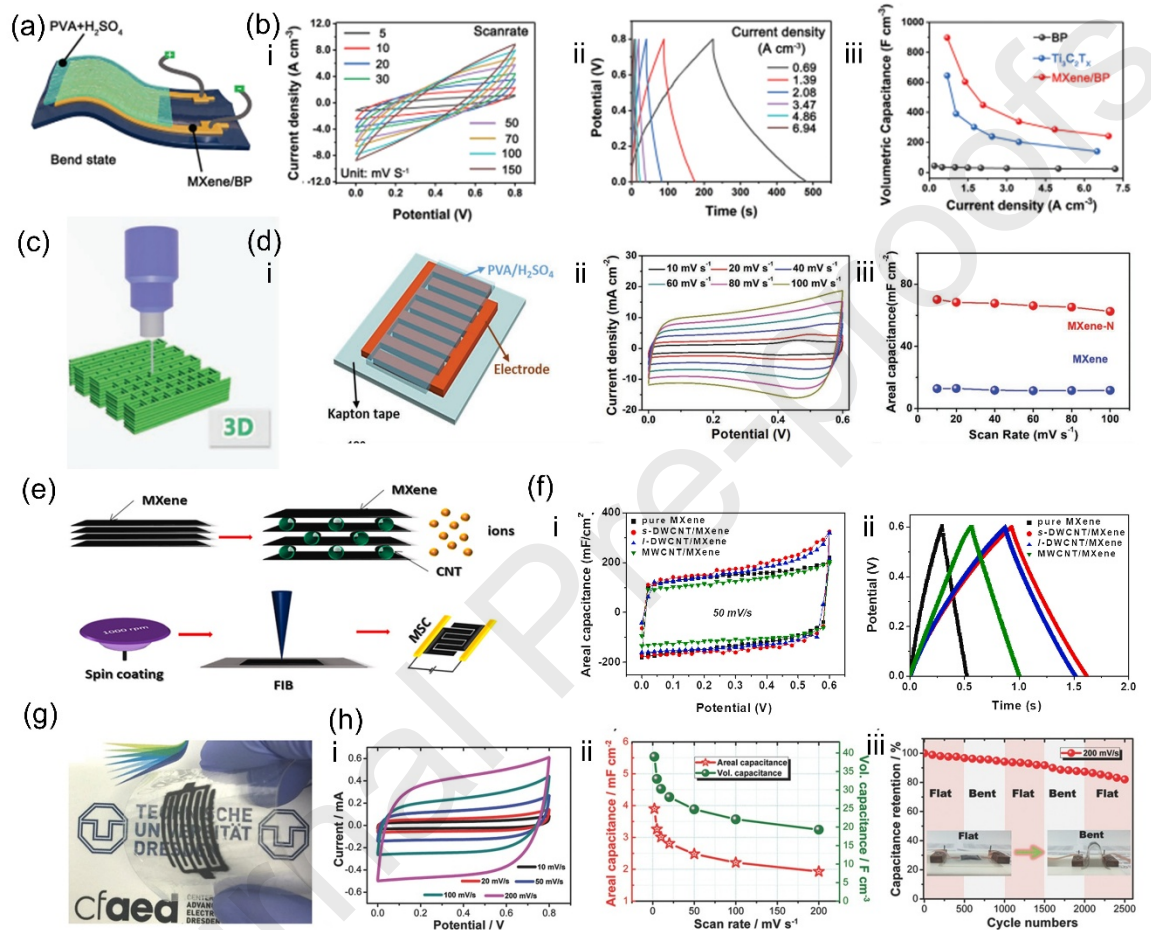


Fig. 38 (a) Schematic illustration of MXene/BP-based MSC with PVA- H_2SO_4 electrolyte (b)i.CV profiles as a function of different scan rates ii. GCD curves at different current densities iii. Volumetric capacitance at different current densities. Reproduced with permission from [170] ©2021WILEY-VCH (c) Schematic representation of extrusion printed pattern (d) i. Schematic representation of all-MXene-based printed MSC ii.CV profiles of all printed MSC at different scan rates iii. Comparative analysis of specific capacitance as a function of scan rates of printed MSCs with MXene and N-MXene inks. Reproduced with permission from [198] ©2019 WILEY-VCH (e) FIB assisted MXene/CNT composite-based MSC fabrication technique (f) i. Comparative analysis of CV profiles at a scan rate of 50mV/s ii. GCD curves of printed MSCs

with different MXene inks. Reproduced with permission from [67] © 2020ElsevierLtd. (g) Pictorial presentation of flexible in-plane MSC based on EG: MXene composite electrodes (h) i.CV curves at different scan rates ii. The specific capacitance at different scan rates iii. Capacitance retention at various bending modes over 2500 cycles. The inset represents the photograph of the flexible MSC in both flat and bend states. Reproduced with permission from [205] © 2016 WILEY-VCH

The synthesized material was further formulated into a printable ink with controlled viscosity for the fabrication of MSC through screen printing with a binder and extrusion printing without a binder. The electrochemical analysis of the MXene ink was carried out by applying a PVA-H₂SO₄ gel electrolyte as shown in **Fig. 38(d)(i)**. CV curves carried out at various scans from 10 -100 mV s⁻¹ exhibit pseudocapacitive behavior of the N-MXene inks. The GCD curves obtained at different current densities illustrate the reversible reaction of the printed MSCs. The comparative areal capacitance of the N-MXene outperforms the specific capacitance of the pristine MScs. The 3D interconnected network, abundant active sites, and tuned ion-conducting paths of the crumpled N-MXene enhance the charge storage behavior of the N-MXene. The N-MXene acquires a specific capacitance of 70.1 mF cm⁻², which is around 5 times higher than the pristine MXene MSC. Along with excellent energy storage performance, the N-MXene exhibits remarkable cyclic stability of 92 % over 7000 cycles. The printed device demonstrates excellent mechanical stability without compromising the electrochemical properties of the printed MSCs. The MSCs can be upscaled by connecting in both series and parallel, which extends the operating windows and widens the applicability of the printed MSCs. This work highlights the optimization of ink rheology for different high-performance MSC printing techniques.

Fig. 38(e) reveals the synthesis technique of few-layer MXene nanosheets and the further fabrication process of IDT MSCs[80]. In-situ leached MXene nanosheets were mixed with CNT to prepare a nanocomposite solution, which was further spin-coated over a Si-substrate. The composite film was exposed to the FIB apparatus to etch out the designated area and fabricate the IDT electrodes. The as-prepared MSCs underwent electrochemical studies after applying PVA-H₂SO₄ gel electrolyte. The comparative CV profiles as shown in **Fig. 38(f)(i)** depict the symmetric curves of different composites, where s-DWCNT exhibits

the highest capacitive performance. The GCD curve of the composites agrees with the higher charge-discharge time demonstrated by s-DWCNT/MXene composite electrodes. The higher electrochemical performance of the s-DWCNT/CNT composites is attributed to the excellent ionic conductivity and narrow gaps between the electrodes. Agglomeration and restacking of MXene in MXene/MWCNT composites result in lesser capacitive performance. Overall, the optimized composite MSC exhibits a remarkable specific capacitance of 317 mF cm^{-2} with a capacitance retention of 32.8% demonstrating the advantage of electronic structure engineering and optimized electrode design. This work explores the possibility of MXene-based hybrids for the fabrication of high-performance on-chip MSCs. MXene-based composites have shown huge potential in the fabrication of high-performance energy storage devices. Tuned and modified stable electronic structure provides abundant electrode-electrolyte interface and porous channels as a path for efficient ion migration.

Fig. 38(g) depicts the real-time image of in-plane MSC fabricated from EGMX hybrid ink. Researchers have employed a solution processing technique for synthesizing MXene-graphene ink for high-performance MSC fabrication[548]. The MXene sheets between graphene layers act as an active material and provide a larger space for the ion shuttling. In addition to this, it prevents the restacking of the graphene sheets. The electrochemical performance of the EG: MXene electrodes represents enhanced electrochemical performance as compared to EG and MXene alone, which delivers a specific capacitance of 184 F cm^{-3} . As in-plane MSCs have huge demand in flexible and on-chip energy storage applications, spray coating was employed to fabricate the flexible MSC over the PET substrate, as shown in **Fig. 38(h)(i)**. The electrochemical performance of the printed MSC under PVA/H₃PO₄ gel electrolyte exhibits symmetric rectangular CV profiles depicting EDLC behavior at various scan rates ranging from 10-200 mV/s (**Fig. 38(h)(ii)**). The MSC acquires a remarkable areal capacitance of 3.26 mF cm^{-2} and volumetric capacitance of 33 F cm^{-3} which exhibits the excellent electrochemical performance of the IDT MScs. Both the areal and volumetric capacitance at various scan rates are depicted in **Fig. 38(h)(iii)**. In addition to this, the MSC attains a capacity retention of 82 % over 2500 cycles with different flat and bend states, which makes it reliable over a long run application. The overall fabrication strategy and compositing

of MXene with exfoliated graphene opens up opportunities for high-performance MSC fabrication utilizing functional composite inks for wearable and flexible applications.

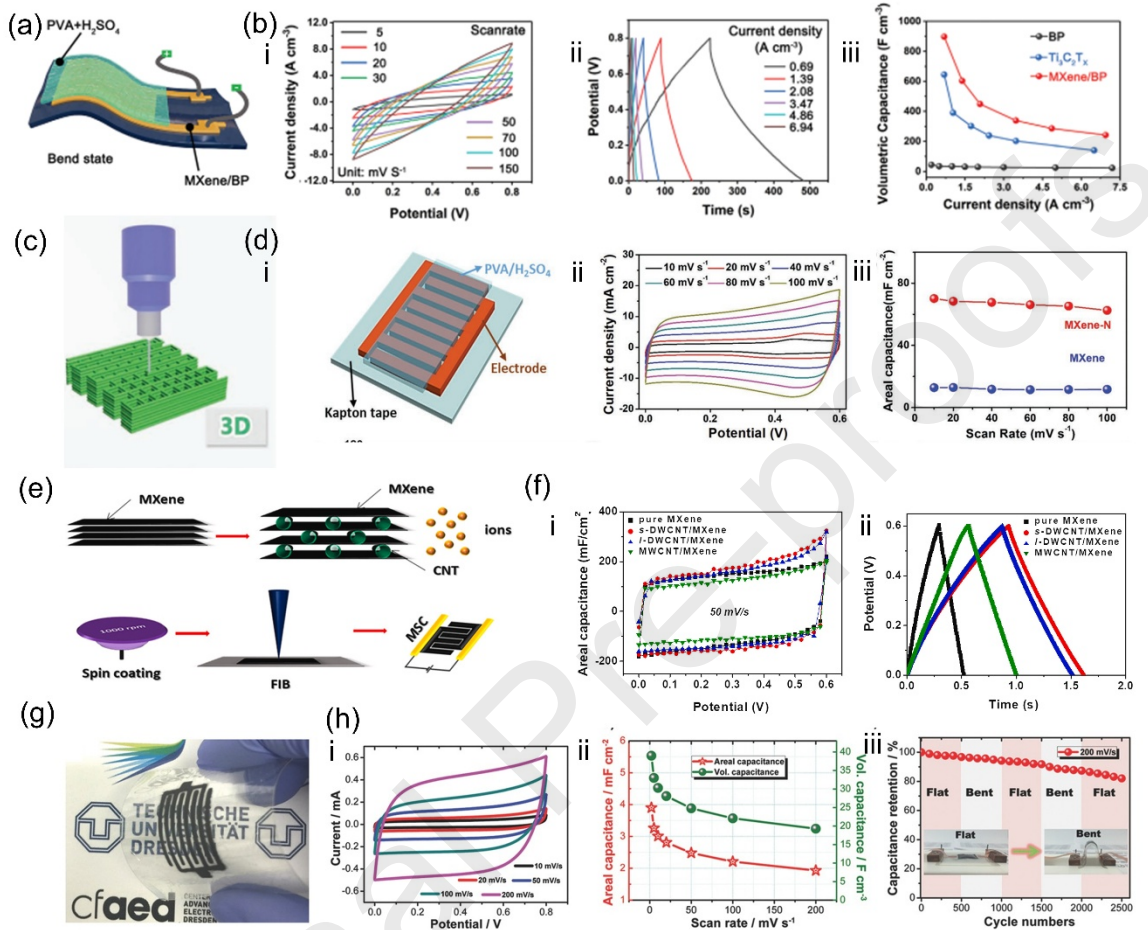


Fig. 39 (a) Demonstration of an MXene-based integrated micro-sensory system. Reproduced with permission from [251] ©2023 WILEY-VCH (b) Specific capacitance retention over 10,000 cycles for MXene electrodes prepared by 8h and 24h sonication time. Reproduced with permission from [237] ©2022 Elsevier (c) Electrochemical performance of MXene thin film electrodes. Reproduced with permission from [102] ©2023 WILEY-VCH (d) Electrochemical performance of 3D printed MXene-based electrodes. Reproduced with permission from [256] ©2024 WILEY-VCH

3D printed MXene-based MSC in water in salt electrolyte exhibited excellent electrochemical performance with a wide potential window of 1.8V[251]. The Water in LiBr electrolyte facilitates ion conduction, limits the decomposition of water, and provides

abundant electrochemically active sites. Benefiting from the increased number of patterns, capacitance increased gradually. The 3D-printed MSC attains a specific capacitance of 4 F cm^{-2} and cyclic stability of 96% after 10,000 cycles. The MSC exhibits excellent electrochemical performance below the freezing point owing to the presence of highly concentrated Liquid in the LiBr electrolyte. **Fig. 39(a)(i-ii)** exhibits the symmetric CD profiles of MSCs connected in series and parallel 5 devices connected in series attain a voltage of 9V, and devices connected in parallel exhibit a linear increase in capacity contributed from the gradual increment of the current ratings. The MSCs exhibited excellent capacitance retention under mechanical fluctuation as well as at various bending angles ranging from 0-180 ° (**Fig. 39(a)(iii)**). Further integration of 3D printed planar MXene-based MSCs was integrated with the humidity sensory system as depicted in **Fig. 39(b)**. The MSC continuously powers the sensory system over repeated cycles. The response value fluctuated between 10.7 % and 8.1 %. The sensor was more susceptible to wet wipes, which attain a response of 65-75 % and make it a reliable printed self-powered sensor. Ultrasound-assisted synthesized MXene with tuned interlayer spacing exhibits an excellent specific capacitance of 270.5 F/g and cyclic stability of 95.52 % over 10,000 cycles. **Fig. 39(b)** represents the capacitance retention for 8 h and 24 h sonicated monolayer MXenes. The multi-layered samples exhibit enhanced capacitance retention owing to the superior chemical stability of the electrolyte. Ultrasound contributes to the efficient etching of MXene, leading to the formation of an accordion-like structure, which also contributes to the 16-fold increment in the specific capacitance due to the smooth ion migration through the layered MXene architecture. The Ti_2VC_2 MXene exhibits excellent pseudo-capacitance contributed by the transition metal oxide and metallic conductivity. The electrochemical analysis carried out in 1M H_2SO_4 exhibits at various scans from 2-100 mV/s[102]. The MXene film attains a specific capacitance of 518 F/g and retains a capacitance. The capacitance retention obtained was about 93 % over 20,000 cycles. The study illustrates the capacitive and diffusive contribution of MXene-based electrodes as shown in **Fig. 39(c)(iii)**. The capacitive contribution was enhanced from 77 % to 88 % by shifting the scan rate from 2mV/s to 20 mV/s. The comparative specific capacitance of different thickness MXene films is portrayed in **Fig. 39(c)(iv)**. The enhanced electrochemical performance is attributed to the vanadium heterostructure and hydrated proton intercalation. Surface functionalized MXene MSC was 3D printed, which exhibits excellent electrochemical performance. The real-time

image of MSC is portrayed in **Fig. 39d (i)** [256]. CV and GCD profiles as shown in **Fig. 39d(ii-iii)** exhibit pseudo-capacitive behavior and symmetric profiles on changing the scan rate. The printed MSC with MXene-C ink exhibits a specific capacitance of 68 mF/cm^2 which is twice the pristine MSC capacitance. The enhanced performance is attributed to the enhanced interlayer spacing and surface-functionalized MXene sheets. The MSC retains a remarkable capacitance retention of 97 % over 10,000 cycles. Additionally, the MSC exhibits constant specific capacitance at various bending angles from $60\text{-}120^\circ$. The excellent flexibility and unmatched electrochemical performance exhibited by the printed MSC make it a suitable candidate for high-performance portable power units. Asymmetric MSC exhibits excellent energy storage properties due to the presence of NiS and nitrogen grafted along the MXene layers. **Fig. 40(a)(i)** depicts the pictorial representation of AMSC comprised of P NiS/N-MX//rGO[349]. The comparative CV profiles exhibit the working window of the AMSC around 1.5 V. The CV profile at different potential windows is exhibited in **Fig. 40(a)(iii)**, which is comparatively larger than the existing MSCs. Further CV and GCD analysis portray the pseudocapacitive behavior of the MXene composite-based electrodes. A linear shift in the current rating was observed in the CV profiles on increasing the scan rates, confirming the enhancement in the capacitance. GCD profiles obtained from different current densities illustrate the symmetric charge-discharge curves with excellent specific capacitance. **Fig. 40(a)(vi)** depicts the areal and volumetric capacitance of MXene MSC measured from GCD curves. The MSC exhibits a remarkable volumetric capacitance of 429 F/cm^3 . The composite ink overcomes the drawback of restacking, and the porous structure provides abundant active sites for fast redox reaction, and printed electrodes reattain the inherent properties of the composites.

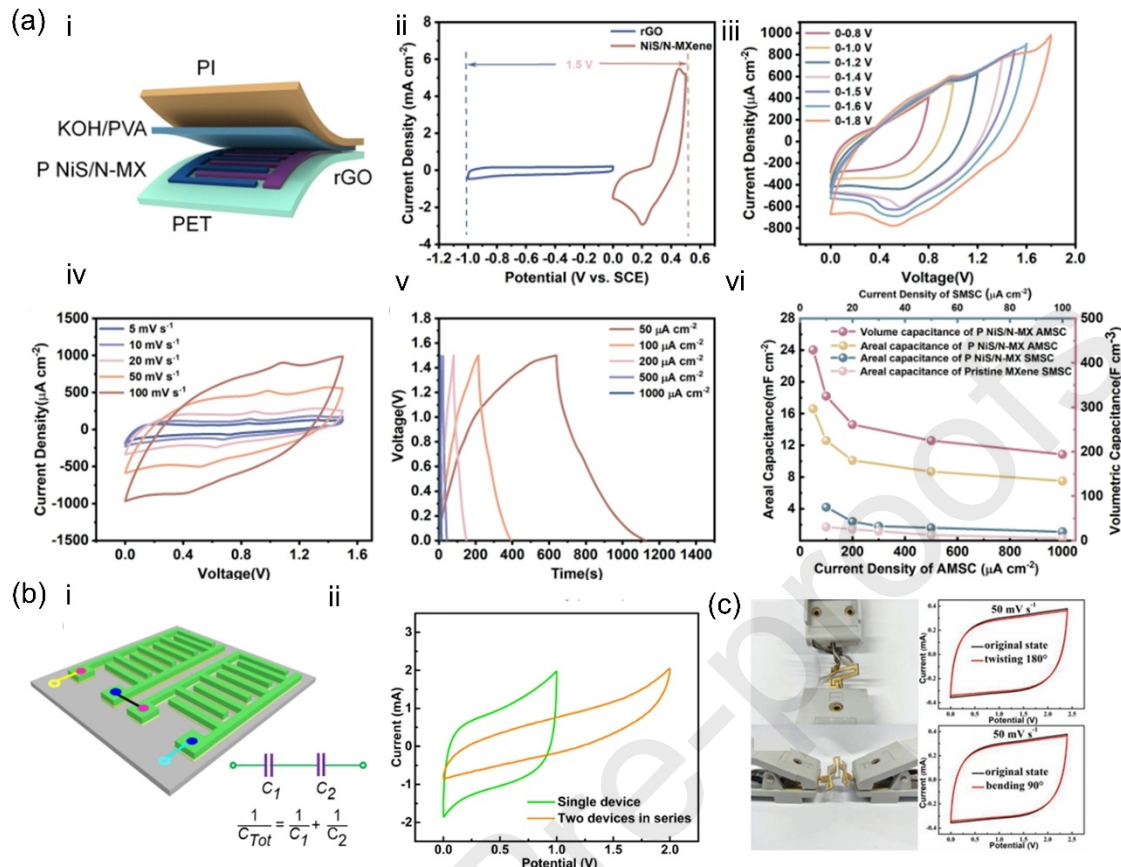


Fig. 40 (a) Pictorial presentation of P NiS/rGO AMSC and corresponding electrochemical performance. Reproduced with permission from [349]©2023 Elsevier (b) (i) Illustration of MXene QD MSCs (ii) CV profile of single and two-MSCs in series. Reproduced with permission from[348] ©2024 Elsevier (c) Illustration of MXene MSC electrochemical performance under bending and twisting. Reproduced with permission from[241] ©2019 WILEY-VCH

Fig. 40(b) illustrates the defect-rich N-doped MXene QD-based MSC[348]. The MSC attains a specific capacitance of 33.1 F/cm³ and excellent cyclic stability over 10,000 cycles. The nano-engineered MXene QDs provide abundant active sites and shorter ion migration paths, resulting in higher specific capacity. **Fig. 40(b)(ii)** illustrates the CV profile of 2-MSCs connected in series, which obtains an extended voltage window of 2V. The structure-engineered MXene offers specific surface and chemical states that contribute to the enhanced electrochemical performance of the MSC due to the quantum confinement, surface defects, and redox-active sites. MXene-based flexible devices exhibit excellent capacitance retention

owing to the mechanical strength and inherent flexibility of MXene sheets. **Fig. 40(c)** exhibits the excellent flexibility of the MXene-based MSC due to the island-bridge architecture. The in-situ recorded CV profiles at a scan rate of 50 mV/s exhibit negligible deviation while twisting at 180° and a bending angle of 90°. MXene/BC composites with the kirigami structure exhibit an areal capacitance of 111.5 mF/cm² with excellent

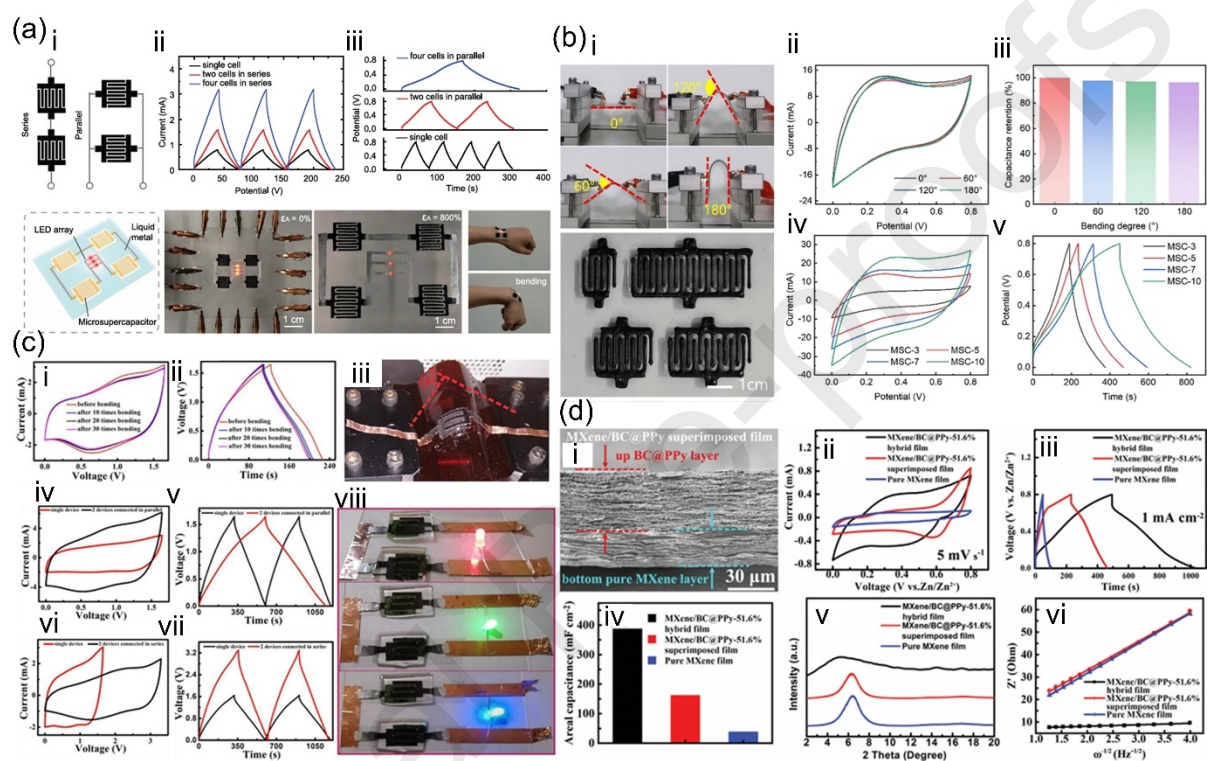


Fig. 41 (a) MXene MSC-based self-powered system and upscaling of MSCs by serial and parallel connection. Reproduced with permission from[249] ©2023 WILEY-VCH. (b) Electrochemical performance of MXene-based flexible MSC under mechanical stimulus. Reproduced with permission from[250] ©2023 Elsevier (c) Electrochemical performance of ZIHMSC and demonstration of energy storage performance of the MSC. Reproduced with permission from [248]©2022 Elsevier (d)Electrochemical performance attributed to BC@PPy reinforcement MXene-based MSC. Reproduced with permission from[247] ©2023WILEY-VCH

Fig. 41(a)(i) illustrates the circuit diagram of 4-MSCs connected to construct the self-powered wearable electronics. The GCD profiles attained by MSCs connected serially and

parallelly are illustrated in **Fig. 41(a)(ii-iii)**. The MSCs connected serially exhibit symmetric charge-discharge curves with a linear increment in the voltage window, keeping the constant coulombic efficiency. Further, a stretchable LED array was attached to MSCs in series. The electronic systems exhibit stable performance under 800 % strain, exhibiting the ultra-stretchability of the energy storage unit. The self-powered electronic system was placed over the wrist, which exhibited stable performance irrespective of hand movements. **Fig. 41(b)** exhibited the stable electrochemical performance of a 3D-printed MXene-based additive-free electrode[250]. The MSC attains a specific capacitance of 2.337 F cm^{-2} with a cyclic retention of 93.1 % over 10,000 cycles. The MXene exhibited excellent structural stability under bending at different angles ranging from 0-180° as depicted from the CV profiles carried out at a scan rate of 5mV/s. The increment of layers leads to the capacitance linearly, as evidenced by the CV and GCD profiles shown in **Fig. 41(b)(v-vi)**. The printed MSCs are connected in series and parallelly to power the LED, depicting the scalability of the 3D printing technique. Flexible Zn ion MXene-based MSC attracts attention due to the realization of excellent energy and power density. PAM hydrogel-based MSC attains a specific capacitance of 129 mF/cm^2 and a capacitance retention of 77 % beyond 10,000 cycles. **Fig. 41(c)** illustrates the electrochemical performance of MXene-based Zn-ion MSC[248]. The flexible MSC exhibits excellent stability under various bending cycles carried out under CV and CD cycles carried out at a scan rate of 10 mV/s and a current density of 1.15 mA/cm^2 . The real-time image of MSC in a bending state proves the excellent flexibility with structural stability. Further integration of 2 devices in series and parallel extends the potential window that enables the MSC to power miniature electronics and LEDs. MSCs lag battery level energy density, which is overcome by researchers by interlayer engineering of MXene. BC@PPy -MXene composite widens the interlayer spacing and prevents the restacking of MXene sheets, which effectively enhances ion and electron transportation, enhancing the specific capacitance up to 388 mF/cm^2 . The structure engineering enhances the capacitance by around 10-fold. The structural stability of the MXene composite favors excellent capacity retention over 25,000 cycles[247]. **Fig. 41(d)(i)** represents the cross-section image of the stable MXene layer supported by the BC@PPy network that enhances the electrochemical performance of the Zn-ion MSC. The comparative electrochemical analysis depicted in **Fig. 41(d)(ii-iii)** represents the enhanced capacitive property of MXene/BC @PPy -51.6 % film as compared to the pure MXene and superimposed

film. The specific capacitance attained by the hybrid film is highest owing to the faster ion migration and enhanced electrochemically active sites. The d-spacing calculated from the XRD analysis suggests the expansion of the interlayer spacing of MXene, which allows smooth migration of ions.

14. Summary and perspective

The excellent electronic structure, electrochemical, and mechanical properties of MXene exhibit great potential in the field of printed energy storage units. The pseudo-capacitance-dominated electrochemical properties outperformed other conventional materials in the micro supercapacitor application. The exceptional demand for micro energy storage devices has broadened the possibility of hybridization of MXene with other active materials like Transition metal dichalcogenides (TMDCs), carbon allotropes, conducting polymers, etc. This strategy, though, enhances the electrochemical performance, and the printability and conductivity of pristine MXene are altered. So, the ink viscosity for high-precision electrode designs is inevitable for printing high-performance MSCs. The fabrication techniques provide enormous opportunities for developing rationally designed electrodes with tuneable electrochemical properties over various substrates. Despite these advantages and advancements in MXene-based MSCs, there are challenges to commercialization and large-scale production. The existing challenges and future directions are summarized below (**Fig. 42**).

- 1. Limited Voltage window.*

A series of MXenes have been explored by researchers for energy storage applications. However, the operating window for MXene-based MSC is limited to 0.6 V, which not only compromises the capacitance but also restricts the widespread application. To overcome this issue, electronic structure modification and hybridization of the material with other electroactive materials are desired to extend the potential window of the MSC. This will boost the capacitance and enhance the energy density of the printed MSC.

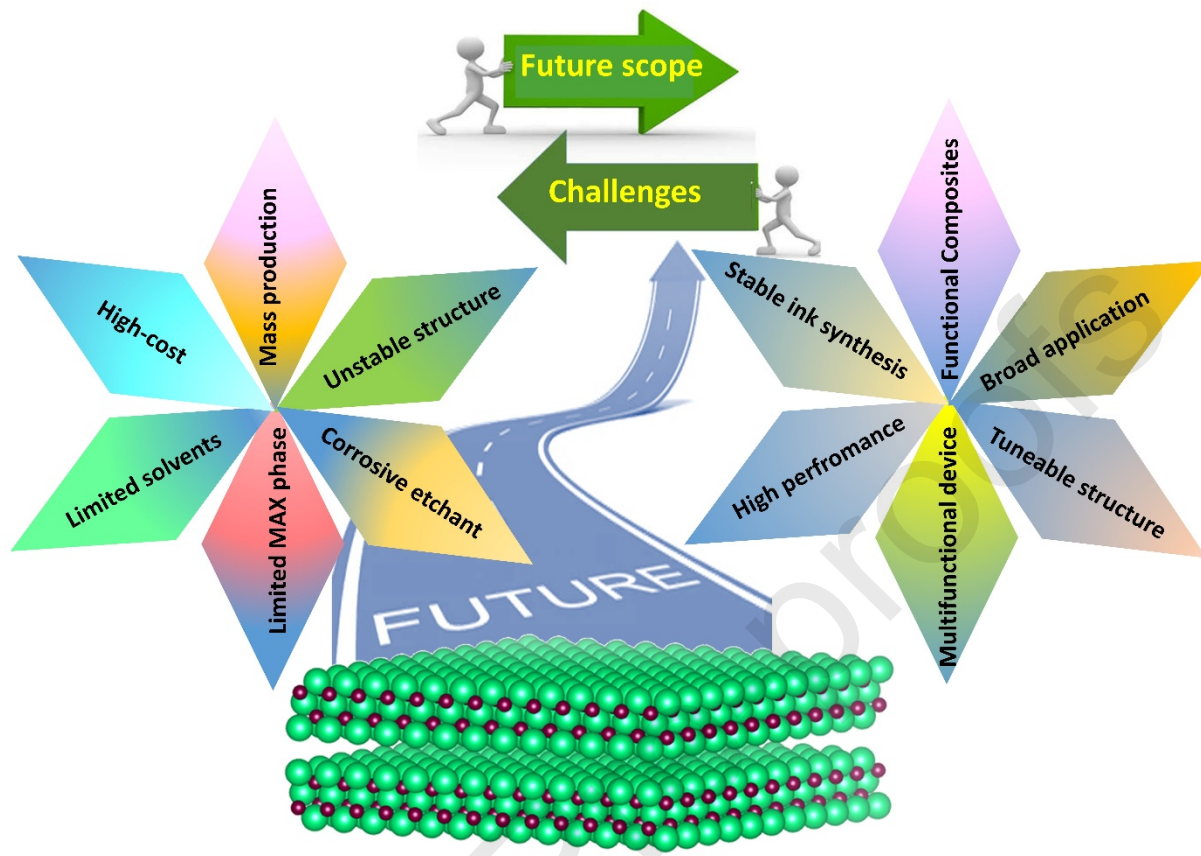


Fig. 42 Challenges and Future Prospects of MXene-based MSCs in Next-generation high-performance Energy Storage Application

2. Material stability.

MXene, though, acquires an excellent electronic structure with abundant porosity and excellent electrical conductivity, the sheet-like structure suffers restacking that hinders the ion migration and reduces the electrochemical performance. MXene ink is also prone to oxidation, reduces the cycle life and needs to be stored in an inert atmosphere.

3. Rheology optimization.

MXene exhibits excellent dispersibility in a wide range of solvents owing to the superhydrophobic sheets and negative zeta potential. However, flake size and sheet thickness affect the viscosity and rheology. So, the standardization in synthesis techniques for high-quality ink formulation is lacking in the current situation. Some important synthesis

techniques with constant rheological parameters can help in the large-scale synthesis of high-quality ink for high-performance MSC fabrication.

4. Simulation modeling and Numerical analysis.

MXene ink formulation and experimental analysis is a time-consuming and costly process that needs to be synchronized with numerical studies like simulation and modeling. Software-assisted analysis can simulate the electronic structure and guide for formulation of high-quality ink. In addition to this desired electrochemical performance can be attained by grafting composite additives that can be analyzed promptly by numerical analysis and density function theories (DFT). Further, the electrode architecture can be optimized for higher electrochemical performance.

5. Integrated energy system development.

MXene MSCs though, exhibit excellent electrochemical performance the integration of MSCs with other electronics is challenging due to structural constraints. So, resolution electrodes with printed circuitry can open up paths for the successful integration of MXene MSCs with other energy harvesters as well as microelectronics. This concept can be beneficial for on-chip storage and functional device fabrication for next-generation IoT and wearable electronics fabrication.

6. Self-powered system development.

The high-performance MXene MSCs need a power source to be charged efficiently. Coupling of the MSCs with various energy sources enables to construction self-powered energy system. Solar, wind, nanogenerators, etc, can be integrated with the MSCs to construct a self-powered energy system, benefiting from the fast-charging ability of the energy system.

7. Smart MSCs.

MXene, being an excellent material for energy storage, also has the potential to explore its applicability for smart applications like photochromic, self-healing, shape-memory, and EMI shielding properties for multi-functional applicability not limited to energy storage.

8. Commercialization of MXene MSC

MXene has huge potential for commercialization only if it overcomes the limitations in scalable synthesis techniques, oxidation prevention, and is economical to procure. Low-cost HF-free green synthesis technique can be up-scaled economically without compromising the inherent electrochemical properties. Benefiting from these advanced microfabrication techniques, like inkjet printing, extrusion printing, and roll-to-roll manufacturing process, can pave the pathway one step forward for commercialization. Addressing the aforementioned bottlenecks with start-ups and industrial collaboration for optimization and prototyping of MXene-based MSC can be the road map to bring MXene from the laboratory to market.

Acknowledgment

This work was supported by the Basic Science Research Program (RS-2023-NR077252) & Regional Leading Research Center (RS-2024-00405278) through the National Research Foundation of Korea (NRF) grant funded by the Korea Government (MSIT).

References

- [1] K. Dissanayake and D. Kularatna-Abeywardana, "A review of supercapacitors: Materials, technology, challenges, and renewable energy applications," *J Energy Storage*, vol. 96, p. 112563, Aug. 2024, doi: 10.1016/j.est.2024.112563.
- [2] A. Abdisattar *et al.*, "Recent advances and challenges of current collectors for supercapacitors," *Electrochim commun*, vol. 142, p. 107373, Sep. 2022, doi: 10.1016/j.elecom.2022.107373.
- [3] P. Lamba *et al.*, "Recent advancements in supercapacitors based on different electrode materials: classifications, synthesis methods and comparative performance," *J Energy Storage*, vol. 48, p. 103871, 2022.
- [4] P. Sharma and V. Kumar, "Current technology of supercapacitors: A review," *J Electron Mater*, vol. 49, no. 6, pp. 3520–3532, 2020.

- [5] S. A. Delbari *et al.*, "Transition metal oxide-based electrode materials for flexible supercapacitors: A review," *J Alloys Compd*, vol. 857, p. 158281, 2021.
- [6] Y. Wang *et al.*, "Phosphidated Ni-Mn layered double hydroxide-based electrode material with superior electrochemical performance for supercapacitors," *J Energy Storage*, vol. 44, p. 103311, 2021, doi: <https://doi.org/10.1016/j.est.2021.103311>.
- [7] Y. Wang *et al.*, "Supercapacitor devices based on graphene materials," *The Journal of Physical Chemistry C*, vol. 113, no. 30, pp. 13103–13107, 2009.
- [8] R. Dubey and V. Guruviah, "Review of carbon-based electrode materials for supercapacitor energy storage," *Ionics (Kiel)*, vol. 25, no. 4, pp. 1419–1445, 2019.
- [9] B. Xu, H. Zhang, H. Mei, and D. Sun, "Recent progress in metal-organic framework-based supercapacitor electrode materials," *Coord Chem Rev*, vol. 420, p. 213438, Oct. 2020, doi: [10.1016/j.ccr.2020.213438](https://doi.org/10.1016/j.ccr.2020.213438).
- [10] H. Chen, L. Hu, M. Chen, Y. Yan, and L. Wu, "Nickel-Cobalt Layered Double Hydroxide Nanosheets for High-performance Supercapacitor Electrode Materials," *Adv Funct Mater*, vol. 24, no. 7, pp. 934–942, Feb. 2014, doi: [10.1002/adfm.201301747](https://doi.org/10.1002/adfm.201301747).
- [11] S. Panda, K. Deshmukh, S. K. Khadheer Pasha, J. Theerthagiri, S. Manickam, and M. Y. Choi, "MXene based emerging materials for supercapacitor applications: Recent advances, challenges, and future perspectives," *Coord Chem Rev*, vol. 462, p. 214518, Jul. 2022, doi: [10.1016/j.ccr.2022.214518](https://doi.org/10.1016/j.ccr.2022.214518).
- [12] S. Kumar, G. Saeed, L. Zhu, K. N. Hui, N. H. Kim, and J. H. Lee, "0D to 3D carbon-based networks combined with pseudocapacitive electrode material for high energy density supercapacitor: A review," *Chemical Engineering Journal*, vol. 403, p. 126352, Jan. 2021, doi: [10.1016/j.cej.2020.126352](https://doi.org/10.1016/j.cej.2020.126352).
- [13] H. Li and J. Liang, "Recent Development of Printed Micro-Supercapacitors: Printable Materials, Printing Technologies, and Perspectives," Jan. 01, 2020, *Wiley-VCH Verlag*. doi: [10.1002/adma.201805864](https://doi.org/10.1002/adma.201805864).
- [14] W. Zhao, M. Jiang, W. Wang, S. Liu, W. Huang, and Q. Zhao, "Flexible Transparent Supercapacitors: Materials and Devices," *Adv Funct Mater*, vol. 31, no. 11, Mar. 2021, doi: [10.1002/adfm.202009136](https://doi.org/10.1002/adfm.202009136).
- [15] S. Venkateshalu and A. N. Grace, "MXenes—A new class of 2D layered materials: Synthesis, properties, applications as supercapacitor electrode and beyond," *Appl Mater Today*, vol. 18, p. 100509, Mar. 2020, doi: [10.1016/j.apmt.2019.100509](https://doi.org/10.1016/j.apmt.2019.100509).
- [16] M. A. Bissett, S. D. Worrall, I. A. Kinloch, and R. A. W. Dryfe, "Comparison of Two-Dimensional Transition Metal Dichalcogenides for Electrochemical Supercapacitors," *Electrochim Acta*, vol. 201, pp. 30–37, May 2016, doi: [10.1016/j.electacta.2016.03.190](https://doi.org/10.1016/j.electacta.2016.03.190).

- [17] X. Liu, R. Ma, Y. Bando, and T. Sasaki, "A General Strategy to Layered Transition-Metal Hydroxide Nanocones: Tuning the Composition for High Electrochemical Performance," *Advanced Materials*, vol. 24, no. 16, pp. 2148–2153, Apr. 2012, doi: 10.1002/adma.201104753.
- [18] H. Yi *et al.*, "Recent Advance of Transition-Metal-Based Layered Double Hydroxide Nanosheets: Synthesis, Properties, Modification, and Electrocatalytic Applications," *Adv Energy Mater*, vol. 11, no. 14, p. 2002863, Apr. 2021, doi: 10.1002/aenm.202002863.
- [19] J. P. Das, S. S. Nardekar, D. Kesavan, K. Bhunia, V. Ravichandran, and S.-J. Kim, "Unveiling the effect of growth time on bifunctional layered hydroxide electrodes for high-performance energy storage and green energy conversion," *J Mater Chem A Mater*, vol. 12, no. 31, pp. 20179–20190, 2024, doi: 10.1039/D4TA02940B.
- [20] X. Wang, F. Huang, F. Rong, P. He, R. Que, and S. P. Jiang, "Unique MOF-derived hierarchical MnO₂ nanotubes@NiCo-LDH/CoS₂ nanocage materials as high performance supercapacitors," *J Mater Chem A Mater*, vol. 7, no. 19, pp. 12018–12028, 2019, doi: 10.1039/C9TA01951K.
- [21] Z. Zhang *et al.*, "Exquisitely functionalized porphyrin-COF self-supporting nanofilm for high-performance in-plane micro-supercapacitor," *Appl Surf Sci*, vol. 680, p. 161327, Jan. 2025, doi: 10.1016/j.apsusc.2024.161327.
- [22] N. An *et al.*, "A novel COF/MXene film electrode with fast redox kinetics for high-performance flexible supercapacitor," *Chemical Engineering Journal*, vol. 458, p. 141434, Feb. 2023, doi: 10.1016/j.cej.2023.141434.
- [23] Z. Li *et al.*, "Tailoring the thermal conductivity of Poly(dimethylsiloxane)/Hexagonal boron nitride composite," *Polymer (Guildf)*, vol. 177, no. April, pp. 262–273, 2019, doi: 10.1016/j.polymer.2019.06.012.
- [24] J. Chen, X. Huang, B. Sun, Y. Wang, Y. Zhu, and P. Jiang, "Vertically Aligned and Interconnected Boron Nitride Nanosheets for Advanced Flexible Nanocomposite Thermal Interface Materials," *ACS Appl Mater Interfaces*, vol. 9, no. 36, pp. 30909–30917, 2017, doi: 10.1021/acsami.7b08061.
- [25] S. Venkateshalu *et al.*, "Phosphorene, antimonene, silicene and siloxene based novel 2D electrode materials for supercapacitors-A brief review," *J Energy Storage*, vol. 48, p. 104027, Apr. 2022, doi: 10.1016/j.est.2022.104027.
- [26] Q. Zhou, W. Ju, Y. Yong, Y. Liu, and J. Li, "Quantum capacitance of supercapacitor electrodes based on germanene influenced by vacancy and co-doping: A first-principles study," *Comput Mater Sci*, vol. 188, p. 110131, Feb. 2021, doi: 10.1016/j.commatsci.2020.110131.

- [27] A. Zia, Z.-P. Cai, A. B. Naveed, J.-S. Chen, and K.-X. Wang, "MXene, silicene and germanene: preparation and energy storage applications," *Mater Today Energy*, vol. 30, p. 101144, Dec. 2022, doi: 10.1016/j.mtener.2022.101144.
- [28] J. Wei, M. Sajjad, J. Zhang, D. Li, and Z. Mao, "The rise of novel 2D materials beyond graphene: A comprehensive review of their potential as supercapacitor electrodes," *Surfaces and Interfaces*, vol. 42, p. 103334, Nov. 2023, doi: 10.1016/j.surfin.2023.103334.
- [29] E. Redondo and M. Pumera, "MXene-functionalised 3D-printed electrodes for electrochemical capacitors," *Electrochim commun*, vol. 124, p. 106920, 2021, doi: 10.1016/j.elecom.2021.106920.
- [30] J. Zhang, S. Seyedin, Z. Gu, W. Yang, X. Wang, and J. M. Razal, "MXene: A potential candidate for yarn supercapacitors," *Nanoscale*, vol. 9, no. 47, pp. 18604–18608, 2017, doi: 10.1039/c7nr06619h.
- [31] M. M. Baig, I. H. Gul, S. M. Baig, and F. Shahzad, "2D MXenes: Synthesis, properties, and electrochemical energy storage for supercapacitors—A review," *Journal of Electroanalytical Chemistry*, vol. 904, p. 115920, 2022.
- [32] V. Navakoteswara Rao *et al.*, "Synergistic integration of MXene nanosheets with CdS@TiO₂ core@shell S-scheme photocatalyst for augmented hydrogen generation," *Chemical Engineering Journal*, vol. 471, p. 144490, Sep. 2023, doi: 10.1016/j.cej.2023.144490.
- [33] C. Zhan, M. Naguib, M. Lukatskaya, P. R. C. Kent, Y. Gogotsi, and D. Jiang, "Understanding the MXene Pseudocapacitance," *J Phys Chem Lett*, vol. 9, no. 6, pp. 1223–1228, Mar. 2018, doi: 10.1021/acs.jpclett.8b00200.
- [34] X. Zhan, C. Si, J. Zhou, and Z. Sun, "MXene and MXene-based composites: synthesis, properties and environment-related applications," *Nanoscale Horiz*, vol. 5, no. 2, pp. 235–258, 2020, doi: 10.1039/C9NH00571D.
- [35] J.-C. Lei, X. Zhang, and Z. Zhou, "Recent advances in MXene: Preparation, properties, and applications," *Front Phys (Beijing)*, vol. 10, no. 3, pp. 276–286, Jun. 2015, doi: 10.1007/s11467-015-0493-x.
- [36] J. V. Vaghasiya, C. C. Mayorga-Martinez, Z. Sofer, and M. Pumera, "MXene-Based Flexible Supercapacitors: Influence of an Organic Ionic Conductor Electrolyte on the Performance," *ACS Appl Mater Interfaces*, vol. 12, no. 47, pp. 53039–53048, 2020, doi: 10.1021/acsami.0c12879.
- [37] Y. Li, Z. Lu, B. Xin, Y. Liu, Y. Cui, and Y. Hu, "All-solid-state flexible supercapacitor of Carbonized MXene/Cotton fabric for wearable energy storage," *Appl Surf Sci*, vol. 528, p. 146975, 2020, doi: 10.1016/j.apsusc.2020.146975.
- [38] A. Levitt, J. Zhang, G. Dion, Y. Gogotsi, and J. M. Razal, "MXene-Based Fibers, Yarns, and Fabrics for Wearable Energy Storage Devices," *Adv Funct Mater*, vol. 30, no. 47, 2020, doi: 10.1002/adfm.202000739.

- [39] Y. Xie *et al.*, "High-voltage asymmetric MXene-based on-chip micro-supercapacitors," *Nano Energy*, vol. 74, Aug. 2020, doi: 10.1016/j.nanoen.2020.104928.
- [40] P. Eghbali, A. Hassani, S. Wactawek, K.-Y. Andrew Lin, Z. Sayyar, and F. Ghanbari, "Recent advances in design and engineering of MXene-based catalysts for photocatalysis and persulfate-based advanced oxidation processes: A state-of-the-art review," *Chemical Engineering Journal*, vol. 480, p. 147920, Jan. 2024, doi: 10.1016/j.cej.2023.147920.
- [41] Y. Wang, T. Guo, Z. Tian, K. Bibi, Y. Zhang, and H. N. Alshareef, "MXenes for Energy Harvesting," *Advanced Materials*, vol. 34, no. 21, May 2022, doi: 10.1002/adma.202108560.
- [42] Y. Gogotsi and Q. Huang, "MXenes: Two-Dimensional Building Blocks for Future Materials and Devices," *ACS Nano*, vol. 15, no. 4, pp. 5775–5780, Apr. 2021, doi: 10.1021/acsnano.1c03161.
- [43] M. S. Javed *et al.*, "The Emergence of 2D MXenes Based Zn-Ion Batteries: Recent Development and Prospects," *Small*, vol. 18, no. 26, Jul. 2022, doi: 10.1002/smll.202201989.
- [44] S. Siddique *et al.*, "Fluorine-free MXenes via molten salt Lewis acidic etching: Applications, challenges, and future outlook," *Prog Mater Sci*, vol. 139, p. 101183, Oct. 2023, doi: 10.1016/j.pmatsci.2023.101183.
- [45] F. Ezzah Ab Latif *et al.*, "Evolution of MXene and its 2D heterostructure in electrochemical sensor applications," *Coord Chem Rev*, vol. 471, p. 214755, Nov. 2022, doi: 10.1016/j.ccr.2022.214755.
- [46] J. Sun, K. Gao, X. Lin, C. Gao, D. Ti, and Z. Zhang, "Laser-Assisted Fabrication of Microphotocapacitors with High Energy Density and Output Voltage," *ACS Appl Mater Interfaces*, vol. 13, no. 1, pp. 419–428, Jan. 2021, doi: 10.1021/acsami.0c16677.
- [47] J. Zhang, G. Zhang, T. Zhou, and S. Sun, "Recent Developments of Planar Micro-Supercapacitors: Fabrication, Properties, and Applications," *Adv Funct Mater*, vol. 30, no. 19, p. 1910000, May 2020, doi: 10.1002/adfm.201910000.
- [48] J. Li *et al.*, "Scalable Fabrication and Integration of Graphene Microsupercapacitors through Full Inkjet Printing," *ACS Nano*, vol. 11, no. 8, pp. 8249–8256, Aug. 2017, doi: 10.1021/acsnano.7b03354.
- [49] X. D. Zhu *et al.*, "Laser-assisted one-step fabrication of interlayer-spacing-regulated three-dimensional MXene-based micro-supercapacitors," *Chemical Engineering Journal*, vol. 483, Mar. 2024, doi: 10.1016/j.cej.2024.149253.
- [50] J. Orangi, F. Hamade, V. A. Davis, and M. Beidaghi, "3D Printing of Additive-Free 2D $Ti_3C_2T_x$ (MXene) Ink for Fabrication of Micro-Supercapacitors with Ultra-High Energy Densities," *ACS Nano*, vol. 14, no. 1, pp. 640–650, Jan. 2020, doi: 10.1021/acsnano.9b07325.

- [51] S. Uzun *et al.*, "Additive-Free Aqueous MXene Inks for Thermal Inkjet Printing on Textiles," *Small*, vol. 17, no. 1, Jan. 2021, doi: 10.1002/smll.202006376.
- [52] B. Zazoum, A. Bachri, and J. Nayfeh, "Functional 2D MXene Inks for Wearable Electronics," *Materials*, vol. 14, no. 21, p. 6603, Nov. 2021, doi: 10.3390/ma14216603.
- [53] L. Yu, Z. Fan, Y. Shao, Z. Tian, J. Sun, and Z. Liu, "Versatile N-Doped MXene Ink for Printed Electrochemical Energy Storage Application," *Adv Energy Mater*, vol. 9, no. 34, p. 1901839, Sep. 2019, doi: 10.1002/aenm.201901839.
- [54] C. J. Zhang *et al.*, "Additive-free MXene inks and direct printing of micro-supercapacitors," *Nat Commun*, vol. 10, no. 1, pp. 1–9, 2019.
- [55] D. Wen *et al.*, "Inkjet Printing Transparent and Conductive MXene (Ti₃C₂Tx) Films: A Strategy for Flexible Energy Storage Devices," *ACS Appl Mater Interfaces*, vol. 13, no. 15, pp. 17766–17780, 2021, doi: 10.1021/acsami.1c00724.
- [56] G. Zou *et al.*, "3D-printed zn-ion hybrid capacitor enabled by universal divalent cation-gelated additive-free Ti₃C₂ mxene ink," *ACS Nano*, vol. 15, no. 2, pp. 3098–3107, 2021, doi: 10.1021/acsnano.0c09646.
- [57] H. Li, X. Li, J. Liang, and Y. Chen, "Hydrous RuO₂ -Decorated MXene Coordinating with Silver Nanowire Inks Enabling Fully Printed Micro-Supercapacitors with Extraordinary Volumetric Performance," *Adv Energy Mater*, vol. 9, no. 15, Apr. 2019, doi: 10.1002/aenm.201803987.
- [58] S. Abdolhosseinzadeh, R. Schneider, A. Verma, J. Heier, F. Nüesch, and C. Zhang, "Turning Trash into Treasure: Additive Free MXene Sediment Inks for Screen-Printed Micro-Supercapacitors," *Advanced Materials*, vol. 32, no. 17, 2020, doi: 10.1002/adma.202000716.
- [59] J. Li *et al.*, "MXene-conducting polymer electrochromic microsupercapacitors," *Energy Storage Mater*, vol. 20, pp. 455–461, Jul. 2019, doi: 10.1016/j.ensm.2019.04.028.
- [60] Y. Zhou *et al.*, "Ti₃C₂Tx MXene-Reduced Graphene Oxide Composite Electrodes for Stretchable Supercapacitors," *ACS Nano*, vol. 14, no. 3, pp. 3576–3586, 2020, doi: 10.1021/acsnano.9b10066.
- [61] B. Akuzum *et al.*, "Rheological Characteristics of 2D Titanium Carbide (MXene) Dispersions: A Guide for Processing MXenes," *ACS Nano*, vol. 12, no. 3, pp. 2685–2694, Mar. 2018, doi: 10.1021/acsnano.7b08889.
- [62] J. Zhang *et al.*, "Additive-Free MXene Liquid Crystals and Fibers," *ACS Cent Sci*, vol. 6, no. 2, pp. 254–265, Feb. 2020, doi: 10.1021/acscentsci.9b01217.
- [63] P. Das and Z.-S. Wu, "MXene for energy storage: present status and future perspectives," *Journal of Physics: Energy*, vol. 2, no. 3, p. 032004, Jul. 2020, doi: 10.1088/2515-7655/ab9b1d.

- [64] J. S. Nah *et al.*, "A wearable microfluidics-integrated impedimetric immunosensor based on Ti₃C₂Tx MXene incorporated laser-burned graphene for noninvasive sweat cortisol detection," *Sens Actuators B Chem*, vol. 329, no. November, p. 129206, 2021, doi: 10.1016/j.snb.2020.129206.
- [65] Q. Li *et al.*, "Microsupercapacitors: Femtosecond Laser-Etched MXene Microsupercapacitors with Double-Side Configuration via Arbitrary On- and Through-Substrate Connections (Adv. Energy Mater. 24/2020)," *Adv Energy Mater*, vol. 10, no. 24, Jun. 2020, doi: 10.1002/aenm.202070104.
- [66] M. Li *et al.*, "3D Printed Supercapacitor: Techniques, Materials, Designs, and Applications," *Adv Funct Mater*, vol. 33, no. 1, Jan. 2023, doi: 10.1002/adfm.202208034.
- [67] X. Yan, Y. Tong, X. Wang, F. Hou, and J. Liang, "Extrusion-Based 3D-Printed Supercapacitors: Recent Progress and Challenges," *Energy & Environmental Materials*, 2022.
- [68] A. Chiolerio, S. Bocchini, and S. Porro, "Inkjet printed negative supercapacitors: synthesis of polyaniline-based inks, doping agent effect, and advanced electronic devices applications," *Adv Funct Mater*, vol. 24, no. 22, pp. 3375–3383, 2014.
- [69] M. H. Ervin, L. T. Le, and W. Y. Lee, "Inkjet-printed flexible graphene-based supercapacitor," *Electrochim Acta*, vol. 147, pp. 610–616, 2014.
- [70] M. Idrees, S. Ahmed, Z. Mohammed, N. S. Korivi, and V. Rangari, "3D printed supercapacitor using porous carbon derived from packaging waste," *Addit Manuf*, vol. 36, p. 101525, Dec. 2020, doi: 10.1016/j.addma.2020.101525.
- [71] L. Li, Z. Lou, W. Han, D. Chen, K. Jiang, and G. Shen, "Highly Stretchable Micro-Supercapacitor Arrays with Hybrid MWCNT/PANI Electrodes," *Adv Mater Technol*, vol. 2, no. 3, p. 1600282, Mar. 2017, doi: 10.1002/admt.201600282.
- [72] Y.-Y. Peng *et al.*, "All-MXene (2D titanium carbide) solid-state microsupercapacitors for on-chip energy storage," *Energy Environ Sci*, vol. 9, no. 9, pp. 2847–2854, 2016, doi: 10.1039/C6EE01717G.
- [73] H. Hu and T. Hua, "An easily manipulated protocol for patterning of MXenes on paper for planar micro-supercapacitors," *J Mater Chem A Mater*, vol. 5, no. 37, pp. 19639–19648, 2017, doi: 10.1039/C7TA04735E.
- [74] Q. Yang *et al.*, "MXene/graphene hybrid fibers for high performance flexible supercapacitors," *J. Mater. Chem. A*, vol. 5, no. 42, pp. 22113–22119, 2017, doi: 10.1039/C7TA07999K.
- [75] P. Salles, E. Quain, N. Kurra, A. Sarycheva, and Y. Gogotsi, "Automated Scalpel Patterning of Solution Processed Thin Films for Fabrication of Transparent MXene Microsupercapacitors," *Small*, vol. 14, no. 44, Nov. 2018, doi: 10.1002/smll.201802864.

- [76] S. Xu, Y. Dall’Agnese, G. Wei, C. Zhang, Y. Gogotsi, and W. Han, “Screen-printable microscale hybrid device based on MXene and layered double hydroxide electrodes for powering force sensors,” *Nano Energy*, vol. 50, pp. 479–488, Aug. 2018, doi: 10.1016/j.nanoen.2018.05.064.
- [77] W. Yang *et al.*, “3D Printing of Freestanding MXene Architectures for Current-Collector-Free Supercapacitors,” *Advanced Materials*, vol. 31, no. 37, Sep. 2019, doi: 10.1002/adma.201902725.
- [78] L. Qin *et al.*, “Polymer-MXene composite films formed by MXene-facilitated electrochemical polymerization for flexible solid-state microsupercapacitors,” *Nano Energy*, vol. 60, pp. 734–742, Jun. 2019, doi: 10.1016/j.nanoen.2019.04.002.
- [79] S. Zheng *et al.*, “Multitasking MXene Inks Enable High-Performance Printable Microelectrochemical Energy Storage Devices for All-Flexible Self-Powered Integrated Systems,” *Advanced Materials*, vol. 33, no. 10, Mar. 2021, doi: 10.1002/adma.202005449.
- [80] E. Kim *et al.*, “Microsupercapacitor with a 500 nm gap between MXene/CNT electrodes,” *Nano Energy*, vol. 81, Mar. 2021, doi: 10.1016/j.nanoen.2020.105616.
- [81] Z. Cao, J. Fu, M. Wu, T. Hua, and H. Hu, “Synchronously manipulating Zn²⁺ transfer and hydrogen/oxygen evolution kinetics in MXene host electrodes toward symmetric Zn-ions micro-supercapacitor with enhanced areal energy density,” *Energy Storage Mater*, vol. 40, pp. 10–21, Sep. 2021, doi: 10.1016/j.ensm.2021.04.047.
- [82] K. Hantanasirisakul *et al.*, “Effects of Synthesis and Processing on Optoelectronic Properties of Titanium Carbonitride MXene,” *Chemistry of Materials*, vol. 31, no. 8, pp. 2941–2951, Apr. 2019, doi: 10.1021/acs.chemmater.9b00401.
- [83] H. Chen, Y. Wen, Y. Qi, Q. Zhao, L. Qu, and C. Li, “Pristine Titanium Carbide MXene Films with Environmentally Stable Conductivity and Superior Mechanical Strength,” *Adv Funct Mater*, vol. 30, no. 5, Jan. 2020, doi: 10.1002/adfm.201906996.
- [84] J. Wang *et al.*, “Highly Conductive MXene Film Actuator Based on Moisture Gradients,” *Angewandte Chemie - International Edition*, vol. 59, no. 33, pp. 14029–14033, Aug. 2020, doi: 10.1002/anie.202003737.
- [85] C. J. Zhang *et al.*, “Transparent, Flexible, and Conductive 2D Titanium Carbide (MXene) Films with High Volumetric Capacitance,” *Advanced Materials*, vol. 29, no. 36, Sep. 2017, doi: 10.1002/adma.201702678.
- [86] R. M. Ronchi, J. T. Arantes, and S. F. Santos, “Synthesis, structure, properties and applications of MXenes: Current status and perspectives,” Oct. 15, 2019, Elsevier Ltd. doi: 10.1016/j.ceramint.2019.06.114.
- [87] K. S. Novoselov *et al.*, “Electric Field Effect in Atomically Thin Carbon Films,” *Science* (1979), vol. 306, no. 5696, pp. 666–669, Oct. 2004, doi: 10.1126/science.1102896.

- [88] M. Khazaei, A. Ranjbar, K. Esfarjani, D. Bogdanovski, R. Dronskowski, and S. Yunoki, "Insights into exfoliation possibility of MAX phases to MXenes," *Physical Chemistry Chemical Physics*, vol. 20, no. 13, pp. 8579–8592, 2018, doi: 10.1039/C7CP08645H.
- [89] M. Naguib *et al.*, "Two-Dimensional Transition Metal Carbides," *ACS Nano*, vol. 6, no. 2, pp. 1322–1331, Feb. 2012, doi: 10.1021/nn204153h.
- [90] M. Alhabeb *et al.*, "Guidelines for Synthesis and Processing of Two-Dimensional Titanium Carbide ($Ti_{3-x}C_2T_x$ MXene)," *Chemistry of Materials*, vol. 29, no. 18, pp. 7633–7644, Sep. 2017, doi: 10.1021/acs.chemmater.7b02847.
- [91] M. Naguib *et al.*, "Two-Dimensional Nanocrystals Produced by Exfoliation of $Ti_{3-x}AlC_2$," *Advanced Materials*, vol. 23, no. 37, pp. 4248–4253, Oct. 2011, doi: 10.1002/adma.201102306.
- [92] P. Srivastava, A. Mishra, H. Mizuseki, K.-R. Lee, and A. K. Singh, "Mechanistic Insight into the Chemical Exfoliation and Functionalization of $Ti_{3-x}C_2$ MXene," *ACS Appl Mater Interfaces*, vol. 8, no. 36, pp. 24256–24264, Sep. 2016, doi: 10.1021/acsami.6b08413.
- [93] T. Hu, M. Hu, B. Gao, W. Li, and X. Wang, "Screening Surface Structure of MXenes by High-Throughput Computation and Vibrational Spectroscopic Confirmation," *The Journal of Physical Chemistry C*, vol. 122, no. 32, pp. 18501–18509, Aug. 2018, doi: 10.1021/acs.jpcc.8b04427.
- [94] E. Lee and D.-J. Kim, "Review—Recent Exploration of Two-Dimensional MXenes for Gas Sensing: From a Theoretical to an Experimental View," *J Electrochem Soc*, vol. 167, no. 3, p. 037515, Jan. 2020, doi: 10.1149/2.0152003JES.
- [95] M. Murugesan, K. R. Nagavenkatesh, P. Devendran, N. Nallamuthu, C. Sambathkumar, and M. Krishna Kumar, "Scalable synthesis of 2D-layered Ti_3C_2 MXene by HF etching method; electrochemical investigations and device fabrication to enhancing capacitive nature," *Materials Science and Engineering: B*, vol. 309, Nov. 2024, doi: 10.1016/j.mseb.2024.117607.
- [96] M. Anayee *et al.*, "Role of acid mixtures etching on the surface chemistry and sodium ion storage in $Ti_{3-x}C_2T_x$ MXene," *Chemical Communications*, vol. 56, no. 45, pp. 6090–6093, 2020, doi: 10.1039/D0CC01042A.
- [97] Y. Ying *et al.*, "Two-Dimensional Titanium Carbide for Efficiently Reductive Removal of Highly Toxic Chromium(VI) from Water," *ACS Appl Mater Interfaces*, vol. 7, no. 3, pp. 1795–1803, Jan. 2015, doi: 10.1021/am5074722.
- [98] H. Li, X. Li, J. Liang, and Y. Chen, "Hydrous RuO₂-Decorated MXene Coordinating with Silver Nanowire Inks Enabling Fully Printed Micro-Supercapacitors with Extraordinary Volumetric Performance," *Adv Energy Mater*, vol. 9, no. 15, Apr. 2019, doi: 10.1002/aenm.201803987.

- [99] S. Shi, R. Zhong, L. Li, C. Wan, and C. Wu, "Ultrasound-assisted synthesis of graphene@MXene hybrid: A novel and promising material for electrochemical sensing," *Ultrason Sonochem*, vol. 90, Nov. 2022, doi: 10.1016/j.ultsonch.2022.106208.
- [100] A. Lipatov, M. Alhabeb, M. R. Lukatskaya, A. Boson, Y. Gogotsi, and A. Sinitskii, "Effect of Synthesis on Quality, Electronic Properties and Environmental Stability of Individual Monolayer Ti₃C₂ MXene Flakes," *Adv Electron Mater*, vol. 2, no. 12, Dec. 2016, doi: 10.1002/aelm.201600255.
- [101] J. Halim *et al.*, "Synthesis and Characterization of 2D Molybdenum Carbide (MXene)," *Adv Funct Mater*, vol. 26, no. 18, pp. 3118–3127, May 2016, doi: 10.1002/adfm.201505328.
- [102] Z. He *et al.*, "Pseudocapacitance of Bimetallic Solid-Solution MXene for Supercapacitors with Enhanced Electrochemical Energy Storage," *Adv Funct Mater*, vol. 33, no. 52, Dec. 2023, doi: 10.1002/adfm.202305251.
- [103] M. A. Hope *et al.*, "NMR reveals the surface functionalisation of Ti₃C₂ MXene," *Physical Chemistry Chemical Physics*, vol. 18, no. 7, pp. 5099–5102, 2016, doi: 10.1039/C6CP00330C.
- [104] S. Kajiyama *et al.*, "Enhanced Li-Ion Accessibility in MXene Titanium Carbide by Steric Chloride Termination," *Adv Energy Mater*, vol. 7, no. 9, May 2017, doi: 10.1002/aenm.201601873.
- [105] W. Sun *et al.*, "Electrochemical etching of Ti₂AlC to Ti₂CT_x (MXene) in low-concentration hydrochloric acid solution," *J. Mater. Chem. A*, vol. 5, no. 41, pp. 21663–21668, 2017, doi: 10.1039/C7TA05574A.
- [106] S. Yang *et al.*, "Fluoride-Free Synthesis of Two-Dimensional Titanium Carbide (MXene) Using A Binary Aqueous System," *Angewandte Chemie*, vol. 130, no. 47, pp. 15717–15721, Nov. 2018, doi: 10.1002/ange.201809662.
- [107] S. Yang *et al.*, "Fluoride-Free Synthesis of Two-Dimensional Titanium Carbide (MXene) Using A Binary Aqueous System," *Angewandte Chemie - International Edition*, vol. 57, no. 47, pp. 15491–15495, Nov. 2018, doi: 10.1002/anie.201809662.
- [108] L. Liu *et al.*, "In Situ Synthesis of MXene with Tunable Morphology by Electrochemical Etching of MAX Phase Prepared in Molten Salt," *Adv Energy Mater*, vol. 13, no. 7, Feb. 2023, doi: 10.1002/aenm.202203805.
- [109] M. Shen *et al.*, "One-Pot Green Process to Synthesize MXene with Controllable Surface Terminations using Molten Salts," *Angewandte Chemie*, vol. 133, no. 52, pp. 27219–27224, Dec. 2021, doi: 10.1002/ange.202110640.
- [110] Z. Wu *et al.*, "One-step in-situ synthesis of Sn-nanoconfined Ti₃C₂T_x MXene composites for Li-ion battery anode," *Electrochim Acta*, vol. 407, Mar. 2022, doi: 10.1016/j.electacta.2022.139916.

- [111] S. Y. Pang, W. F. Io, L. W. Wong, J. Zhao, and J. Hao, "Efficient Energy Conversion and Storage Based on Robust Fluoride-Free Self-Assembled 1D Niobium Carbide in 3D Nanowire Network," *Advanced Science*, vol. 7, no. 10, May 2020, doi: 10.1002/advs.201903680.
- [112] M. Naguib *et al.*, "Two-Dimensional Nanocrystals Produced by Exfoliation of Ti_3AlC_2 ," *Advanced Materials*, vol. 23, no. 37, pp. 4248–4253, Oct. 2011, doi: 10.1002/adma.201102306.
- [113] G. Deysher *et al.*, "Synthesis of Mo_4VAlC_4 MAX Phase and Two-Dimensional Mo_4VC_4 MXene with Five Atomic Layers of Transition Metals," *ACS Nano*, vol. 14, no. 1, pp. 204–217, Jan. 2020, doi: 10.1021/acsnano.9b07708.
- [114] J. Zhou *et al.*, "A Two-Dimensional Zirconium Carbide by Selective Etching of Al_3C_3 from Nanolaminated $Zr_3Al_3C_5$," *Angewandte Chemie International Edition*, vol. 55, no. 16, pp. 5008–5013, Apr. 2016, doi: 10.1002/anie.201510432.
- [115] X. Sang *et al.*, "Atomic Defects in Monolayer Titanium Carbide ($Ti_3C_2T_x$) MXene," *ACS Nano*, vol. 10, no. 10, pp. 9193–9200, Oct. 2016, doi: 10.1021/acsnano.6b05240.
- [116] J. Zhou *et al.*, "Synthesis and Electrochemical Properties of Two-Dimensional Hafnium Carbide," *ACS Nano*, vol. 11, no. 4, pp. 3841–3850, Apr. 2017, doi: 10.1021/acsnano.7b00030.
- [117] M. Naguib *et al.*, "Two-dimensional transition metal carbides," *ACS Nano*, vol. 6, no. 2, pp. 1322–1331, Feb. 2012, doi: 10.1021/nn204153h.
- [118] B. Anasori *et al.*, "Two-Dimensional, Ordered, Double Transition Metals Carbides (MXenes)," *ACS Nano*, vol. 9, no. 10, pp. 9507–9516, Oct. 2015, doi: 10.1021/acsnano.5b03591.
- [119] J. Halim *et al.*, "Synthesis and Characterization of 2D Molybdenum Carbide (MXene)," *Adv Funct Mater*, vol. 26, no. 18, pp. 3118–3127, May 2016, doi: 10.1002/adfm.201505328.
- [120] A. Feng *et al.*, "Two-dimensional MXene Ti₃C₂ produced by exfoliation of Ti₃AlC₂," *Mater Des*, vol. 114, pp. 161–166, Jan. 2017, doi: 10.1016/j.matdes.2016.10.053.
- [121] X. Wang *et al.*, "A new etching environment (FeF₃/HCl) for the synthesis of two-dimensional titanium carbide MXenes: a route towards selective reactivity vs. water," *J. Mater. Chem. A*, vol. 5, no. 41, pp. 22012–22023, 2017, doi: 10.1039/C7TA01082F.
- [122] F. Liu *et al.*, "Preparation of Ti₃C₂ and Ti₂C MXenes by fluoride salts etching and methane adsorptive properties," *Appl Surf Sci*, vol. 416, pp. 781–789, Sep. 2017, doi: 10.1016/j.apsusc.2017.04.239.
- [123] M. Ghidiu *et al.*, "Synthesis and characterization of two-dimensional Nb₄C₃ (MXene)," *Chem. Commun.*, vol. 50, no. 67, pp. 9517–9520, 2014, doi: 10.1039/C4CC03366C.

- [124] M. Ghidiu, J. Halim, S. Kota, D. Bish, Y. Gogotsi, and M. W. Barsoum, "Ion-Exchange and Cation Solvation Reactions in Ti_3C_2 MXene," *Chemistry of Materials*, vol. 28, no. 10, pp. 3507–3514, May 2016, doi: 10.1021/acs.chemmater.6b01275.
- [125] F. Liu *et al.*, "Preparation of High-Purity V_2C MXene and Electrochemical Properties as Li-Ion Batteries," *J Electrochem Soc*, vol. 164, no. 4, pp. A709–A713, Feb. 2017, doi: 10.1149/2.0641704jes.
- [126] B. Soundiraraju and B. K. George, "Two-Dimensional Titanium Nitride (Ti_2N) MXene: Synthesis, Characterization, and Potential Application as Surface-Enhanced Raman Scattering Substrate," *ACS Nano*, vol. 11, no. 9, pp. 8892–8900, Sep. 2017, doi: 10.1021/acsnano.7b03129.
- [127] W. Sun *et al.*, "Electrochemical etching of Ti_2AlC to Ti_2CT_x (MXene) in low-concentration hydrochloric acid solution," *J. Mater. Chem. A*, vol. 5, no. 41, pp. 21663–21668, 2017, doi: 10.1039/C7TA05574A.
- [128] S.-Y. Pang *et al.*, "Universal Strategy for HF-Free Facile and Rapid Synthesis of Two-dimensional MXenes as Multifunctional Energy Materials," *J Am Chem Soc*, vol. 141, no. 24, pp. 9610–9616, Jun. 2019, doi: 10.1021/jacs.9b02578.
- [129] S. Yang *et al.*, "Fluoride-Free Synthesis of Two-Dimensional Titanium Carbide (MXene) Using A Binary Aqueous System," *Angewandte Chemie International Edition*, vol. 57, no. 47, pp. 15491–15495, Nov. 2018, doi: 10.1002/anie.201809662.
- [130] M. Li *et al.*, "Element Replacement Approach by Reaction with Lewis Acidic Molten Salts to Synthesize Nanolaminated MAX Phases and MXenes," *J Am Chem Soc*, vol. 141, no. 11, pp. 4730–4737, Mar. 2019, doi: 10.1021/jacs.9b00574.
- [131] Y. Li *et al.*, "A general Lewis acidic etching route for preparing MXenes with enhanced electrochemical performance in non-aqueous electrolyte," *Nat Mater*, vol. 19, no. 8, pp. 894–899, Aug. 2020, doi: 10.1038/s41563-020-0657-0.
- [132] T. Li *et al.*, "Fluorine-Free Synthesis of High-Purity $Ti_3C_2T_x$ (T=OH, O) via Alkali Treatment," *Angewandte Chemie International Edition*, vol. 57, no. 21, pp. 6115–6119, May 2018, doi: 10.1002/anie.201800887.
- [133] G. Li, L. Tan, Y. zhang, B. Wu, and L. Li, "Highly Efficiently Delaminated Single-Layered MXene Nanosheets with Large Lateral Size," *Langmuir*, vol. 33, no. 36, pp. 9000–9006, Sep. 2017, doi: 10.1021/acs.langmuir.7b01339.
- [134] X. Xie *et al.*, "Surface Al leached Ti_3AlC_2 as a substitute for carbon for use as a catalyst support in a harsh corrosive electrochemical system," *Nanoscale*, vol. 6, no. 19, pp. 11035–11040, 2014, doi: 10.1039/C4NR02080D.
- [135] S. Zada *et al.*, "Algae Extraction Controllable Delamination of Vanadium Carbide Nanosheets with Enhanced Near-Infrared Photothermal Performance," *Angewandte*

Chemie International Edition, vol. 59, no. 16, pp. 6601–6606, Apr. 2020, doi: 10.1002/anie.201916748.

- [136] A. El Ghazaly *et al.*, “Ultrafast, One-Step, Salt-Solution-Based Acoustic Synthesis of Ti_3C_2 MXene,” *ACS Nano*, vol. 15, no. 3, pp. 4287–4293, Mar. 2021, doi: 10.1021/acsnano.0c07242.
- [137] T. Li *et al.*, “Fluorine-Free Synthesis of High-Purity $Ti_3C_2T_x$ ($T=OH, O$) via Alkali Treatment ,” *Angewandte Chemie*, vol. 130, no. 21, pp. 6223–6227, May 2018, doi: 10.1002/ange.201800887.
- [138] J. Xuan *et al.*, “Organic-Base-Driven Intercalation and Delamination for the Production of Functionalized Titanium Carbide Nanosheets with Superior Photothermal Therapeutic Performance,” *Angewandte Chemie*, vol. 128, no. 47, pp. 14789–14794, Nov. 2016, doi: 10.1002/ange.201606643.
- [139] G. Li, L. Tan, Y. zhang, B. Wu, and L. Li, “Highly Efficiently Delaminated Single-Layered MXene Nanosheets with Large Lateral Size,” *Langmuir*, vol. 33, no. 36, pp. 9000–9006, Sep. 2017, doi: 10.1021/acs.langmuir.7b01339.
- [140] T. Li *et al.*, “Fluorine-Free Synthesis of High-Purity $Ti_3C_2T_x$ ($T=OH, O$) via Alkali Treatment,” *Angewandte Chemie International Edition*, vol. 57, no. 21, pp. 6115–6119, May 2018, doi: 10.1002/anie.201800887.
- [141] F. Wang *et al.*, “One-step Synthesis of Organic Terminal 2D Ti_3C_2Tx MXene Nanosheets by Etching of Ti_3AlC_2 in an Organic Lewis Acid Solvent,” *Angewandte Chemie - International Edition*, vol. 63, no. 23, Jun. 2024, doi: 10.1002/anie.202405315.
- [142] W. Eom, H. Shin, and T. H. Han, “Tracking the thermal dynamics of Ti_3C_2Tx MXene with XPS and two-dimensional correlation spectroscopy,” *Appl Phys Lett*, vol. 122, no. 21, May 2023, doi: 10.1063/5.0143298.
- [143] K. Mahabari, R. D. Mohili, M. Patel, A. H. Jadhav, K. Lee, and N. K. Chaudhari, “HF-free microwave-assisted synthesis of MXene as an electrocatalyst for hydrogen evolution in alkaline media,” *Nanoscale Adv*, vol. 6, no. 21, pp. 5388–5397, 2024, doi: 10.1039/D4NA00250D.
- [144] J. Zhou *et al.*, “MXene-Polymer Hybrid for High-Performance Gas Sensor Prepared by Microwave-Assisted In-Situ Intercalation,” *Adv Mater Technol*, vol. 7, no. 9, Sep. 2022, doi: 10.1002/admt.202101565.
- [145] H. Renuka *et al.*, “Energy-efficient synthesis of Ti_3C_2Tx MXene for electromagnetic shielding,” *Mater Sci Semicond Process*, vol. 185, Jan. 2025, doi: 10.1016/j.mssp.2024.108966.
- [146] J. Zhu *et al.*, “Rapid one-step scalable microwave synthesis of $Ti_3C_2T_x$ XMxene,” *Chemical Communications*, vol. 57, no. 94, pp. 12611–12614, Dec. 2021, doi: 10.1039/d1cc04989e.

- [147] M. A. K. Purbayanto *et al.*, "Microwave-Assisted Hydrothermal Synthesis of Photocatalytic Truncated-Bipyramidal TiO₂/Ti₃CN Heterostructures Derived from Ti₃CN MXene," *Langmuir*, Oct. 2024, doi: 10.1021/acs.langmuir.4c02444.
- [148] J. Zhou *et al.*, "MXene-Polymer Hybrid for High-Performance Gas Sensor Prepared by Microwave-Assisted In-Situ Intercalation," *Adv Mater Technol*, vol. 7, no. 9, Sep. 2022, doi: 10.1002/admt.202101565.
- [149] J. Mei, G. A. Ayoko, C. Hu, J. M. Bell, and Z. Sun, "Two-dimensional fluorine-free mesoporous Mo₂C MXene via UV-induced selective etching of Mo₂Ga₂C for energy storage," *Sustainable Materials and Technologies*, vol. 25, Sep. 2020, doi: 10.1016/j.susmat.2020.e00156.
- [150] D. C. Geng *et al.*, "Direct synthesis of large-area 2D Mo₂C on in situ grown graphene," *Advanced Materials*, vol. 29, no. 35, Sep. 2017, doi: 10.1002/adma.201700072.
- [151] X. Zhang, Z. Zhang, and Z. Zhou, "MXene-based materials for electrochemical energy storage," *Journal of Energy Chemistry*, vol. 27, no. 1, pp. 73–85, Jan. 2018, doi: 10.1016/j.jecchem.2017.08.004.
- [152] Y. Feng, M. Zhang, H. Yan, Y. Zhang, R. Guo, and H. Wang, "Microwave-assisted efficient exfoliation of MXene and its composite for high-performance supercapacitors," *Ceram Int*, vol. 48, no. 7, pp. 9518–9526, Apr. 2022, doi: 10.1016/j.ceramint.2021.12.149.
- [153] Z. Yuan, L. Wang, J. Cao, L. Zhao, and W. Han, "Ultraviolet-Assisted Construction of Nitrogen-Rich Ag@Ti₃C₂T_x MXene for Highly Efficient Hydrogen Evolution Electrocatalysis and Supercapacitor," *Adv Mater Interfaces*, vol. 7, no. 23, Dec. 2020, doi: 10.1002/admi.202001449.
- [154] B.-M. Jun, S. Kim, H. Rho, C. M. Park, and Y. Yoon, "Ultrasound-assisted Ti₃C₂T_x MXene adsorption of dyes: Removal performance and mechanism analyses via dynamic light scattering," *Chemosphere*, vol. 254, p. 126827, Sep. 2020, doi: 10.1016/j.chemosphere.2020.126827.
- [155] S. Rouhi, M. Bay, O. Aydin, E. S. Sicim, F. Ay, and N. Kosku Perkgöz, "Large-Area Growth of Mo₂C Thin Films and MXene Structures via PVD-CVD Hybrid Technique," *New Journal of Chemistry*, 2025, doi: 10.1039/D4NJ05530F.
- [156] J. Halim *et al.*, "Synthesis and Characterization of 2D Molybdenum Carbide (MXene)," *Adv Funct Mater*, vol. 26, no. 18, pp. 3118–3127, May 2016, doi: 10.1002/adfm.201505328.
- [157] M. Murugesan, K. R. Nagavenkatesh, P. Devendran, N. Nallamuthu, C. Sambathkumar, and M. Krishna Kumar, "Scalable synthesis of 2D-layered Ti₃C₂ MXene by HF etching method; electrochemical investigations and device fabrication to enhancing capacitive nature," *Materials Science and Engineering: B*, vol. 309, p. 117607, Nov. 2024, doi: 10.1016/j.mseb.2024.117607.

- [158] S. Wang, Y. Liu, Y. Liu, and W. Hu, "Effect of HF etching on titanium carbide (Ti₃C₂Tx) microstructure and its capacitive properties," *Chemical Engineering Journal*, vol. 452, p. 139512, Jan. 2023, doi: 10.1016/j.cej.2022.139512.
- [159] X. Zhang, W. Zhang, and H. Zhao, "Comparative study on fabrication and energy storage performance of $\text{Ti}_3\text{C}_2\text{Tx}$ MXene by using hydrofluoric acid and in situ forming of hydrofluoric acid-based approaches," *Int J Energy Res*, vol. 46, no. 11, pp. 15559–15570, Sep. 2022, doi: 10.1002/er.8252.
- [160] C. Zhou *et al.*, "A review of etching methods of MXene and applications of MXene conductive hydrogels," *Eur Polym J*, vol. 167, p. 111063, Mar. 2022, doi: 10.1016/j.eurpolymj.2022.111063.
- [161] A. Gentile *et al.*, "Critical Analysis of MXene Production with In-Situ HF Forming Agents for Sustainable Manufacturing," *ChemElectroChem*, vol. 9, no. 23, Dec. 2022, doi: 10.1002/celc.202200891.
- [162] P. Liu, R. Pan, B. Li, Z. Su, B. Lin, and M. Tong, "Mild and Efficient Method for the In Situ Preparation of High-Quality MXene Materials Enabled by Hexafluoro Complex Anion Contained Salts Etching," *Adv Funct Mater*, vol. 34, no. 2, Jan. 2024, doi: 10.1002/adfm.202308532.
- [163] B. Gurzeda, N. Boulanger, A. Nordenström, C. Dejoie, and A. V. Talyzin, "Pristine MXene: In Situ XRD Study of MAX Phase Etching with HCl+LiF Solution," *Advanced Science*, vol. 11, no. 48, Dec. 2024, doi: 10.1002/advs.202408448.
- [164] T. Zhang *et al.*, "Synthesis of two-dimensional Ti₃C₂Tx MXene using HCl+LiF etchant: Enhanced exfoliation and delamination," *J Alloys Compd*, vol. 695, pp. 818–826, Feb. 2017, doi: 10.1016/j.jallcom.2016.10.127.
- [165] A. Sinha, K. Ma, and H. Zhao, "2D Ti₃C₂Tx flakes prepared by in-situ HF etchant for simultaneous screening of carbamate pesticides," *J Colloid Interface Sci*, vol. 590, pp. 365–374, May 2021, doi: 10.1016/j.jcis.2021.01.063.
- [166] T. Yin *et al.*, "Synthesis of Ti₃C₂F_x MXene with controllable fluorination by electrochemical etching for lithium-ion batteries applications," *Ceram Int*, vol. 47, no. 20, pp. 28642–28649, Oct. 2021, doi: 10.1016/j.ceramint.2021.07.023.
- [167] J. Chen *et al.*, "Simplified Synthesis of Fluoride-Free Ti₃C₂T_x via Electrochemical Etching toward High-Performance Electrochemical Capacitors," *ACS Nano*, vol. 16, no. 2, pp. 2461–2470, Feb. 2022, doi: 10.1021/acsnano.1c09004.
- [168] Y. Li *et al.*, "A general Lewis acidic etching route for preparing MXenes with enhanced electrochemical performance in non-aqueous electrolyte," *Nat Mater*, vol. 19, no. 8, pp. 894–899, Aug. 2020, doi: 10.1038/s41563-020-0657-0.

- [169] A. Masih, S. Tripathi, V. S. Raj, and O. P. Thakur, "Optimum ultrasonication duration for effective antimicrobial activity of Ti₃C₂-MXene," *Mater Chem Phys*, vol. 328, p. 129979, Dec. 2024, doi: 10.1016/j.matchemphys.2024.129979.
- [170] N. Khatun and S. C. Roy, "Optimization of etching and sonication time to prepare monolayer Ti₃C₂T MXene flakes: A structural, vibrational, and optical spectroscopy study," *Micro and Nanostructures*, vol. 167, p. 207256, Jul. 2022, doi: 10.1016/j.micrna.2022.207256.
- [171] H. Song, Y. Ma, Q. Yao, C. Liu, X. Li, and X. Tao, "Freeze-sonication delamination method of high crystalline-quality MXene with high yield," *Chemical Engineering Journal*, vol. 491, p. 151909, Jul. 2024, doi: 10.1016/j.cej.2024.151909.
- [172] G. Kumar, A. Ahlawat, H. Bhardwaj, G. K. Sahu, P. S. Rana, and P. R. Solanki, "Ultrasonication-assisted synthesis of transition metal carbide of MXene: an efficient and promising material for photocatalytic organic dyes degradation of rhodamine B and methylene blue in wastewater," *Environmental Science and Pollution Research*, vol. 31, no. 26, pp. 38232–38250, May 2024, doi: 10.1007/s11356-024-33505-5.
- [173] W. Zhang and X. Zhang, "The effect of ultrasound on synthesis and energy storage mechanism of Ti₃C₂T_x MXene," *Ultrason Sonochem*, vol. 89, p. 106122, Sep. 2022, doi: 10.1016/j.ultsonch.2022.106122.
- [174] H. Shi *et al.*, "Ambient-Stable Two-Dimensional Titanium Carbide (MXene) Enabled by Iodine Etching," *Angewandte Chemie International Edition*, vol. 60, no. 16, pp. 8689–8693, Apr. 2021, doi: 10.1002/anie.202015627.
- [175] P. Huang and W.-Q. Han, "Recent Advances and Perspectives of Lewis Acidic Etching Route: An Emerging Preparation Strategy for MXenes," *Nanomicro Lett*, vol. 15, no. 1, p. 68, Dec. 2023, doi: 10.1007/s40820-023-01039-z.
- [176] Y. Ou, P. Zhang, R. A. Soomro, N. Qiao, H. Cui, and B. Xu, "Enhancing the lithium storage properties of molten salt-etched Ti₃C₂T_x through sequential intercalation of alkali ions," *Inorg Chem Front*, vol. 11, no. 5, pp. 1423–1433, 2024, doi: 10.1039/D3QI02205F.
- [177] Q. Wu *et al.*, "MXene titanium carbide with high specific capacitance fabricated by microwave-assisted selective etching," *Applied Physics A*, vol. 127, no. 5, p. 360, May 2021, doi: 10.1007/s00339-021-04530-9.
- [178] A. Numan *et al.*, "Microwave-assisted rapid MAX phase etching and delamination: A paradigm shift in MXene synthesis," *Mater Chem Phys*, vol. 288, p. 126429, Sep. 2022, doi: 10.1016/j.matchemphys.2022.126429.
- [179] F. E. A. Latif *et al.*, "Microwave-assisted hydrothermal synthesis of Ti₃C₂T_x MXene: A sustainable and scalable approach using alkaline etchant," *J Mol Struct*, vol. 1329, p. 141407, May 2025, doi: 10.1016/j.molstruc.2025.141407.

- [180] F. N. M. Azlan, M. A. A. M. Abdah, Y. S. Tan, M. N. Mustafa, R. Walvekar, and M. Khalid, "Microwave-etched V₂C MXene-activated carbon hybrid as a high-performance anode material for lithium-ion batteries," *J Energy Storage*, vol. 72, p. 108620, Nov. 2023, doi: 10.1016/j.est.2023.108620.
- [181] M. Öper, U. Yorulmaz, C. Sevik, F. Ay, and N. Kosku Perkgöz, "Controlled CVD growth of ultrathin Mo₂C (MXene) flakes," *J Appl Phys*, vol. 131, no. 2, Jan. 2022, doi: 10.1063/5.0067970.
- [182] V. Thirumal, R. Yuvakkumar, P. S. Kumar, G. Ravi, S. P. Keerthana, and D. Velauthapillai, "Facile single-step synthesis of MXene@CNTs hybrid nanocomposite by CVD method to remove hazardous pollutants," *Chemosphere*, vol. 286, p. 131733, Jan. 2022, doi: 10.1016/j.chemosphere.2021.131733.
- [183] S. Ravuri *et al.*, "High yield and wide lateral size growth of α -Mo₂C: exploring the boundaries of CVD growth of bare MXene analogues," *Nanotechnology*, vol. 35, no. 15, p. 155601, Apr. 2024, doi: 10.1088/1361-6528/ad1c97.
- [184] S. Kumar *et al.*, "Supercapacitors based on Ti₃C₂Tx MXene extracted from supernatant and current collectors passivated by CVD-graphene," *Sci Rep*, vol. 11, no. 1, p. 649, Jan. 2021, doi: 10.1038/s41598-020-80799-9.
- [185] D. Wang *et al.*, "Direct synthesis and chemical vapor deposition of 2D carbide and nitride MXenes," *Science* (1979), vol. 379, no. 6638, pp. 1242–1247, Mar. 2023, doi: 10.1126/science.add9204.
- [186] C. E. Shuck and Y. Gogotsi, "Taking MXenes from the lab to commercial products," *Chemical Engineering Journal*, vol. 401, Dec. 2020, doi: 10.1016/j.cej.2020.125786.
- [187] B. Anasori and Y. Gogotsi, "The global expansion of MXenes," *Graphene and 2D Materials*, vol. 8, no. 3–4, pp. 39–41, Dec. 2023, doi: 10.1007/s41127-023-00067-1.
- [188] S. F. Hansen *et al.*, "Maximizing the safety and sustainability of MXenes," *Sci Rep*, vol. 14, no. 1, Dec. 2024, doi: 10.1038/s41598-024-82063-w.
- [189] M. A. Zaed, K. H. Tan, R. Saidur, N. Abdullah, and A. K. Pandey, "Invited viewpoint: pathways to low-cost MXene synthesis," *J Mater Sci*, vol. 59, no. 18, pp. 7575–7594, May 2024, doi: 10.1007/s10853-024-09666-6.
- [190] Y. Wei, P. Zhang, R. A. Soomro, Q. Zhu, and B. Xu, "Advances in the Synthesis of 2D MXenes," *Advanced Materials*, vol. 33, no. 39, Oct. 2021, doi: 10.1002/adma.202103148.
- [191] T. Amrillah, C. Abdullah, A. Hermawan, F. Sari, and V. Alviani, "Towards Greener and More Sustainable Synthesis of MXenes: A Review," *Nanomaterials*, vol. 12, no. 23, p. 4280, Dec. 2022, doi: 10.3390/nano12234280.

- [192] Z. Huang *et al.*, "Green and scalable electrochemical routes for cost-effective mass production of MXenes for supercapacitor electrodes," *Carbon Energy*, vol. 5, no. 10, Oct. 2023, doi: 10.1002/cey2.295.
- [193] V. Dananjaya *et al.*, "MXenes and its composite structures: synthesis, properties, applications, 3D/4D printing, and artificial intelligence; machine learning integration," Jun. 01, 2025, *Elsevier Ltd.* doi: 10.1016/j.pmatsci.2025.101433.
- [194] P. Lakhe *et al.*, "Process Safety Analysis for Ti₃C₂T_x MXene Synthesis and Processing," *Ind Eng Chem Res*, vol. 58, no. 4, pp. 1570–1579, Jan. 2019, doi: 10.1021/acs.iecr.8b05416.
- [195] K. R. G. Lim, M. Shekhirev, B. C. Wyatt, B. Anasori, Y. Gogotsi, and Z. W. Seh, "Fundamentals of MXene synthesis," Aug. 01, 2022, *Nature Publishing Group*. doi: 10.1038/s44160-022-00104-6.
- [196] C. E. Shuck *et al.*, "Scalable Synthesis of Ti₃C₂T_x MXene," *Adv Eng Mater*, vol. 22, no. 3, Mar. 2020, doi: 10.1002/adem.201901241.
- [197] Z. Sun *et al.*, "Selective Lithiation–Expansion–Microexplosion Synthesis of Two-Dimensional Fluoride-Free Mxene," *ACS Mater Lett*, vol. 1, no. 6, pp. 628–632, Dec. 2019, doi: 10.1021/acsmaterialslett.9b00390.
- [198] S.-H. Seok *et al.*, "Synthesis of high quality 2D carbide MXene flakes using a highly purified MAX precursor for ink applications," *Nanoscale Adv*, vol. 3, no. 2, pp. 517–527, 2021, doi: 10.1039/D0NA00398K.
- [199] Y. Z. N. Htwe *et al.*, "Progress in etching-driven MXene synthesis and utilization in conductive inks for printed electronics applications: A comprehensive review," *Synth Met*, vol. 306, p. 117631, Aug. 2024, doi: 10.1016/j.synthmet.2024.117631.
- [200] M. A. Zaed, K. H. Tan, N. Abdullah, R. Saidur, A. K. Pandey, and A. M. Saleque, "Cost analysis of MXene for low-cost production, and pinpointing of its economic footprint," *Open Ceramics*, vol. 17, Mar. 2024, doi: 10.1016/j.oceram.2023.100526.
- [201] S. Jolly, M. P. Paranthaman, and M. Naguib, "Synthesis of Ti₃C₂T_z MXene from low-cost and environmentally friendly precursors," *Mater Today Adv*, vol. 10, Jun. 2021, doi: 10.1016/j.mtadv.2021.100139.
- [202] H. Huang *et al.*, "Scalable, and low-cost treating-cutting-coating manufacture platform for MXene-based on-chip micro-supercapacitors," *Nano Energy*, vol. 69, p. 104431, Mar. 2020, doi: 10.1016/j.nanoen.2019.104431.
- [203] S. Seena, S. Susanna Victoria Backiyaleela, S. Sinthika, R. Anand, and V. S. Vasantha, "An Eco-Friendly and Cost-Effective Strategy for the Synthesis of High-Purity MXene," *The Journal of Physical Chemistry C*, vol. 129, no. 17, pp. 8228–8238, May 2025, doi: 10.1021/acs.jpcc.5c00235.

- [204] S. Kim *et al.*, "Sustainable and eco-friendly syntheses of green MXenes for advanced battery applications," *Nano Converg*, vol. 12, no. 1, p. 39, Jul. 2025, doi: 10.1186/s40580-025-00504-2.
- [205] M. Rahman and M. S. Al Mamun, "Future prospects of MXenes: synthesis, functionalization, properties, and application in field effect transistors," *Nanoscale Adv*, vol. 6, no. 2, pp. 367–385, 2024, doi: 10.1039/D3NA00874F.
- [206] K. H. Tan, M. A. Zaed, R. Saidur, N. Abdullah, N. A. I. M. Ishak, and J. Cherusseri, "Strategic Insights for Bulk Production of MXene: A Review," in *E3S Web of Conferences*, EDP Sciences, Feb. 2024. doi: 10.1051/e3sconf/202448801003.
- [207] A. Ungureanu *et al.*, "Systematic Life Cycle Environmental Impact Comparison of Alternative Synthetic Strategies for Ti₃C₂T_x MXene," *ACS Sustain Chem Eng*, vol. 12, no. 15, pp. 5893–5906, Apr. 2024, doi: 10.1021/acssuschemeng.3c08491.
- [208] M. Mim *et al.*, "MXene: A Roadmap to Sustainable Energy Management, Synthesis Routes, Stabilization, and Economic Assessment," *ACS Omega*, Jul. 2024, doi: 10.1021/acsomega.4c04849.
- [209] T. Li *et al.*, "Fluorine-Free Synthesis of High-Purity Ti₃C₂T_x (T=OH, O) via Alkali Treatment," *Angewandte Chemie*, vol. 130, no. 21, pp. 6223–6227, May 2018, doi: 10.1002/ange.201800887.
- [210] C. E. Shuck and Y. Gogotsi, "Taking MXenes from the lab to commercial products," *Chemical Engineering Journal*, vol. 401, p. 125786, Dec. 2020, doi: 10.1016/j.cej.2020.125786.
- [211] X. Shi *et al.*, "Scalable, High-Yield Monolayer MXene Preparation from Multilayer MXene for Many Applications," *Angewandte Chemie - International Edition*, vol. 64, no. 6, Feb. 2025, doi: 10.1002/anie.202418420.
- [212] J. H. Kim *et al.*, "Large-Area Ti₃C₂T_x-MXene Coating: Toward Industrial-Scale Fabrication and Molecular Separation," *ACS Nano*, vol. 15, no. 5, pp. 8860–8869, May 2021, doi: 10.1021/acsnano.1c01448.
- [213] M. Dadashi Firouzjaei, S. K. Nemani, M. Sadrzadeh, E. K. Wujcik, M. Elliott, and B. Anasori, "Life-Cycle Assessment of Ti₃C₂T_x MXene Synthesis," *Advanced Materials*, vol. 35, no. 31, Aug. 2023, doi: 10.1002/adma.202300422.
- [214] L. Yin *et al.*, "Rapid and reversible semi-solidification of MXene nanosheets via efficient capture for industrial applications," *Carbon N Y*, vol. 234, Mar. 2025, doi: 10.1016/j.carbon.2024.119966.
- [215] M. Yu and X. Feng, "Scalable Manufacturing of MXene Films: Moving toward Industrialization," Aug. 05, 2020, *Cell Press*. doi: 10.1016/j.matt.2020.07.011.

- [216] M. W. Barsoum and Y. Gogotsi, "Removing roadblocks and opening new opportunities for MXenes," *Ceram Int*, vol. 49, no. 14, pp. 24112–24122, Jul. 2023, doi: 10.1016/j.ceramint.2022.10.051.
- [217] K. D. Verma and K. K. Kar, "Cost-effective synthesis route for ultra-high purity of Ti₃AlC₂ MAX phase with enhanced performance of Ti₃C₂Tx MXene and MXene/NiO composite for supercapacitor application," *Chemical Engineering Journal*, vol. 504, p. 158938, Jan. 2025, doi: 10.1016/j.cej.2024.158938.
- [218] T. A. Oyehan, S. A. Ganiyu, C. Pfrang, M. Walker, and E. Valsami-Jones, "Low cost MXene synthesis for regenerative adsorption of benzene, toluene, ethylbenzene and xylene (BTEX)," *Chemical Engineering Journal*, vol. 492, p. 152217, Jul. 2024, doi: 10.1016/j.cej.2024.152217.
- [219] S. Seena, S. Susanna Victoria Backiyaleela, S. Sinthika, R. Anand, and V. S. Vasantha, "An Eco-Friendly and Cost-Effective Strategy for the Synthesis of High-Purity MXene," *The Journal of Physical Chemistry C*, vol. 129, no. 17, pp. 8228–8238, May 2025, doi: 10.1021/acs.jpcc.5c00235.
- [220] M. Li *et al.*, "Element Replacement Approach by Reaction with Lewis Acidic Molten Salts to Synthesize Nanolaminated MAX Phases and MXenes," *J Am Chem Soc*, vol. 141, no. 11, pp. 4730–4737, Mar. 2019, doi: 10.1021/jacs.9b00574.
- [221] M. Ostermann *et al.*, "Pulsed Electrochemical Exfoliation for an HF-Free Sustainable MXene Synthesis," *Small*, vol. 21, no. 22, Jun. 2025, doi: 10.1002/smll.202500807.
- [222] A. J. Borah, V. Natu, A. Biswas, and A. Srivastava, "A review on recent progress in synthesis, properties, and applications of MXenes," *Oxford Open Materials Science*, vol. 5, no. 1, Jan. 2025, doi: 10.1093/oxfmat/itae017.
- [223] D. T. Cuskelley, E. H. Kisi, and H. O. Sugo, "MAX phase – Alumina composites via exchange reaction in the M+1AlC systems (M=Ti, V, Cr, Nb, or Ta)," *J Solid State Chem*, vol. 233, pp. 150–157, Jan. 2016, doi: 10.1016/j.jssc.2015.10.024.
- [224] C. Li, S. Kota, C. Hu, and M. W. Barsoum, "On the synthesis of low-cost, titanium-based mxenes," *Journal of Ceramic Science and Technology*, vol. 7, no. 3, pp. 301–306, Sep. 2016, doi: 10.4416/JCST2016-00042.
- [225] C. Liang, F. Tai, Z. Wang, Z. Zhang, Z. Huang, and Q. Cheng, "High-Yield Production of MXene Nanosheets by Graphite-Assisted Ball-Milling," *CCS Chemistry*, pp. 1–17, Jul. 2025, doi: 10.31635/ccschem.025.202506110.
- [226] J. Wu, S. Xu, Y. Li, T. Mo, Y. Wang, and Y. Yang, "Competitive oxidation mechanism endows MXene-based supercapacitors with high-temperature tolerance and self-healing capability," *Energy Storage Mater*, vol. 74, Jan. 2025, doi: 10.1016/j.ensm.2024.103928.

- [227] C.-W. Wu, B. Unnikrishnan, I.-W. P. Chen, S. G. Harroun, H.-T. Chang, and C.-C. Huang, "Excellent oxidation resistive MXene aqueous ink for micro-supercapacitor application," *Energy Storage Mater.*, vol. 25, pp. 563–571, Mar. 2020, doi: 10.1016/j.ensm.2019.09.026.
- [228] X. Zhao *et al.*, "The Role of Antioxidant Structure in Mitigating Oxidation in $Ti_3C_2T_x$ and Ti_2CT_x MXenes," *Adv Mater Interfaces*, vol. 9, no. 20, Jul. 2022, doi: 10.1002/admi.202200480.
- [229] N. R. Vempuluru *et al.*, "Nanocluster catalyst driving ampere-level current density in direct seawater electrolysis quantum leap towards sustainable energy," *Materials Science and Engineering: R: Reports*, vol. 167, p. 101092, Jan. 2026, doi: 10.1016/j.mser.2025.101092.
- [230] M. R. Lukatskaya *et al.*, "Room-Temperature Carbide-Derived Carbon Synthesis by Electrochemical Etching of MAX Phases," *Angewandte Chemie International Edition*, vol. 53, no. 19, pp. 4877–4880, May 2014, doi: 10.1002/anie.201402513.
- [231] Z. Zeng, Y. Yan, J. Chen, P. Zan, Q. Tian, and P. Chen, "Boosting the Photocatalytic Ability of Cu₂O Nanowires for CO₂ Conversion by MXene Quantum Dots," *Adv Funct Mater*, vol. 29, no. 2, Jan. 2019, doi: 10.1002/adfm.201806500.
- [232] Y. Li, L. Ding, Y. Guo, Z. Liang, H. Cui, and J. Tian, "Boosting the Photocatalytic Ability of g-C₃N₄ for Hydrogen Production by Ti₃C₂ MXene Quantum Dots," *ACS Appl Mater Interfaces*, vol. 11, no. 44, pp. 41440–41447, Nov. 2019, doi: 10.1021/acsami.9b14985.
- [233] W. Yuan *et al.*, "MXene Nanofibers as Highly Active Catalysts for Hydrogen Evolution Reaction," *ACS Sustain Chem Eng*, vol. 6, no. 7, pp. 8976–8982, Jul. 2018, doi: 10.1021/acssuschemeng.8b01348.
- [234] P. Lian *et al.*, "Alkalized Ti₃C₂ MXene nanoribbons with expanded interlayer spacing for high-capacity sodium and potassium ion batteries," *Nano Energy*, vol. 40, pp. 1–8, Oct. 2017, doi: 10.1016/j.nanoen.2017.08.002.
- [235] K. Nasrin, D. Mukhilan, M. Arshad, M. Arunkumar, and M. Sathish, "Intralayered oswald ripening impelled nanoarchitectonics of MXene nanorods on MXene nanosheets with boron carbon nitride for robust supercapacitor application," *Electrochim Acta*, vol. 469, Nov. 2023, doi: 10.1016/j.electacta.2023.143251.
- [236] T. Su *et al.*, "Monolayer Ti₃C₂ Tx as an Effective Co-catalyst for Enhanced Photocatalytic Hydrogen Production over TiO₂," *ACS Appl Energy Mater*, vol. 2, no. 7, pp. 4640–4651, Jul. 2019, doi: 10.1021/acsael.8b02268.
- [237] X. Zhang, W. Zhang, and H. Zhao, "Electrochemical performance of Ti₃C₂Tx MXenes obtained via ultrasound assisted LiF-HCl method," *Mater Today Commun*, vol. 33, Dec. 2022, doi: 10.1016/j.mtcomm.2022.104384.

- [238] P. Zhang *et al.*, "In Situ Ice Template Approach to Fabricate 3D Flexible MXene Film-Based Electrode for High Performance Supercapacitors," *Adv Funct Mater*, vol. 30, no. 47, Nov. 2020, doi: 10.1002/adfm.202000922.
- [239] Y. Zhu, K. Rajouâ, S. Le Vot, O. Fontaine, P. Simon, and F. Favier, "Modifications of MXene layers for supercapacitors," *Nano Energy*, vol. 73, Jul. 2020, doi: 10.1016/j.nanoen.2020.104734.
- [240] J. Wei, F. Hu, Y. Pan, C. Lv, L. Bian, and Q. Ouyang, "Design strategy for metal-organic framework assembled on modifications of MXene layers for advanced supercapacitor electrodes," *Chemical Engineering Journal*, vol. 481, Feb. 2024, doi: 10.1016/j.cej.2024.148793.
- [241] S. Jiao, A. Zhou, M. Wu, and H. Hu, "Kirigami Patterning of MXene/Bacterial Cellulose Composite Paper for All-Solid-State Stretchable Micro-Supercapacitor Arrays," *Advanced Science*, vol. 6, no. 12, Jun. 2019, doi: 10.1002/advs.201900529.
- [242] M. Xia *et al.*, "Ionization-bombardment assisted deposition of MXene/SiC heterostructure for micro-supercapacitor with enhanced sodium storage," *Chemical Engineering Journal*, vol. 428, Jan. 2021, doi: 10.1016/j.cej.2021.131114.
- [243] W. Zhao *et al.*, "Interlayer Hydrogen-Bonded Metal Porphyrin Frameworks/MXene Hybrid Film with High Capacitance for Flexible All-Solid-State Supercapacitors," *Small*, vol. 15, no. 18, May 2019, doi: 10.1002/smll.201901351.
- [244] W. Chen, D. Zhang, K. Yang, M. Luo, P. Yang, and X. Zhou, "Mxene (Ti₃C₂Tx)/cellulose nanofiber/porous carbon film as free-standing electrode for ultrathin and flexible supercapacitors," *Chemical Engineering Journal*, vol. 413, Jun. 2021, doi: 10.1016/j.cej.2020.127524.
- [245] X. Zhang, Y. Liu, S. Dong, J. Yang, and X. Liu, "Flexible electrode based on multi-scaled MXene (Ti₃C₂Tx) for supercapacitors," *J Alloys Compd*, vol. 790, pp. 517–523, Jun. 2019, doi: 10.1016/j.jallcom.2019.03.219.
- [246] S. Jiao, A. Zhou, M. Wu, and H. Hu, "Kirigami Patterning of MXene/Bacterial Cellulose Composite Paper for All-Solid-State Stretchable Micro-Supercapacitor Arrays," *Advanced Science*, vol. 6, no. 12, Jun. 2019, doi: 10.1002/advs.201900529.
- [247] W. Cheng, J. Fu, H. Hu, and D. Ho, "Interlayer Structure Engineering of MXene-Based Capacitor-Type Electrode for Hybrid Micro-Supercapacitor toward Battery-Level Energy Density," *Advanced Science*, vol. 8, no. 16, Aug. 2021, doi: 10.1002/advs.202100775.
- [248] X. Li *et al.*, "A flexible Zn-ion hybrid micro-supercapacitor based on MXene anode and V₂O₅ cathode with high capacitance," *Chemical Engineering Journal*, vol. 428, Jan. 2022, doi: 10.1016/j.cej.2021.130965.

- [249] M. Wang *et al.*, "Ultrastretchable MXene Microsupercapacitors," *Small*, vol. 19, no. 21, May 2023, doi: 10.1002/smll.202300386.
- [250] M. Yuan *et al.*, "3D printing quasi-solid-state micro-supercapacitors with ultrahigh areal energy density based on high concentration MXene sediment," *Chemical Engineering Journal*, vol. 451, Jan. 2023, doi: 10.1016/j.cej.2022.138686.
- [251] Y. Zhu *et al.*, "Three-dimensional (3D)-printed MXene high-voltage aqueous micro-supercapacitors with ultrahigh areal energy density and low-temperature tolerance," *Carbon Energy*, vol. 6, no. 8, Aug. 2024, doi: 10.1002/cey.2.481.
- [252] R. Li *et al.*, "Flexible and high-performance electrochromic devices enabled by self-assembled 2D TiO₂/MXene heterostructures," *Nat Commun*, vol. 12, no. 1, Dec. 2021, doi: 10.1038/s41467-021-21852-7.
- [253] D. C. Geng *et al.*, "Direct synthesis of large-area 2D Mo₂C on in situ grown graphene," *Advanced Materials*, vol. 29, no. 35, Sep. 2017, doi: 10.1002/adma.201700072.
- [254] Y. Xie *et al.*, "Unraveling the Ionic Storage Mechanism of Flexible Nitrogen-Doped MXene Films for High-Performance Aqueous Hybrid Supercapacitors," *Small*, Dec. 2024, doi: 10.1002/smll.202405817.
- [255] P. Sun *et al.*, "Nitrogen and sulfur co-doped MXene ink without additive for high-performance inkjet-printing micro-supercapacitors," *Chemical Engineering Journal*, vol. 450, Dec. 2022, doi: 10.1016/j.cej.2022.138372.
- [256] R. R. Neiber, J. Kumar, B. P. Sharma, W. L. Ding, and X. Lu, "Ultra Stable Ink with Promising Areal Capacitance as Advanced Micro-Supercapacitor and Unique Metal Absorptivity Enabled by Surface Functionalization of Titanium Carbide (MXene)," *Adv Funct Mater*, Dec. 2024, doi: 10.1002/adfm.202406481.
- [257] Y. Zhu, J. Wang, H. Chu, Y.-C. Chu, and H. M. Chen, "*In Situ / Operando* Studies for Designing Next-Generation Electrocatalysts," *ACS Energy Lett*, vol. 5, no. 4, pp. 1281–1291, Apr. 2020, doi: 10.1021/acsenergylett.0c00305.
- [258] A. Gurlo and R. Riedel, "In Situ and Operando Spectroscopy for Assessing Mechanisms of Gas Sensing," *Angewandte Chemie International Edition*, vol. 46, no. 21, pp. 3826–3848, May 2007, doi: 10.1002/anie.200602597.
- [259] D. Liu *et al.*, "Review of Recent Development of In Situ/Operando Characterization Techniques for Lithium Battery Research," *Advanced Materials*, vol. 31, no. 28, Jul. 2019, doi: 10.1002/adma.201806620.
- [260] J. Guo *et al.*, "High-Energy/Power and Low-Temperature Cathode for Sodium-Ion Batteries: In Situ XRD Study and Superior Full-Cell Performance," *Advanced Materials*, vol. 29, no. 33, Sep. 2017, doi: 10.1002/adma.201701968.

- [261] J.-C. Dong *et al.*, "In situ Raman spectroscopic evidence for oxygen reduction reaction intermediates at platinum single-crystal surfaces," *Nat Energy*, vol. 4, no. 1, pp. 60–67, Dec. 2018, doi: 10.1038/s41560-018-0292-z.
- [262] X. H. Liu *et al.*, "In Situ TEM Experiments of Electrochemical Lithiation and Delithiation of Individual Nanostructures," *Adv Energy Mater*, vol. 2, no. 7, pp. 722–741, Jul. 2012, doi: 10.1002/aenm.201200024.
- [263] X. H. Liu and J. Y. Huang, "In situ TEM electrochemistry of anode materials in lithium ion batteries," *Energy Environ Sci*, vol. 4, no. 10, p. 3844, 2011, doi: 10.1039/c1ee01918j.
- [264] M. H. Nielsen, S. Aloni, and J. J. De Yoreo, "In situ TEM imaging of CaCO₃ nucleation reveals coexistence of direct and indirect pathways," *Science* (1979), vol. 345, no. 6201, pp. 1158–1162, Sep. 2014, doi: 10.1126/science.1254051.
- [265] D.-J. Liu and H. J. Robota, "In situ XANES characterization of the Cu oxidation state in Cu-ZSM-5 during NO decomposition catalysis," *Catal Letters*, vol. 21, no. 3–4, pp. 291–301, 1993, doi: 10.1007/BF00769481.
- [266] C. Lamberti *et al.*, "Determination of the oxidation and coordination state of copper on different Cu-based catalysts by XANES spectroscopy in situ or in operando conditions," *Phys. Chem. Chem. Phys.*, vol. 5, no. 20, pp. 4502–4509, 2003, doi: 10.1039/B305810G.
- [267] Z. Zhang *et al.*, "Characterizing Batteries by In Situ Electrochemical Atomic Force Microscopy: A Critical Review," *Adv Energy Mater*, vol. 11, no. 38, Oct. 2021, doi: 10.1002/aenm.202101518.
- [268] S. Lang, Y. Shi, Y. Guo, D. Wang, R. Wen, and L. Wan, "Insight into the Interfacial Process and Mechanism in Lithium–Sulfur Batteries: An In Situ AFM Study," *Angewandte Chemie International Edition*, vol. 55, no. 51, pp. 15835–15839, Dec. 2016, doi: 10.1002/anie.201608730.
- [269] J. Hao Ran Huang, S. W. Tseng, and I. W. Peter Chen, "In-situ electrochemical XRD and raman probing of ion transport dynamics in ionic liquid-etched Ti₃C₂T_x MXene for energy storage applications," *Chemical Engineering Journal*, vol. 503, Jan. 2025, doi: 10.1016/j.cej.2024.158232.
- [270] B. Mendoza-Sánchez *et al.*, "On the atomic structure of monolayer V₄C₃Tz and the study of charge storage processes in an acidic electrolyte using SPEIS and in-situ X-ray absorption spectroscopy," *Energy Storage Mater*, vol. 71, Aug. 2024, doi: 10.1016/j.ensm.2024.103566.
- [271] M. R. Lukatskaya, S. M. Bak, X. Yu, X. Q. Yang, M. W. Barsoum, and Y. Gogotsi, "Probing the Mechanism of High Capacitance in 2D Titanium Carbide Using in Situ X-Ray Absorption Spectroscopy," *Adv Energy Mater*, vol. 5, no. 15, Aug. 2015, doi: 10.1002/aenm.201500589.

- [272] X. Mu *et al.*, "Revealing the Pseudo-Intercalation Charge Storage Mechanism of MXenes in Acidic Electrolyte," *Adv Funct Mater*, vol. 29, no. 29, Jul. 2019, doi: 10.1002/adfm.201902953.
- [273] X. Wang *et al.*, "Titanium Carbide MXene Shows an Electrochemical Anomaly in Water-in-Salt Electrolytes," *ACS Nano*, vol. 15, no. 9, pp. 15274–15284, Sep. 2021, doi: 10.1021/acsnano.1c06027.
- [274] L. Liu *et al.*, "Heteroatom doped S, N-MXene/rGO flexible film for supercapacitor applications," *Chemical Engineering Journal*, vol. 506, Jan. 2025, doi: 10.1016/j.cej.2025.160320.
- [275] X. Wang *et al.*, "Surface Redox Pseudocapacitance of Partially Oxidized Titanium Carbide MXene in Water-in-Salt Electrolyte," *ACS Energy Lett*, vol. 7, no. 1, pp. 30–35, Jan. 2022, doi: 10.1021/acsenergylett.1c02262.
- [276] B. Gurzeda, N. Boulanger, A. Nordenström, C. Dejoie, and A. V. Talyzin, "Pristine MXene: In Situ XRD Study of MAX Phase Etching with HCl+LiF Solution," *Advanced Science*, Dec. 2024, doi: 10.1002/advs.202408448.
- [277] D. Johnson, K. Hansen, R. Yoo, and A. Djire, "Elucidating the Charge Storage Mechanism on Ti₃C₂ MXene through In Situ Raman Spectroelectrochemistry," *ChemElectroChem*, vol. 9, no. 18, Sep. 2022, doi: 10.1002/celc.202200555.
- [278] E. Pranada, D. Johnson, R. Yoo, and A. Djire, "Subsurface oxygen reduction reaction activity on Ti₂N MXene revealed by in situ Raman spectroelectrochemistry," *Sustain Energy Fuels*, vol. 7, no. 4, pp. 956–964, Jan. 2023, doi: 10.1039/d2se01532c.
- [279] J. Come *et al.*, "Nanoscale Elastic Changes in 2D Ti₃C₂Tx (MXene) Pseudocapacitive Electrodes," *Adv Energy Mater*, vol. 6, no. 9, May 2016, doi: 10.1002/aenm.201502290.
- [280] N. Ashraf, M. Isa khan, A. Majid, M. Rafique, and M. B. Tahir, "A review of the interfacial properties of 2-D materials for energy storage and sensor applications," *Chinese Journal of Physics*, vol. 66, pp. 246–257, Aug. 2020, doi: 10.1016/j.cjph.2020.03.035.
- [281] H. Liu *et al.*, "Defect Engineering of 2D Materials for Electrochemical Energy Storage," *Adv Mater Interfaces*, vol. 7, no. 15, Aug. 2020, doi: 10.1002/admi.202000494.
- [282] J. Wang, V. Malgras, Y. Sugahara, and Y. Yamauchi, "Electrochemical energy storage performance of 2D nanoarchitected hybrid materials," *Nat Commun*, vol. 12, no. 1, p. 3563, Jun. 2021, doi: 10.1038/s41467-021-23819-0.
- [283] Y. Zhu, L. Peng, Z. Fang, C. Yan, X. Zhang, and G. Yu, "Structural Engineering of 2D Nanomaterials for Energy Storage and Catalysis," *Advanced Materials*, vol. 30, no. 15, Apr. 2018, doi: 10.1002/adma.201706347.

- [284] L. Lin, J. Chen, D. Liu, X. Li, G. G. Wallace, and S. Zhang, "Engineering 2D Materials: A Viable Pathway for Improved Electrochemical Energy Storage," *Adv Energy Mater*, vol. 10, no. 45, Dec. 2020, doi: 10.1002/aenm.202002621.
- [285] S. Zhai *et al.*, "2D materials for 1D electrochemical energy storage devices," *Energy Storage Mater*, vol. 19, pp. 102–123, May 2019, doi: 10.1016/j.ensm.2019.02.020.
- [286] X. Zhang, L. Hou, A. Ciesielski, and P. Samori, "2D Materials Beyond Graphene for High-Performance Energy Storage Applications," *Adv Energy Mater*, vol. 6, no. 23, Dec. 2016, doi: 10.1002/aenm.201600671.
- [287] E. Pomerantseva and Y. Gogotsi, "Two-dimensional heterostructures for energy storage," *Nat Energy*, vol. 2, no. 7, p. 17089, Jun. 2017, doi: 10.1038/nenergy.2017.89.
- [288] B. Mendoza-Sánchez and Y. Gogotsi, "Synthesis of Two-Dimensional Materials for Capacitive Energy Storage," *Advanced Materials*, vol. 28, no. 29, pp. 6104–6135, Aug. 2016, doi: 10.1002/adma.201506133.
- [289] S. Yang, P. Zhang, A. S. Nia, and X. Feng, "Emerging 2D Materials Produced via Electrochemistry," *Advanced Materials*, vol. 32, no. 10, Mar. 2020, doi: 10.1002/adma.201907857.
- [290] Y. Dong, Z.-S. Wu, W. Ren, H.-M. Cheng, and X. Bao, "Graphene: a promising 2D material for electrochemical energy storage," *Sci Bull (Beijing)*, vol. 62, no. 10, pp. 724–740, May 2017, doi: 10.1016/j.scib.2017.04.010.
- [291] T. Tan, X. Jiang, C. Wang, B. Yao, and H. Zhang, "2D Material Optoelectronics for Information Functional Device Applications: Status and Challenges," *Advanced Science*, vol. 7, no. 11, Jun. 2020, doi: 10.1002/advs.202000058.
- [292] M. C. Lemme, D. Akinwande, C. Huyghebaert, and C. Stampfer, "2D materials for future heterogeneous electronics," *Nat Commun*, vol. 13, no. 1, p. 1392, Mar. 2022, doi: 10.1038/s41467-022-29001-4.
- [293] N. R. Glavin *et al.*, "Emerging Applications of Elemental 2D Materials," *Advanced Materials*, vol. 32, no. 7, Feb. 2020, doi: 10.1002/adma.201904302.
- [294] S. Kang *et al.*, "2D semiconducting materials for electronic and optoelectronic applications: potential and challenge," *2d Mater*, vol. 7, no. 2, p. 022003, Feb. 2020, doi: 10.1088/2053-1583/ab6267.
- [295] S. Manzeli, D. Ovchinnikov, D. Pasquier, O. V. Yazyev, and A. Kis, "2D transition metal dichalcogenides," *Nat Rev Mater*, vol. 2, no. 8, p. 17033, Jun. 2017, doi: 10.1038/natrevmats.2017.33.
- [296] X. Zang *et al.*, "Enhancing Capacitance Performance of Ti₃C₂T_x MXene as Electrode Materials of Supercapacitor: From Controlled Preparation to Composite Structure

- Construction," *Nanomicro Lett*, vol. 12, no. 1, p. 77, Dec. 2020, doi: 10.1007/s40820-020-0415-5.
- [297] B. K. Deka *et al.*, "3D-Printed Structural Supercapacitor with MXene-N@Zn-Co Selenide Nanowire Based Woven Carbon Fiber Electrodes," *ACS Energy Lett*, vol. 8, no. 2, pp. 963–971, Feb. 2023, doi: 10.1021/acsenergylett.2c02505.
- [298] C. I. Idumah, F. U. Iwuchukwu, I. Okoye, and J. E. Ogbu, "Construction, Characterization, Properties and Electromagnetic Interference Applications of MXene Polymeric nanoarchitectures," *Polymer-Plastics Technology and Materials*, vol. 63, no. 1, pp. 1–22, Jan. 2024, doi: 10.1080/25740881.2023.2267097.
- [299] X. Zang *et al.*, "Enhancing Capacitance Performance of Ti₃C₂T_x MXene as Electrode Materials of Supercapacitor: From Controlled Preparation to Composite Structure Construction," *Nanomicro Lett*, vol. 12, no. 1, p. 77, Dec. 2020, doi: 10.1007/s40820-020-0415-5.
- [300] B. K. Deka *et al.*, "3D-Printed Structural Supercapacitor with MXene-N@Zn-Co Selenide Nanowire Based Woven Carbon Fiber Electrodes," *ACS Energy Lett*, vol. 8, no. 2, pp. 963–971, Feb. 2023, doi: 10.1021/acsenergylett.2c02505.
- [301] A. Saleh *et al.*, "Inkjet-printed Ti₃C₂T_x MXene electrodes for multimodal cutaneous biosensing," *Journal of Physics: Materials*, vol. 3, no. 4, p. 044004, Oct. 2020, doi: 10.1088/2515-7639/abb361.
- [302] R. Garg, A. Agarwal, and M. Agarwal, "A review on MXene for energy storage application: effect of interlayer distance," *Mater Res Express*, vol. 7, no. 2, p. 022001, Feb. 2020, doi: 10.1088/2053-1591/ab750d.
- [303] P. Das and Z.-S. Wu, "MXene for energy storage: present status and future perspectives," *Journal of Physics: Energy*, vol. 2, no. 3, p. 032004, Jul. 2020, doi: 10.1088/2515-7655/ab9b1d.
- [304] S. Nahirniak, A. Ray, and B. Saruhan, "Challenges and Future Prospects of the MXene-Based Materials for Energy Storage Applications," *Batteries*, vol. 9, no. 2, p. 126, Feb. 2023, doi: 10.3390/batteries9020126.
- [305] X. Hui, X. Ge, R. Zhao, Z. Li, and L. Yin, "Interface Chemistry on MXene-Based Materials for Enhanced Energy Storage and Conversion Performance," *Adv Funct Mater*, vol. 30, no. 50, Dec. 2020, doi: 10.1002/adfm.202005190.
- [306] S. Jangra *et al.*, "A review on overcoming challenges and pioneering advances: MXene-based materials for energy storage applications," *J Energy Storage*, vol. 101, p. 113810, Nov. 2024, doi: 10.1016/j.est.2024.113810.
- [307] J. Nan *et al.*, "Nanoengineering of 2D MXene-Based Materials for Energy Storage Applications," *Small*, vol. 17, no. 9, Mar. 2021, doi: 10.1002/smll.201902085.

- [308] M. Q. Long *et al.*, "Recent advances on MXene based materials for energy storage applications," *Materials Today Sustainability*, vol. 19, p. 100163, Nov. 2022, doi: 10.1016/j.mtsust.2022.100163.
- [309] T. Xu *et al.*, "Ultralight MXene/carbon nanotube composite aerogel for high-performance flexible supercapacitor," *Adv Compos Hybrid Mater*, vol. 6, no. 3, p. 108, Jun. 2023, doi: 10.1007/s42114-023-00675-8.
- [310] W. Liang and I. Zhitomirsky, "MXene–carbon nanotube composite electrodes for high active mass asymmetric supercapacitors," *J Mater Chem A Mater*, vol. 9, no. 16, pp. 10335–10344, 2021, doi: 10.1039/D0TA12485K.
- [311] Y. Zhang, Z. Feng, X. Wang, H. Hu, and M. Wu, "MXene/carbon composites for electrochemical energy storage and conversion," *Materials Today Sustainability*, vol. 22, p. 100350, Jun. 2023, doi: 10.1016/j.mtsust.2023.100350.
- [312] M. Zhao *et al.*, "Flexible MXene/Carbon Nanotube Composite Paper with High Volumetric Capacitance," *Advanced Materials*, vol. 27, no. 2, pp. 339–345, Jan. 2015, doi: 10.1002/adma.201404140.
- [313] M. Du, Y. Lu, Y. Yang, and Z. Huang, "Construction of MOF-derived Ni-Co-Se/MXene heterostructured composite as hybrid supercapacitor cathode," *J Alloys Compd*, vol. 1010, p. 177460, Jan. 2025, doi: 10.1016/j.jallcom.2024.177460.
- [314] L. Gaba *et al.*, "Hybridization of metal-organic frameworks and MXenes: Expanding horizons in supercapacitor applications," *Adv Colloid Interface Sci*, vol. 332, p. 103268, Oct. 2024, doi: 10.1016/j.cis.2024.103268.
- [315] A. Ganiyat Olatoye, W. Li, E. Oluwaseyi Fagbohun, X. Zeng, Y. Zheng, and Y. Cui, "High-performance asymmetric supercapacitor based on nickel-MOF anchored MXene//NPC/rGO," *Journal of Electroanalytical Chemistry*, vol. 928, p. 117036, Jan. 2023, doi: 10.1016/j.jelechem.2022.117036.
- [316] Shavita, K. K. Thakur, A. L. Sharma, and S. Singh, "Exploring MXene-MOF composite for supercapacitor application," *Mater Chem Phys*, vol. 322, p. 129463, Aug. 2024, doi: 10.1016/j.matchemphys.2024.129463.
- [317] H. Zhou *et al.*, "Layered NiFe-LDH/MXene nanocomposite electrode for high-performance supercapacitor," *Int J Hydrogen Energy*, vol. 45, no. 23, pp. 13080–13089, Apr. 2020, doi: 10.1016/j.ijhydene.2020.03.001.
- [318] J. Guo *et al.*, "Double layers combined with MXene and in situ grown NiAl-LDH arrays on nickel foam for enhanced asymmetric supercapacitors," *Ionics (Kiel)*, vol. 28, no. 6, pp. 2967–2977, Jun. 2022, doi: 10.1007/s11581-022-04520-8.
- [319] D. S. Abraham, M. Vinoba, and M. Bhagiyalakshmi, "NiFe-LDH/MoS₂/MXene Nanocomposites as an Electrode Material for Battery-Type Supercapacitors," *ACS Appl Nano Mater*, vol. 7, no. 6, pp. 5791–5801, Mar. 2024, doi: 10.1021/acsanm.3c03779.

- [320] J. Chen, Y. Ren, H. Zhang, J. Qi, Y. Sui, and F. Wei, "Ni-Co-Fe layered double hydroxide coated on Ti₃C₂ MXene for high-performance asymmetric supercapacitor," *Appl Surf Sci*, vol. 562, p. 150116, Oct. 2021, doi: 10.1016/j.apsusc.2021.150116.
- [321] N. An *et al.*, "A novel COF/MXene film electrode with fast redox kinetics for high-performance flexible supercapacitor," *Chemical Engineering Journal*, vol. 458, Feb. 2023, doi: 10.1016/j.cej.2023.141434.
- [322] X. Zhu *et al.*, "Microfluidic-Assembled Covalent Organic Frameworks@Ti₃C₂Tx MXene Vertical Fibers for High-Performance Electrochemical Supercapacitors," *Advanced Materials*, vol. 35, no. 46, Nov. 2023, doi: 10.1002/adma.202307186.
- [323] Q. Geng *et al.*, "Covalent-Induced Heterostructure of Covalent-Organic Frameworks and MXene as Advanced Electrodes with Motivated Pseudocapacitance Performance," *ChemElectroChem*, vol. 9, no. 16, Aug. 2022, doi: 10.1002/celc.202200340.
- [324] S. M. Varghese, V. V. Mohan, S. Suresh, E. Bhoje Gowd, and R. B. Rakhi, "Synergistically modified Ti₃C₂Tx MXene conducting polymer nanocomposites as efficient electrode materials for supercapacitors," *J Alloys Compd*, vol. 973, p. 172923, Feb. 2024, doi: 10.1016/j.jallcom.2023.172923.
- [325] M. A. A. M. Abdah *et al.*, "Advancements in MXene-polymer composites for high-performance supercapacitor applications," *J Energy Storage*, vol. 63, p. 106942, Jul. 2023, doi: 10.1016/j.est.2023.106942.
- [326] K. Li *et al.*, "All-pseudocapacitive asymmetric MXene-carbon-conducting polymer supercapacitors," *Nano Energy*, vol. 75, p. 104971, Sep. 2020, doi: 10.1016/j.nanoen.2020.104971.
- [327] L. Qin *et al.*, "Polymer-MXene composite films formed by MXene-facilitated electrochemical polymerization for flexible solid-state microsupercapacitors," *Nano Energy*, vol. 60, pp. 734–742, Jun. 2019, doi: 10.1016/j.nanoen.2019.04.002.
- [328] T. Zhao *et al.*, "A Supercapacitor Architecture for Extreme Low-Temperature Operation Featuring MXene/Carbon Nanotube Electrodes with Vertically Aligned Channels and a Novel Freeze-Resistant Electrolyte," *Adv Funct Mater*, vol. 34, no. 24, Jun. 2024, doi: 10.1002/adfm.202314825.
- [329] X. Yang *et al.*, "3D Porous Oxidation-Resistant MXene/Graphene Architectures Induced by In Situ Zinc Template toward High-Performance Supercapacitors," *Adv Funct Mater*, vol. 31, no. 20, May 2021, doi: 10.1002/adfm.202101087.
- [330] W. Song, K. Wang, X. Lian, F. Zheng, and H. Niu, "Non-preoxidation synthesis of MXene integrated flexible carbon film for supercapacitors," *Chemical Engineering Journal*, vol. 493, Aug. 2024, doi: 10.1016/j.cej.2024.152804.

- [331] Y. Wang *et al.*, "MXene/Graphdiyne nanotube composite films for Free-Standing and flexible Solid-State supercapacitor," *Chemical Engineering Journal*, vol. 450, Dec. 2022, doi: 10.1016/j.cej.2022.138398.
- [332] R. Sinha *et al.*, "MXene/Biomass-derived activated carbon composite for supercapacitor applications," *Carbon N Y*, vol. 236, Mar. 2025, doi: 10.1016/j.carbon.2025.120101.
- [333] D. Wen *et al.*, "Direct inkjet printing of flexible MXene/graphene composite films for supercapacitor electrodes," *J Alloys Compd*, vol. 900, Apr. 2022, doi: 10.1016/j.jallcom.2021.163436.
- [334] S. Siva Shalini, Y. P. Fu, and A. Chandra Bose, "Synergetic Interplay of MnNi-MOF Composite with 2D MXene for Improved Supercapacitor Application," *Chemical Engineering Journal*, vol. 500, Nov. 2024, doi: 10.1016/j.cej.2024.156751.
- [335] D. S. Shivade *et al.*, "Folic acid-assisted in situ solvothermal synthesis of Ni-MOF/MXene composite for high-performance supercapacitors," *J Energy Storage*, vol. 100, Oct. 2024, doi: 10.1016/j.est.2024.113754.
- [336] C. Liu, Y. Bai, W. Li, F. Yang, G. Zhang, and H. Pang, "In Situ Growth of Three-Dimensional MXene/Metal–Organic Framework Composites for High-Performance Supercapacitors," *Angewandte Chemie - International Edition*, vol. 61, no. 11, Mar. 2022, doi: 10.1002/anie.202116282.
- [337] H. Guo *et al.*, "Zeolite-imidazole framework derived nickel-cobalt hydroxide on ultrathin MXene nanosheets for long life and high performance supercapacitance," *J Alloys Compd*, vol. 888, Dec. 2021, doi: 10.1016/j.jallcom.2021.161250.
- [338] R. Zhang *et al.*, "Synergistically coupling of 3D FeNi-LDH arrays with Ti₃C₂Tx-MXene nanosheets toward superior symmetric supercapacitor," *Nano Energy*, vol. 91, Jan. 2022, doi: 10.1016/j.nanoen.2021.106633.
- [339] W. Wang, D. Jiang, X. Chen, K. Xie, Y. Jiang, and Y. Wang, "A sandwich-like nano-micro LDH-MXene-LDH for high-performance supercapacitors," *Appl Surf Sci*, vol. 515, Jun. 2020, doi: 10.1016/j.apsusc.2020.145982.
- [340] Y. Gao, J. Lin, X. Chen, Z. Tang, G. Qin, and G. Wang, "Engineering 2D MXene and LDH into 3D Hollow Framework for Boosting Photothermal Energy Storage and Microwave Absorption," *Small*, vol. 19, no. 49, Dec. 2023, doi: 10.1002/smll.202303113.
- [341] K. Kasirajan, P. Rajkumar, H. G. Kwon, J. H. Yim, J. Kim, and H. K. Choi, "Electrostatically self-assembled dual-functional MXene/CoNiMn-LDH composites for biocompatible electrochemical energy storage and non-enzymatic glucose sensor applications," *Appl Mater Today*, vol. 39, Aug. 2024, doi: 10.1016/j.apmt.2024.102263.
- [342] C. Zhang, R. Guo, H. Wang, X. Xie, and C. Du, "Composite electrodes with NiCoAl-LDH coated Ti₃C₂Tx MXene and incorporated Ag nanowires for screen-printable in-

- plane hybrid supercapacitors on textiles," *Appl Surf Sci*, vol. 598, Oct. 2022, doi: 10.1016/j.apsusc.2022.153796.
- [343] L. Luo, Q. Kong, Q. Zhang, J. Zhang, M. Fan, and W. Zhao, "Synergistically coupling of ternary hydrotalcite and Ti₃C₂Tx-MXene nanosheets boosting electronic transmission in energy storage," *J Power Sources*, vol. 613, Sep. 2024, doi: 10.1016/j.jpowsour.2024.234940.
 - [344] S. Ren *et al.*, "Conductive MXene/Polymer Composites for Transparent Flexible Supercapacitors," *Small*, vol. 20, no. 35, Aug. 2024, doi: 10.1002/smll.202401346.
 - [345] W. Zheng, Y. Yang, L. Fan, D. Ye, W. Xu, and J. Xu, "Ultralight PPy@PVA/BC/MXene composite aerogels for high-performance supercapacitor eltrodes and pressure sensors," *Appl Surf Sci*, vol. 624, Jul. 2023, doi: 10.1016/j.apsusc.2023.157138.
 - [346] B. Chen, Q. Song, Z. Zhou, and C. Lu, "A Novel Sandwiched Porous MXene/Polyaniline Nanofibers Composite Film for High Capacitance Supercapacitor Electrode," *Adv Mater Interfaces*, vol. 8, no. 12, Jun. 2021, doi: 10.1002/admi.202002168.
 - [347] M. Zhang, F. Héraly, M. Yi, and J. Yuan, "Multitasking tartaric-acid-enabled, highly conductive, and stable MXene/conducting polymer composite for ultrafast supercapacitor," *Cell Rep Phys Sci*, vol. 2, no. 6, Jun. 2021, doi: 10.1016/j.xcrp.2021.100449.
 - [348] W. Liu *et al.*, "Engineered MXene quantum dots for micro-supercapacitors with excellent capacitive behaviors," *Nano Energy*, vol. 122, Apr. 2024, doi: 10.1016/j.nanoen.2024.109332.
 - [349] P. Sun *et al.*, "An inkjet-printing ink based on porous NiS/N-MXene for high-performance asymmetric micro-supercapacitors and self-powered microelectronics," *Chemical Engineering Journal*, vol. 474, Oct. 2023, doi: 10.1016/j.cej.2023.145466.
 - [350] H. Adamu, S. I. Abba, P. B. Anyin, Y. Sani, and M. Qamar, "Artificial intelligence-navigated development of high-performance electrochemical energy storage systems through feature engineering of multiple descriptor families of materials," *Energy Advances*, vol. 2, no. 5, pp. 615–645, 2023, doi: 10.1039/D3YA00104K.
 - [351] X. Liu, K. Fan, X. Huang, J. Ge, Y. Liu, and H. Kang, "Recent advances in artificial intelligence boosting materials design for electrochemical energy storage," *Chemical Engineering Journal*, vol. 490, p. 151625, Jun. 2024, doi: 10.1016/j.cej.2024.151625.
 - [352] K. Min, B. Choi, K. Park, and E. Cho, "Machine learning assisted optimization of electrochemical properties for Ni-rich cathode materials," *Sci Rep*, vol. 8, no. 1, p. 15778, Oct. 2018, doi: 10.1038/s41598-018-34201-4.
 - [353] C. Lv *et al.*, "Machine Learning: An Advanced Platform for Materials Development and State Prediction in Lithium-Ion Batteries," *Advanced Materials*, vol. 34, no. 25, Jun. 2022, doi: 10.1002/adma.202101474.

- [354] X. Bai *et al.*, "Heterojunction of MXenes and MN₄-graphene: Machine learning to accelerate the design of bifunctional oxygen electrocatalysts," *J Colloid Interface Sci*, vol. 664, pp. 716–725, Jun. 2024, doi: 10.1016/j.jcis.2024.03.073.
- [355] P. Kumar K, K. Deepthi Jayan, P. Sharma, and M. Alruqi, "Thermo-electro-rheological properties of graphene oxide and MXene hybrid nanofluid for vanadium redox flow battery: Application of explainable ensemble machine learning with hyperparameter optimization," *FlatChem*, vol. 43, p. 100606, Jan. 2024, doi: 10.1016/j.flatc.2023.100606.
- [356] Y. Xiong *et al.*, "First principles and interpretable machine learning aided the exploration of defective MXene for nitrogen reduction reaction," *Surfaces and Interfaces*, vol. 59, p. 105932, Feb. 2025, doi: 10.1016/j.surfin.2025.105932.
- [357] H. Yao *et al.*, "A machine learning strategy-incorporated BiFeO₃/Ti₃C₂ MXene electrochemical platform for simple, rapid detection of Pb²⁺ with high sensitivity," *Chemosphere*, vol. 340, p. 139728, Nov. 2023, doi: 10.1016/j.chemosphere.2023.139728.
- [358] I. Baskin and Y. Ein-Eli, "Electrochemoinformatics as an Emerging Scientific Field for Designing Materials and Electrochemical Energy Storage and Conversion Devices—An Application in Battery Science and Technology," *Adv Energy Mater*, vol. 12, no. 48, Dec. 2022, doi: 10.1002/aenm.202202380.
- [359] Z. Li, S. Zou, Z. Wang, G. Postole, L. Hu, and H. Zhao, "Machine learning in electrochemical oxidation process: A mini-review," *Chinese Chemical Letters*, p. 110526, Oct. 2024, doi: 10.1016/j.cclet.2024.110526.
- [360] R. Ding, J. Chen, Y. Chen, J. Liu, Y. Bando, and X. Wang, "Unlocking the potential: machine learning applications in electrocatalyst design for electrochemical hydrogen energy transformation," *Chem Soc Rev*, vol. 53, no. 23, pp. 11390–11461, 2024, doi: 10.1039/D4CS00844H.
- [361] M. Tamtaji *et al.*, "Machine learning for design principles for single atom catalysts towards electrochemical reactions," *J Mater Chem A Mater*, vol. 10, no. 29, pp. 15309–15331, 2022, doi: 10.1039/D2TA02039D.
- [362] A. Aravind, D. Dhinasekaran, and A. R. Rajendran, "Titanium Mxene: A Promising Material for Next-Generation Optical Biosensors and Machine Learning Integration," *Analysis & Sensing*, vol. 5, no. 2, Mar. 2025, doi: 10.1002/anse.202400095.
- [363] K. I. Nassar, T. L. P. Galvão, J. D. Gouveia, and J. R. B. Gomes, "Predicting Adsorption Energies on MXene Surfaces Using Machine Learning to Enhance Catalyst Design for the Water–Gas Shift Reaction," *The Journal of Physical Chemistry C*, vol. 129, no. 5, pp. 2512–2524, Feb. 2025, doi: 10.1021/acs.jpcc.4c08353.
- [364] N. C. Frey, J. Wang, G. I. Vega Bellido, B. Anasori, Y. Gogotsi, and V. B. Shenoy, "Prediction of Synthesis of 2D Metal Carbides and Nitrides (MXenes) and Their

Precursors with Positive and Unlabeled Machine Learning," *ACS Nano*, vol. 13, no. 3, pp. 3031–3041, Mar. 2019, doi: 10.1021/acsnano.8b08014.

- [365] C. Rong, L. Zhou, B. Zhang, and F. Z. Xuan, "Machine learning for mechanics prediction of 2D MXene-based aerogels," *Composites Communications*, vol. 38, Feb. 2023, doi: 10.1016/j.coco.2022.101474.
- [366] L. Wang *et al.*, "Machine learning assisted screening of MXenes pseudocapacitive materials," *J Power Sources*, vol. 564, Apr. 2023, doi: 10.1016/j.jpowsour.2023.232834.
- [367] Y. Liu, O. C. Esan, Z. Pan, and L. An, "Machine learning for advanced energy materials," Mar. 01, 2021, *Elsevier B.V.* doi: 10.1016/j.egyai.2021.100049.
- [368] L. Pradhan *et al.*, "Supercapacitor properties of partially oxidised-MXene quantum dots/graphene hybrids: Fabrication of flexible/wearable micro-supercapacitor devices," *Chemical Engineering Journal*, vol. 497, Oct. 2024, doi: 10.1016/j.cej.2024.154587.
- [369] M. Shariq *et al.*, "Machine learning models for prediction of electrochemical properties in supercapacitor electrodes using MXene and graphene nanoplatelets," *Chemical Engineering Journal*, vol. 484, Mar. 2024, doi: 10.1016/j.cej.2024.149502.
- [370] S. Krishna and A. Mir, "Unlocking the potential of Ti₃C₂ electrodes: a data-driven capacitance prediction study," *Energy Advances*, Oct. 2024, doi: 10.1039/d4ya00460d.
- [371] G. Wang, R. Zhang, H. Zhang, and K. Cheng, "Aqueous MXene inks for inkjet-printing microsupercapacitors with ultrahigh energy densities," *J Colloid Interface Sci*, vol. 645, pp. 359–370, Sep. 2023, doi: 10.1016/j.jcis.2023.04.155.
- [372] P. Sun *et al.*, "Nitrogen and sulfur co-doped MXene ink without additive for high-performance inkjet-printing micro-supercapacitors," *Chemical Engineering Journal*, vol. 450, p. 138372, Dec. 2022, doi: 10.1016/j.cej.2022.138372.
- [373] S. Uzun *et al.*, "Additive-Free Aqueous MXene Inks for Thermal Inkjet Printing on Textiles," *Small*, vol. 17, no. 1, Jan. 2021, doi: 10.1002/smll.202006376.
- [374] J. Ma *et al.*, "Aqueous MXene/PH1000 Hybrid Inks for Inkjet-Printing Micro-Supercapacitors with Unprecedented Volumetric Capacitance and Modular Self-Powered Microelectronics," *Adv Energy Mater*, vol. 11, no. 23, Jun. 2021, doi: 10.1002/aenm.202100746.
- [375] L. Zeng, S. Ling, D. Du, H. He, X. Li, and C. Zhang, "Direct Ink Writing 3D Printing for High-Performance Electrochemical Energy Storage Devices: A Minireview," *Advanced Science*, vol. 10, no. 32, Nov. 2023, doi: 10.1002/advs.202303716.
- [376] J. Zhao *et al.*, "Printable Ink Design towards Customizable Miniaturized Energy Storage Devices," *ACS Mater Lett*, vol. 2, no. 9, pp. 1041–1056, Sep. 2020, doi: 10.1021/acsmaterialslett.0c00176.

- [377] L. Yu, Z. Fan, Y. Shao, Z. Tian, J. Sun, and Z. Liu, "Versatile N-Doped MXene Ink for Printed Electrochemical Energy Storage Application," *Adv Energy Mater*, vol. 9, no. 34, Sep. 2019, doi: 10.1002/aenm.201901839.
- [378] C. Zhu *et al.*, "Constructing Ti₃C₂T_x-MXene-based gradient woodpile structure by direct ink writing 3D printing for efficient microwave absorption," *International Journal of Minerals, Metallurgy and Materials*, vol. 32, no. 3, pp. 657–667, Mar. 2025, doi: 10.1007/s12613-024-3022-5.
- [379] N. Kong *et al.*, "Environmentally stable MXene ink for direct writing flexible electronics," *Nanoscale*, vol. 14, no. 17, pp. 6299–6304, 2022, doi: 10.1039/D1NR07387G.
- [380] P.-Z. Jiang *et al.*, "Direct ink writing of multifunctional gratings with gel-like MXene/norepinephrine ink for dynamic electromagnetic interference shielding and patterned Joule heating," *Nano Res*, vol. 17, no. 3, pp. 1585–1594, Mar. 2024, doi: 10.1007/s12274-023-6044-9.
- [381] S. Zheng *et al.*, "Multitasking MXene Inks Enable High-Performance Printable Microelectrochemical Energy Storage Devices for All-Flexible Self-Powered Integrated Systems," *Advanced Materials*, vol. 33, no. 10, Mar. 2021, doi: 10.1002/adma.202005449.
- [382] X. Zang *et al.*, "Laser-sculptured ultrathin transition metal carbide layers for energy storage and energy harvesting applications," *Nat Commun*, vol. 10, no. 1, p. 3112, Jul. 2019, doi: 10.1038/s41467-019-10999-z.
- [383] Q. Li *et al.*, "Femtosecond Laser-Etched MXene Microsupercapacitors with Double-Side Configuration via Arbitrary On- and Through-Substrate Connections," *Adv Energy Mater*, vol. 10, no. 24, Jun. 2020, doi: 10.1002/aenm.202000470.
- [384] Y. Jo *et al.*, "Indirect laser photothermal writing of high areal capacitance micro-supercapacitors with expanded thick MXene electrodes," *J Energy Storage*, vol. 97, p. 112746, Sep. 2024, doi: 10.1016/j.est.2024.112746.
- [385] I. Hussain *et al.*, "Flexible MXenes for printing energy storage devices," *Chemical Engineering Journal*, vol. 497, p. 154978, Oct. 2024, doi: 10.1016/j.cej.2024.154978.
- [386] S. Abdolhosseinzadeh, J. Heier, and C. (John) Zhang, "Printing and coating MXenes for electrochemical energy storage devices," *Journal of Physics: Energy*, vol. 2, no. 3, p. 031004, Jul. 2020, doi: 10.1088/2515-7655/aba47d.
- [387] M. Yang *et al.*, "Printing assembly of flexible devices with oxidation stable MXene for high performance humidity sensing applications," *Sens Actuators B Chem*, vol. 364, p. 131867, Aug. 2022, doi: 10.1016/j.snb.2022.131867.
- [388] S. Abdolhosseinzadeh, R. Schneider, A. Verma, J. Heier, F. Nüesch, and C. (John) Zhang, "Turning Trash into Treasure: Additive Free MXene Sediment Inks for Screen-Printed Micro-Supercapacitors," *Advanced Materials*, vol. 32, no. 17, Apr. 2020, doi: 10.1002/adma.202000716.

- [389] S. Xu, Y. Dall’Agnese, G. Wei, C. Zhang, Y. Gogotsi, and W. Han, “Screen-printable microscale hybrid device based on MXene and layered double hydroxide electrodes for powering force sensors,” *Nano Energy*, vol. 50, pp. 479–488, Aug. 2018, doi: 10.1016/j.nanoen.2018.05.064.
- [390] J. Zhang *et al.*, “Recent Advances in MXene-Based Fibers, Yarns, and Fabrics for Wearable Energy Storage Devices Applications,” *ACS Appl Electron Mater*, vol. 5, no. 9, pp. 4704–4725, Sep. 2023, doi: 10.1021/acsaelm.3c00238.
- [391] A. Levitt *et al.*, “Bath Electrospinning of Continuous and Scalable Multifunctional MXene-Infiltrated Nanoyarns,” *Small*, vol. 16, no. 26, Jul. 2020, doi: 10.1002/smll.202002158.
- [392] Z. Zhou *et al.*, “Layer-by-layer assembly of MXene and carbon nanotubes on electrospun polymer films for flexible energy storage,” *Nanoscale*, vol. 10, no. 13, pp. 6005–6013, 2018, doi: 10.1039/C8NR00313K.
- [393] S. Seyedin, E. R. S. Yanza, and J. M. Razal, “Knittable energy storing fiber with high volumetric performance made from predominantly MXene nanosheets,” *J Mater Chem A Mater*, vol. 5, no. 46, pp. 24076–24082, 2017, doi: 10.1039/C7TA08355F.
- [394] A. Levitt, J. Zhang, G. Dion, Y. Gogotsi, and J. M. Razal, “MXene-Based Fibers, Yarns, and Fabrics for Wearable Energy Storage Devices,” *Adv Funct Mater*, vol. 30, no. 47, Nov. 2020, doi: 10.1002/adfm.202000739.
- [395] A. S. Levitt, M. Alhabeb, C. B. Hatter, A. Sarycheva, G. Dion, and Y. Gogotsi, “Electrospun MXene/carbon nanofibers as supercapacitor electrodes,” *J Mater Chem A Mater*, vol. 7, no. 1, pp. 269–277, 2019, doi: 10.1039/C8TA09810G.
- [396] J. Kang, J. B.-H. Tok, and Z. Bao, “Self-healing soft electronics,” *Nat Electron*, vol. 2, no. 4, pp. 144–150, Apr. 2019, doi: 10.1038/s41928-019-0235-0.
- [397] Y. Cao *et al.*, “Self-healing electronic skins for aquatic environments,” *Nat Electron*, vol. 2, no. 2, pp. 75–82, Feb. 2019, doi: 10.1038/s41928-019-0206-5.
- [398] S. Iravani, N. Rabiee, and P. Makvandi, “Advancements in MXene-based composites for electronic skins,” *J Mater Chem B*, vol. 12, no. 4, pp. 895–915, 2024, doi: 10.1039/D3TB02247A.
- [399] W. Zhao, J. Jiang, W. Chen, Y. He, T. Lin, and L. Zhao, “Radiation synthesis of rapidly self-healing, durable, and flexible poly(ionic liquid)/MXene gels with anti-freezing property for multi-functional strain sensors,” *Chemical Engineering Journal*, vol. 468, p. 143660, Jul. 2023, doi: 10.1016/j.cej.2023.143660.
- [400] L. Zhang *et al.*, “Semi-embedded robust MXene/AgNW sensor with self-healing, high sensitivity and a wide range for motion detection,” *Chemical Engineering Journal*, vol. 434, p. 134751, Apr. 2022, doi: 10.1016/j.cej.2022.134751.

- [401] S. Bin Choi, J. S. Meena, J. Joo, and J.-W. Kim, "Autonomous self-healing wearable flexible heaters enabled by innovative MXene/polycaprolactone composite fibrous networks and silver nanowires," *Adv Compos Hybrid Mater.*, vol. 6, no. 6, p. 227, Dec. 2023, doi: 10.1007/s42114-023-00809-y.
- [402] J. S. Choi, J. S. Meena, S. Bin Choi, S. Jung, and J. Kim, "Water-Triggered Self-Healing of $Ti_3C_2T_x$ MXene Standalone Electrodes: Systematic Examination of Factors Affecting the Healing Process," *Small*, vol. 20, no. 20, May 2024, doi: 10.1002/smll.202306434.
- [403] J.-N. Ma *et al.*, "Heterogeneous self-healing assembly of MXene and graphene oxide enables producing free-standing and self-reparable soft electronics and robots," *Sci Bull (Beijing)*, vol. 67, no. 5, pp. 501–511, Mar. 2022, doi: 10.1016/j.scib.2021.11.015.
- [404] M. Li *et al.*, "Flexible Accelerated-Wound-Healing Antibacterial MXene-Based Epidermic Sensor for Intelligent Wearable Human-Machine Interaction," *Adv Funct Mater.*, vol. 32, no. 47, Nov. 2022, doi: 10.1002/adfm.202208141.
- [405] Y. Cheng *et al.*, "High-strength MXene sheets through interlayer hydrogen bonding for self-healing flexible pressure sensor," *Chemical Engineering Journal*, vol. 453, p. 139823, Feb. 2023, doi: 10.1016/j.cej.2022.139823.
- [406] J. Wu, S. Xu, Y. Li, T. Mo, Y. Wang, and Y. Yang, "Competitive oxidation mechanism endows MXene-based supercapacitors with high-temperature tolerance and self-healing capability," *Energy Storage Mater.*, vol. 74, p. 103928, Jan. 2025, doi: 10.1016/j.ensm.2024.103928.
- [407] H. Wan *et al.*, "MXene-Mediated Cellulose Conductive Hydrogel with Ultrastretchability and Self-Healing Ability," *ACS Nano*, vol. 17, no. 20, pp. 20699–20710, Oct. 2023, doi: 10.1021/acsnano.3c08859.
- [408] H. Yin *et al.*, "MXene-based conductive hydrogels with toughness and self-healing enhancement by metal coordination for flexible electronic devices," *Materials Today Physics*, vol. 47, p. 101537, Sep. 2024, doi: 10.1016/j.mtphys.2024.101537.
- [409] C. Qiao, H. Wu, X. Xu, Z. Guan, and W. Ou-Yang, "Electrical Conductivity Enhancement and Electronic Applications of 2D $Ti_3C_2T_x$ MXene Materials," *Adv Mater Interfaces*, vol. 8, no. 24, Dec. 2021, doi: 10.1002/admi.202100903.
- [410] Q. Li *et al.*, "Ultrastretchable High-Conductivity MXene-Based Organohydrogels for Human Health Monitoring and Machine-Learning-Assisted Recognition," *ACS Appl Mater Interfaces*, vol. 15, no. 15, pp. 19435–19446, Apr. 2023, doi: 10.1021/acsami.3c00432.
- [411] Z. Guo *et al.*, "High Electrical Conductivity 2D MXene Serves as Additive of Perovskite for Efficient Solar Cells," *Small*, vol. 14, no. 47, Nov. 2018, doi: 10.1002/smll.201802738.

- [412] P. Liu *et al.*, "Surface termination modification on high-conductivity MXene film for energy conversion," *J Alloys Compd*, vol. 829, p. 154634, Jul. 2020, doi: 10.1016/j.jallcom.2020.154634.
- [413] X. Wang *et al.*, "A lightweight MXene-Coated nonwoven fabric with excellent flame Retardancy, EMI Shielding, and Electrothermal/Photothermal conversion for wearable heater," *Chemical Engineering Journal*, vol. 430, p. 132605, Feb. 2022, doi: 10.1016/j.cej.2021.132605.
- [414] H. Xu *et al.*, "Lightweight Ti_2CT_x MXene/Poly(vinyl alcohol) Composite Foams for Electromagnetic Wave Shielding with Absorption-Dominated Feature," *ACS Appl Mater Interfaces*, vol. 11, no. 10, pp. 10198–10207, Mar. 2019, doi: 10.1021/acsami.8b21671.
- [415] J. Liu *et al.*, "Hydrophobic, Flexible, and Lightweight MXene Foams for High-Performance Electromagnetic-Interference Shielding," *Advanced Materials*, vol. 29, no. 38, Oct. 2017, doi: 10.1002/adma.201702367.
- [416] S. Subramanyam *et al.*, "Advancing sustainable energy storage with MXenes: A comprehensive analysis of fabrication techniques and applications," *J Energy Storage*, vol. 101, p. 114067, Nov. 2024, doi: 10.1016/j.est.2024.114067.
- [417] N. H. Solangi *et al.*, "Insight mechanism of MXene for the future generation of highly efficient energy storage device," *Materials Today Sustainability*, vol. 27, p. 100896, Sep. 2024, doi: 10.1016/j.mtsust.2024.100896.
- [418] S. He, Q. Zhu, R. A. Soomro, and B. Xu, "MXene derivatives for energy storage applications," *Sustain Energy Fuels*, vol. 4, no. 10, pp. 4988–5004, 2020, doi: 10.1039/D0SE00927J.
- [419] K. Li *et al.*, "3D MXene Architectures for Efficient Energy Storage and Conversion," *Adv Funct Mater*, vol. 30, no. 47, Nov. 2020, doi: 10.1002/adfm.202000842.
- [420] T. Guo *et al.*, "Rational Design of $Ti_3C_2T_x$ MXene Inks for Conductive, Transparent Films," *ACS Nano*, vol. 17, no. 4, pp. 3737–3749, Feb. 2023, doi: 10.1021/acsnano.2c11180.
- [421] D. Wen *et al.*, "Inkjet Printing Transparent and Conductive MXene ($Ti_3C_2T_x$) Films: A Strategy for Flexible Energy Storage Devices," *ACS Appl Mater Interfaces*, vol. 13, no. 15, pp. 17766–17780, Apr. 2021, doi: 10.1021/acsami.1c00724.
- [422] Y. Deng *et al.*, "Transparent electromagnetic interference shielding materials using MXene," *Carbon Energy*, vol. 6, no. 11, Nov. 2024, doi: 10.1002/cey2.593.
- [423] W. Li *et al.*, "Multilayer-structured transparent MXene/PVDF film with excellent dielectric and energy storage performance," *J Mater Chem C Mater*, vol. 7, no. 33, pp. 10371–10378, 2019, doi: 10.1039/C9TC02715G.

- [424] C. (John) Zhang and V. Nicolosi, "Graphene and MXene-based transparent conductive electrodes and supercapacitors," *Energy Storage Mater*, vol. 16, pp. 102–125, Jan. 2019, doi: 10.1016/j.ensm.2018.05.003.
- [425] C. J. Zhang *et al.*, "Transparent, Flexible, and Conductive 2D Titanium Carbide (MXene) Films with High Volumetric Capacitance," *Advanced Materials*, vol. 29, no. 36, Sep. 2017, doi: 10.1002/adma.201702678.
- [426] M. Y. Jung, C. Lee, J. Park, J. W. Son, Y. J. Yun, and Y. Jun, "Transparent supercapacitors with networked MXene on NiCo-layered double hydroxide," *Chemical Engineering Journal*, vol. 490, Jun. 2024, doi: 10.1016/j.cej.2024.151556.
- [427] S. Guo *et al.*, "MXene-based all-solid flexible electrochromic microsupercapacitor," *Microsyst Nanoeng*, vol. 10, no. 1, Dec. 2024, doi: 10.1038/s41378-024-00720-6.
- [428] Y. Wang, Y. Yuan, H. Y. Geng, W. Yang, and X. Chen, "Boosting Ion Diffusion Kinetics of MXene Inks with Water-in-Salt Electrolyte for Screen-Printed Micro-Supercapacitors," *Adv Funct Mater*, vol. 34, no. 34, Aug. 2024, doi: 10.1002/adfm.202400887.
- [429] L. Li, W. Liu, K. Jiang, D. Chen, F. Qu, and G. Shen, "In-Situ Annealed Ti₃C₂T_x MXene Based All-Solid-State Flexible Zn-Ion Hybrid Micro Supercapacitor Array with Enhanced Stability," *Nanomicro Lett*, vol. 13, no. 1, Dec. 2021, doi: 10.1007/s40820-021-00634-2.
- [430] M. Hu *et al.*, "A flour-based one-stop supercapacitor with intrinsic self-healability and stretchability after self-healing and biodegradability," *Energy Storage Mater*, vol. 21, pp. 174–179, Sep. 2019, doi: 10.1016/j.ensm.2018.12.013.
- [431] Y. Yue *et al.*, "Highly Self-Healable 3D Microsupercapacitor with MXene–Graphene Composite Aerogel," *ACS Nano*, vol. 12, no. 5, pp. 4224–4232, May 2018, doi: 10.1021/acsnano.7b07528.
- [432] Y. Yue *et al.*, "Highly Self-Healable 3D Microsupercapacitor with MXene–Graphene Composite Aerogel," *ACS Nano*, vol. 12, no. 5, pp. 4224–4232, May 2018, doi: 10.1021/acsnano.7b07528.
- [433] J. S. Choi, J. S. Meena, S. Bin Choi, S. B. Jung, and J. W. Kim, "Water-Triggered Self-Healing of Ti₃C₂T_x MXene Standalone Electrodes: Systematic Examination of Factors Affecting the Healing Process," *Small*, vol. 20, no. 20, May 2024, doi: 10.1002/smll.202306434.
- [434] Y. Zhang *et al.*, "Mussel-inspired self-healing adhesive MXene hydrogel for epidermal electronics," *Device*, vol. 2, no. 3, Mar. 2024, doi: 10.1016/j.device.2023.100253.
- [435] K. Chen *et al.*, "Ultra-stretchable, adhesive, and self-healing MXene/polyampholytes hydrogel as flexible and wearable epidermal sensors," *Colloids Surf A Physicochem Eng Asp*, vol. 645, Jul. 2022, doi: 10.1016/j.colsurfa.2022.128897.

- [436] W. Ma, W. Cai, W. Chen, P. Liu, J. Wang, and Z. Liu, "A novel structural design of shielding capsule to prepare high-performance and self-healing MXene-based sponge for ultra-efficient electromagnetic interference shielding," *Chemical Engineering Journal*, vol. 426, Dec. 2021, doi: 10.1016/j.cej.2021.130729.
- [437] J. N. Ma *et al.*, "Heterogeneous self-healing assembly of MXene and graphene oxide enables producing free-standing and self-reparable soft electronics and robots," *Sci Bull (Beijing)*, vol. 67, no. 5, pp. 501–511, Mar. 2022, doi: 10.1016/j.scib.2021.11.015.
- [438] X. Li *et al.*, "Self-Healing Microsupercapacitors with Size-Dependent 2D MXene," *ChemElectroChem*, vol. 7, no. 3, pp. 821–829, Feb. 2020, doi: 10.1002/celc.201902099.
- [439] J. Tian, Z. Sun, C. Shi, and Z. Huang, "Rapid fabrication of tough sodium alginate/MXene/poly(vinyl alcohol) dual-network hydrogel electrolytes for flexible all-solid-state supercapacitors," Sep. 01, 2023, Elsevier B.V. doi: 10.1016/j.ijbiomac.2023.125937.
- [440] Y. Cheng *et al.*, "Maximizing the ion accessibility and high mechanical strength in nanoscale ion channel MXene electrodes for high-capacity zinc-ion energy storage," *Sci Bull (Beijing)*, vol. 67, no. 21, pp. 2216–2224, Nov. 2022, doi: 10.1016/j.scib.2022.10.003.
- [441] J. Liang, C. Jiang, and W. Wu, "Printed flexible supercapacitor: Ink formulation, printable electrode materials and applications," *Appl Phys Rev*, vol. 8, no. 2, Jun. 2021, doi: 10.1063/5.0048446.
- [442] X. Tian, "Direct ink writing of 2D material-based supercapacitors," *2d Mater*, vol. 9, no. 1, p. 012001, Jan. 2022, doi: 10.1088/2053-1583/ac3f43.
- [443] J. Azadmanjiri, N. R. Thuniki, F. Guzzetta, and Z. Sofer, "Liquid Metals-Assisted Synthesis of Scalable 2D Nanomaterials: Prospective Sediment Inks for Screen-Printed Energy Storage Applications," *Adv Funct Mater*, vol. 31, no. 17, Apr. 2021, doi: 10.1002/adfm.202010320.
- [444] T.-T. Huang and W. Wu, "Scalable nanomanufacturing of inkjet-printed wearable energy storage devices," *J Mater Chem A Mater*, vol. 7, no. 41, pp. 23280–23300, 2019, doi: 10.1039/C9TA05239A.
- [445] S. Xu *et al.*, "Binder-free Ti₃C₂T_x MXene electrode film for supercapacitor produced by electrophoretic deposition method," *Chemical Engineering Journal*, vol. 317, pp. 1026–1036, Jun. 2017, doi: 10.1016/j.cej.2017.02.144.
- [446] S. Uzun *et al.*, "Additive-Free Aqueous MXene Inks for Thermal Inkjet Printing on Textiles," *Small*, vol. 17, no. 1, Jan. 2021, doi: 10.1002/smll.202006376.
- [447] K. Maleski, V. N. Mochalin, and Y. Gogotsi, "Dispersions of Two-Dimensional Titanium Carbide MXene in Organic Solvents," *Chemistry of Materials*, vol. 29, no. 4, pp. 1632–1640, Feb. 2017, doi: 10.1021/acs.chemmater.6b04830.

- [448] A. VahidMohammadi, J. Rosen, and Y. Gogotsi, "The world of two-dimensional carbides and nitrides (MXenes)," *Science* (1979), vol. 372, no. 6547, Jun. 2021, doi: 10.1126/science.abf1581.
- [449] I. Ihsanullah, "MXenes (two-dimensional metal carbides) as emerging nanomaterials for water purification: Progress, challenges and prospects," *Chemical Engineering Journal*, vol. 388, p. 124340, May 2020, doi: 10.1016/j.cej.2020.124340.
- [450] S. Abdolhosseinzadeh *et al.*, "MXene Inks for High-Throughput Printing of Electronics," *Adv Electron Mater*, vol. 11, no. 2, Feb. 2025, doi: 10.1002/aelm.202400170.
- [451] A. Bhat, S. Anwer, K. S. Bhat, M. I. H. Mohideen, K. Liao, and A. Qurashi, "Prospects challenges and stability of 2D MXenes for clean energy conversion and storage applications," *NPJ 2D Mater Appl*, vol. 5, no. 1, p. 61, Jun. 2021, doi: 10.1038/s41699-021-00239-8.
- [452] S. Liu, G. Liu, G. Chen, G. Liu, and W. Jin, "Scale-up fabrication of two-dimensional material membranes: challenges and opportunities," *Curr Opin Chem Eng*, vol. 39, p. 100892, Mar. 2023, doi: 10.1016/j.coche.2022.100892.
- [453] I. Hussain *et al.*, "The rise of 4D printing Technology: 2D MXenes for different applications," *Chemical Engineering Journal*, vol. 508, p. 160856, Mar. 2025, doi: 10.1016/j.cej.2025.160856.
- [454] R. Krishnamoorthy and S. R. Das, "Inkjet-printed flexible MXetronics : Present status and future prospects," *Applied Research*, vol. 3, no. 4, Aug. 2024, doi: 10.1002/appl.202300085.
- [455] Z. Aghayar, M. Malaki, and Y. Zhang, "MXene-Based Ink Design for Printed Applications," *Nanomaterials*, vol. 12, no. 23, p. 4346, Dec. 2022, doi: 10.3390/nano12234346.
- [456] M. Kaleem Shabbir *et al.*, "Two-Dimensional MXene-Based Electrocatalysts: Challenges and Opportunities," *The Chemical Record*, vol. 24, no. 8, Aug. 2024, doi: 10.1002/tcr.202400047.
- [457] J. H. Kim *et al.*, "Large-Area $Ti_3C_2T_x$ -MXene Coating: Toward Industrial-Scale Fabrication and Molecular Separation," *ACS Nano*, vol. 15, no. 5, pp. 8860–8869, May 2021, doi: 10.1021/acsnano.1c01448.
- [458] X. Chen, R. Yang, and X. Wu, "Printing of MXene-based materials and the applications: a state-of-the-art review," *2d Mater*, vol. 9, no. 4, p. 042002, Oct. 2022, doi: 10.1088/2053-1583/ac8009.
- [459] H. Li and J. Liang, "Recent Development of Printed Micro-Supercapacitors: Printable Materials, Printing Technologies, and Perspectives," *Advanced Materials*, vol. 32, no. 3, Jan. 2020, doi: 10.1002/adma.201805864.

- [460] J. Ma *et al.*, "Aqueous MXene/PH1000 Hybrid Inks for Inkjet-Printing Micro-Supercapacitors with Unprecedented Volumetric Capacitance and Modular Self-Powered Microelectronics," *Adv Energy Mater*, vol. 11, no. 23, Jun. 2021, doi: 10.1002/aenm.202100746.
- [461] E. Quain *et al.*, "Direct Writing of Additive-Free MXene-in-Water Ink for Electronics and Energy Storage," *Adv Mater Technol*, vol. 4, no. 1, Jan. 2019, doi: 10.1002/admt.201800256.
- [462] H. Li and J. Liang, "Recent Development of Printed Micro-Supercapacitors: Printable Materials, Printing Technologies, and Perspectives," *Advanced Materials*, vol. 32, no. 3, Jan. 2020, doi: 10.1002/adma.201805864.
- [463] T. Trantidou, Y. Elani, E. Parsons, and O. Ces, "Hydrophilic surface modification of PDMS for droplet microfluidics using a simple, quick, and robust method via PVA deposition," *Microsyst Nanoeng*, vol. 3, no. 1, p. 16091, Apr. 2017, doi: 10.1038/micronano.2016.91.
- [464] A. Sajedi-Moghaddam, E. Rahmanian, and N. Naseri, "Inkjet-Printing Technology for Supercapacitor Application: Current State and Perspectives," *ACS Appl Mater Interfaces*, vol. 12, no. 31, pp. 34487–34504, Aug. 2020, doi: 10.1021/acsami.0c07689.
- [465] G. Hu *et al.*, "Functional inks and printing of two-dimensional materials," *Chem Soc Rev*, vol. 47, no. 9, pp. 3265–3300, 2018, doi: 10.1039/C8CS00084K.
- [466] H. Huang *et al.*, " $Ti_{3-x}C_2T_x$ MXene-Based Micro-Supercapacitors with Ultrahigh Volumetric Energy Density for All-in-One Si-Electronics," *ACS Nano*, vol. 16, no. 3, pp. 3776–3784, Mar. 2022, doi: 10.1021/acsnano.1c08172.
- [467] T. Trantidou, Y. Elani, E. Parsons, and O. Ces, "Hydrophilic surface modification of PDMS for droplet microfluidics using a simple, quick, and robust method via PVA deposition," *Microsyst Nanoeng*, vol. 3, no. 1, p. 16091, Apr. 2017, doi: 10.1038/micronano.2016.91.
- [468] K. Mao *et al.*, "High-capacitance MXene anode based on Zn-ion pre-intercalation strategy for degradable micro Zn-ion hybrid supercapacitors," *Nano Energy*, vol. 103, p. 107791, Dec. 2022, doi: 10.1016/j.nanoen.2022.107791.
- [469] X. Feng *et al.*, "Functional integrated electromagnetic interference shielding in flexible micro-supercapacitors by cation-intercalation typed Ti_3C_2Tx MXene," *Nano Energy*, vol. 72, p. 104741, Jun. 2020, doi: 10.1016/j.nanoen.2020.104741.
- [470] B. Derby, "Inkjet Printing of Functional and Structural Materials: Fluid Property Requirements, Feature Stability, and Resolution," *Annu Rev Mater Res*, vol. 40, no. 1, pp. 395–414, Jun. 2010, doi: 10.1146/annurev-matsci-070909-104502.

- [471] X. Jiang *et al.*, "Inkjet-printed MXene micro-scale devices for integrated broadband ultrafast photonics," *NPJ 2D Mater Appl*, vol. 3, no. 1, p. 34, Sep. 2019, doi: 10.1038/s41699-019-0117-3.
- [472] K. Maleski, V. N. Mochalin, and Y. Gogotsi, "Dispersions of Two-Dimensional Titanium Carbide MXene in Organic Solvents," *Chemistry of Materials*, vol. 29, no. 4, pp. 1632–1640, Feb. 2017, doi: 10.1021/acs.chemmater.6b04830.
- [473] V. Kamysbayev *et al.*, "Covalent surface modifications and superconductivity of two-dimensional metal carbide MXenes," *Science* (1979), vol. 369, no. 6506, pp. 979–983, Aug. 2020, doi: 10.1126/science.aba8311.
- [474] J. Azadmanjiri *et al.*, "Prospective advances in MXene inks: screen printable sediments for flexible micro-supercapacitor applications," *J Mater Chem A Mater*, vol. 10, no. 9, pp. 4533–4557, 2022, doi: 10.1039/D1TA09334G.
- [475] C. Zhang *et al.*, "Additive-free MXene inks and direct printing of micro-supercapacitors," *Nat Commun*, vol. 10, no. 1, p. 1795, Apr. 2019, doi: 10.1038/s41467-019-09398-1.
- [476] W. A. Haider *et al.*, "Structural Engineering and Coupling of Two-Dimensional Transition Metal Compounds for Micro-Supercapacitor Electrodes," *ACS Cent Sci*, vol. 6, no. 11, pp. 1901–1915, Nov. 2020, doi: 10.1021/acscentsci.0c01022.
- [477] K. Maleski, C. E. Ren, M.-Q. Zhao, B. Anasori, and Y. Gogotsi, "Size-Dependent Physical and Electrochemical Properties of Two-Dimensional MXene Flakes," *ACS Appl Mater Interfaces*, vol. 10, no. 29, pp. 24491–24498, Jul. 2018, doi: 10.1021/acsami.8b04662.
- [478] S. Abdolhosseinzadeh, X. Jiang, H. Zhang, J. Qiu, and C. (John) Zhang, "Perspectives on solution processing of two-dimensional MXenes," *Materials Today*, vol. 48, pp. 214–240, Sep. 2021, doi: 10.1016/j.mattod.2021.02.010.
- [479] K. Mao *et al.*, "High-capacitance MXene anode based on Zn-ion pre-intercalation strategy for degradable micro Zn-ion hybrid supercapacitors," *Nano Energy*, vol. 103, p. 107791, Dec. 2022, doi: 10.1016/j.nanoen.2022.107791.
- [480] X. Feng *et al.*, "Functional integrated electromagnetic interference shielding in flexible micro-supercapacitors by cation-intercalation typed Ti₃C₂T_x MXene," *Nano Energy*, vol. 72, p. 104741, Jun. 2020, doi: 10.1016/j.nanoen.2020.104741.
- [481] J. Luo *et al.*, "Pillared Structure Design of MXene with Ultralarge Interlayer Spacing for High-Performance Lithium-Ion Capacitors," *ACS Nano*, vol. 11, no. 3, pp. 2459–2469, Mar. 2017, doi: 10.1021/acsnano.6b07668.
- [482] S. Zheng *et al.*, "Ionic liquid pre-intercalated MXene films for ionogel-based flexible micro-supercapacitors with high volumetric energy density," *J Mater Chem A Mater*, vol. 7, no. 16, pp. 9478–9485, 2019, doi: 10.1039/C9TA02190F.

- [483] Q. Zhang, H. Lai, R. Fan, P. Ji, X. Fu, and H. Li, "High Concentration of $Ti_3C_2T_x$ MXene in Organic Solvent," *ACS Nano*, vol. 15, no. 3, pp. 5249–5262, Mar. 2021, doi: 10.1021/acsnano.0c10671.
- [484] Q. Gao, M. Feng, E. Li, C. Liu, C. Shen, and X. Liu, "Mechanical, Thermal, and Rheological Properties of $Ti_3C_2T_x$ MXene/ Thermoplastic Polyurethane Nanocomposites," *Macromol Mater Eng*, vol. 305, no. 10, Oct. 2020, doi: 10.1002/mame.202000343.
- [485] E. Guzmán, J. Tajuelo, J. M. Pastor, M. Á. Rubio, F. Ortega, and R. G. Rubio, "Shear rheology of fluid interfaces: Closing the gap between macro- and micro-rheology," *Curr Opin Colloid Interface Sci*, vol. 37, pp. 33–48, Sep. 2018, doi: 10.1016/j.cocis.2018.05.004.
- [486] A. Sajedi-Moghaddam, E. Rahmanian, and N. Naseri, "Inkjet-Printing Technology for Supercapacitor Application: Current State and Perspectives," *ACS Appl Mater Interfaces*, vol. 12, no. 31, pp. 34487–34504, Aug. 2020, doi: 10.1021/acsami.0c07689.
- [487] S. Naficy *et al.*, "Graphene oxide dispersions: tuning rheology to enable fabrication," *Mater. Horiz.*, vol. 1, no. 3, pp. 326–331, 2014, doi: 10.1039/C3MH00144J.
- [488] B. Akuzum *et al.*, "Rheological Characteristics of 2D Titanium Carbide (MXene) Dispersions: A Guide for Processing MXenes," *ACS Nano*, vol. 12, no. 3, pp. 2685–2694, Mar. 2018, doi: 10.1021/acsnano.7b08889.
- [489] K. A. S. Usman *et al.*, "Inducing liquid crystallinity in dilute MXene dispersions for facile processing of multifunctional fibers," *J Mater Chem A Mater*, vol. 10, no. 9, pp. 4770–4781, 2022, doi: 10.1039/D1TA09547A.
- [490] A. Kamyshny and S. Magdassi, "Conductive nanomaterials for 2D and 3D printed flexible electronics," *Chem Soc Rev*, vol. 48, no. 6, pp. 1712–1740, 2019, doi: 10.1039/C8CS00738A.
- [491] M. Greaves, M. Mende, J. Wang, W. Yang, and S. Barg, "Investigating the rheology of 2D titanium carbide (MXene) dispersions for colloidal processing: Progress and challenges," *J Mater Res*, vol. 36, no. 22, pp. 4578–4600, Nov. 2021, doi: 10.1557/s43578-021-00282-7.
- [492] W. Yang *et al.*, "3D Printing of Freestanding MXene Architectures for Current-Collector-Free Supercapacitors," *Advanced Materials*, vol. 31, no. 37, Sep. 2019, doi: 10.1002/adma.201902725.
- [493] J. Zhang *et al.*, "Additive-Free MXene Liquid Crystals and Fibers," *ACS Cent Sci*, vol. 6, no. 2, pp. 254–265, Feb. 2020, doi: 10.1021/acscentsci.9b01217.
- [494] Z. Fan *et al.*, "3D Printing of Porous Nitrogen-Doped Ti_3C_2 MXene Scaffolds for High-Performance Sodium-Ion Hybrid Capacitors," *ACS Nano*, vol. 14, no. 1, pp. 867–876, Jan. 2020, doi: 10.1021/acsnano.9b08030.

- [495] Y. Wu *et al.*, "Surface terminals reconstruction: The way to widen the output voltage of MXene-based aqueous symmetrical micro-supercapacitors," *Nano Res*, vol. 16, no. 5, pp. 6780–6788, May 2023, doi: 10.1007/s12274-022-5262-x.
- [496] H. Huang *et al.*, "Ti₃C₂T_x MXene-Based Micro-Supercapacitors with Ultrahigh Volumetric Energy Density for All-in-One Si-Electronics," *ACS Nano*, vol. 16, no. 3, pp. 3776–3784, Mar. 2022, doi: 10.1021/acsnano.1c08172.
- [497] Y. Shao *et al.*, "Room-temperature high-precision printing of flexible wireless electronics based on MXene inks," *Nat Commun*, vol. 13, no. 1, Dec. 2022, doi: 10.1038/s41467-022-30648-2.
- [498] A. Sajedi-Moghaddam, E. Rahmanian, and N. Naseri, "Inkjet-printing technology for supercapacitor application: Current state and perspectives," *ACS Appl Mater Interfaces*, vol. 12, no. 31, pp. 34487–34504, 2020.
- [499] Q. Zhang *et al.*, "Direct Ink Writing of Moldable Electrochemical Energy Storage Devices: Ongoing Progress, Challenges, and Prospects," *Adv Eng Mater*, vol. 23, no. 7, Jul. 2021, doi: 10.1002/adem.202100068.
- [500] M. Li *et al.*, "3D Printed Supercapacitor: Techniques, Materials, Designs, and Applications," *Adv Funct Mater*, vol. 33, no. 1, Jan. 2023, doi: 10.1002/adfm.202208034.
- [501] P. Jiang, Z. Ji, X. Zhang, Z. Liu, and X. Wang, "Recent advances in direct ink writing of electronic components and functional devices," *Progress in Additive Manufacturing*, vol. 3, no. 1–2, pp. 65–86, Jun. 2018, doi: 10.1007/s40964-017-0035-x.
- [502] J. Yan *et al.*, "Direct-ink writing 3D printed energy storage devices: From material selectivity, design and optimization strategies to diverse applications," *Materials Today*, vol. 54, pp. 110–152, Apr. 2022, doi: 10.1016/j.mattod.2022.03.014.
- [503] A. Paul, N. C. Murmu, and T. Kuila, "Current trends in micro-supercapacitor devices," *EcoEnergy*, vol. 3, no. 1, pp. 3–24, Mar. 2025, doi: 10.1002/ece2.71.
- [504] M. Montanino and G. Sico, "Gravure Printing for Lithium-Ion Batteries Manufacturing: A Review," *Batteries*, vol. 9, no. 11, p. 535, Oct. 2023, doi: 10.3390/batteries9110535.
- [505] C. Zhao, Y. Liu, S. Beirne, J. Razal, and J. Chen, "Recent Development of Fabricating Flexible Micro-Supercapacitors for Wearable Devices," *Adv Mater Technol*, vol. 3, no. 9, Sep. 2018, doi: 10.1002/admt.201800028.
- [506] Y.-Z. Zhang *et al.*, "Printed supercapacitors: materials, printing and applications," *Chem Soc Rev*, vol. 48, no. 12, pp. 3229–3264, 2019, doi: 10.1039/C7CS00819H.
- [507] J. Azadmanjiri *et al.*, "Prospective advances in MXene inks: screen printable sediments for flexible micro-supercapacitor applications," *J Mater Chem A Mater*, vol. 10, no. 9, pp. 4533–4557, 2022, doi: 10.1039/D1TA09334G.

- [508] Y. C. Goswami and S. Begzaad, "Printable supercapacitors and their printing technologies: A review," *Energy Storage*, vol. 6, no. 4, Jun. 2024, doi: 10.1002/est2.666.
- [509] R. R. Suresh *et al.*, "Fabrication of screen-printed electrodes: opportunities and challenges," *J Mater Sci*, vol. 56, no. 15, pp. 8951–9006, May 2021, doi: 10.1007/s10853-020-05499-1.
- [510] L. Liu, Y. Feng, and W. Wu, "Recent progress in printed flexible solid-state supercapacitors for portable and wearable energy storage," *J Power Sources*, vol. 410–411, pp. 69–77, Jan. 2019, doi: 10.1016/j.jpowsour.2018.11.012.
- [511] H. Li, J. Luo, S. Ding, and J. Ding, "Laser-machined micro-supercapacitors: from microstructure engineering to smart integrated systems," *Nanoscale*, vol. 16, no. 31, pp. 14574–14588, 2024, doi: 10.1039/D4NR01860E.
- [512] H. Liu, Z. Sun, Y. Chen, W. Zhang, X. Chen, and C.-P. Wong, "Laser Processing of Flexible In-Plane Micro-supercapacitors: Progresses in Advanced Manufacturing of Nanostructured Electrodes," *ACS Nano*, vol. 16, no. 7, pp. 10088–10129, Jul. 2022, doi: 10.1021/acsnano.2c02812.
- [513] R. Kumar *et al.*, "Laser processing of graphene and related materials for energy storage: State of the art and future prospects," *Prog Energy Combust Sci*, vol. 91, p. 100981, Jul. 2022, doi: 10.1016/j.pecs.2021.100981.
- [514] S. Zhu, Z. Xu, H. Tao, D. Yang, X. Tang, and Y. Wang, "Planar micro-supercapacitors toward high performance energy storage devices: design, application and prospects," *Energy Advances*, vol. 2, no. 6, pp. 765–783, 2023, doi: 10.1039/D3YA00080J.
- [515] C. Zhu, Y. Fu, and Y. Yu, "Designed Nanoarchitectures by Electrostatic Spray Deposition for Energy Storage," *Advanced Materials*, vol. 31, no. 1, Jan. 2019, doi: 10.1002/adma.201803408.
- [516] J. Wang, F. Li, F. Zhu, and O. G. Schmidt, "Recent Progress in Micro-Supercapacitor Design, Integration, and Functionalization," *Small Methods*, vol. 3, no. 8, Aug. 2019, doi: 10.1002/smtd.201800367.
- [517] J. Qiu, H. Zhao, and Y. Lei, "Emerging smart design of electrodes for micro-supercapacitors: A review," *SmartMat*, vol. 3, no. 3, pp. 447–473, Sep. 2022, doi: 10.1002/smm2.1094.
- [518] P. Zhang *et al.*, "Advanced Three-Dimensional Microelectrode Architecture Design for High-Performance On-Chip Micro-Supercapacitors," *ACS Nano*, vol. 16, no. 11, pp. 17593–17612, Nov. 2022, doi: 10.1021/acsnano.2c07609.
- [519] Q. Muhammad Saqib *et al.*, "Miniaturizing Power: Harnessing Micro-Supercapacitors for advanced micro-electronics," *Chemical Engineering Journal*, vol. 490, p. 151857, Jun. 2024, doi: 10.1016/j.cej.2024.151857.

- [520] M. M. Baig *et al.*, "3D printing of hydrogels for flexible micro-supercapacitors," *FlexMat*, vol. 1, no. 1, pp. 79–99, Apr. 2024, doi: 10.1002/flm2.14.
- [521] D. Qi, Y. Liu, Z. Liu, L. Zhang, and X. Chen, "Design of Architectures and Materials in In-Plane Micro-supercapacitors: Current Status and Future Challenges," *Advanced Materials*, vol. 29, no. 5, Feb. 2017, doi: 10.1002/adma.201602802.
- [522] M. Beidaghi and Y. Gogotsi, "Capacitive energy storage in micro-scale devices: recent advances in design and fabrication of micro-supercapacitors," *Energy Environ Sci*, vol. 7, no. 3, p. 867, 2014, doi: 10.1039/c3ee43526a.
- [523] F. Li *et al.*, "Recent developments of stamped planar micro-supercapacitors: Materials, fabrication and perspectives," *Nano Materials Science*, vol. 3, no. 2, pp. 154–169, Jun. 2021, doi: 10.1016/j.nanoms.2020.10.003.
- [524] S. Hwang, T. Hwang, H. Kong, S. Lee, and J. Yeo, "Novel fabrication method of hierarchical planar micro-supercapacitor via laser-induced localized growth of manganese dioxide nanowire arrays," *Appl Surf Sci*, vol. 552, p. 149382, Jun. 2021, doi: 10.1016/j.apsusc.2021.149382.
- [525] J. Qin *et al.*, "2D In-Plane Mesoporous N-Doped Carbon for Co-Planar Integrated Microsystem of Micro-Supercapacitor and Pressure Sensor," *Small Methods*, Mar. 2025, doi: 10.1002/smtd.202402205.
- [526] N. Kurra, B. Ahmed, Y. Gogotsi, and H. N. Alshareef, "MXene-on-Paper Coplanar Microsupercapacitors," *Adv Energy Mater*, vol. 6, no. 24, Dec. 2016, doi: 10.1002/aenm.201601372.
- [527] X. Huang and P. Wu, "A Facile, High-Yield, and Freeze-and-Thaw-Assisted Approach to Fabricate MXene with Plentiful Wrinkles and Its Application in On-Chip Micro-Supercapacitors," *Adv Funct Mater*, vol. 30, no. 12, Mar. 2020, doi: 10.1002/adfm.201910048.
- [528] Y. Zhang *et al.*, "Flexible Self-Powered Integrated Sensing System with 3D Periodic Ordered Black Phosphorus@MXene Thin-Films," *Advanced Materials*, vol. 33, no. 22, Jun. 2021, doi: 10.1002/adma.202007890.
- [529] C. Zhang *et al.*, "Stamping of flexible, coplanar micro-supercapacitors using MXene inks," *Adv Funct Mater*, vol. 28, no. 9, p. 1705506, 2018.
- [530] X. Li, H. Li, X. Fan, X. Shi, and J. Liang, "3D-Printed Stretchable Micro-Supercapacitor with Remarkable Areal Performance," *Adv Energy Mater*, vol. 10, no. 14, p. 1903794, Apr. 2020, doi: 10.1002/aenm.201903794.
- [531] Y.-Y. Peng *et al.*, "All-MXene (2D titanium carbide) solid-state microsupercapacitors for on-chip energy storage," *Energy Environ Sci*, vol. 9, no. 9, pp. 2847–2854, 2016, doi: 10.1039/C6EE01717G.

- [532] N. Kurra, B. Ahmed, Y. Gogotsi, and H. N. Alshareef, "MXene-on-Paper Coplanar Microsupercapacitors," *Adv Energy Mater*, vol. 6, no. 24, p. 1601372, Dec. 2016, doi: 10.1002/aenm.201601372.
- [533] B.-S. Shen, H. Wang, L.-J. Wu, R.-S. Guo, Q. Huang, and X.-B. Yan, "All-solid-state flexible microsupercapacitor based on two-dimensional titanium carbide," *Chinese Chemical Letters*, vol. 27, no. 10, pp. 1586–1591, Oct. 2016, doi: 10.1016/j.cclet.2016.04.012.
- [534] H. Huang *et al.*, "Extraordinary Areal and Volumetric Performance of Flexible Solid-State Micro-Supercapacitors Based on Highly Conductive Freestanding $Ti_3C_2T_x$ Films," *Adv Electron Mater*, vol. 4, no. 8, Aug. 2018, doi: 10.1002/aelm.201800179.
- [535] P. Li *et al.*, "Fabrication of high-performance MXene-based all-solid-state flexible microsupercapacitor based on a facile scratch method," *Nanotechnology*, vol. 29, no. 44, p. 445401, Nov. 2018, doi: 10.1088/1361-6528/aadad4.
- [536] E. Quain *et al.*, "Direct Writing of Additive-Free MXene-in-Water Ink for Electronics and Energy Storage," *Adv Mater Technol*, vol. 4, no. 1, Jan. 2019, doi: 10.1002/admt.201800256.
- [537] S. Xu, W. Liu, X. Liu, X. Kuang, and X. Wang, "A MXene based all-solid-state microsupercapacitor with 3D interdigital electrode," in *2017 19th International Conference on Solid-State Sensors, Actuators and Microsystems (TRANSDUCERS)*, IEEE, Jun. 2017, pp. 706–709. doi: 10.1109/TRANSDUCERS.2017.7994146.
- [538] C. Couly *et al.*, "Asymmetric Flexible MXene-Reduced Graphene Oxide Micro-Supercapacitor," *Adv Electron Mater*, vol. 4, no. 1, Jan. 2018, doi: 10.1002/aelm.201700339.
- [539] N. Wang, J. Liu, Y. Zhao, M. Hu, R. Qin, and G. Shan, "Laser-Cutting Fabrication of Mxene-Based Flexible Micro-Supercapacitors with High Areal Capacitance," *ChemNanoMat*, vol. 5, no. 5, pp. 658–665, May 2019, doi: 10.1002/cnma.201800674.
- [540] H. Hu, Z. Bai, B. Niu, M. Wu, and T. Hua, "Binder-free bonding of modularized MXene thin films into thick film electrodes for on-chip micro-supercapacitors with enhanced areal performance metrics," *J Mater Chem A Mater*, vol. 6, no. 30, pp. 14876–14884, 2018, doi: 10.1039/C8TA04737E.
- [541] N. Darmiani, A. Iraji zad, A. Esfandiar, and P. Asen, "Cauliflower-Like Ni/MXene-Bridged Fiber-Shaped Electrode for Flexible Microsupercapacitor," *Energy & Fuels*, vol. 36, no. 4, pp. 2140–2148, Feb. 2022, doi: 10.1021/acs.energyfuels.1c03618.
- [542] Q. Jiang *et al.*, "MXene electrochemical microsupercapacitor integrated with triboelectric nanogenerator as a wearable self-charging power unit," *Nano Energy*, vol. 45, pp. 266–272, Mar. 2018, doi: 10.1016/j.nanoen.2018.01.004.
- [543] T. Cheng *et al.*, "Flexible Transparent Bifunctional Capacitive Sensors with Superior Areal Capacitance and Sensing Capability based on PEDOT:PSS/MXene/Ag Grid

Hybrid Electrodes," *Adv Funct Mater*, vol. 33, no. 5, Jan. 2023, doi: 10.1002/adfm.202210997.

- [544] P. Sun *et al.*, "Nitrogen and sulfur co-doped MXene ink without additive for high-performance inkjet-printing micro-supercapacitors," *Chemical Engineering Journal*, vol. 450, p. 138372, Dec. 2022, doi: 10.1016/j.cej.2022.138372.
- [545] A. Sangili *et al.*, "Stable carbon encapsulated titanium carbide MXene aqueous ink for fabricating high-performance supercapacitors," *Energy Storage Mater*, vol. 53, pp. 51–61, Dec. 2022, doi: 10.1016/j.ensm.2022.08.038.
- [546] D. Wen *et al.*, "Direct inkjet printing of flexible MXene/graphene composite films for supercapacitor electrodes," *J Alloys Compd*, vol. 900, p. 163436, Apr. 2022, doi: 10.1016/j.jallcom.2021.163436.
- [547] D. Wen *et al.*, "Inkjet Printing Transparent and Conductive MXene ($Ti_3C_2T_x$) Films: A Strategy for Flexible Energy Storage Devices," *ACS Appl Mater Interfaces*, vol. 13, no. 15, pp. 17766–17780, Apr. 2021, doi: 10.1021/acsami.1c00724.
- [548] H. Li *et al.*, "Flexible All-Solid-State Supercapacitors with High Volumetric Capacitances Boosted by Solution Processable MXene and Electrochemically Exfoliated Graphene," *Adv Energy Mater*, vol. 7, no. 4, p. 1601847, Feb. 2017, doi: 10.1002/aenm.201601847.

Credit author statement

Jyoti Prakash Das: Writing-original draft, methodology, conceptualization, formal analysis, software
Dr. V. Navakoteswara Rao: Writing-review and editing, validation, formal analysis.
Prof. Sang-Jae Kim: Writing-review and editing, resources, project administration, supervision

Declaration of interests

The authors declare that they have no known competing financial interests or personal relationships that could have appeared to influence the work reported in this paper.

The authors declare the following financial interests/personal relationships which may be considered as potential competing interests: